2531

NASA
Contractor Report 175048

USAAVSCOM
Technical Report 86-C-4

Thermal-Mechanical Fatigue Behavior of Nickel-Base Superalloys

R.M. Pelloux and N. Marchand
Massachusetts Institute of Technology
Cambridge, Massachusetts

March 1986

Prepared for
Lewis Research Center
Under Grant NAG 3-280

NASA
National Aeronautics and
Space Administration

U.S. ARMY AVIATION SYSTEMS COMMAND

Contents

Introduction

Any component exposed to repeated rapid thermal transients will fail by thermal fatigue. Thermal fatigue degradation mechanisms involve accumulation of damage, crack initiation, slow crack growth and failure by fast fracture.

The material properties other than ductility which are important in thermal fatigue are hot tensile strength, elastic modulus, thermal conductivity and thermal expansion. Oxidation resistance also plays an important role in thermal fatigue. The interactions between material properties, imposed thermal cycle, and component geometry define the ability of a structure to resist thermal fatigue. However, the synergistic effects between these variables are quite complex, and prediction of thermal fatigue behavior from basic properties is difficult. A major objective of most high-temperature fatigue programs is to develop and verify models for thermal fatigue by comparing experimental data with analytical and/or computer-derived predictions of thermal fatigue life.

Prediction of crack propagation rates in structural components from specimen data generated in the laboratory is only possible if a parameter can be found which characterizes the severity of the stress and strain cycles near the crack tip. Such a parameter is needed to match a particular loading and crack length in a component with the correct equivalent specimen loading and crack length. In cases of cyclic loading mainly involving linear elastic deformation (small scale yielding), the stress intensity factor (ΔK) is a widely used and successful parameter. However, the stress intensity factor may not be

applicable for some hot section components, since in these areas cracks may grow through regions of substantial plastic deformation.

The prediction of propagation life in engine components requires the consideration of thermal-mechanical fatigue (TMF) cycles. The problem of thermomechanically driven crack growth in the presence of significant inelastic strains is a challenging problem. In order for a single parameter to be useful for predicting thermal-mechanical crack growth in components, it should satisfy the following conditions:

1) It should predict crack growth rate from a single crack growth rate versus parameter curve. In this way, cracks of different lengths loaded in such a way as to yield the same value of the parameter, experience the same crack growth rate.
2) It should correctly predict fatigue crack growth rates independently of part geometry.
3) It should be calculable for complex real part geometries.

Obviously, parameters not satisfying the above requirements would be of limited value, since component or simulated component testing would always be required to obtain crack growth rate information.

In this research program, it was proposed to asses the suitability of various parameters for correlating high temperature and thermal-mechanical crack growth rates. A parameter was sought which can correlate data for the full range of conditions from elastic stress and strain cycling to substantially plastic strain cycling. The ultimate goal of establishing such a parameter is

the prediction of the propagation life of real engine components, since it is known that cracks initiate early in fatigue life.

As secondary goals, the crack growth data generated were combined with optical, SEM, and TEM observations to assess a sound fundamental mechanistic understanding of the thermal-mechanical fatigue behavior of typical nickel-based superalloys.

Program Approach

Fatigue crack growth data in TMF conditions have been obtained on tubular specimens for many years [1]. This specimen geometry prevents the formation of thermal gradients in the cross section of the materials, thus facilitating the data reduction step. The TMF crack growth data were reduced [2] using ΔK_{ε}, ΔK, ΔJ, $\Delta CTOD$ and Tomkin's model. All of them (except $\Delta CTOD$) failed to predict the TMF data within a factor of five. One of the main problems with the analysis of the fracture mechanics data of tubular specimen is that there is no well-established equation which describes the state of stress and strain ahead of a crack when significant plastic deformation takes place. This is not surprising because all the equations developed for this geometry have assumed a pure elastic behavior.

In order to achieve our main goal, thermal-mechanical fatigue data were obtained on conventional fracture mechanics specimens (SEN) for which well-established equations to describe the stress-strain field ahead of the crack exist. The data generated by the test procedure (cycling under stress or strain control) were analyzed in terms of the mechanical stresses and strains, and

thermal stresses and strains, in order to assess their respective influence on crack growth behavior. Using these values and known fracture mechanics solutions, various fracture mechanics parameters were computed in order to estimate which one is the best and how it can be improved for life prediction in TMF conditions.

The material used in this contract were tested in a program designed to span a wide range of variables at sufficient depth to allow a fundamental mechanistic understanding of the problem. The test program was designed to provide sufficient data to clearly define the link between the environment and the materials. In order to achieve the above, test specimens were examined in detail after testing. Transmission electron microscopy (TEM) and scanning electron microscopy (SEM) analysis as well as more conventional techniques were used. The main differences between the conventional and the TMF crack growth approach used in this program may be summarized as follows:

Conventional Approach to TMF Crack Growth	Proposed Approach to TMF Crack Growth
-tubular specimen	-fracture mechanics specimen
-no thermal gradient in the cross section	-small thermal gradient in the specimen
- complex data reduction	-easy data reduction
-no available fracture	-solutions for the case of

mechanics solution for the case of significant inelastic deformation

significant plastic deformation are available

-this approach is used qualitatively to assess the TMF behavior of different alloys

-quantitative comparison of the crack growth data

The experimental program consisted of five interrelated tasks which were achieved in chronological order.

2.1 Task I: Literature Survey

During the first year of this work, an extensive literature survey of high temperature fatigue behavior was undertaken, with special emphasis on TMF data. The testing procedures relevant to TMF behavior were also reviewed; it was shown that the TMF behavior is a strong function of the controlled parameters and the testing procedure.

2.2 Task II: Problem Definition

Testing capability requirements and testing conditions were defined in collaboration with P&WA engineers for significant hot section cracking locations of commercial aircraft engines. These locations include first-stage turbine vanes, first-stage turbine blades, and combustor liners. Cracking in hot

section vanes, blades and combustor liners share many features in common. These common features are:

1. Relatively high temperatures (typical temperature in the range of 400°C to 980°C);

2. Time-dependent nonlinear material behavior;

3. Variable cyclic strains and temperatures leading to thermal-mechanical fatigue conditions and;

4. Predominantly thermal loading, leading to a strain-controlled, rather than load-controlled situation.

The similar cracking characteristic between combustors, vanes and blades listed above imply that testing capability requirements and testing programs for the vanes and blades closely parallel those for the combustor liners.

The requirements for testing facilities and test specimens for TMF testing are:

1. Strain control to simulate the thermal loading of the component since most high temperature components are under strain-controlled conditions. The mechanical strain (total strain minus thermal strain) was controlled.

2. Strain hold times to simulate steady state conditions undergone during normal operation of nuclear reactor and gas turbine engines.

During this period the test specimen is undergoing creep/relaxation behavior.

3. Controlled transient heating and cooling to simulate the component strain/temperature phase relationship.

4. Compressive load-carrying capability of the specimen to sustain compressive stresses which develop in the heating period of the cycle.

5. Crack length measurement capability to obtain crack growth data in TMF conditions.

TMF crack propagation included testing of the base metal only, since this type of cracking is readily studied by a fracture mechanics approach. The amount of component life spent in starting a crack in the coating has to be addressed in terms of crack initiation techniques. TMF tests should include several testing conditons in order to simulate the various strain-temperature relations at various locations in an actual component.

Testing included both isothermal tests at the minimum and maximum temperature of the TMF tests. The following variables were included in the testing procedures:

1. strain range, 0.10 to 1.0%

2. mean strain, R = -1 and 0.5

3. strain rate, set by the maximum transient heating and cooling rate that can be experimentally obtained.

The alloys selected for this reseach program are:

1. Inconel X-750

2. Hastelloy-X

3. B-1900+Hf

2.2.1 Inconel X-750

Inconel X-750 is a corrosion and oxidation resistant material with good tensile and creep properties at elevated temperatures. Typical applications include land-based gas turbine parts, nuclear reactor springs, bolts, bellows and forming tools. The temperature range of interest is from 300 to 650°C.

2.2.2 Hastelloy-X

This material is used extensively at Pratt & Whitney Aircraft in commercial aircraft engine combustor liners. Hastelloy-X is a nickel base alloy strengthened by a solid solution of chromium and molybdenum.

2.2.3 B-1900 + Hf

This material is also used extensively at Pratt & Whitney Aircraft for commercial engines; typical applications are vanes and blades (third stage). B-1900 is an advanced conventionally cast nickel base alloy with γ/γ' hardening. When casting the test specimens, great care is taken to reproduce the microstructue encountered in actual component parts.

2.3 Task III: Design and Construction of Testing Unit

The apparatus which was built is a computer-controlled thermal fatigue testing system consisting primarily of a closed-loop servo-controlled electro-hydraulic tension compression fatige machine (MTS 810 model 906.06), a high frequency oscillator for industrial heating (Lepel Model T-2.5-1-K01-BW), an air compressor for cooling, a low frequency function generator (Exact model 504), a data acquisition and control system (HP-6942A), a programmable high resolution DVM (HP-3478) and a main frame computer (HP 9816S). The system is capable of testing specimens of different size and configuration (SEN, CT, hollow tube, etc.) and to withstand a fatigue loading of 25 000 lbf (11 350Kgf). The test specimen is mounted in a verticle plane into two end grips of high tensile steel. The specimen alignment is insured by the use of a Wood's metal pot which prevents the development of a net bending moment in the specimen. Because of DC potential drop technique is used to monitor crack growth, the lower grip is electrically insulated from the system by means of a ceramic coating. The ends of the end grips are water cooled by means of copper coils surrounding them. The system and its capabilities are described in detail in Appendix I.

2.4 Task IV: Mechanical Behavior

2.4.1 Basic Properties

Tensile specimens were tested to qualify the materials. Tests were conducted at room temperature and up-to 982°C. Metallographic specimens were taken from the same locations to qualify materials. Conventional creep type specimens were tested at various temperatures to characterize the deformation behavior of the materials. For Hastelloy-X and B-1900+Hf complete strain versus time behavior were measured to determine creep rates in the primary and steady state regimes.

2.4.2 TMF testing

The TMF response of the materials was determined using single-edge-notched (SEN) specimens under stress- or strain-controlled testing. The test program was designed to evaluate the small scale yielding and fully plastic fatigue crack propagation behavior.

A series of fatigue tests were performed using precracked Inconel X-750 specimens under a constant range of applied loads; the strain and potential were measured as dependent variables. Isothermal crack growth tests were performed at 400°C and 925°C. In-phase cycling (maximum temperature at maximum stress) and out-of-phase cycling (maximum temperature at minimum stress) between 400⇌925°C were run in the elastic range to assess the ability of fracture mechanic to correlate TMF crack growth. Isothermal strain-controlled tests at 400° and 925°C were run. In-phase and out-of-phase cycling (400⇌925°C) were performed at two strain ranges i.e. (elastic and

fully plastic) levels. Measurement of the opening stress, as determined by the potential drop, provided useful information on the influence of environment and plasticity on crack propagation rates under TMF conditions.

2.4.3 Damage Characterization

The microscopy of failed specimens included detailed TEM and fractographic study of microstructural changes such as γ' coarsening, carbine precipitation, grain boundary cracking, oxide cracking, and oxide penetration. Microscopic studies were performed on both isothermal and TMF failed specimens in order to assess differences in microstructural damages associated with thermal-mechanical fatigue.

2.5 Task V: Data Analysis

In order to determine the respective influences of thermally and mechanically driven crack growth, relevant fracture mechanics parameters were computed in terms of thermal strains, mechanical strains and total strains. It was then realized that the conventional definitions of the fracture mechanics parameters (ΔK, ΔK_ε, etc.) cannot apply to displacement controlled crack growth experiment. Proper analytical solutions for ΔK and ΔK_ε for displacement controlled testing were derived. The detail of the derivations are given in Appendix II.

The results obtained for Inconel X-750 are shown in Appendix III. Results of damage analysis concerning B-1900+Hf are shown in Appendix IV. The TMF crack growth data of B-1900+Hf and Hastelloy-X under elastic and fully plastic

conditions are shown in Appendix V. A complete analysis of the data is discussed in [1].

3. Main Achievements

The main achievements of this research program are:

1. Completion of a literature survey of the thermal-mechanical fatigue data published in the open literature. This literature survey covered the different experimental procedures for TMF testing. Following this review a new approach to the TMF problem was proposed.
2. Agreement with Pratt & Whitney Aircraft to cooperate on TMF research. P&WA provided materials and insight as to determining the relevant testing conditions for TMF.
3. A fully computerized testing system to run various TMF test was built. The software to run the isothermal and TMF tests, as well as to analyze the data were developed. A correction procedure to the potential drop technique to measure crack lengths and crack opening (or closure) (stress) was also produced.
4. Isothermal and TMF tests (with and without cracks) were performed. Tests were run as to cover the complete range of strain ranges, i.e. from elastic strain regimes to fully plastic strain ranges. Special care was taken to duplicate the temperature ranges and strain ranges experienced by in-service components.
5. Fracture mechanics solutions for displacement controlled SEN testing conditons were developed. It was shown that conventional

fracture mechanics solutions developed for stress-controlled conditions overestimated the true driving force for cracking.

6. Damage under isothermal and TMF conditions were identified for B-1900+Hf. A sound mechanistic understanding of TMF in this alloy was achieved.

7. Various parameters were computed to correlate TMF crack growth data. The use of the stress intensity factor (derived for displacement controlled) corrected for the opening and closing of the crack was shown to be a successful parameter.

References

1. N. Marchand, "Thermal-Mechanical Fatigue Behavior of Nickel-Base Superalloys", Doctoral Dissertation, M.I.T., December 1985.

2. G.J. Meyers, "Fracture Mechanics Criteria for Turbine Engines and Hot Section Components", NASA CR-167896, 1982.

Appendix A - Test Equipment & Test Procedures

Submitted to ASTM J. Test & Eval.

A Computerized Test System for Thermal-Mechanical Fatigue Crack Growth

by

N. Marchand* and R.M. Pelloux **

* Research Assistant, Department of Materials Science and Engineering, M.I.T., Cambridge, MA 02139, USA

** Professor, Department of Materials Science and Engineering, M.I.T., Cambridge, MA 02139, USA

Abstract

A computerized testing system to measure fatigue crack growth under thermal-mechanical fatigue conditions was built and is described in detail in this paper. Built around a servo-hydraulic machine, the system is capable of push-pull test under stress or strain controlled conditions in the temperature range of 25-1050°C. Both temperature and mechanical strain are independently controlled by the closed loop system to simulate complex in-service strain-temperature relationship.

A DC electrical potential method is used to measure crack growth rates. The correction procedure of the potential signal to take into account power-line and RF-induced noises and thermal changes, is described in detail. It is shown that the potential drop technique can be used for physical mechanism studies and for modelling of crack tip processes.

Introduction

During the past two decades, the design criteria and the material property requirements for critical structural components of gas turbine engines has changed. Until the mid-sixties, most critical components such as turbine disks and blades were life limited by the creep and stress rupture properties of their materials. However, a demand for improved performance of advanced engines has led to marked increases in operating temperature and stresses. The result has been a transition from creep to low cycle fatigue as the dominant life limiting factor in over 75 percent of turbine components.

Low cycle fatigue (LCF)--defined as the initiation, slow crack growth and failure by fast fracture in less than $5x10^4$ cycles--is a stochastic process having considerable variability. To provide a safe operating life, the LCF approach has been to use a lower bound on the mean cyclic life that is equivalent to a probability of 1/1000 of initiating a detectable crack (1/32 inch) during the design lifetime of the component. In practice, this translates into 999 out of 1000 components, which are retired from service after reaching their design lifetime, although they are still structurally sound. In an attempt to utilize the remaining life of these 999 components without sacrificing structural safety, the U.S. Air Force and the major aircraft engine manufacturers have implemented a revised life management philosophy named retirement-for-cause (RFC) or on-condition lifing. Under RFC, components undergo periodic inspections and return to service if no cracks larger than a "critical" size are detected. This procedure relies on two premises. First, the cracks larger than a "critical" size must be detected with a high degree of reliability. Second, the crack growth rates under in-service conditions have to

be predicted with high accuracy such that cracks smaller than the "critical" size will not grow to a catastrophic size during one inspection interval.

Whereas the RFC is being applied to existing engines, the newly implemented Engine Structural Integrity Program (ENSIP) is a specification for future engines that requires a damage tolerant approach for all critical components. Under this program, flaws or defects are assumed to exist in the component at the time of production. Design calculations and component testing must demonstrate that such defects will not grow to a catastrophic size within the lifetime of the engine. In this scenario, the ability to measure and analytically predict crack growth under typical engine operating conditions is a key technology. These conditions, as shown in Figure 1, include variation in temperature, strain ratio, sustained load/strain hold time, as well as interactive effects.

There are, at the present time, some sophisticated testing assemblies which are capable of reproducing the complex stress-strain-temperature cycles described in Figure 1 [2-4]. However, these equipments are very expensive, which partly explains why most of the high temperature fatigue tests are still conducted under isothermal conditions. These test systems use tubular specimen geometry and some fatigue crack growth data has been generated with this geometry in the last ten years [4-7]. Unfortunately, this geometry is not easily suitable for crack growth measurement and it is no surprise that crack growth rates data lower than 10^{-6} m/cycle have not been measured. Adequate fatigue life prediction relies on the knowledge of experimental crack growth data in the range of 10^{-10} to 10^{-6} m/cycle under TMF conditions. Therefore, a newer approach to TMF crack growth testing must be considered to meet the requirements of RFC and ENSIP.

The purpose of this paper is to describe a computerized testing unit capable of measuring thermal-mechanical fatigue crack growth (TMFCG) rates in the range from 10^{-10} to 10^{-3} m/cycle. The control system and the correction procedure of the DC potential signal is described in detail.

Basic Requirements

The testing capability and testing conditions for TMF testing of specimens are those that allow the duplication of in-service conditions. The requirements for testing facilities and test specimens for crack growth TMF testing are:

1. Strain control to simulate the thermal loading of the component since most high temperature components are under strain-controlled conditions. The mechanical strain (total strain minus thermal strain) should be controlled.
2. Strain hold time to simulate steady state conditions during normal operating of gas turbine engines. This period consists of a creep/ relaxation behavior.
3. Crack length measurement capability to obtain crack growth data in TMF conditions.
4. Controlled transient heating and cooling to simulate a component strain/temperature phase relationship similar to the one shown in Figure 2.
5. Compressive load-carrying capability of the specimen to sustain compressive stresses which developed in the heating period of the cycle.

TMF crack propagation should include testing of the base metal only, since this type of cracking is readily studied by a fracture mechanics approach. The amount of component life spent in starting a crack in the coating has to be addressed in terms of crack initiation techniques [10]. TMF tests should include several testing conditions in order to simulate the various strain-temperature relations at various locations in an actual component.

Design of test unit

The apparatus which was assembled is a computer-controlled thermal fatigue testing system consisting primarily of a closed-loop servo-controlled electro-hydraulic tension compression fatigue machine (MTS 810 model 906.06), a high frequency oscillator for industrial heating (Lepel Model T-2.5-1-KO1-BW), an air compressor for cooling, a low frequency function generator (Exact model 504), a data acquisition and control system (HP-6942A), a programmable high resolution voltmeter (DVM HP-3478), and a main frame computer (HP 9816S). Figure 3 shows the control block diagram of this system.

The system is capable of testing specimens of different size and configuration (SEN, CT, hollow tube, etc.) and to withstand a fatigue loading of 25,000 lbf (11.350 Kgf). The test specimen is mounted in two end grips of high tensile strength steel. The specimen alignment is insured by the use of a Wood's metal pot, which prevents the development of a net bending moment in the specimen. Because a DC potential drop technique is used to monitor crack growth, the lower grip is electrically insulated from the system by means of a ceramic coating. The ends of the end grips are water cooled.

The demand-signal generators

The demand-signal generation system provides separate demand signal for the control of specimen strain or applied stress and temperature. A programmable temperature controller is used to generate the driving signal to the high frequency generator and the air valve driver. It is also providing trigger signals to the DVM, computer, and function generators (if required). The computer and the data acquisition and control system provide the command signals for the stress and strain controlled cycling. Proper coding and decoding of trigger signals from the temperature controller to the computer allow the system to generate any strain/stress/temperature cycling. Feedback signals from measuring points on the machine and specimen are compared continuously with the demand signals in the electronic control equipment. The difference between corresponding signals (i.e., the error) controls the power delivered to the hydraulic actuator or the heating circuit unit in such a way that the error in the test variable is reduced; careful choice of relative signal magnitudes (amplification) allows adequate control of each variable.

Control of strain or stress

Control of specimen strain is achieved by control of the displacement between two knife-edges of the strain detector attached to the specimen surface. This axial strain extensometer consists of a linear differential transformer (LVDT), and a transmitter consisting of two shims which link together two sets of Invar arms, each supporting an alumina rod. The feedback signal from the LVDT is compared with the demand signal and the difference between the two, the error signal, is used to control the driving signal to the servovalve. The command signals (mean strain and amplitude) are sent by the

Multiprogrammer (HP 6942A) which is controlled by the 9816S. Figure 4 shows a block diagram of the strain controlled closed-loop unit. In the system, the set point command (mean stress or strain) is fed directly to the servo controller of the MTS unit.

The amplitude command signal was obtained by feeding the output of a twelve bits voltage D/A converter directly into the MTS servocontroller. A memory card can be used to continuously supply preloaded data to the D/A. A timer card determines the time between each analog voltage change such that the changes are perceived in the test as continuous as possible and not as a series of step changes.

Data acquisition and control unit

The command signals are sent by this data acquisition and control unit called Multiprogrammer or HP-6942A. It is composed of an internal main microprocessor, memory buffers for I/O and data storage, a real time clock and a backplane where separate plug-in cards are connected. Each plug-in I/O card is equipped with its own microprocessor.

Instructions to run the test and values of the stress (in lbs) or strain (in %) for the mean and amplitude are typed-in on the HP-9816S at the beginning of the test. These values are then converted into their corresponding binary code and voltage are sent to the Multiprogrammer which in turn decodes them and re-programs the appropriate I/O cards.

With the proper I/O cards, the system has the following capabilities:

1. data acquisition
2. measurement ranges
3. control

4. synthesis

Acquisition

Analog measurements from up to 16 channels (can be increased to 960 channels) may be acquired at 33,000 readings per second, depending upon the scanner system configuration. Random access to any channel, as well as continuous scanning, are easily accomplished. Figure 5 shows a diagram of the scanning system configuration implemented in our system. The signal may be digitized at rates up to 33 KHz by the A/D and stored on a memory card. Each memory card can store up to 64 K readings. The digitizing process takes place independently of all other Multiprogrammer activity, that is, the data acquisition are achieved in parallel without any interruption from the control activities.

Measurement Ranges

Proper switches on the A/D converters are used to select and measure voltage range from ± 25 mV to ± 10V full scale in the presence of 250V of common-mode voltage. The resolution can then be varied from 12 μV to 5 mV.

Control and Synthesis

As stated earlier, twelve bits voltage D/A converters provide outputs for analog programmable instrument and stimulus of units under test (mean stress/strain and amplitude). A memory card can be used to continuously suply preloaded data to the D/A card at rates of up to 10 KHz. Any type of waveforms

may be loaded into the memory card from the computer and used as stimuli for tests. Random fatigue loading can therefore easily be achieved without modification to the system (hardware). Any repeatable wave shape (sine, square, triangular, etc.) can also be preloaded into a memory card. A timer card determined the time between each analog voltage change such that the changes are perceived in the test as continuous as possible and to achieve cycling at a pre-determined frequency.

Control of temperature

The specimens are heated by a radio frequency unit. For TMF tests, low frequency heaters (10 KHz) are often used [5-8] because they produce lower wall thickness gradients than do the higher frequency (450 KHz) heaters and because there are fewer ground-loop problems with the 10 KHz heaters than with the 450 KHz heaters. However, it is the author's belief that high frequency induction heating is preferable because of its fast response, making it possible to provide high heating rates and capabale of inducing considerable thermal stresses in specimens of small cross-section. In this case, the heating mode is close to that encountered in-service, since the heat is generated within the surface layer of the specimen. Temperature measurement is accomplished by thermocouples welded onto the specimen. A thermistor is used with the temperature controller to provide a stabilized cold junction.

As pointed out by Carden [9], there is a relationship between the heating method, the design of the specimen, and temperature measurement and control. Radio frequency induction requires close coil-to-specimen spacing and small grip ends which makes difficult the mounting of additional measurement devices and obscures access to and visibility of the surface for replication,

etc.; also, the coil has a high voltage RF potential requiring insulation and safety precaution. A temperature disturbance occurs at the thermocouple mass in the field, as well as at specimen locations spaced to the coil. Finally, there might be possible RF induction-induced ground loop problems in the instrumentation cabling.

In order to minimize these potential problems, great care must be taken to use properly shielded cables. The coils were machined as to maintain constant coil-to-specimen spacing. This was achieved by using a mold having oversized dimensions of the specimen. Before each test, the coils were carefully positioned around the specimen as to minimize the temperature difference between the four faces of the specimen. The temperature variation along the gauge length of the specimen has been measured to be less than 10°C and accurate to ±1°C.

The amplified signal from the thermocouple (Figure 6) is compared with the demand signal which was programmed. A difference between the demand and feedback signals caused by the specimen temperature being too low, causes an increase in the power supplied to the coil. The increased power passing through the coil increases the temperature of the specimen and hence reduces the error. If the temperature is too high, the power to the coil is reduced. Compressed air is used to cool the specimen during the cool down portion of the temperature cycle. The air valve is best controlled by the temperature programmer which opens or closes a solid state relay that drives the power to the air valve. With this technique, the air flow is always synchronized to the temperature cycle and is repeatable. The cooling rate is controlled by the heater ballasting the air blast cooling.

The limits of the system, in terms of heating and maximum temperature, were also tested. Heating rates in excess of 20°C /sec. have been obtained

with the test rig and single edge notch specimen geometry (see Test Rig Verification Procedure). For faster rates, some control accuracy is sacrificed and a detailed thermal analysis has to be performed to determine the time-temperature distribution in the specimen. Using different specimen geometry and coil design, control heating rates in excess of 200°C/sec. were achieved with an identical heating/cooling unit [10]. The maximum uniform temperature that can be reached is a function of the specimen geometry and specimen-to-coil distance. With the present configuration of specimen and coil design, the upper limit of the temperature cycles is 1050°C. In the development work, specimens were tested between 400 and 925°C. A six degree per second heating and cooling ramp was programmed and run. The dynamic performance of the system is shown in Figure 7. Five thermocouples were used and the temperature of each thermocouple was always within ten degrees of the requested profile throughout the test.

Crack Growth Measurement

Crack length measurements during thermal-mechanical fatigue cycling under either elastic or plastic strains have been performed mostly by optical measurements [5-8, 11-13] and by cellulose acetate replica [14] on tubular centered notched specimens. In these experiments, the surface crack lengths must be converted to a mean crack length for the tube used [8]

$$a = R \sin^{-1} (2a_p/D_o) \qquad (1)$$

where a is the mean crack length, R the mean radius of the tube, D_o the outer diameter of the tube, and $2a_p$ the total projected length measured by

microscope. This equation applies only if the crack grows symmetrically in a fan direction. Although stress and strain intensity solutions for this geometry exist [15], they require precise measurement of the crack length which is, in practice, very difficult to achieve. The resolution claimed [8] for optical measurements is in the range of 80-120 μm, depending on the crack tip resolution and providing the measurements are taken at maximum tensile load.

There have been few attempts to measure crack length in TMF conditions using the potential drop technique [11-12] on a 12.7 mm diameter push-pull specimen. Using a starter notch 200 μm deep, experimenters have been able to resolve accurately a crack increment of 40 μm, and the corresponding growth rates were measured to better than 10^{-8} m/cycle [12]. The method of potential drop has been used satisfactorily for isothermal conditions for numerous materials [16-20] and preliminary experiments by the authors have shown that it can be used satisfactorily provided that the electrical noises are adequately filtered and that the calibration curve is properly corrected in order to take into account changes of potential with temperature [18].

The electrical noises induced in the potential probes by RF heating can be eliminated by the use of a band-pass filter centered on a 430-460 KHz frequency range. Power line surges, transients, and RF induced power-line noises can be taken care of by the following technique. First, a 10 KHz band-pass filter is used to eliminate the induced-noise of the 10 KHz Master oscillator of the MTS console used to provide excitation to the servo-valves LVDT's. Second, the DVM is programmed to convert the analog signal in 10 power line cycles (PLC). In this mode, 1 PLC is used for the runup time, the A/D operation repeated ten times. The resulting ten readings are then averaged and the answer becomes a single reading. This, with the built-in broad band filter, greatly reduces the emf noise induced by the power-line fluctuations. A

schematic of the DC potential system is shown in Figure 8. Because the potential, the temperature, the load, and the strain are recorded synchronously, it is possible to take into account the thermal variation of the potential. The procedure is the following. First, the changes in potential as a function of the temperature and strain or stress ($V(T,\sigma)$) is measured. Then a thermal cycle at zero stress is recorded ($V(T, \sigma = 0)$). The effect of the applied stress or strain is obtained by subtracting $V(T,\sigma=0)$ from $V(T,\sigma)$) to yield $V(\sigma)$. The procedure is outlined in Figure 9. To assess crack growth, the peak potential of each cycle ($V(T,\sigma)$) is recorded, and plots of the voltage versus applied number of cycles are obtained. Using well-known solutions [16-17] relating (V/Vo) to (a/ao) for the single-edge notch specimen geometry, the crack lengths versus N curves are derived. Improved sensitivity can be achieved through the use of reference probes [19-21] where the ratio (V(t)/Vo) is corrected by multiplying by (V^o_{ref}/V_{ref}), the ratio of the initial reference probe signal to the reference probe signal at time t. The resolution achieved under TMF conditions on single edge notch specimens is better than 10 μm.

A close look at the potential signals shown in Figure 9 indicates that they can be used to generate information on the mechanisms taking place at the crack tip. By noting that $V(T,\sigma)$ and $V(T, \sigma = 0)$ are also functions of the geometry, we can write

$$V(\sigma) = V(T, \sigma, geo) - V(T, \sigma = 0, geo). \qquad (2)$$

Therefore, for a given temperature T and zero applied stress, the expected value of $V(\sigma)$ is zero if the geometry of the crack, which include crack length and configuration, is unchanged. However, if $V(\sigma)$ is not equal to zero at zero applied stress, then the geometry terms in $V(T, \sigma, geo)$ and $V(T, \sigma = 0, geo)$ must be different (see Equation 2). Assuming that the crack increment during the thermal cycle is negligible, then the difference associated with the

geometry term is solely a function of the configuration. The applied stress required (see Figure 9.b) to give $V(\sigma) = 0$ represents the minimum necessary stress to re-establish in the specimen the same crack configuration. Because the transition point where $V(\sigma)$ equal zero corresponds to the transition between the tensile and compressive part of the cycle (see Figure 9), it is logical to assume that this change in configuration is a change in the opening of the crack [18-20].

From Figure 9 other information can be derived from the analysis of the $V(\sigma)$ potential curves. That is, to determine when the crack is growing within one cycle. In Figure 9.b, the $V(\sigma)$ curve for in-phase cycling shows a hump near the maximum stress whereas at low ΔK (Figure 9.a) and for out-of-phase cycling, the $V(\sigma)$ curve is continuous without discontinuity. Such an increase in potential usually reflects a sudden increase in crack length [16-21]. Therefore, it can be concluded that under this particular condition and specific loading the crack growth was happening at the peak applied load/strain. On the other hand, for the other conditions shown in Figure 9, it is logical to assume that the crack was growing in a continuous fashion in the tensile going part of the cycle ($0 < \sigma < \sigma_{max}$). The crack extension during a single cycle can be estimated by comparing the values of $V(T,\sigma)$ at the beginning and at the end of the cycle. Local estimate of the crack growth rate within one cycle can be computed by dividing the increment in crack length by the time spent in the tension going part of the cycle (time interval for which $V(\sigma) > 0$). If a hump is seen on the $V(\sigma)$ the time interval between the hump and $V(\sigma) = 0$ must be taken.

From the above analysis of the $V(\sigma)$ curves it can be concluded that the potential drop method has the capability of monitoring crack extension during a cycle, whereas the optical measurement and compliance methods are limited

for growth measurement to no less than one cycle. Therefore, detailed analysis of the crack growth process can be achieved and this is particularly important in trying to determine the mechanisms involved with TMF crack growth.

Test Rig Verification Procedure

TMF and isothermal fatigue crack growth tests were performed under strain control on single edge notch specimen (11.7 x 4.4) mm^2 of cross-section with a starter notch approximately 1 mm deep which is cut by electro-discharge machining. The specimen were pre-cracked in fatigue at 10 Hz at room temperature up to a ΔK of about 20 MPa $\sqrt{m}$. Axial strain was measured with a calibrated LVDT along a gauge length of 12.5 mm. Temperature and mechanical strain were computer-controlled by the same triangular waveforms shown in Figure 2. The thermal strains (ε_{th}) were measured by cycling the temperature at zero load. The total strain, computed by adding the ε_{th} to a pre-selected mechanical strain (ε_{mec}) were used for the control. Every five cycles the V(T) potentials were re-setted and the thermal strains checked for any drift. The software developed to run the tests is given elsewhere [22]. The frequency was kept constant at 0.0056 Hz (1/3 cpm) and the temperature cycled between 400 and 925°C. Figure 10 shows ε_{th}, ε_{mec}, ε_{tot}, and σ as a function of time within one cycle for both in-phase and out-of-phase cycling. Typical hysterisis loop obtained by plotting σ and ε_{mec} are shown in Figure 11. From the potential versus time curves similar to one shown in Figure 9, the (a/w) vs N curves were derived. The crack growth rates were computed using a seven-point incremental polynomial method (ASTM E647-81). The ΔK_{ε}, the strain intensity factor, were computed using a superposition method derived for an edge crack in a plate with no bending and fixed-end displacements [22-

24]. The crack growth rates as a function of ΔK_ε are shown in Figure 12. Data on the same material but obtained by conventional optical measurements [7], are also reported. As can be seen from Figure 12, the data from the TMFCG set-up agrees quite well with data taken from conventional TMFCG test apparatus provided the K's are calculated, assuming no free-end rotation of the specimen. However, our data covered three orders of magnitude lower than those previously reported. As expected from our knowledge of crack growth mechanisms in isothermal testing, the TMFCG curves are also characterized by a "threshold" regime which did not exist in the data generated by conventional TMFCG methods.

The crack growth rates are ranked, in terms of severity of damage in the following order; isothermal (at T_{max}), in-phase, and out-of-phase cycling. However, correction of the K's to take into account closure which has been previously defined as the applied stress at which $V(\sigma) = 0$ (see Figure 9), have shown that the stress intensity factor correlates very well the testing conditions for high strength/low ductility materials like X-750 and B-1900+Hf [18, 23]. Research is under way to determine if similar corrections can be applied for the fully-plastic regime [25-26].

Summary

A thermal-mechanical fatigue test rig has been built around a conventional servo-hydraulic machine to simulate complex stress-strain-temperature cycles as experienced for in-service components. The system and its capabilities have been described in detail. A corrected DC potential drop technique used to accurately measure crack lengths was shown to yield better

capabilities for low crack growth rate measurements than the conventional methods used in TMFCG testing.

It has been shown that solid specimen geometries can be used to simulate almost any type of in-service conditions. Although these geometries might require proper thermal analysis to determine the thermal distribution in the cross-section, it has some substantial advantages over the tubular geometries. The most important advantage is that it allows deterministic crack length measurements and the use of accurate fracture mechanics solution.

Further, the choice of fracture mechanics criteria as the failure criteria for aircraft components requires a careful monitoring of specimens during testing, which obviously increases the experimenter's effort considerably. This extra work, however, is justified by the greater relevance of the data available to the designer.

Acknowledgements

This work was sponsored by the National Aeronautics and Space Administration under Grant No. NAG3-280.

References

1. J.M. Larsen and T. Nicholas, "Cumulative Damage Modelling of Fatigue Crack Growth", presented at AGARD Specialists' Meeting of the Propulsion and Energetics Panel on Engine Cyclic Durability by Analysis and Testing, Lisse, Netherlands, 1984; to be published in AGARD Conference Proceedings.

2. S.W. Hopkins, "Low-Cycle Thermal Mechanical Fatigue Testing", ASTM STP 612, 1976, p. 157-169.

3. E.G. Ellison, "Thermal-Mechanical Strain Cycling and Testing at Higher Temperature", in Measurement of High Temperature Mechanical Properties of Materials, ed. by M.S. Loveday, M.F. Day and B.F. Dyson, NPL, HMSO, 1982, p. 204-224.

4. M. Okazaki and T. Koizumi, "Crack Propagation of Steels During Low-Cycle Thermal-Mechanical and Isothermal Fatigue at Elevated Temperatures", Met. Trans., Vol. 14A, 1984, p. 1641-1648.

5. A.E. Gemma, B.S. Langer and G.R. Leverant, "Thermal-Mechanical Fatigue Crack Propagation in an Anisotropic (Directionally Solidified) Nickel-Base Superalloy", ASTM STP 612, 1976, p. 199-213.

6. G.R. Leverant, T.E. Strangman, and B.S. Langer, "Parameters Controlling the Thermal-Fatigue Properties of Conventionally-Cast and Directionally-Solidified Turbine Alloys", in Superalloys: Metallurgy and Manufacturers, ed. by B.H. Kear, D.R. Muzuka, J.K. Tien, and S.T. Wlodek, Claxtor Pub., 1976, p. 285-295.

7. A.E. Gemma, F.X. Ashland, and R.M. Masci, "The Effects of Stress Dwells and Varying Mean Strain on Crack Growth During Thermal-Mechanical Fatigue", J. Test. Eval. (JTEVA), Vol. 9, 1981, p. 209-215.

8. G.J. Meyers, "Fracture Mechanics Criteria for Turbine Engines and Hot Section Components", NASA CR-167896, 1982.

9. A.E. Carden, "Fatigue at Elevated Temperatures: A Review of Test Methods", ASTM STP 520, 1973, p. 195-223.

10. F.A. McClintock, J.W. Holmes and K.S. Ohara, "Thermal Fatigue of Monocrystal Nickel-Base Superalloy", to be presented at ASTM Conference

on "Low-Cycle Fatigue - Directions for the Future", Lake George, New York, September 30 - October 4, 1985.

11. R.P. Skelton, "Environment Crack Growth in 1/2 Cr-Mo-V Steel During Isothermal High Strain Fatigue and Temperature Cycling", Mat. Sci. Eng., Vol. 35, 1978, p. 287-298.

12. R.P. Skelton, "The Effect of Microstructure and Tensile Dwell on the Growth of Short Fatigue Cracks in 316 Steel at 625°C", Proc. of Conf. on Mechanical Behavior and Nuclear Application of Stainless Steels at Elevated Temperature, ed. Metals Soc., London, 1981, p. 19/1-19/12.

13. R.P. Skelton, "Crack Initiation and Growth in Single Metals Components During Thermal Cycling", in Fatigue at High Temperature, ed. by R.P. Skelton, App. Sci. Pub., London, 1983, p. 1-62.

14. C.A. Rau, A.E. Gemma and G.R. Leverant, "Thermal-Mechanical Fatigue Crack Propagation in Nickel and Cobalt Base Superalloys Under Various Strain-Temperature Cycles", ASTM STP 520, 1973, p. 165-178.

15. F. Erdogan and M. Ratwani, "Fatigue and Fracture of Cylindrical Shells Containing a Circumferential Crack", Int. J. Frac. Mech., Vol. 6, 1970, p. 379-382.

16. M. Hicks and A.C. Pickard, "A Comparison of Theoretical and Experimental Methods of Calibrating the Electrical Potential Drop Technique for Crack Length Determination", Int. J. Fract., Vol. 20, 1982, p. 91-101.

17. M.P. Halliday and C.J. Beevers, "The DC Electrical Potential Method for Crack Length Measurement", in The Measurement of Crack Length and Shape During Fracture and Fatigue, ed. by C.J. Beevers, EMAS Pub., 1980, p. 85-112.

18. N. Marchand and R.M. Pelloux, "Thermal-Mechanical Fatigue Crack Growth in Inconel X-750", in Time-Dependent Fracture, ed. by K. Krausz and A.S. Krausz, Martinus Nijhoff, in press.

19. T.A. Prater and L.F. Coffin, "Experimental Cycle Analysis of Fatigue Crack Growth in Compact Type Specimen Geometries", General Electric Technical Information Series, Report No. 82CRD039, 1982, 18 pgs.

20. R.P. Gangloff, "Electrical Potential Monitoring of the Formation and Growth of Small Fatigue Cracks in Embrittling Environment", in

Advances in Crack Length Measurement, ed. by C.J. Beevers, EMAS Pub., 1982, p. 175-230.

21. I.P. Vasatis and R.M. Pelloux, "The Application of the DC Potential Drop Technique in the Creep Stress-Rupture Testing", to be published.

22. N. Marchand, "Thermal-Mechanical Fatigue Behavior of Nickel-Based Superalloys", ScD Dissertation, Mass. Inst. of Technology, Cambridge, MA, 1985.

23. N. Marchand and R.M. Pelloux, "Thermal-Mechanical Fatigue Crack Growth in B-1900+Hf", to be published in the Proc. of the Conf. on High Temperature Alloys for Gas Turbine Application, Liege, Belgium, October 6-9, 1986.

24. N. Marchand, D.M. Parks and R.M. Pelloux, "K_I-Calculations in Single Edge Notch Specimen with Linearly Varying End Displacements", submitted to Eng. Frac. Mech.

25. N. Marchand and R.M. Pelloux, "Fracture Mechanics Criteria in Turbine Components Materials", to be published.

26. N. Marchand, G. L'Esperance and R.M. Pelloux, "Thermal-Mechanical Fatigue Responses of Cast B-1900+Hf", to be presented at the ASTM Conference on "Low Cycle Fatigue - Directions for the Future", Lake George, New York, September 30 - October 4, 1985.

List of Captions

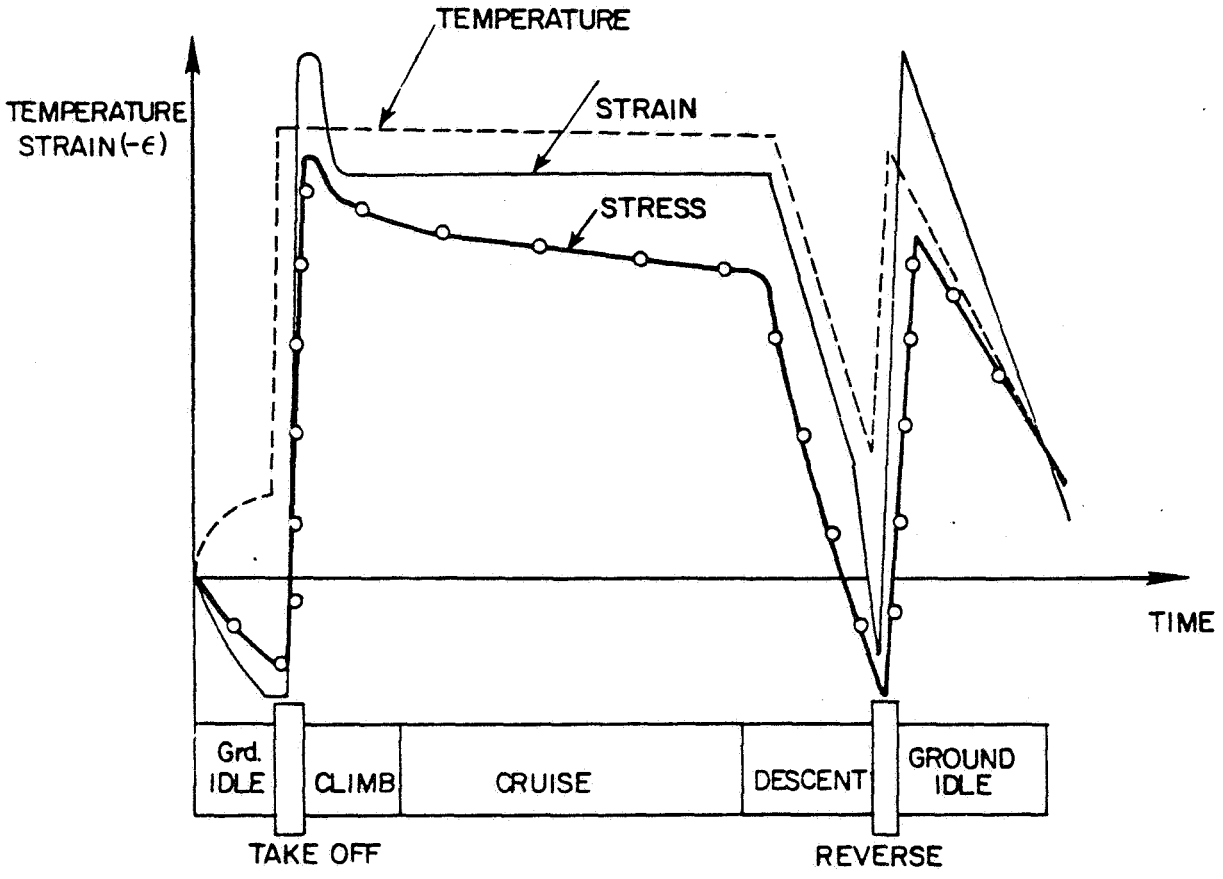

Figure 1 Stress-strain-temperature cycle experienced by turbine components

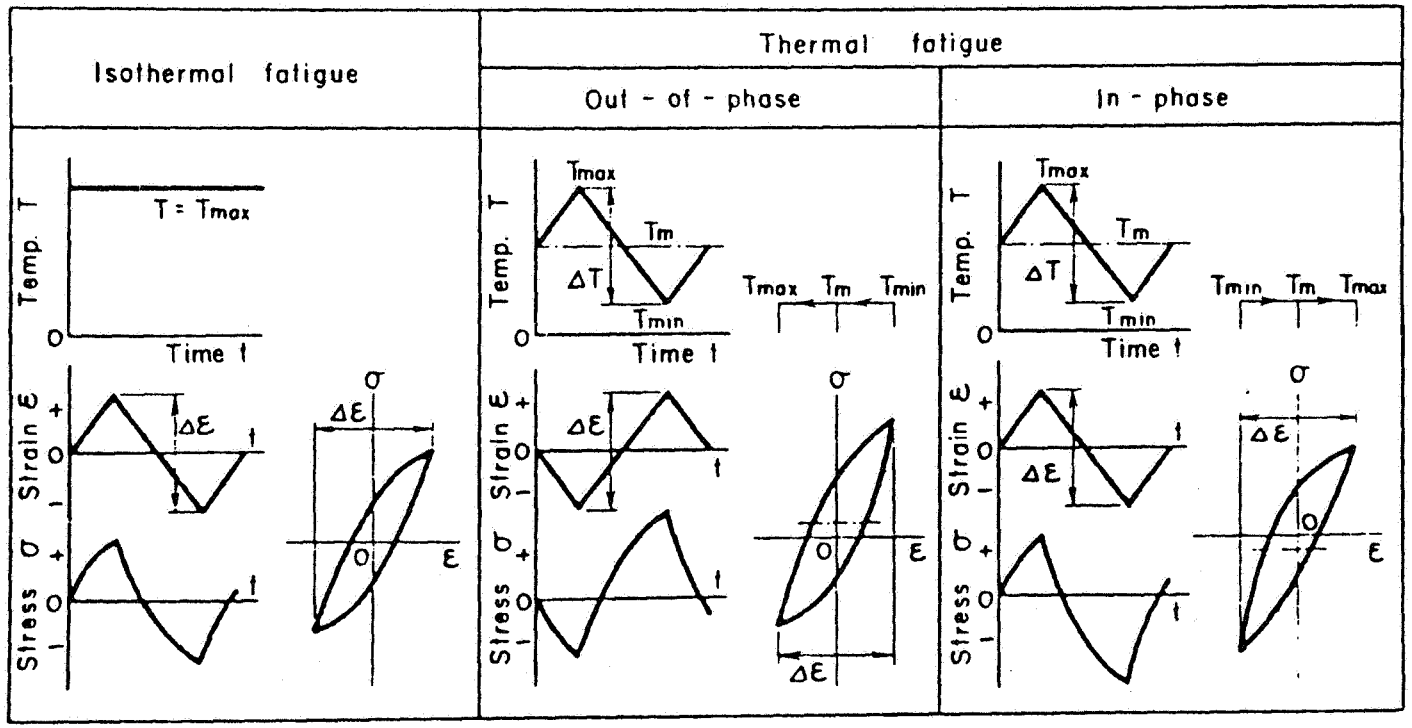

Figure 2 Schematic diagram showing waveforms of temperature, strain and stress in thermal and isothermal fatigue tests.

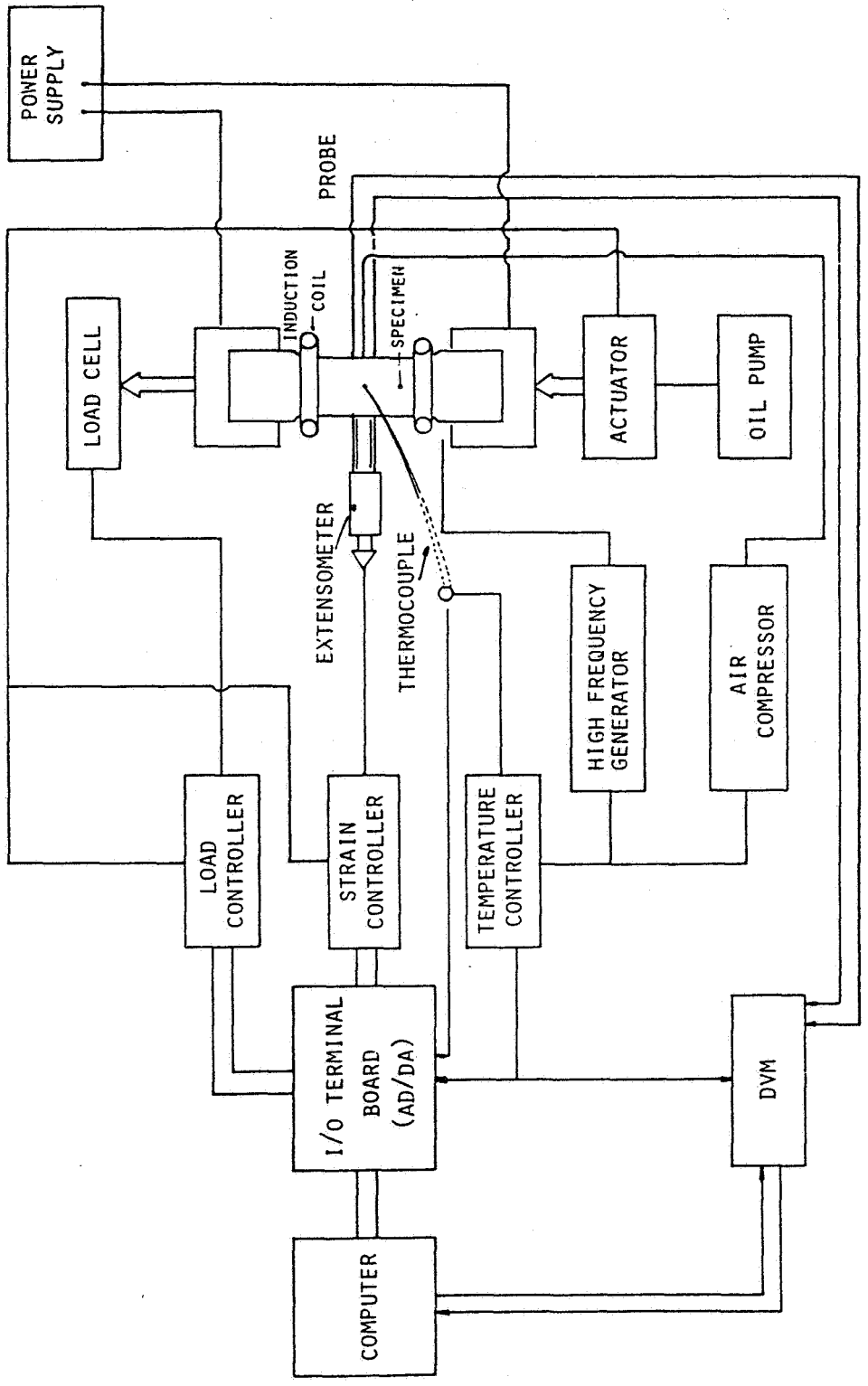

Figure 3 Diagram showing the control system of apparatus used for thermal-mechanical fatigue test

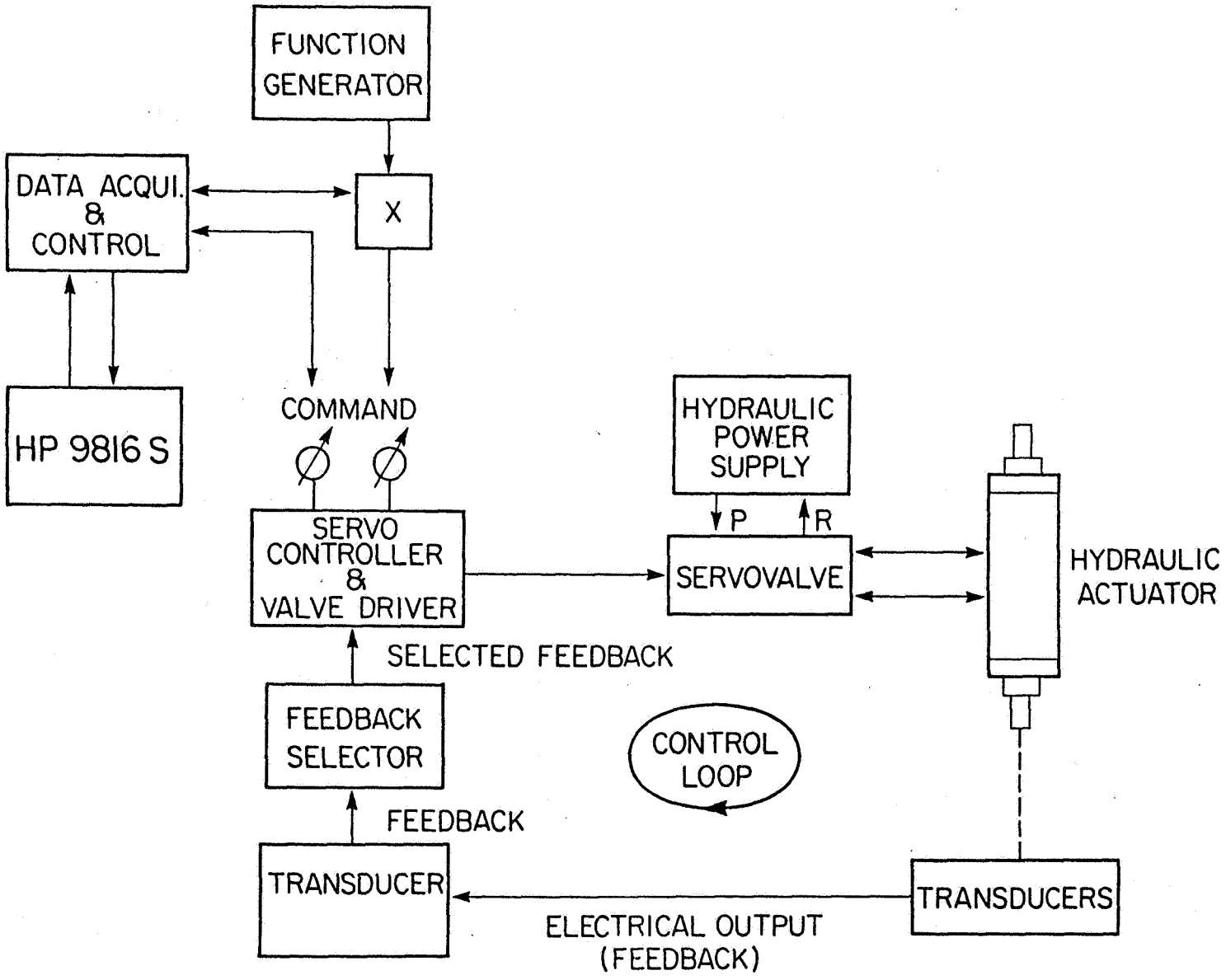

Figure 4 Block diagram of the strain-controlled closed-loop unit

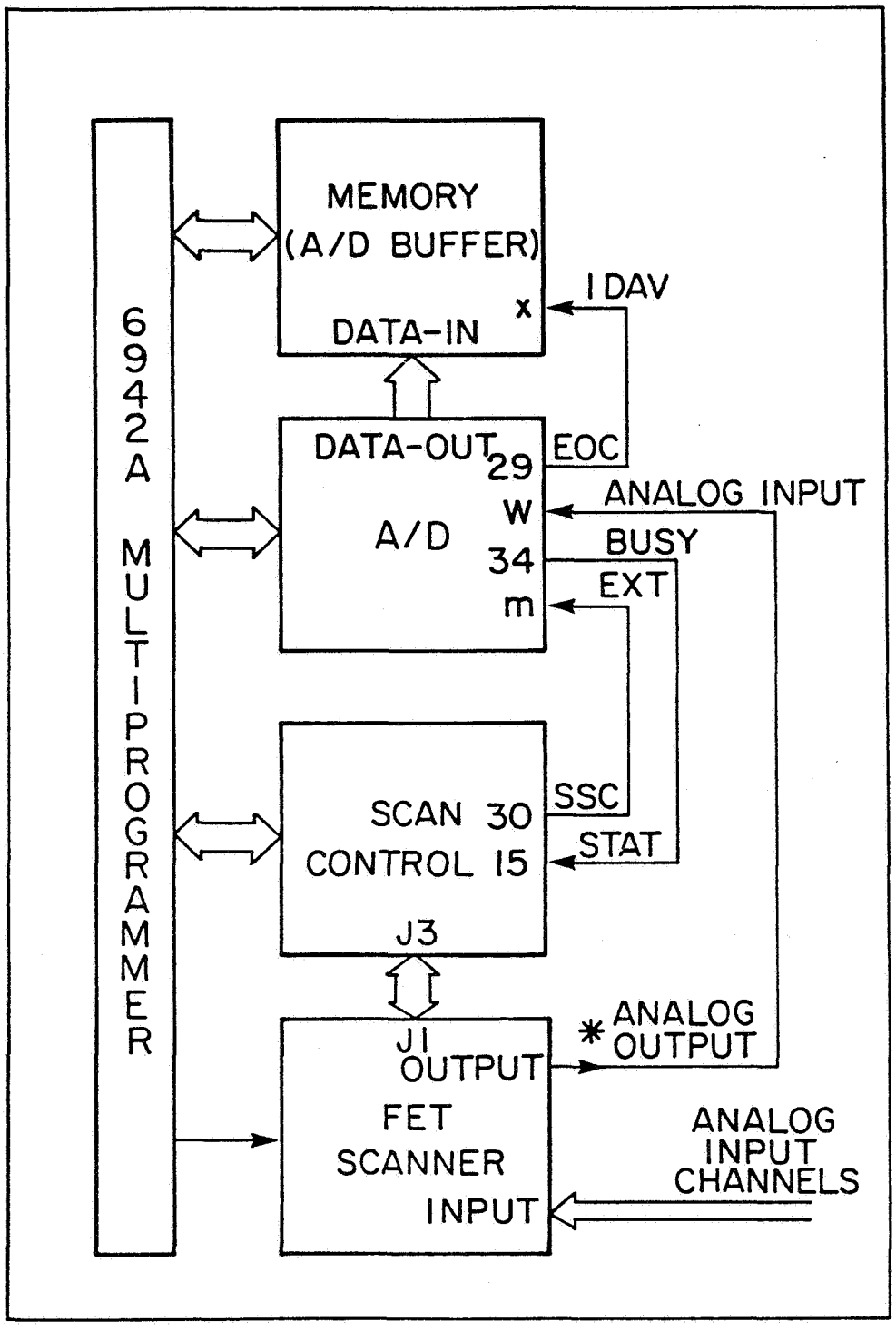

Figure 5 Configuration for sequential scanning with buffered A/D

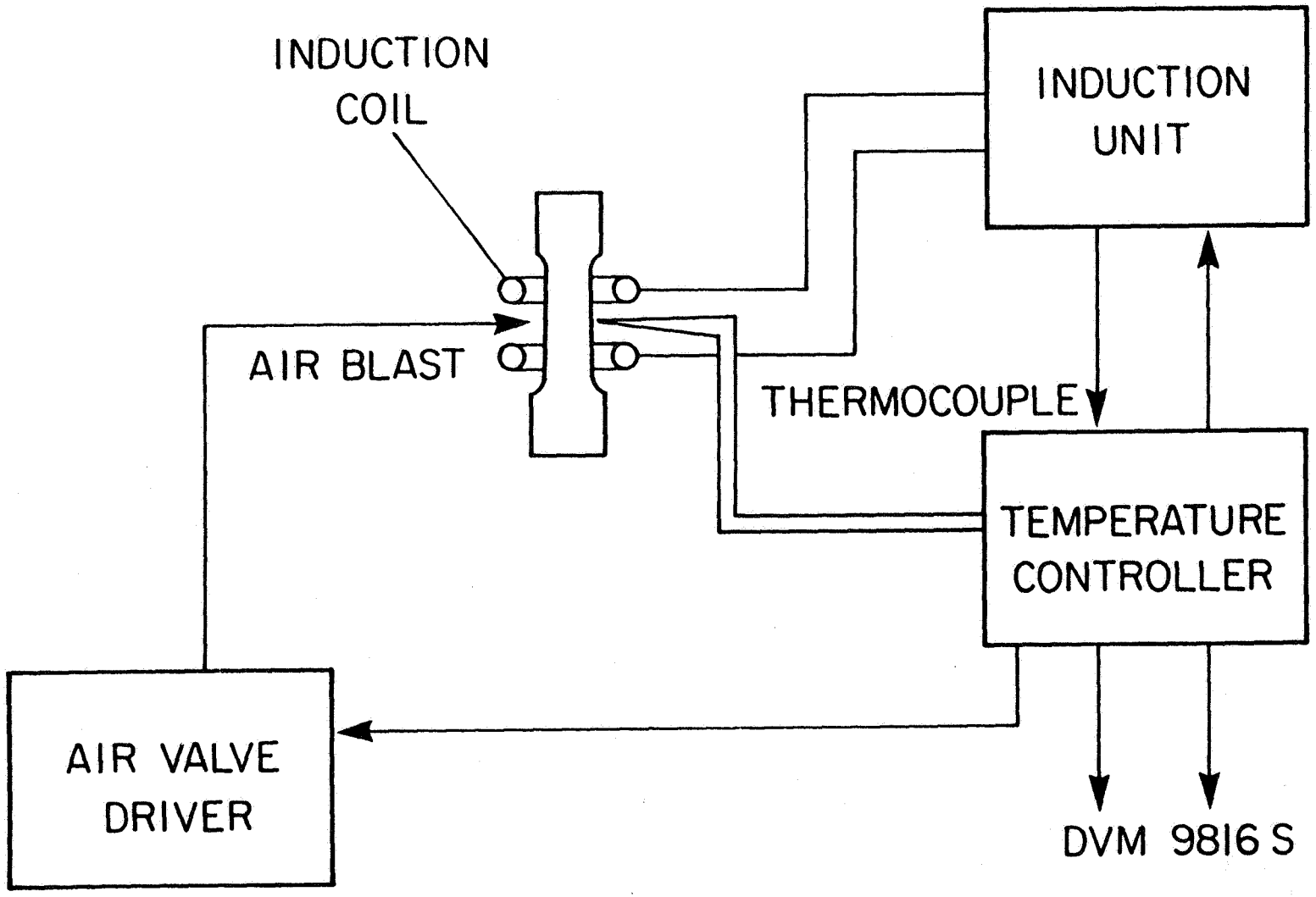

Figure 6 Block diagram of the temperature control unit

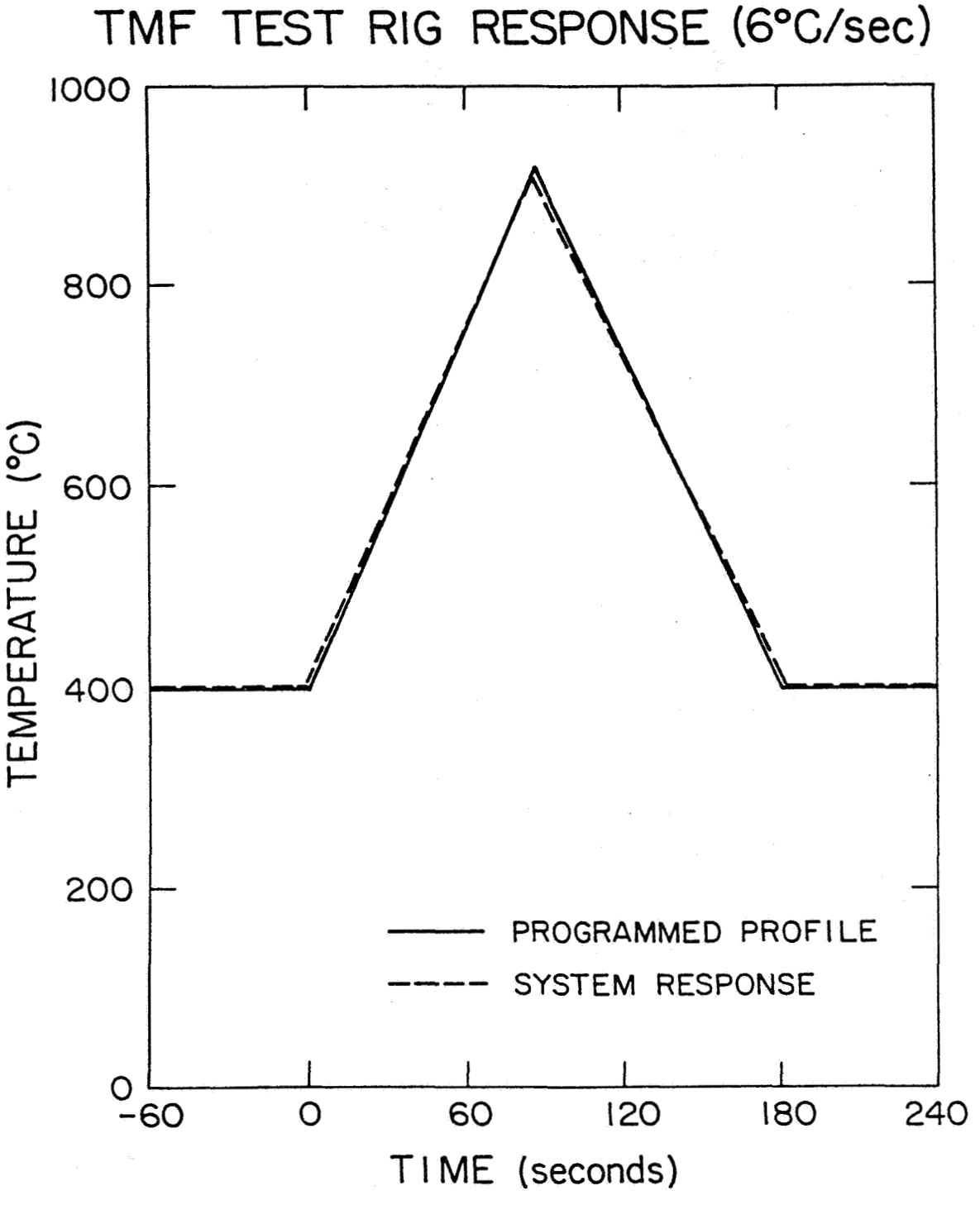

Figure 7 Programmed profile and thermal fatigue system for an 6°C/sec. triangular waveform

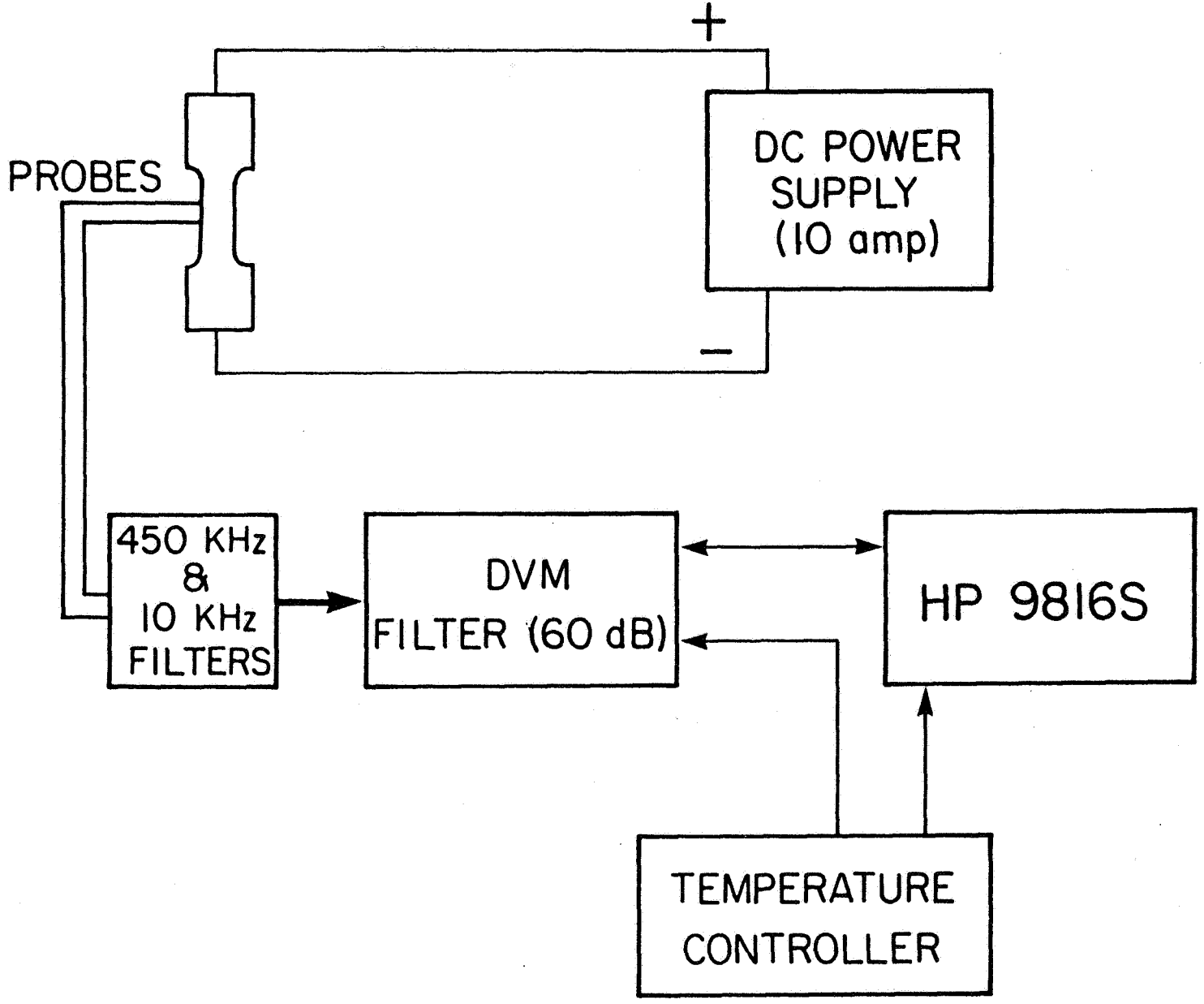

Figure 8 Schematic of the DC potential system.

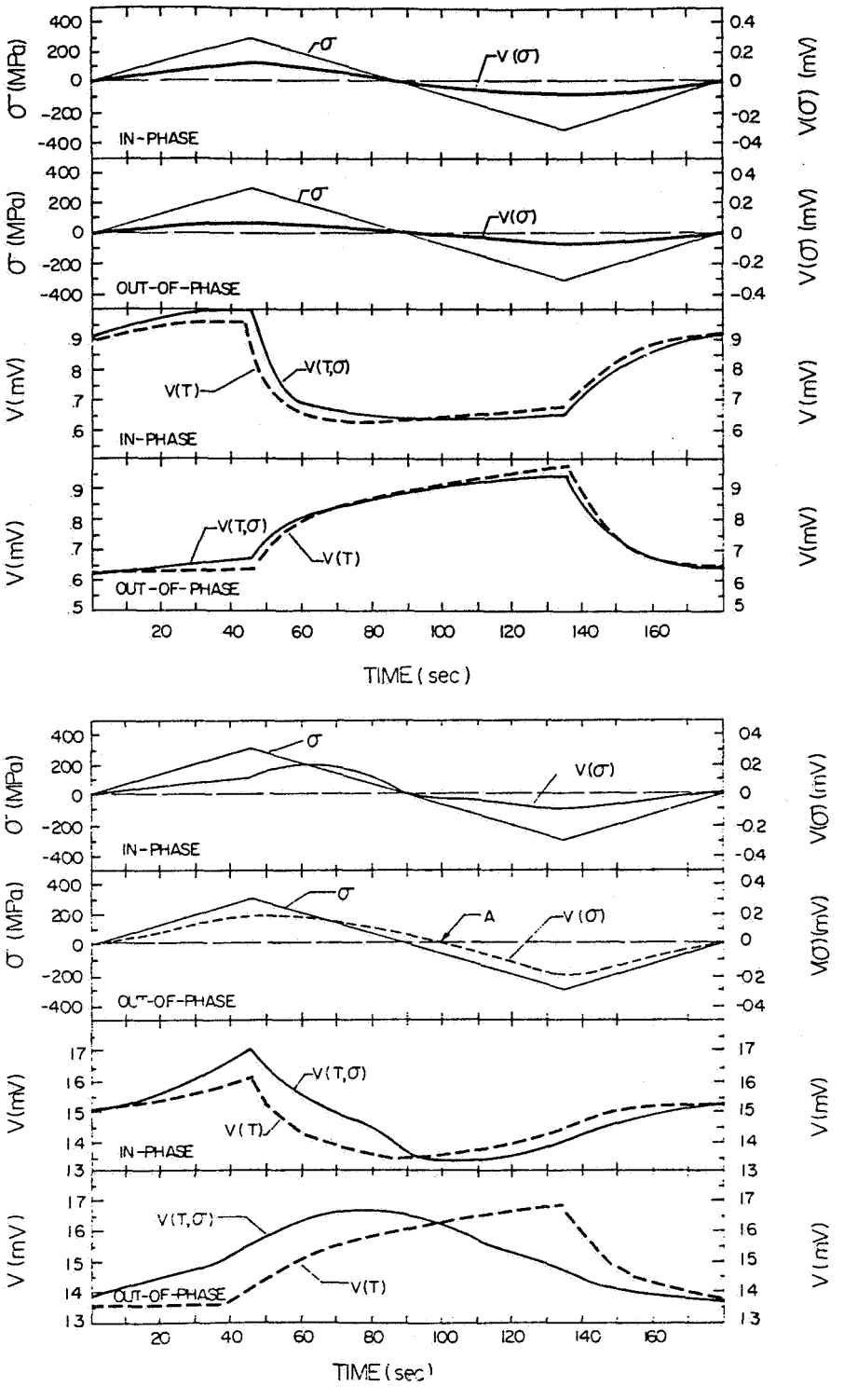

Figure 9 Potential curves V(T,σ), V(T) and V(σ) for TMFCG tests. (a) Inconel X-750, 25 MPa $\sqrt{m}$, (b) Inconel X-750, 50 MPa $\sqrt{m}$

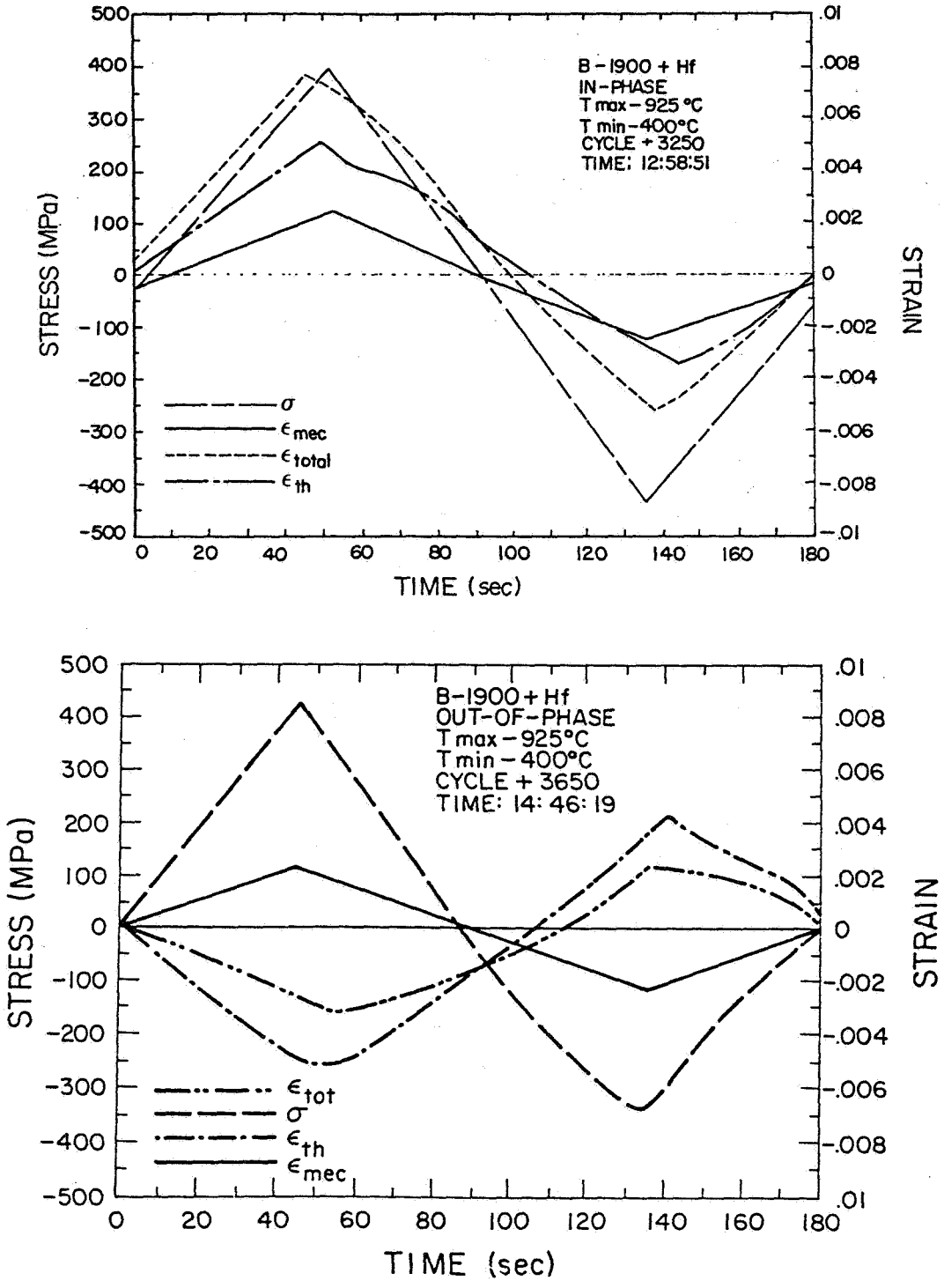

Figure 10 Stress, mechanical strain, thermal strain and total strain as a function of time (one cycle). (a) In-phase, (b) Out-of-phase

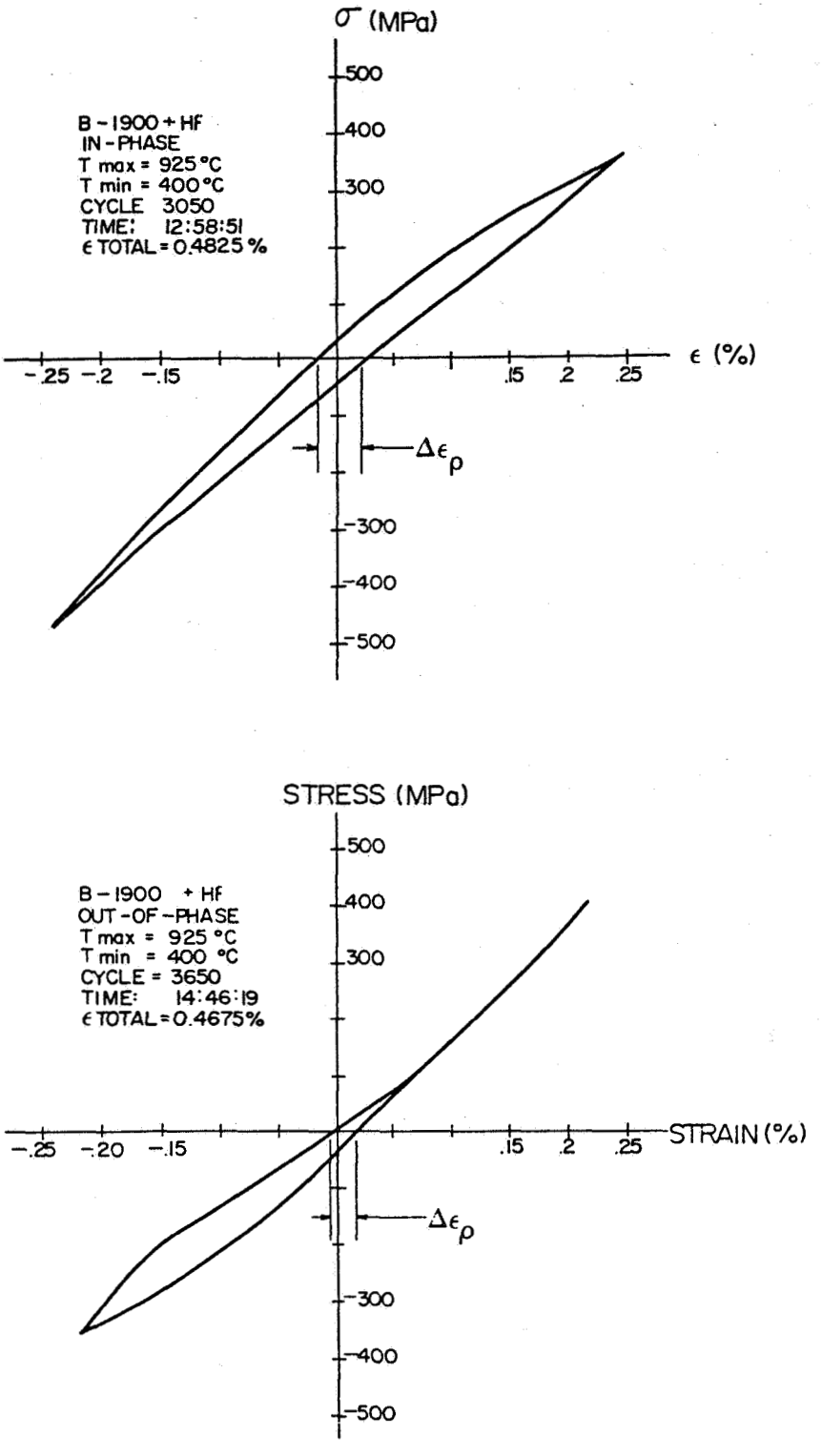

Figure 11 Typical hysterisis loop obtained under TMF conditions. (a) In-phase, (b) Out-of-phase

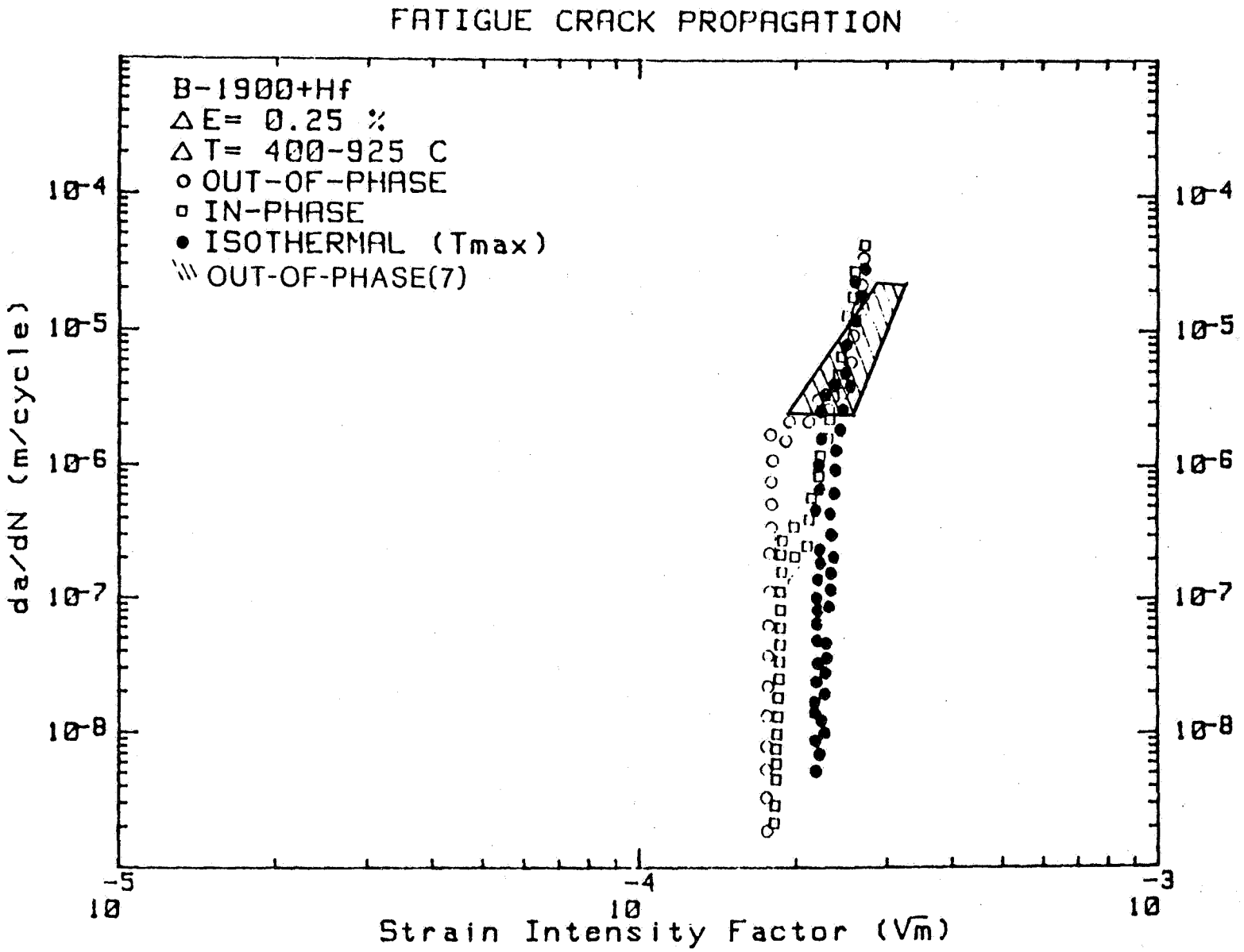

Figure 12 Fatigue crack growth rates under TMF conditions

Appendix B - Fracture Mechanics Analysis

K_I-Solutions for Single Edge Notch Specimens under Fixed End Displacements

by

N. Marchand*, D. M. Parks** and R. M. Pelloux***

Abstract

The K_I solution for a finite length single-edge notch specimen loaded under fixed end-displacements is derived using a crack compliance analysis. Numerical and experimental checks of the K_I solution are provided. Good agreement between the experimental and numerical solutions is observed. The applicability of conventional fracture mechanics to correlate crack growth data generated under displacement control is discussed.

* Research Assistant, Department of Material Science and Engineering, Massachusetts Institute of Technology, Cambridge, MA 02139

** Associate Professor, Department of Mechanical Engineering, Massachusetts Institute of Technology, Cambridge, MA 02139

*** Professor, Department of Material Science and Engineering, Massachusetts Institute of Technology, Cambridge, MA 02139

INTRODUCTION

The single-edge-notch (SEN) geometry with end constraints has received considerable attention in analytical fracture mechanics because of its frequent use as a test specimen. The problem of a SEN specimen with fixed-end displacements has been studied by several authors [1-3]. In particular, the formulation of Harris [2] has received much attention because of its ease of application. However, we felt that the closing bending moments associated with zero far-field relative rotation were perhaps more significant than those implied by Harris' solution, and this premise motivated the present analysis.

ANALYSIS

The presence of a crack in a rectangular sheet of thickness B loaded by uniform imposed end displacements cause the line of action of the applied load to shift relative to the specimen centerline. This shift produces a bending moment that tends to close the crack. For the SEN geometries, the only known boundary conditions are the imposed displacements, and the applied stresses are not known a priori and must be determined.

We consider an isotropic linear elastic sub-specimen of length L that is "sufficiently long" compared to crack length (a) and specimen width (W). The specimen is of thickness B and is subject to opposing forces N and moments M as shown schematically in Fig. 1. The line of action of the force N is taken as the mid-specimen. The following considerations are restricted to mode I behavior although the argument can be

generalized to include other modes.

The relative displacement δ and rotation θ of the specimen ends can be taken as the sum of a "crack" and "no-crack" parts:

$$\begin{bmatrix} \delta_{tot} \\ \theta_{tot} \end{bmatrix} = \begin{bmatrix} \delta_c \\ \theta_c \end{bmatrix} + \begin{bmatrix} \delta_{nc} \\ \theta_{nc} \end{bmatrix} . \qquad (1)$$

The compliance of the "no-crack" beam gives its extension δ_{nc} and rotation θ_{nc} in terms of the tensile force N acting throughout its center and the corresponding moment M[4]:

$$\begin{bmatrix} \delta_{nc} \\ \theta_{nc} \end{bmatrix} = \begin{bmatrix} L/E'A & 0 \\ 0 & L/E'I \end{bmatrix} \begin{bmatrix} N \\ M \end{bmatrix} , \qquad (2)$$

where E' = E(Young's modulus) for plane stress and $E/(1-\nu^2)$ for plane strain, ν being the Poisson's ratio. The section moment of inertia $I = BW^3/12$ and the cross section area $A = BW$ can be substituted into Eq. 2 to yield:

$$\begin{bmatrix} \delta_{nc} \\ \theta_{nc} \end{bmatrix} = \begin{bmatrix} L/E'BW & 0 \\ 0 & 12L/E'BW^3 \end{bmatrix} \begin{bmatrix} N \\ M \end{bmatrix} \qquad (3)$$

The expression for the "cracked" terms are obtained by considering the complementary energy of the specimen U in terms of N and M,

$$U(N,M) = \frac{1}{2} [N\ M] \left[\begin{bmatrix} \delta_{nc} \\ \theta_{nc} \end{bmatrix} + \begin{bmatrix} \delta_c \\ \theta_c \end{bmatrix} \right] , \qquad (4)$$

where the matrix scalar product is indicated. Since the "no-crack" terms given in Eq. 3 are independent of crack length, the energy release rate is

$$\frac{\partial U}{\partial a} = \frac{1}{2} [N\ M] \cdot \begin{bmatrix} \partial\delta_c/\partial a \\ \partial\theta_c/\partial a \end{bmatrix} . \qquad (5)$$

With the standard relation between G (fracture mechanics energy release rate) and K_I, the change in complementary energy with respect to crack length a is equal to [5]:

$$\frac{\partial U}{\partial a} = B \frac{K_I^2}{E'} . \qquad (6)$$

The stress intensity factor for combined tension and bending can be obtained by superposition of the stress intensity factors applicable to tension and bending. Therefore, in matrix form

$$K_I = \begin{bmatrix} \frac{\partial K}{\partial N} & \frac{\partial K}{\partial M} \end{bmatrix} \begin{bmatrix} N \\ M \end{bmatrix} . \qquad (7)$$

Highly accurate functional forms of $\partial K/\partial N$ and $\partial K/\partial M$ can be obtained from the compilations of Tada et. al. [5] where, for example

$$\frac{\partial K}{\partial N} = \frac{(\pi a)^{1/2}}{BW}\sqrt{\frac{2W}{\pi a}\tan\left(\frac{\pi a}{2W}\right)}\left[\frac{0.752+2.02\left(\frac{a}{W}\right) + 0.37\left(1-\sin\left(\frac{\pi a}{2W}\right)\right)^3}{\cos\left(\frac{\pi a}{2W}\right)}\right] \tag{8.1a}$$

$$\equiv (\pi a)^{1/2}\cdot F_1\left(\frac{a}{W}\right)/BW \ , \tag{8.1b}$$

$$\frac{\partial K}{\partial M} = \frac{6(\pi a)^{1/2}}{BW^2}\sqrt{\frac{2W}{\pi a}\tan\left(\frac{\pi a}{2W}\right)}\left[\frac{0.923 + 0.199\ \left(1-\sin\left(\frac{\pi a}{2W}\right)\right)^4}{\cos\left(\frac{\pi a}{2W}\right)}\right] \tag{8.2a}$$

$$\equiv (\pi a)^{1/2}\cdot F_2(a/W)\cdot \frac{6}{BW^2} \ . \tag{8.2b}$$

Note that in Eq. (8.1b, 8.2b), alternative non-dimensional function F_1, F_2 are introduced in such a manner as to facilitate K-calibrations in terms of a nominal stress "σ" as $K_I = F\cdot\sigma\cdot(\pi a)^{1/2}$. For tension, $\sigma = N/BW$, while for bending $\sigma = 6M/BW^2$. Now equating Eq. 5 and Eq. 6 and inserting Eq. 7 into Eq. 6, one obtains

$$\frac{1}{2}\begin{bmatrix} \frac{\partial \delta_c}{\partial a} \\ \\ \frac{\partial \theta_c}{\partial a} \end{bmatrix} = \frac{B}{E'}\begin{bmatrix} \left(\frac{\partial K}{\partial N}\right)^2 & \left(\frac{\partial K}{\partial N}\right)\left(\frac{\partial K}{\partial M}\right) \\ \\ \left(\frac{\partial K}{\partial N}\right)\left(\frac{\partial K}{\partial M}\right) & \left(\frac{\partial K}{\partial M}\right)^2 \end{bmatrix}\begin{bmatrix} N \\ M \end{bmatrix} . \tag{9}$$

Integrating Eq. 9 with respect to "a" provides the "crack" compliance matrix:

$$\begin{bmatrix} \delta_c \\ \theta_c \end{bmatrix} = \begin{bmatrix} C_{11} & C_{12} \\ C_{21} & C_{22} \end{bmatrix} \begin{bmatrix} N \\ M \end{bmatrix} \quad , \tag{10}$$

where

$$C_{11} = \frac{2B}{E'} \int_0^a \left[\left(\frac{\partial K(a')}{\partial N} \right) \right]^2 da' = \frac{\partial \delta_c}{\partial N} \tag{11.1}$$

$$C_{12} = C_{21} = \frac{2B}{E'} \int_0^a \left(\frac{\partial K(a')}{\partial N} \right) \left(\frac{\partial K(a')}{\partial M} \right) da' = \frac{\partial \delta_c}{\partial M} = \frac{\partial \theta_c}{\partial N} \tag{11.2}$$

$$C_{22} = \frac{2B}{E'} \int_0^a \left[\left(\frac{\partial K(a')}{\partial M} \right) \right]^2 da' = \frac{\partial \theta_c}{\partial M} \quad . \tag{11.3}$$

The generalized forces N, M can now be evaluated in terms of imposed displacements δ_{tot}, θ_{tot} by using Eqs. 1, 3 and 10, providing

$$\theta_{tot} = \frac{12L}{E'BW^3} M + C_{22}M + C_{21}N \qquad (12.1)$$

$$\delta_{tot} = \frac{L}{E'BW} N + C_{11}N + C_{21}M \quad , \qquad (12.2)$$

or, on multiplying by E'B;

$$E'B\theta_{tot} = \frac{12L}{W^3} M + E'BC_{22}M + E'BC_{21}N \qquad (13.1)$$

$$E'B\delta_{tot} = \frac{L}{W} N + E'BC_{11}N + E'BC_{21}M. \qquad (13.2)$$

For fixed-end displacement with no shear force $\theta_{tot} = 0$ and $\delta_{tot} = \delta$. Then from Eq. 13.1 we get

$$\frac{M}{W} = -\left[\frac{E'BWC_{12}}{12(L/W)+EBW^2C_{22}}\right] N \quad , \qquad (14)$$

while Eq. 13.2 can be re-written

$$E'B\delta = [\frac{L}{W} + E'BC_{11}]\ N + E'BWC_{21}\ (\frac{M}{W})\ . \tag{15}$$

On defining the dimensionless cracked compliance $\hat{C}_{ij}$ as

$$\hat{C}_{11} = E'BC_{11} \tag{16.1}$$

$$\hat{C}_{22} = E'BW^2C_{22} \tag{16.2}$$

$$\hat{C}_{12} = \hat{C}_{21} = E'BWC_{12} = E'BWC_{21}\ , \tag{16.3}$$

Eq. 14 simplifies to

$$\frac{M}{W} = \frac{-\hat{C}_{12}}{12(\frac{L}{W}) + \hat{C}_{22}} \cdot N \tag{17}$$

while Eq. 15 simplifies to

$$E'B\delta = (\frac{L}{W} + \hat{C}_{11})\ N + \hat{C}_{12}\ \frac{M}{W}\ . \tag{18}$$

When Eq. 17 is inserted into Eq. 18, the axial force N can be obtained as

$$N = E'BW\frac{\delta}{L} \cdot \frac{1}{\{1+\frac{W}{L}\left[\hat{C}_{11} - \frac{(\hat{C}_{12})^2}{(12(\frac{L}{W}) + \hat{C}_{22})}\right]\}} \cdot \tag{19}$$

The substitution of Eq. 19 into Eq. 17 provides

$$\frac{\dot{M}}{W} = \frac{E'BW\delta}{L} \cdot \frac{\left\{\frac{-\hat{C}_{12}}{(12(L/W) + \hat{C}_{22})}\right\}}{\left\{1 + \frac{W}{L}\left[\hat{C}_{11} - \frac{(\hat{C}_{12})^2}{(12(L/W)+\hat{C}_{22})}\right]\right\}} \cdot \tag{20}$$

Eq. 19 and 20, respectively provide the force N and bending moment M applied to the crack in terms of the imposed relative displacement δ under conditions of zero relative rotation. Note from Eq. 20 that, since the $\hat{C}_{ij}$ are inherently non-negative, the sign of M is indeed negative, tending to close the crack.

The total stress intensity factor for this specimen is, by superposition, the sum of that due to tension and that due to bending. Due to linearity,

$$K_I = \frac{\partial K}{\partial N} \cdot N + \frac{\partial K}{\partial M} \cdot M \quad , \tag{21}$$

and on combining Eqs. (8.1b, 8.2b, 19, 20) we obtain

$$K_I = \frac{E'\delta}{L} \cdot (\pi a)^{1/2} \cdot \frac{F_1(\xi)\left\{1 - 6 \cdot \frac{F_2(\xi)}{F_1(\xi)} \cdot \frac{\hat{C}_{12}(\xi)}{12\left(\frac{L}{W}\right) + \hat{C}_{22}(\xi)}\right\}}{\left\{1 + \frac{W}{L}\left[\hat{C}_{11}(\xi) - \frac{\hat{C}_{12}^2(\xi)}{12\left(\frac{L}{W}\right) + \hat{C}_{22}(\xi)}\right]\right\}} \quad , \tag{22}$$

where $\xi = a/W$. As shown in [6], the terms $\hat{C}_{ij}(\xi)$ are normalized dimensionless cracked compliances which need be calculated only once. In the present application, the integrals of Eq. 11 were numerically evaluated in increments of dimensionless crack length $\Delta\xi = \Delta a/W$ of size 0.01 using Simpson's rule. If we now substitute the nominal stress value $\sigma \equiv E'\delta/L$ into Eq. 22, we recover the familiar form

$$K_I = \sigma\sqrt{\pi a} \cdot G(\xi,\eta) \ , \tag{23}$$

where

$$G(\xi,\eta) = \frac{F_1(\xi) \cdot \left\{1 - \dfrac{6F_2(\xi)\cdot\hat{C}_{12}(\xi)}{F_1(\xi)[12\eta + \hat{C}_{22}(\xi)]}\right\}}{\left\{1 + \dfrac{1}{\eta}\left[\hat{C}_{11}(\xi) - \dfrac{\hat{C}_{12}(\xi)^2}{(12\eta + \hat{C}_{22}(\xi))}\right]\right\}} \ , \tag{24}$$

and $\xi = a/W$, $\eta = L/W$.

In Fig. 2, plots of $G(\xi, \eta)$ versus a/W are given for different values of L/W. The dimensionless functions F_1 and F_2 of Tada et. al. [5] (see Eqs. 8.1b, 8.2b) for pure tension and pure bending, respectively, are also shown for reference purposes. Finally, Fig. 2 also shows the approximate stress intensity factor calibration of the SEN specimen due to Harris [2], who gives

$$K_I = \sigma\sqrt{\pi a}\ F_H(a/W) \tag{25a}$$

with

$$F_H(a/W) = \left\{\frac{25}{20-13(a/W)-7(a/W)^2}\right\}^{1/2} . \qquad (25b)$$

In the interpretation of Eq. 25a, the nominal stress "σ" is understood to be N/BW, the nominal far-field stress, which in the present application must be determined (analysis) or measured (experiment) in terms of the imposed loading parameter δ.

As can be seen, our solution for G is strongly dependent on both relative crack depth and specimen length-to-width ratio and shows a local maximum with respect to a/W at some intermediate value of a/W for all (L/W) ratios larger than 2. For smaller ratios, the geometric correction factor G shows a monotonic decrease with respect to a/W until very deep cracks, a/W > .9, are considered. Tada's and Harris' geometry correction factors which were derived for tension, F_1 and F_H, under conditions of constant remote uniform tensile stress show a monotone increase with increasing a/W. Tada's bending geometry correction factor F_2 shows a slight decrease with increasing a/W, reaching a minimum value near a/W = 0.15, followed by a monotonic increase.

A basic assumption of the preceding analysis is that the specimen length (L) at which displacement boundary conditions are being imposed is sufficiently long in comparison to the appropriate St. Venant decay distance for the local stress disturbance introduced by the presence of the

crack. For short cracks, $a/W << 1$, the characteristic decay distance is "a", so that providing $L/W > 1$, the analysis should be valid. For very deep cracks, the decay length is specimen width W, so L must in that case exceed some multiple of W. This analysis cannot precisely quantify a requisite minimum value of L/W for any particular maximum value of a/W. However, good agreement has been obtained with Bowie and Freese's solution [3] for low values of $L/W = 2$, the agreement between the two solutions was within one percent for all values of a/W covered by the analysis.

EXPERIMENTAL VERIFICATION

An experimental check of the solution was provided by performing fatigue crack growth tests on SEN specimens subject to imposed displacement loading. The dimensions of the specimen are shown in Fig. 3. The notch, about 1 mm deep, was cut by electro-discharge machining. The test material was B-1900+Hf, a high-strength/low ductility superalloy with good creep and oxidation resistance at elevated temperature. The tests were run under fully reversed strain control condition in the elastic regime ($\Delta\varepsilon = 0.25\%$) in laboratory air. This nominal axial strain was controlled over a gauge length of 12.7 mm which included the crack. The temperature and frequency of the tests were 925° C and 0.1 Hz. Before starting the tests, the specimens were precracked at 10 Hz and room temperature under load-controlled conditions up to a ΔK of about 20 MPa$\sqrt{m}$ (Harris' solution) which corresponds to an a/W ratio of 0.125. Details of the experimental set-up and crack growth measurement technique are given elsewhere [7,8].

Fig. 4 shows the crack growth rates as a function of the strain intensity factor ΔK_ε. The ΔK_ε is used for convenience because fatigue at high temperature is a strain-controlled process. It is defined as follows [9,10]:

$$\Delta K_\varepsilon = \Delta\varepsilon \cdot \sqrt{\pi a} \cdot G(a/W) \ . \tag{26}$$

In the above expression, G (a/W) is the same geometric correction term derived in connection with the stress intensity factor. That is, in Fig. 4, the strain intensity is calculated as $\Delta\varepsilon \cdot \sqrt{\pi a} \cdot F_H(a/W)$ with $\Delta\varepsilon = .25\%$. In spite of the fact that ΔK_ε, so-defined, lacks a rigorous mechanics interpretation, it has been used for correlating crack growth data under strain-controlled conditions [9-12]. Clearly, the non-monotone correlation of fatigue crack growth rate with strain intensity factor range is not to be expected in cracks of macroscopic dimension. Thus, the non-monotonic nature of this correlation strongly suggests that there are deficiencies in this analysis of the strain intensity factor.

To provide a more rigorous understanding of the result, the ΔK_ε were re-defined as

$$\Delta K_\varepsilon = \Delta K/E' \tag{27}$$

where the ΔK is the stress intensity factor derived for stress-controlled (Eq. 25) or displacement-controlled (Eq. 23) conditions. In cases of predominantly elastic behavior, this definition of strain intensity factor is consistent with standard fracture mechanics. Fig.5 re-plots the fatigue crack growth rate versus the cyclic strain intensity factor deduced from Eq. 25 and from the current analysis (Eq. 23) using the value of L/W = 2.17 corresponding to the length of the uniform reduced gauge section of the specimen. In the application of Harris' formulation, the nominal stress σ was calculated using the tensile force N measured by the load cell. It should be noted that the load cell output is insensitive to the shift in load line which is associated with longer cracks. Again, the curve indicates that the correlation between measured fatigue crack growth rate and inferred strain intensity factor is non-monotone. Note, however, that the correlation is somewhat better than that shown in Fig. 4 because the inferred range of ΔK_ε occurring during the tests is reduced. The lower inferred range in the present case is due to the use of the measured load value, which decreases under fixed displacement conditions, due to the increasing crack compliance. This load-shedding is not reflected in the previous definition of ΔK_ε as $\Delta\varepsilon \cdot \sqrt{\pi a} \cdot F_H(a/W)$. The importance of load-shedding in the determination of the actual driving force has been recognized by Leis et. al. [13-14] which also used the measured load in their K calculations.

At this point, it is useful to consider more carefully the mathematical model of an imposed displacement with no rotation over a length "L"

as it relates to an actual specimen, such as that in Fig. 3, and its grips. Two points need to be reviewed. First, the applicability of the zero rotation conditions and secondly, the implication of measuring and controlling the imposed displacement at the back face of the specimen.

In the present case, the zero rotation condition is effectively enforced at the base of the threaded ends of the specimen. Thus, the effective value of L/W for the specimen might be expected to be somewhat greater than that based on the length of uniform reduced gage section. The additional effective length would correspond to the no-crack bending compliance of the tapered shoulders connecting gage section and threaded ends. The tensile part of the additional compliance is not required, since the mean extension δ is measured over the gauge length of $L_{gauge} = 2.17 \cdot W = 25.4$ mm. If we let L_b denote the augmented effective bending length of the specimen, and $\eta_b = L_b/W$, then the modified versions of Eq. 22 is (see Appendix).

$$K_I = \frac{E'\delta}{L} \cdot (\pi a)^{1/2} \cdot G(\xi, \eta, \eta_b) \tag{28}$$

where

$$G(\xi, \eta \eta_b) = \frac{F_1(\xi)\left\{1 - \frac{6F_2(\xi)}{F_1(\xi)} \cdot \frac{\hat{C}_{12}(\xi)}{(12\eta_b + C_{22}(\xi))}\right\}}{\left\{1 + \frac{1}{\eta}\left[\hat{C}_{11}(\xi) - \frac{\hat{C}_{12}^2(\xi)}{(12\eta_b + \hat{C}_{22}(\xi))}\right]\right\}} \tag{29}$$

and, again, $\eta = L/W$.

The other point to consider is the consequence of controlling the back face displacement, δ_{BF} (see Fig. 3) instead of at the centerline of the specimen. Because the displacement δ is controlled at L instead of L_b where no-rotation is effectively enforced, the displacement at the back face is equal to the displacement at the centerline (δ_{cl}) minus the displacement induced by rotation, θ_L, at L, i.e.,

$$\delta_{BF} = \delta_{cl}(L) - \frac{W}{2} \cdot \theta_L. \tag{30}$$

Now, using Eq. 30 with $\delta_{cl}(L)$ given by Eq. 12.2, the final corrected version K_I which takes into account both the effective length (L_b) and back face displacement is given by (See Appendix).

$$K_I = \frac{E'\delta}{L} \cdot (\pi a)^{1/2} \cdot G_c(\xi, \eta, \eta_b) \tag{31}$$

where

$$G_c(\xi,\eta,\eta_b) = \frac{F_1(\xi)\left\{1 - \dfrac{6F_2(\xi)}{F_1(\xi)} \cdot \dfrac{\hat{C}_{12}(\xi)}{(12\eta_b + \hat{C}_{22}(\xi))}\right\}}{\left\{1 + \dfrac{1}{\eta}\left[\hat{C}_W(\xi) - \dfrac{\hat{C}_{12}^2(\xi)}{12\eta_b + \hat{C}_{22}(\xi)} + \dfrac{6\hat{C}_{12}(\xi)(\eta-\eta_b)}{12\eta_b + \hat{C}_{22}(\xi)}\right]\right\}} \tag{32}$$

with η, η_b and ξ defined as before. The additional term appearing in the denominator of Eq. 32, as compared to Eq. 29, is of litte consequence for shorter cracks, and small values of $\eta_b-\eta$. Thus, the fact that back face, as opposed to centerline displacement is monitored is generally of minor significance.

Based on the assumption that $(da/dN)_{max}$ coincides with a maximum in the ΔK_ε (i.e., the correlation is monotone), plots of da/dN versus a/W were compared with plots of $G'_c(a/W)$ versus a/W where

$$G'_c(a/W) \equiv (\pi\xi)^{1/2} \cdot G_c(\xi, \eta, \eta_b) \tag{33}$$

for various values of η_b. Note from Eq. 33 that for prescribed δ, ΔK_ε is linearly proportional to $G'_c(\xi)$. The results are plotted in Fig. 6 versus relative crack depth, a/W. The maximum growth rate, occurring at a/W = 0.52, coincides with the location of maximum $G'_c(\xi,\eta,\eta_b)$ for the case of η_b = 2.5. A plot of da/dN versus ΔK_ε inferred from the present analysis with L_b/W = 2.5 is shown in Fig. 7. A very tight correlation between the crack growth rates and the ΔK_ε's is observed with a monotone correlation, within reasonable limits of experimental scatter. One concludes that our K-solutions (Eq. 28, 31) correlate the data providing the proper "effective" bending length is used. It should be pointed out, that an L_b/W ratio of 2.5 (which corresponds to a length of 29 mm) is the distance between the mid-shoulders of the specimen.

CONCLUSION

For a given geometry and applied end-displacements, Figs. 4 to 6, show that the uncritical use of conventional stress-derived K_I solutions can substantially overestimate the K_I values. While such an eventuality is conservative in application, it is non-conservative when testing to obtain basic materials behavior.

In the present case, the use of the strain intensity factor as represented by Eq. 26 seems to have two important limitations, both of which grow in importance at higher a/W levels. First, this definition of strain intensity factor as crack growth driving parameter does not account for the substantial load-shedding associated with the increasing crack compliance. This limitation can, in part, be mitigated (as in Fig. 5), by monitoring the decreasing load amplitude as the crack extends, and substituting this crack-length-dependent load into a tensile loading intensity factor calibration. The second major limitation of the traditional strain intensity factor defnition is that it fails to account for the development of a closing bending moment, associated with the prescribed zero-rotation boundary condition. This closing bending moment further reduces the effective crack driving force. A complete analysis of tension and bending moment in the specimen is required. When the K-solutions are derived from a line-spring analysis and combined with an effective specimen length, good correlations are found between K and the experimental fatigue crack growth data.

ACKNOWLEDGEMENTS

This work was sponsored by the National Aeronautics and Space Administration under Grant No. NAG3-280. The participation of David M. Parks was supported in part by the Office of Naval Research under Grant #N00014-80-C-0706.

REFERENCES

1. J. M. Bloom, International Journal of Fracture, Vol. 3 (1967), pp. 235-242.

2. D. O. Harris, Trans. of ASME, Journal of Basic Engineering, Vol. 89, (1969), pp. 49-54.

3. O. L. Bowie and C. E. Freese, Engineering Fracture Mechanics, Vol. 14 (1981), pp. 519-526.

4. E. P. Popov, Introduction to Mechanics of Solids, Prentice-Hall, Englewood Cliffs (1968).

5. H. Tada, P. C. Paris, and G. R. Irwin, The Stress Analysis of Cracks Handbook, Del Research Corporation, Hellentown (1973).

6. F. A. McClintock, D. M. Parks, J. W. Holmes and K. W. Bain, Engineering Fracture Mechanics, Vol. 20 (1984), pp. 159-167.

7. N. Marchand and R. M. Pelloux, "A Computerized Test System for Thermal-Mechanical Fatigue Crack Growth", submitted for publication.

8. N. Marchand and R. M. Pelloux, in Time-Dependent Fracture, Martinus Nijhoff (1985), pp. 167-179.

9. R. C. Boettner, C. Laird and A. J. McEvily, Trans. of Metallurgical Society of AIME, Vol. 233 (1965), pp. 379-387.

10. A. J. McEvily, "Fatigue Crack Growth and the Strain Intensity Factor" in Fatigue and Fracture of Aircraft Structures and Materials, AFFDL-TR-70-144 (1970).

11. A. E. Gemma, F. X. Ashland and R. M. Masci, ASTM Journal of Testing and Evaluation, Vol. 9, (1981), pp. 209-213.

12. T. Koizumi and M. Okazaki, Fatigue of Engineering Materials and Structure, Vol. 1 (1979), pp. 509-520.

13. B. N. Leis and T. F. Forte, ASTM STP 743 (1981), pp. 100-124.

14. B. N. Leis, "Displacement Controlled Fatigue Crack Growth in Elastic Plastic Notch Fields and the Short Crack Effect", to appear in a forthcoming issue of Engineering Fracture Mechanics.

APPENDIX

Consider a specimen of gage length L with its associated shoulders. Let's define L_b the effective length at which the zero rotation is enforced ($\theta\big|_{L_b}=0$). Obviously $L_b > L$ and, as a consequence the back face displacement δ_{BF} measured at L will be equal to the centerline displacement minus the angular displacement at L, i.e., $\frac{W}{2}\bullet\theta_L$. Therefore, the known quantities are δ_{BF} (measured at L) and θ_{tot} across L_b. Equations 12.1 and 12.2 can now be written as

$$0 = \theta_{tot}(L_b) = \theta(L_b) = \theta_{nc}(L_b) + \theta_c \qquad (A.1)$$

$$\delta_{BF} = \delta_{tot}(L) = \delta_{nc}(L) + \delta_c(L) - \frac{W}{2}\ \theta(L) \qquad (A.2)$$

Substitute Eq. 10 into A.1 and re-arranging, yielding

$$\frac{M}{W} = \frac{-C_{12}\ E'BW}{12\ \eta_b + C_{22}\ E'BW}\ \cdot N \qquad (A.3)$$

On using the dimensionless crack compliance defined by Eqns. 16.1 to 16.3, Eq. A.3 simplifies to

$$\frac{M}{W} = \frac{-\hat{C}_{12}}{12\,\eta_b + \hat{C}_{22}} \cdot N \qquad (A.4)$$

where $\eta_b = L_b/W$. Noting that $M(L_b) = M(L)$, the displacement δ_{BF} (Eq. A.2) is, using Eq. 10 and A.1,

$$\delta_{BF} = \left[\frac{NL}{BWE'} + C_{11}N + C_{12}M\right] - \frac{W}{2}\left[\frac{12ML}{BW^3} + C_{22}M + C_{12}N\right] \qquad (A.5)$$

which, upon re-arranging and using the dimensionless crack compliance (Eqns. 16.1-16.3) yields

$$N = E'BW\,\frac{\delta_{BF}}{L} \cdot \frac{1}{\left\{1 + \frac{1}{\eta}\left[\hat{C}_{11}(\xi) - \frac{\hat{C}_{12}^2(\xi)}{(12\eta_b + \hat{C}_{22}(\xi))} + \frac{6\hat{C}_{12}(\xi)(\eta-\eta_b)}{(12\eta_b + \hat{C}_{22}(\xi))}\right]\right\}} \qquad (A.6)$$

Finally, recalling that

$$K_I = \frac{N}{BW}\sqrt{\pi a} \cdot F_1(\xi) + \frac{6M}{BW^2} \cdot \sqrt{\pi a} \cdot F_2(\xi) \qquad (A.7)$$

and upon substitution of Eqns. A.4 and A.6 into A.7, we get

$$K_I = \frac{E'\delta_{BF}}{L} \cdot \sqrt{\pi a} \cdot \frac{F_1(\xi)\left\{1 - \frac{6F_2(\xi)}{F_1(\xi)} \cdot \frac{\hat{C}_{12}}{(12\eta_b + \hat{C}_{22})}\right\}}{\left\{1 + \frac{1}{\eta}\left[\hat{C}_{11}(\xi) - \frac{\hat{C}_{12}^2}{12\eta_b + \hat{C}_{22}(\xi)} + \frac{6\hat{C}_{12}(\xi)(\eta-\eta_b)}{12\eta_b + \hat{C}_{22}}\right]\right\}} \qquad (A.8)$$

Equation A.8 corrects for the fact that actual displacements are measured at back face instead of the centerline, and for the fact that the zero-rotation condition is imposed not at L, but at some distance L_b close to the actual grips.

LIST OF CAPTIONS

Fig. 1 Resultant force N and moment M transmitted by the grips to a SEN specimen.

Fig. 2 Geometrical factors F_1, F_2, F_H and Eq. 24 as a function of the dimensionless crack length.

Fig. 3 Single edge notched (SEN) specimen used for the testing (notch: 1 mm deep x 0.025 mm wide).

Fig. 4 FCG rates as a function of the strain intensity factor calculated using Eq. 22.

Fig. 5 FCG rates as a function of the strain intensity factor calculated using Eq. 25.

Fig. 6 FCG rates as a function of a/W and Eq. 33 as a function of a/W for various η_b ratios.

Fig. 7 FCG rates as a function of the strain intensity factor calculated using Eq. 32.

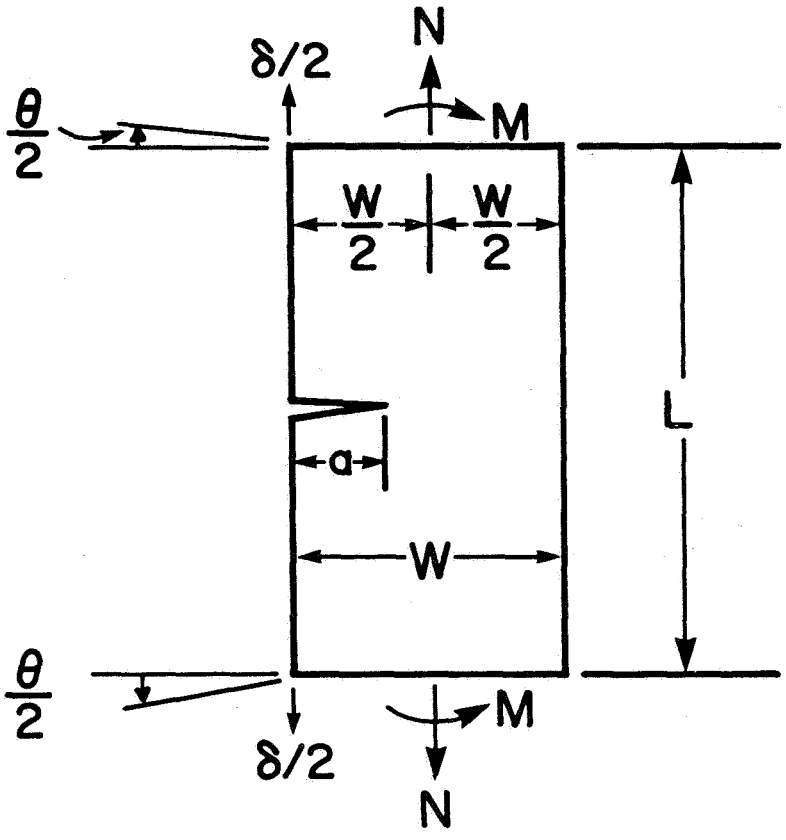

Fig. 1 Resultant force N and moment M transmitted by the grips to a SEN specimen.

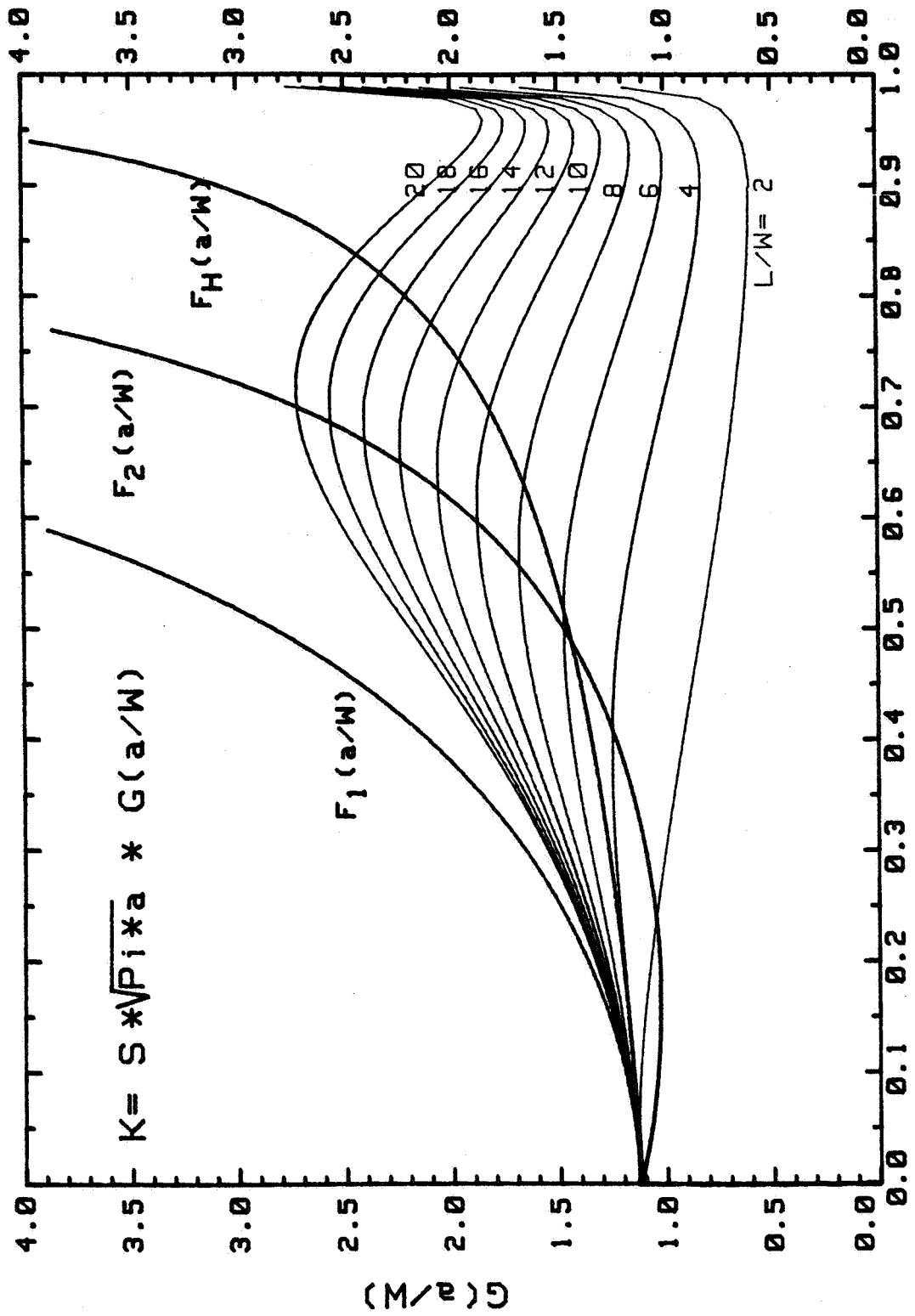

Fig. 2 Geometrical factors F_1, F_2, F_H and Eq. 24 as a function of the dimensionless crack length.

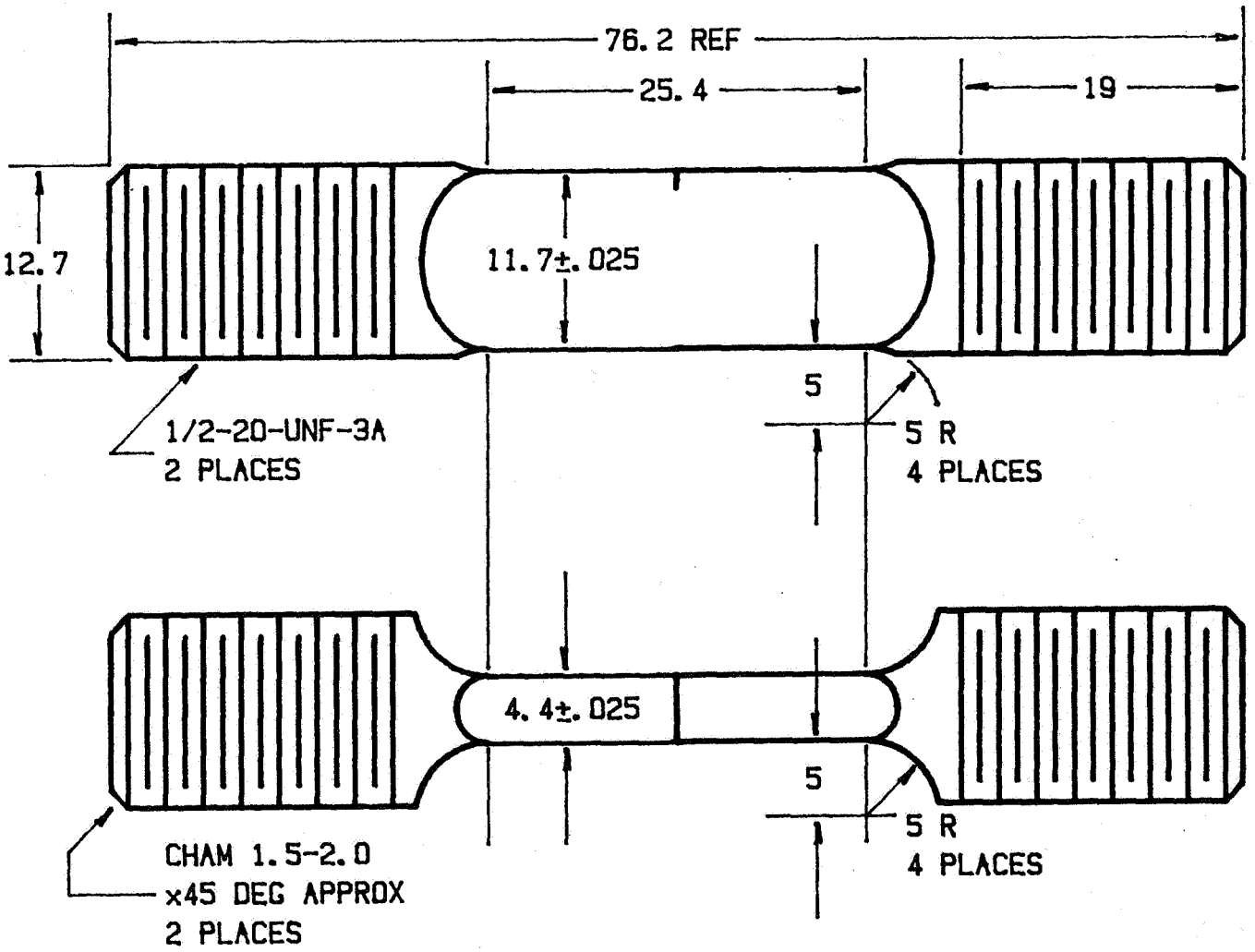

Fig. 3 Single edge notched (SEN) specimen used for the testing (notch: 1 mm deep x 0.025 mm wide).

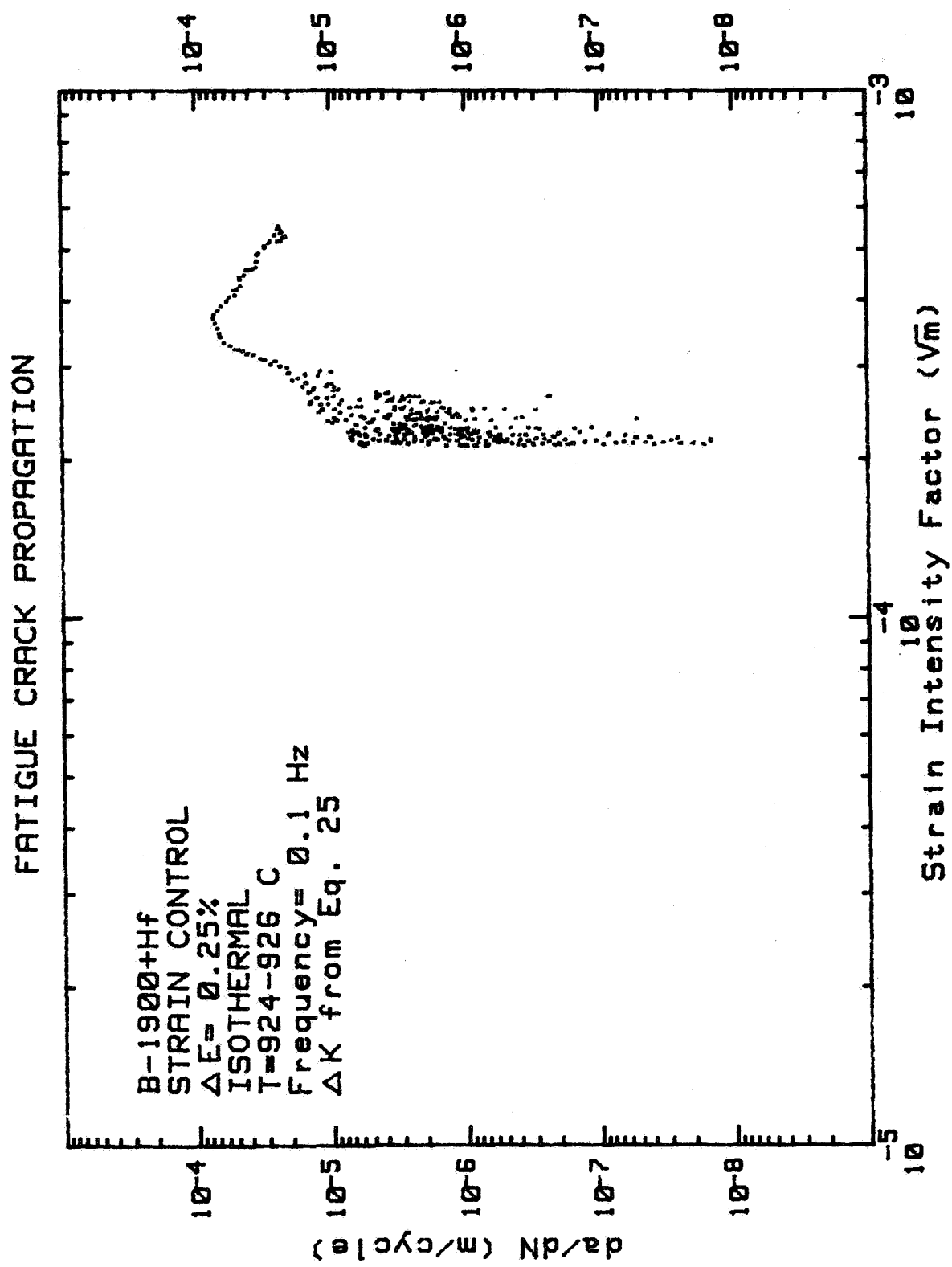

Fig. 4 FCG rates as a function of the strain intensity factor calculated using Eq. 22.

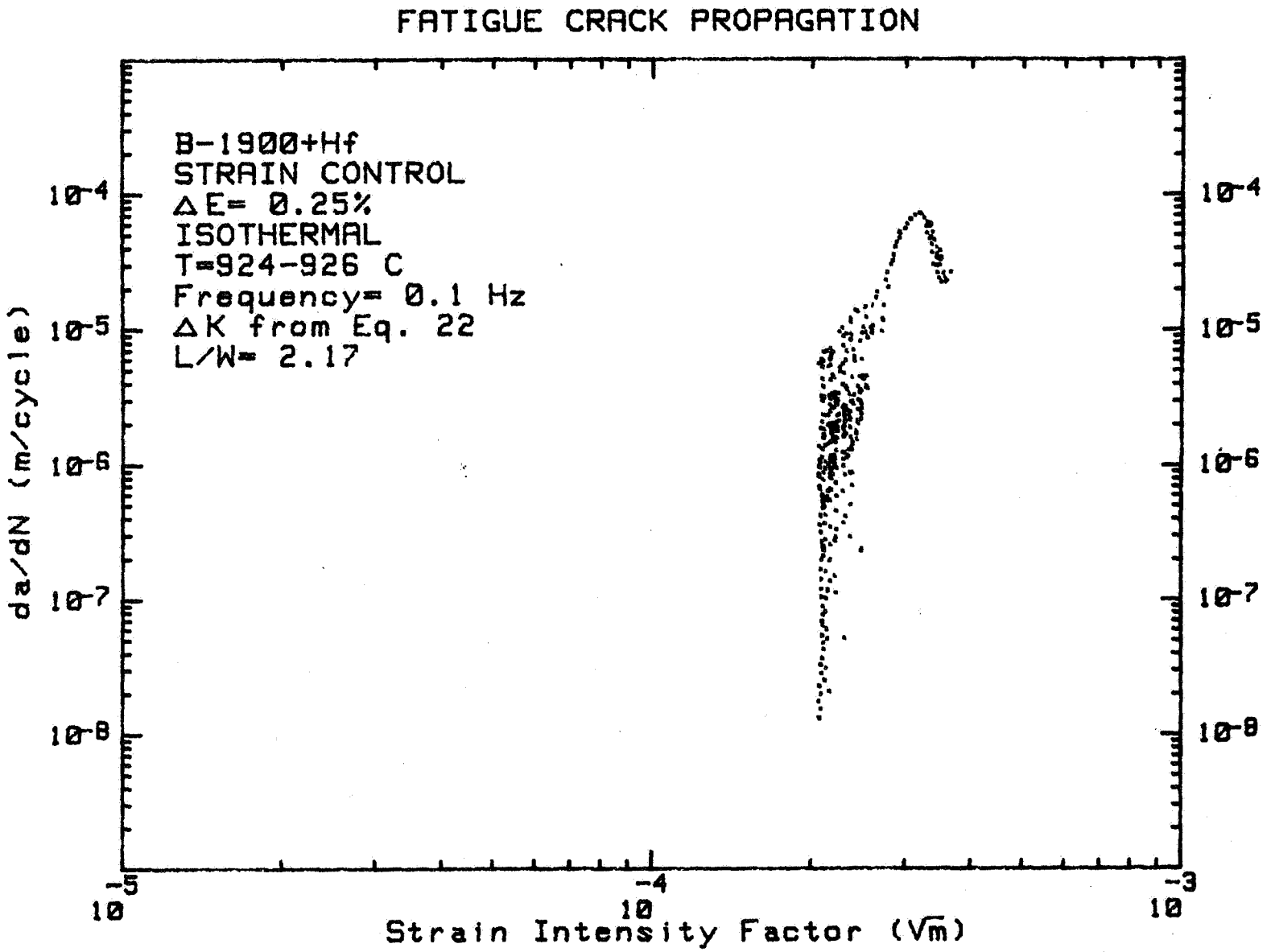

Fig. 5 FCG rates as a function of the strain intensity factor calculated using Eq. 25.

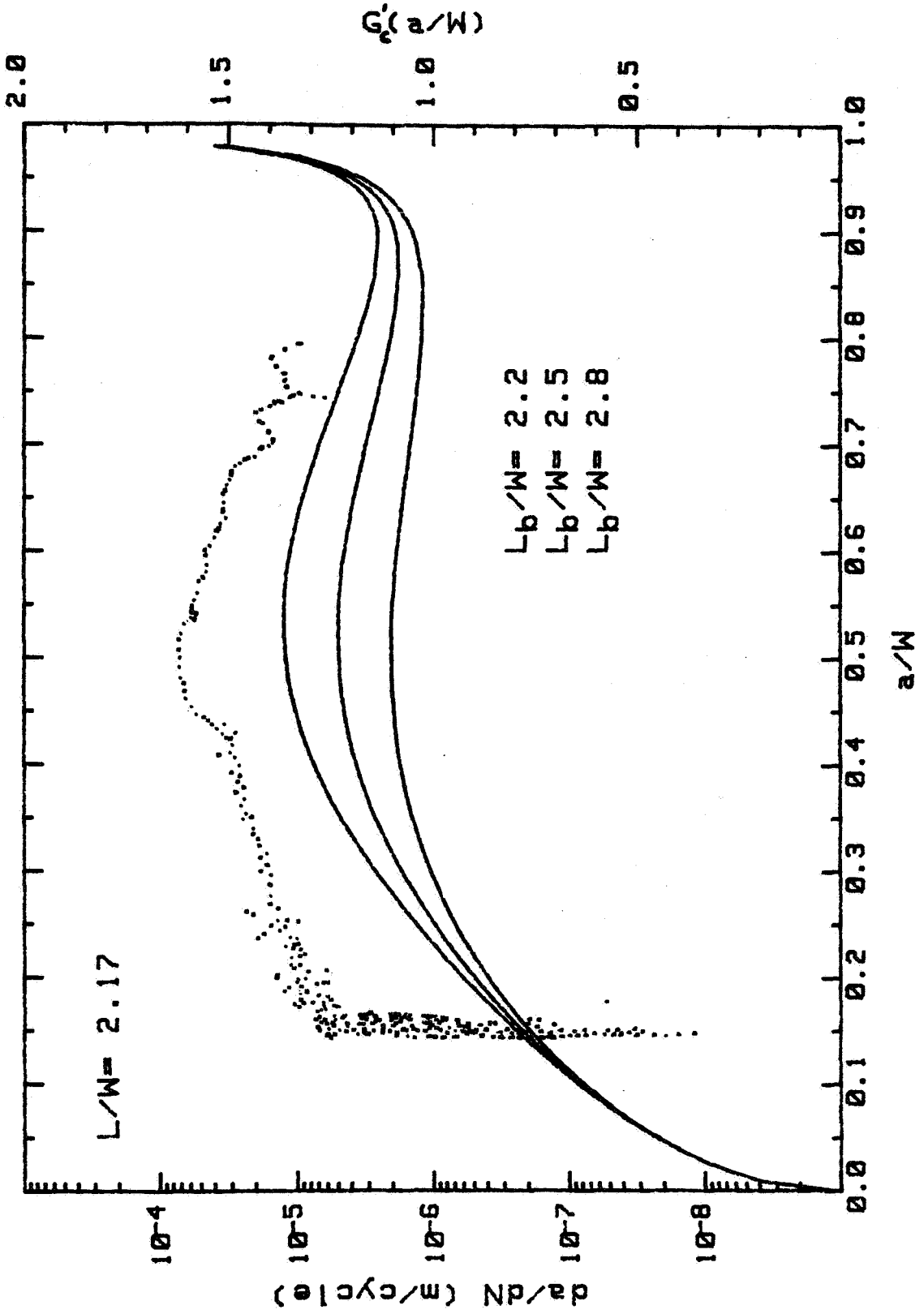

Fig. 6 FCG rates as a function of a/W and Eq. 33 as a function of a/W for various η_b ratios.

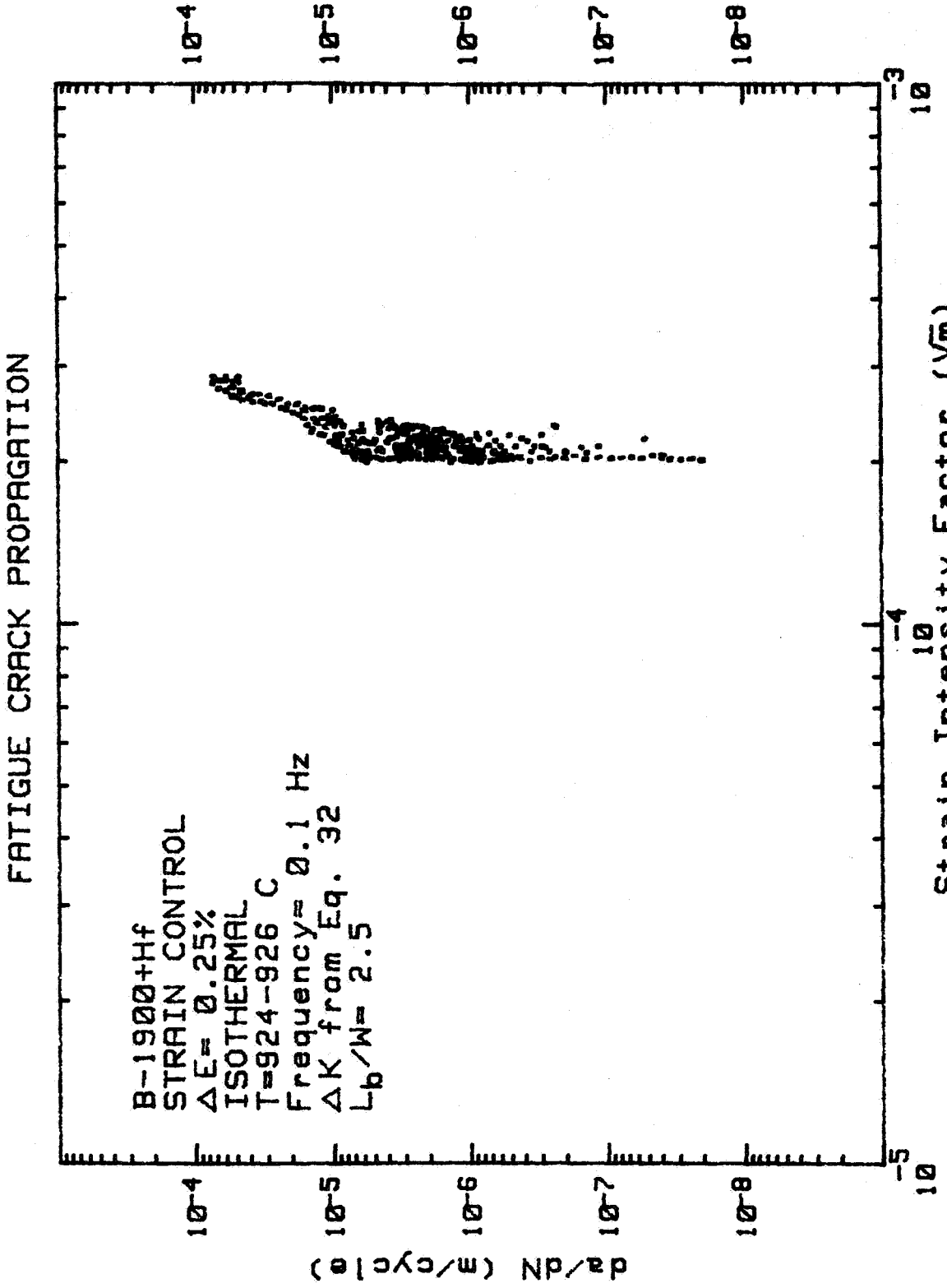

Fig. 7 FCG rates as a function of the strain intensity factor calculated using Eq. 32.

Appendix C - TMFCG in Inconel X-750

THERMAL-MECHANICAL FATIGUE CRACK GROWTH IN INCONEL X-750

Norman Marchand* and Regis M. Pelloux**

*Research Assistant, Department of Materials Science and Engineering, Massachusetts Institute of Technology, Cambridge, MA 02139, USA.

**Professor, Department of Materials Science and Engineering, Massachusetts Institute of Technology, Cambridge, MA 02139, USA

ABSTRACT

Thermal-mechanical fatigue crack growth (TMFCG) was studied in a γ-γ' nickel base superalloy Inconel X-750 under controlled load amplitude in the temperature range from 300 to 650°C. In-phase (T_{max} at σ_{max}), out-of-phase (T_{min} at σ_{max}) and isothermal tests at 650°C were performed on single-edge notch bars under fully reversed cyclic conditions.

A DC electrical potential method was used to measure crack length. The electrical potential response obtained for each cycle of a given wave form and R value yields information on crack closure and crack extension per cycle. The macroscopic crack growth rates are reported as a function of ΔK and the relative magnitude of the TMFCG are discussed in the light of the potential drop information and of the fractographic observations.

INTRODUCTION

Many fatigue problems in high temperature machinery such as gas turbine components involve thermal as well as mechanical loadings. By thermal loading it is meant that the material is subjected to cyclic temperature simultaneously with cyclic stress or strain. Analysis of the local stresses and strains versus temperature and time become very complex, consequently gross simplifications are introduced to analyse and predict the fatigue damage. These simplifications usually involve the use of isothermal data

and life predictions techniques are based upon isothermal testing. In fact, the study of fatigue has generally bypassed real thermal fatigue loading partly because isothermal tests are relatively simple to perform, but also because it has often been felt that such tests carried out at the maximum service temperature would give worst case results. However, several studies which have compared fatigue resistance under thermal cycling conditions with that in isothermal tests have shown that in many cases, the latter, rather than giving a worst case situation, can seriously overestimate the real fatigue life [1-15].

The influence of temperature on low cycle fatigue (LCF) lives is well documented [16-19] but the mechanisms by which temperature influences the fatigue process are not well understood. Low cycle fatigue is generally acknowledged to be directly related to material ductility; however, as ductility increases with temperature, low cycle fatigue life normally decreases. Creep and environmental effects are known to influence LCF behavior, but the relative contributions of these two factors are not easily differentiated. [17-19, 20].

The subject of thermal fatigue which involves combined temperature and stress-strain cycling, is less well understood than isothermal elevated temperature fatigue and only limited data have been gathered on crack growth during thermal-mechanical fatigue (TMF) under conditions of small plastic strain [2, 5-7, 9, 13-14].

The data obtained from thermal-mechanical testing for conventionally cast Co- and Ni-based superalloys, and for directionally solidified Ni-based alloy [5-7, 9, 13] have shown faster crack growth rates than for the equivalent isothermal conditions at T_{max}. Furthermore, crack growth rates under out-of-phase cycling (T_{min} at σ_{max}) were found to be faster than under in-phase cycling (T_{max} at σ_{max}). For a 12 Cr-Mo-V-W steel thermal-mechically cycle between 300 and 600°C, very little difference in growth rates for TMF and isothermal tests were found [21], whereas, an inverse behavior was observed on a 304 SS [15]; that is, faster crack growth rates under in-phase cycling than under out-of-phase cycling.

From the TMF crack growth data available in the open literature, it can be seen that there is no generalization to be made concerning the severity of damage associated with in-phase and out-of-phase cycling, and that there is no hard and fast rule for relating TMF data to isothermal testing.

In order to obtain a better understanding of the TMFCG behavior a research program was established with a two-fold objective. First to assess a sound, fundamental mechanistic under-

tanding of TMF of typical nickel-base superalloys. Second, to assess the suitability of various parameters for correlating high temperature TMFCG rates used for adequate fatigue life predictions of engine components.

EXPERIMENTAL PROCEDURE

Materials and Specimen

The material used in this investigation was a standard chemistry Inconel X-750, a corrosion and oxidation resistant material with good tensile and creep properties at elevated temperatures. The chemical composition, the heat treatment of the as-received annealed material, and the tensile properties at high and room temperature are given in Table 1. The grain size is about 0.12 mm. Single edge notch tensile bar specimens were used in this investigation. The test specimens have a rectangular cross section of 11.7 x 4.4 mm^2 and a starter notch approximately 1 mm deep which is cut by electro-discharge machining. The specimens were precracked in fatigue at 10 Hz at room temperature under a ΔK of about 10-15 $MPa\sqrt{m}$. All the ΔK's were calculated with the expression derived by Harris [22].

$$\Delta K = \Delta\sigma\sqrt{\pi a}\,\frac{5}{[20 - 13(\frac{a}{w}) - 7(\frac{a}{w})^2]^{1/2}} \qquad (1)$$

This formula which was derived for an edge crack in a SEN plate with no bending is suitable for the testing system.

Table 1

(a) Chemical Composition (wt. pct.)

Ni	Cr	Fe	Ti	Al	Nb	Mn	Si	C	Co
72	15.5	7	2.5	0.7	1	0.5	0.2	0.04	1.0

(b) Heat Treatment

Temperature (°C)	Time (hr)	Quench
1150	2	air cool
850	24	air cool
700	20	air cool

(c) Tensile Properties

Temperature (°C)	σ_y (MPa)	σ_{UTS} (MPa)	ε_p (Pct)
24	610	1000	30
300	616	1000	32
650	550	820	7

Apparatus and Test Conditions

The apparatus used in this study was a computer-controlled thermal fatigue testing system which consisted of a closed-loop servo-controlled, electro-hydraulic tension-compression fatigue machine, a high frequency oscillator for induction heating, an air compressor for cooling, a mini-computer, etc. Figure 1 shows the control block diagram of this system.

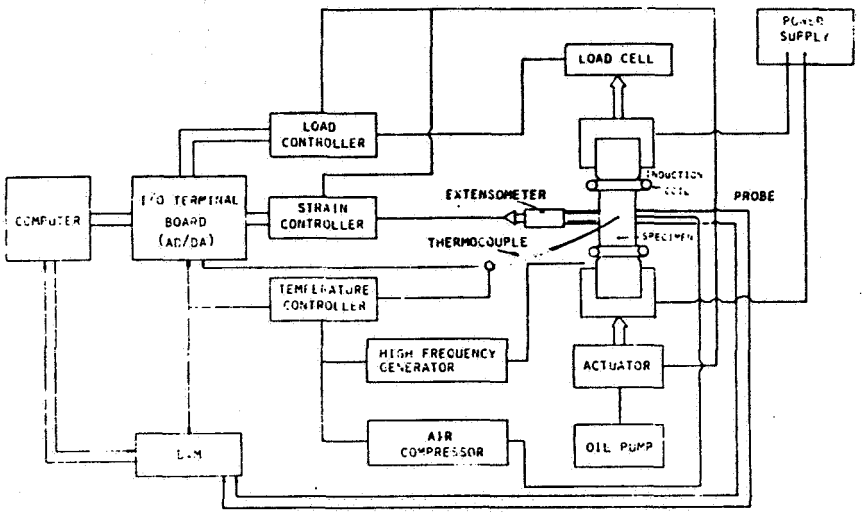

Fig. 1. Diagram showing the control system of apparatus used for TMFCG tests.

The system is capable of testing specimens of different sizes and configuration (SEN, CT, hollow tube, etc.) up to loads of 25,000 lbs. The specimen alignment is insured by the use of a Wood's metal pot which prevents a bending moment in the specimen. Because a DC potential drop technique is used to monitor crack growth, the lower grip is electrically insulated from the system by means of a ceramic coating. The ends of the grips are water cooled by means of copper coils.

Temperature was measured with 0.2 mm diameter chromel-alumel thermocouples which were spot welded along the gauge length. By computer controlling, the temperature in the gauge length was maintained within 5°C of the desired temperature for both axial and transverse directions over the entire period of the test.

Temperature and stress were computer controlled with the output of the thermocouple so that they were in-phase or out-of-phase for the same triangular wave shape. Therefore, specimens were in

tension at low temperature and in compression at high temperature under the out-of-phase cycling, and vice versa under the in-phase fatigue. The temperature range in these tests was 300 to 650°C. The tests were carried out at a frequency of 0.0056 Hz (1/3 cpm) and were run at a R ratio (σ_{min} / σ_{max}) of -1 or 0.05. Isothermal fatigue tests were also conducted under the same frequency at T_{max} for comparison with the results of TMFCG tests. All the tests were carried out in air. Table 2 summarizes the experimental conditions. At least two tests at each condition were performed to insure repeatability of the results.

There have been few attempts to measure crack length in the TMF cycling using the potential drop technique [2]. The method has proved to be satisfactory in isothermal conditions and can be used for TMF testing provided that the electrical noise is adequately filtered and the calibration curve is properly corrected to take into account changes of potential with temperature. This was achieved by using a 450 KHz filter and a high accuracy digital voltmeter programmed to convert the analog signal average over 10 power line cycles (PLC). In this mode, 1 PLC is used for the run-up time with the A/D conversion repeated ten times. The resulting ten readings are then averaged and the answer becomes a single reading.

This system, as opposed to the optical measurement and compliance methods, has the capability of monitoring the crack extension during a single cycle, whereas the previous methods are limited for growth measurement to no more than one cycle. Therefore, detailed analysis of the crack growth process can be performed and this is particularly important in trying to determine the mechanisms involved with TMFCG or with the kinetics of short crack growth.

Table 2

Experimental Conditions

Frequency (Hz)	Temperature (°C)	R-Ratio
0.1	25	0.05
0.0056	650	0.05
0.0056	650	-1
0.0056	300-650 (in-phase)	0.05
0.0056	300-650 (in-phase)	-1
0.0056	650-300 (out-of-phase)	-1

Results and discussion

Figures 2 and 3 show the variation of the potential with

simultaneous change of the net stress and temperature for in-phase and out-of-phase cycling at low and high ΔK. In these figures, the potential change with stress and temperature V(T,σ) and with temperature only V(T) are plotted. The mechanical driving force V(σ) which is the difference between V(T,σ) and V(T) are also plotted. In order to assess crack growth, the peak potential of each cycle was recorded and plots of the voltage versus the number of cycle (N) were obtained. Using an experimental calibration curve, the crack lengths versus N were derived. The crack growth rates were calculated using a seven-point incremental polynomial method. Figure 4 shows the results as a function of ΔK (R = 0.05) and K_{max} (R = -1).

First, it can be seen that the crack growth rates are higher for TMF cycling than for the equivalent isothermal condition (650°C) which is in agreement with the results obtained on other nickel-base alloys [5-7, 9, 13]. Secondly, it is observed (Fig. 4) that the crack growth rates are higher for R = - 1 than for R = 0.05 which indicates that compressive stresses play an important role in the mechanics of TMFCG. Comparison between out-of-phase and in-phase at R = -1 shows that out-of-phase cycling is more damaging than in-phase cycling at high ΔK, whereas at low ΔK, the crack growth rates are the same. The explanation for this behavior can be found in Figs. 2 and 3. At low ΔK the potential curves V(σ) for out-of-phase and in-phase are similar which indicates that the mechanical driving force for cracking are similar and identical crack growth rates are therefore expected. As ΔK increases, however, the V(σ) potential curves for both in-phase and out-of-phase cycling display characteristic features (Fig. 3). The in-phase V(σ) curve shows a smooth increase with σ_{net} up to the maximum followed by a sharp increase at σ_{max}. The potential then remains stable as σ_{net} starts to decrease and sharply falls as σ_{net} approaches zero. In the compression regime the potential smoothly decreases, reaches a minimum at σ_{min}, and finally increases as the stress increases again. On the other hand, the out-of-phase V(σ) potential curves shows (at the same ΔK) a smooth increase with σ_{net} with a peak value at σ_{max}. The potential then decreases down to a minimum value and finally increases again with σ_{net}. The most important feature of these signals is the crossover point (denoted A) for which V(σ) = 0. The crossover point represents the stress to apply to the specimen for the potential to equal V(T). Because V(T) is measured at σ = 0 for the entire thermal cycle, the expected stress to apply is σ = 0. However, if the potential field near the crack tip is disturbed either by a non-zero residual stress-strain field or by geometrical events such as blunting, closure, etc., the V(T, σ = 0) potential might not necessarily equal V(T) and a non-zero stress is required to cancel out the contribution of this phenomena. For the out-of-phase potential, the crossover occurs at a negative stress (σ = -75 MPa at ΔK = 50 MPa$\sqrt{m}$), whereas, it always occurs at zero stress for the in-phase potential. By

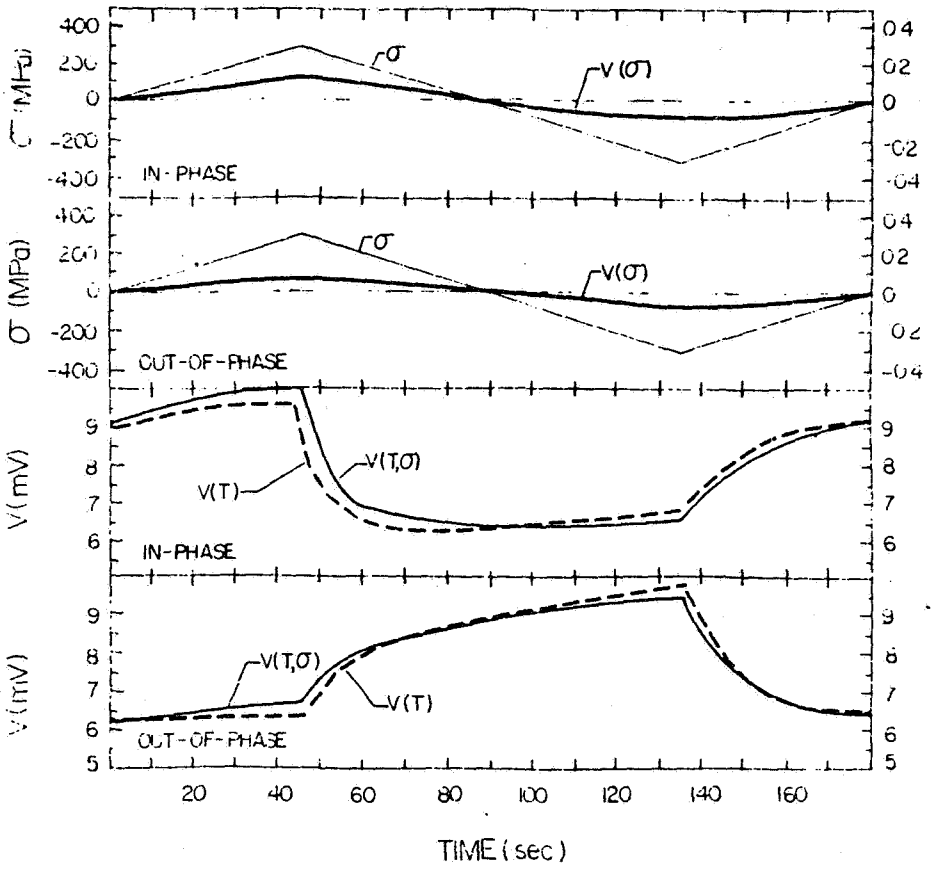

Fig. 2. Potential curves V(T,σ), V(T) and V(σ) for TMFCG of Inconel X-750. $\Delta K = 25$ MPa$\sqrt{m}$.

first assuming that the crossover point occurs near an effective closure stress (σ_{cl}) it follows that the effective stress intensity factor (ΔK_{eff}) for crack growth will be higher for out-of-phase than for in-phase cycling (σ_{cl} is negative). If we plot the crack growth rates as a function of ΔK_{eff}, we find that both in-phase and out-of-phase crack growth rates overlap (Fig. 5).

It is important to note that the absolute amplitude of the V(σ) signal (see Fig. 3) in the compressive regime of the cycle, is much higher for out-of-phase than for in-phase cycling which indicates that the crack surfaces are in contact on a much larger scale than under in-phase cycling. This was confirmed by fractographic observation which shows that out-of-phase cycling leads

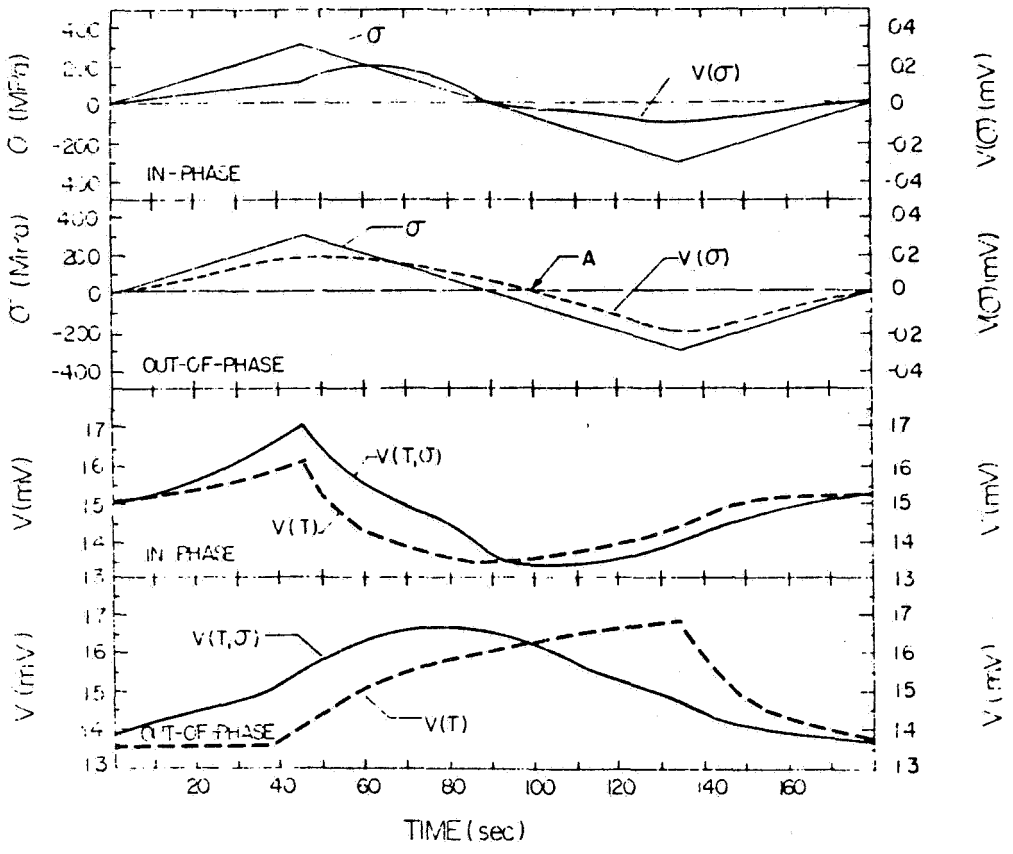

Fig. 3. Potential curves $V(T,\sigma)$. $V(T)$ and $V(\sigma)$ for TMFCG of Inconel X-750. $\Delta K = 50$ MPa$\sqrt{m}$.

to transgranular cracking with considerable mating, whereas, in-phase cycling leads to intergranular fracture with little evidence of mating. The higher crack growth rates at R = -1 than R = 0.05 and the fractographic observations lead to the conclusion that although there should be no cracking at the maximum temperature because of the compressive stress, some form of severe damage is taking place under compressive strain. Also, the surface oxide film formed at high temperature will rupture at low temperature, under maximum tensile stress. This leads to a resharpening of the crack tip with each cycle and results in an increase in growth rate.

The rationale for the negative closure stress in out-of-phase cycling can be found by assuming that the residual stress field at the crack tip is of tensile nature at zero applied stress and that

a negative stress has to be applied in order to cancel it and to close the crack. This negative σ_{cl} also represents the effective contribution to cracking of the damage taking place during the compression part of the cycle.

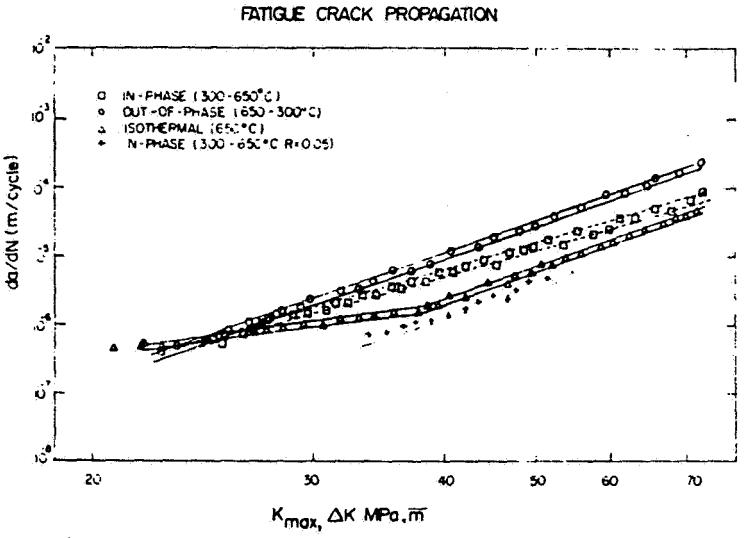

Fig. 4. TMFCG of Inconel X-750 as a function of ΔK.

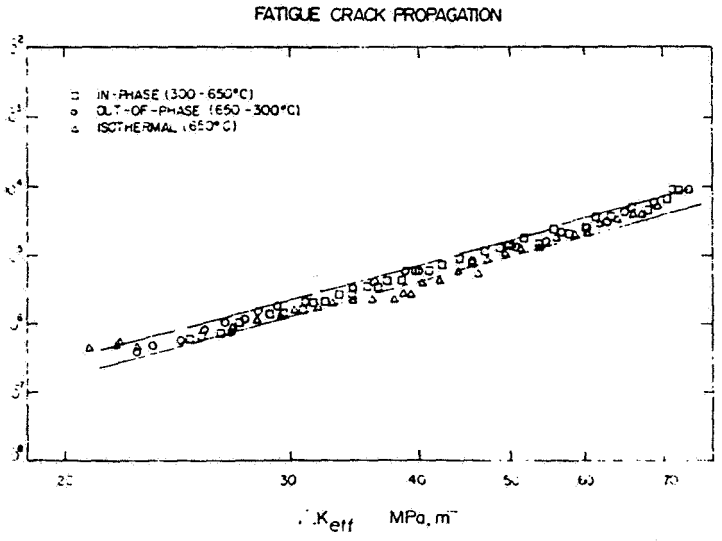

Fig. 5. TMFCG of Inconel X-750 as a function of ΔK_{eff}

The difference in growth rates between the isothermal test (650°C) and the TMF tests were also explained by looking at their respective V(σ) potential curves at low and high K. At low ΔK no significant differences were observed between V(σ) potential curves. At higher ΔK, however, the isothermal V(σ) potential has shown a crossover point taking place at a positive stress. This has the effect of reducing the effective driving force for cracking. By taking into account this σ_{cl} in the computation of ΔK, one finds that the crack growth rates in terms of ΔK_{eff} for both isothermal and TMF tests are similar (Fig. 5). The positive closure stress observed was attributed to the build-up of oxides in the wake of the crack. This is supported by fractographic observation which shows greater oxidation for isothermal testing than for TMF testing.

CONCLUSIONS

Faster crack growth rates were measured in Inconel X-750 cycled between 360 and 650°C under out-of-phase conditions than under in-phase cycling at R = -1 or R = 0.05. This behavior was rationalized by introducing the concept of an effective closure stress which was defined as the applied stress at the crossover point of the V(σ) potential curve. σ_{cl} should represent the effective contribution to cracking of the damage taking place during the compressive part of the cycle. Correlation between TMFCG rates and ΔK appear to be valid provided elastic conditions prevailed in the bulk. Correction to the applied stress can be introduced in order to take into account damage occurring in the compressive part of the last cycle. Further work is needed to assess the suitability of ΔK to more realistic conditions involving TMFCG under cyclic plastic strains.

Acknowledgment: This research work was sponsored by the National Aeronautics and Space Administration under Grant No. NAG3-280.

REFERENCES

1. Sheffler, K. D., Vacuum Thermal-Mechanical Fatigue Behavior of Two Iron-Base Alloys, ASTM STP 612, (1976) 214-226.

2. Skelton, R. P., Environmental Crack Growth in 1/2Cr-Mo-V steel during Isothermal High Strain Fatigue and Temperature Cycling, Mat. Sci. Eng., vol. 2, (1978) 287-298.

3. Fujino, N. and Tarai, S., Effect of Thermal Cycle on Low Cycle Fatigue Life of Steels and Grain Boundary Sliding Characteristics, ICM 3, vol. 2, 1979, 49-58.

4. Kuwabara, K. and Nitta, A., Thermal-Mechanical Low Cycle Fatigue under Creep-Fatigue Interaction in Type 304 Stainless Steel, ICM 3, vol. 2, 1979, 69-78.

5. Rau, C.A., Gemma,A.E.,Leverant, G.R., Thermal-Mechanical Fatigue Crack Propagation in Nickel and Cobalt Base Superalloys under Various Strain-Temperature Cycles, ASTM STP 520 (1973) 166-178.

6. Gemma, A.E., Langer, B.S. and Leverant, G.R., Thermal-Mechanical Fatigue Crack Propagation in Anisotropic Nickel Base Superalloys", ASTM STP 612 (1976) 199-213.

7. Gemma,A.E., Ashland, F.X. and Masci, R.M., The Effects of Stress Dwells and Varying Mean Strain on Crack Growth During Thermal Mechanical Fatigue, J. Test. Eval., vol. 9, no.4, (1981) 209-215.

8. Troshchenko, V.T. and Zaslotskaya, L.A., Fatigue Strength of Superalloys Subjected to Combined Mechanical and Thermal Loading, ICM 3, vol. 2, (1979) 3-12.

9. Meyers, G. J., Fracture Mechanics Criteria for Turbine Engines and Hot Section Components, NASA CR-167896, (1982).

10. Jaske, C.E., Thermal Mechanical Low Cycle Fatigue of AISI 1010 Steel, ASTM STP 612, (1976) 170-198.

11. Westwood, H. J. and Moles, M.D., Creep-Fatigue Problems in Electricity Generation Plants, Can. Met. Quart., vol.18, (1979) 215-230.

12. Bhongbhobhat, S., The Effect of Simultaneously Alternating Temperature and Hold Time in the Low Cycle Fatigue Behavior of Steels, Low Cycle Fatigue Strength and Elasto-Plastic Behavior of Materials, eds. Rie, K.T. and Harbach, E., DVM (1979), 73-82.

13. Leverant, G. R., Strongman, T.E., and Langer, B.S., Parameters Controlling the Thermal Fatigue Properties of Conventional Cast and Directionally-Solidified Turbine Alloys, Superalloys: Metallurgy and Manufactures, ed., Kear, B.H., Muzuka, D.R., Tien, J.K., and Wlodek, S.T., Claxtors Pub.(1976) 285-295.

14. Okazaki, M. and Koizumi, T., Crack Propagation During Low Cycle Thermal-Mechanical and Isothermal Fatigue at Elevated Temperatures, Met. Trans. vol. 14A, (1983) 1641-1648.

15. Kuwabara, K., Nitta, A, and Kitamura, T., Thermal-Mechanical Fatigue Life Prediction in High Temperature Component Materials for Power Plants, Conf. on Advances in Life Prediction Methods, ASME-MPC, Albany, N.Y. (1983) 131-141.

16. Wareing, J., Mechanisms of High Temperature Fatigue and Creep-Fatigue Failure in Engineering Materials, Fatigue at High Temperature, ed. Skelton, R.P., Applied Sci. Pub., (1983) 135-185.

17. Lloyd, G. J. , High Temperature Fatigue and Creep-Fatigue Crack Propagation: Mechanics, Mechanisms and Observed Behavir in Structural Materials, Fatigue at High Temperature, ed. Skelton, R.P., Applied Sci. Pub. (1983) 187-258.

18. Coffin, L. F., Damage Processes in Time Dependent Fatigue - A Review, Creep-Fatigue-Environment Interactions, eds. Pelloux, R. M. and Stoloff, N.S., AIME (1980) 1-23.

19. Mills, W. J. and James, L.A., Effect of Temperature on the Fatigue Crack Propagation Behavior of Inconel X-750, Fat. Eng. Mat. Struct., vol. 3, (1980) 159-175.

20. Skelton, R.P., The Growth of Short Cracks During High Strain Fatigue and Thermal Cycling, ASTM STP 770, (1982) 337-381.

21. Koizumi, T. and Okazaki, M., Crack Growth and Prediction of Endurance in Thermal-Mechanical Fatigue of 12 Cr-Mo-V-W Steel, Fat. Eng. Mat. Struct., vol. 1, (1979) 509-520.

22. Harris, D. O., Stress Intensity Factors for Hollow Circumferentially Notched Round Bars, J. Basic Eng., vol. 89 (1967) 49-54.

Appendix D - TMF in B1900+Hf

THE THERMAL-MECHANICAL CYCLIC STRESS-STRAIN RESPONSES OF CAST B-1900+Hf

by

N. Marchand*, G. L'Espérance** and R.M. Pelloux***

* Research assistant, Department of Material Science and Engineering, Massachusetts Institute of Technology, Cambridge, MA 02139

** NSERC Research Fellow, Department of Metallurgical Engineering, École Polytechnique, Montréal, Québec, Canada, H3C-3A7

*** Professor, Department of Material Science and Engineering, Massachusetts Institute of Technology, Cambridge, MA 02139

Abstract

A study was undertaken to develop an understanding of the fatigue response of superalloy B-1900+Hf under combined thermal and mechanical strain cycling in air. Comparative evaluations were made with existing thermal-mechanical data of B-1900 and with results of a comprehensive study of the fatigue behavior of the same alloy under isothermal conditions. The thermal-mechanical fatigue (TMF) response was investigated for constant amplitude, fully reversed, mechanically strained cycling of uniaxially loaded specimens in the temperature range from 400 to 925°C. Experiments were conducted both with maximum strain in-phase with maximum temperature, and out-of-phase with maximum temperature.

TMF cycling was observed to cause more cyclic hardening than in isothermal fatigue experiments at the maximum and minimum temperatures. In terms of mean stress or plastic strain range, out-of-phase cycling was shown to be more deleterious than in-phase or isothermal cycling. However, few differences were observed in terms of the stabilized stress ranges. The asymmetric cyclic hardening/softening behavior is explained in terms of coarsening of the γ' and associated strain field. For TMF cycling, the high temperature flow stress depends on the density of the misfit dislocations, whereas the low temperature flow stress is controlled by the magnitude and sign of the applied stress. The TMF cracking modes are discussed. The results show that the fracture criteria under TMF cycling is a stress-base phenomenon.

KEY WORDS: thermal-mechanical fatigue, superalloy, cyclic hardening, damage mechanisms, directional coarsening.

Introduction

Most high temperature components operate under conditions of cyclic mechanical non-isothermal loading. The design of these components must consider the effect of plastic strains that are associated with transients as well as with the steady state operating stresses and strains that cause time dependent failure. Figure 1 [1] shows schematically the stress and strain cycles to which gas turbine disk and blade materials are subjected to as a result of rapid start, steady-state operation and rapid shut-down. These stress-strain-temperature cycles produce high strain low cycle fatigue which leads to crack initiation, slow crack growth and failure by fast fracture. As a consequence, it is necessary to investigate the cyclic stress-strain behavior of these structural materials under cyclic temperature conditions. High temperature fatigue studies generally bypass real thermal fatigue loading partly because isothermal tests are simpler and much less expensive to perform, but also because it was felt that such tests carried out at the maximum service temperature would give worst case results. However, several studies which have compared the fatigue resistance under thermal cycling conditions with that of isothermal tests have shown that, in many cases, the latter, rather than giving the worst case situation, can seriously overestimate the fatigue life [2-19].

In the last two decades, a large effort has been made to characterize both fatigue crack initiation and fatigue crack propagation behavior of materials at elevated temperature. It is easy to understand that high temperature fatigue is a complex problem because of the time-dependent processes which intervene, in addition to the cycle-dependent phenomena. At

high temperature, factors such as strain-rate or frequency, waveform signal, hold time and environment have a strong influence. Moreover, most nickel-base superalloys are metallurgically unstable when they are cyclically deformed at high temperature. Therefore, changes in the flow properties of the materials at the crack tip are expected to induce changes in the propagation rate. Any decrease in the work hardening exponent of the crack tip material caused by an increase in strain rate or by an increase in temperature, would cause an increase in crack propagation rate. Similarly, stress relaxation reduces the effective value of the yield stress. All these phenomena, which are temperature-dependent, greatly complicate the prediction of life in real components. Isothermal testing, to study the effects of tests parameters, is at a disadvantage; new design concepts are needed which are based on the knowledge of the cyclic response under thermal cycling if more accurate life prediction methods are to be established.

This paper describes the results of a study where the low cycle fatigue behavior of superalloy B-1900+Hf was investigated for conditions of combined thermal and mechanical strain cycling. Experiments were limited to the two extreme conditions of in-phase and out-of-phase cycling. The objective of this study was to obtain information on thermal-mechanical behavior of a commonly used superalloy. In turn, this information is used to assess the suitability of various parameters for correlating high temperature TMF crack growth. However, since thermal-mechanical fatigue testing is more time consuming, costly, and complicated than isothermal fatigue testing, the approach taken in this program was to conduct a limited study of TMF behavior over the temperature range of 400 to 925°C for correlation with previous isothermal work on the same material.

Review of Experimental Data

Udoguchi and Wada [2], Sheffler [3], Taira et al. [4-5] and others [6-19], in studies of thermal fatigue of high temperature alloys, have shown that thermal fatigue can be shorter than equivalent isothermal fatigue at the maximum temperature of the cycle. More specifically, some of the results, giving N_f as a function of the plastic strain range $\Delta\varepsilon_p$ for an A-286 steel [3], have shown that in-phase cycling (maximum temperature at maximum tensile strain) is more damaging than out-of-phase (maximum temperature at maximum compressive strain), which in turn caused fracture in fewer cycles than isothermal cycling. This was attributed to extensive cumulative grain boundary sliding during thermal cycling. Similar results were obtained for 304 stainless steel [6, 8-9k, 18]. However, when the data is expressed in terms of total strain range $\Delta\varepsilon_t$, Kuwabara and Nitta [8-9] found that isothermal and out-of-phase changed rank and that this new order was consistent with the fraction of intergranular cracks that was observed.

Studies of Cr-Mo steels have pointed out the strong temperature-dependence of the microstructure under TMF conditions [13-16]. It is significant that TMF tests between 200 and 600°C have shown that in-phase cycling gave higher endurance than the isothermal tests at 600°C [13-15]. However, when cycled between 300 and 650°C, out-of-phase cycling gave shorter lives than did isothermal testing at 650°C [16]. These results indicate that when the temperature embraces a ductility minimum in the material, out-of-phase cycling gives shorter lives than isothermal testing at the maximum temperature.

For superalloy IN-738, high strain fatigue tests, in-phase and out-of-phase TMF cycling between 400 and 950°C, all gave the same endurances at a

given $\Delta\varepsilon_t$ level [20]. However, Nitta et al. [18-19] have shown that the endurance of IN-738 depends on the applied strain $\Delta\varepsilon_t$. Their results pointed out that thermal fatigue life of nine different nickel-base alloys strongly depends upon the strength of the alloy. The data obtained by Lindholm and Davidson [7] on conventional B-1900, agreed with the previous conclusion. The dependence of thermal fatigue on strength may not be restricted to superalloys. Jaske [11] found that in order to correlate in-phase, out-of-phase, and isothermal fatigue data for a low carbon steel, a knowledge of both cyclic stress and cyclic strain was necessary. On the basis of stabilized stress range versus cycles to failure, little difference was observed in the behavior of specimens subjected to in-phase and out-of-phase cycling. However, the cyclic hardening characteristics of the alloy tested were very complex, indicating difficulty in predicting the stabilized stress range.

It thus appears that there is no hard and fast rule for relating the thermal-mechanical method to isothermal testing. There are many uncertainties in comparing total endurances only; for example, the number of cycles to initiation may differ, and cracking may be intergranular in isothermal tests but transgranular in the cyclic temperature tests. Obviously, low endurance data will depend on initiation/propagation ratios, ductility, including sensitivity to strain rate, hardening behavior, etc. It should be emphasized that temperature cycling has a marked effect upon the σ-ε loop shape and deformation mode. The materials tested may or may not accomodate differing amounts of deformation before failure, depending upon its microstructural condition, which in turn is dependent upon the condition of cyclic deformation and temperature history. This points out the importance of knowing the temperature and strain history on the instantaneous material response to assess the kinetic of damage accumulation.

Base Material Description

The material for this program was taken from a special quality melt of B-1900+Hf obtained from Certified Alloy Products, Inc., Long Beach, California. The chemical analysis, heat treatment, and tensile properties are shown in Tables I and II. The structure of the material was documented in both the as-cast and fully heat treated conditions. The following observations were made:

The grain size is about 1 to 2 mm (Figure 2a). The replica technique was used to measure and study the gamma prime (γ') size and distribution. The fully heat treated material showed the γ' size to be about 0.6-0.9 μm (Figure 2c). The structure has an interdendritic spacing of about 100 μm and islands of γ'-eutectic surrounded by a zone of fine γ' (0.9 μm) can be observed (Figure 2b). MC carbides near the coarse γ' islands can also be observed.

Apparatus and Test Conditions

The thermal-mechanical fatigue specimens have a rectangular cross-section of 11.7 x 4.4 mm^2. The test section of each specimen was polished with successively finer grades of silicon-carbide paper to produce a bright finish, with finishing marks parallel to the longitudinal axis of the specimen. Specimens were degreased with trichlorethylene, followed by reagent grade acetone before being heated to temperature.

The thermal-mechanical fatigue experiments were conducted using the same basic servocontrolled electrohydraulic test system used for thermal-mechanical fatigue crack growth [23]. Details of the equipment, method of

heating, gripping and alignment procedure, and general experimental procedures are given elsewhere [22-23].

Temperature was measured with 0.2 mm diameter chromel-alumel thermocouples, which were spot welded along the gauge length. By computer control, the temperature in the gauge length was maintained within ±5°C of the desired temperature for both axial and transverse directions throughout the duration of a test. For axial strain measurement, a gauge length of 15 mm was selected on the middle part of the specimen and a contact type extensometer was employed. Temperature and mechanical strain were computer-controlled by the same triangular waveform with in-phase or out-of-phase cycling (see Figure 3). The mechanical strain was obtained by subtracting the thermal strain from the total strain. The thermal strain was measured by cycling the temperature at zero load and stored into the computer. The mechanical strain ($\Delta\varepsilon_{mec}$) was maintained constant at each strain level. The mechanical strain was increased by approximately 10% of its previous value after saturation of the total stress range. This means that for most strain ranges, more than 250 cycles were performed. The frequency was kept constant at 0.0056 Hz (1/3 cpm) for all strain ranges which resulted in varying the strain rates between 0.002 sec^{-1} and 0.007 sec^{-1}.

Results

A. Cyclic Responses

Results of all the experiments conducted in this program are summarized in Tables 3 and 4, where the mechanical strain range, the number of applied cycles at each strain range, the initial and final stress range, and final plastic strain range are listed for both in-phase and out-of-phase cycling. The plastic

strain range was taken as the width of the hysteresis loop at zero stress and therefore includes both time-independent and time-dependent inelastic strain components. Figure 4 shows the thermal strain, the mechanical strain, the total strain, and the stress amplitude as a function of time (one cycle) for both in-phase and out-of-phase cycling. From the load-time and mechanical strain (ε_{mec})-time curves the hysteresis loops were obtained.

Even though strain cycling was fully reversed, the stress cycle was not symmetric about zero because the temperature was different at each extreme of the cycle. Figure 5 shows examples of the loops obtained for both in-phase and out-of-phase cycling. For out-of-phase cycling, a positive (tensile) mean stress is observed and a negative mean stress is observed for the in-phase cycling. That is, for the in-phase cycle, the magnitude of peak compressive stress was greater than the magnitude of peak tensile stress, or $|\sigma_{min}| > |\sigma_{max}|$. The opposite was true for the out-of-phase cycle where $|\sigma_{max}| > |\sigma_{min}|$. Figures 6a and 6b show the type of stress response for in-phase and out-of-phase cycling at a fixed strain range. Figures 7a and 7b summarized the fatigue results. From Figures 6 and 7, the following conclusions can be drawn. First, one can conclude that the mean stress ($\bar{\sigma}$) does not vary much with the number of applied cycles or strain ranges for in-phase cycling. However, $\bar{\sigma}$ does vary with N and $\Delta\varepsilon_{mec}$ for out-of-phase cycling. It is also important to notice that for similar strain ranges, the absolute value of $\bar{\sigma}$ is higher for out-of-phase than for in-phase cycling. Another conclusion that can be drawn is that for all $\Delta\varepsilon_{mec}$, in-phase cycling shows σ_{max} to harden, whereas σ_{min} stayed almost unchanged except at high applied strain range. For out-of-phase cycling, σ_{max} hardened and σ_{min} softened. The softening of σ_{min} being more important than the hardening of σ_{max} results in a drift of $\bar{\sigma}$ to higher value of tensile stress. On the other hand, because σ_{min} stayed almost unchanged and σ_{max} hardened for

in-phase cycling, the net result is a softening of the mean stress, that is $|\bar{\sigma}|$ decreases.

As stated before, the "saturation" was defined such that the change in stress range ($\Delta\sigma$), in about fifty cycles, was lower than two percent. The values of σ_{max}, σ_{min} and $\bar{\sigma}$ are plotted against the strain amplitude ($\Delta\varepsilon_{mec}/2$) to obtain the cyclic stress-strain (CSS) curves for in-phase and out-of-phase cycling. These curves are shown in Figure 8 along with the isothermal CSS curves obtained at 871 and 538°C [21]. Interesting conclusions can be drawn from Figure 8. First, one can see that the CSS curves of in-phase, out-of-phase and isothermal testing coverage at low $\Delta\varepsilon_{mec}/2$ (<0.0012) but diverge as $\Delta\varepsilon_{mec}/2$ increases. At higher $\Delta\varepsilon_{mec}/2$ (but lower than 0.28%), the maximum stress (σ_{max} at 925°C) for in-phase cycling is higher than for isothermal fatigue at 871°C. For $\Delta\varepsilon_{mec}/2 > 0.28\%$, the inverse behavior is observed, that is, a higher hardening rate for isothermal fatigue than for σ_{max} of in-phase cycling. The hardening rate of σ_{min} of in-phase cycling (T = 400°C) is identical to the hardening rate measured for isothermal fatigue at 538°C. For out-of-phase cycling, σ_{min} (at T = 925°C) also shows a higher hardening rate than isothermal fatigue at 871°C (for $\Delta\varepsilon_{mec}/2 < 0.25\%$), and a lower hardening rate for $\Delta\varepsilon_{mec}/2 > 0.25\%$ than isothermal fatigue. However, σ_{max} (T = 400°C) for out-of-phase shows a higher hardening rate than isothermal fatigue at 538°C.

The hardening behaviors of in-phase and out-of-phase cycling were compared by plotting σ_{max} of in-phase and $|\sigma_{min}|$ of out-of-phase, both measured at 925°C (Figure 9). σ_{min} of in-phase cycling and $-\sigma_{max}$ of out-of-phase cycling are also plotted. One can see that the hardening rate at 925°C is higher for in-phase (in tension) than for out-of-phase cycling (in compression). However, the hardening rate at 400°C is higher for out-of-phase cycling (in tension) than for in-phase cycling (in compression) and isothermal testing.

B. Fractographic and TEM Observations

In order to clearly identify the cracking process, the long transverse and longitudinal sections perpendicular to the fracture surface were mounted for metallographic observation. For out-of-phase cycling, multiple cracks were observed along the gauge length. The propagation path is transgranular and appears to proceed interdendritically.
Examination of the specimen failed under in-phase cycling, revealing a varying degree of transgranular and intergranular cracking with a density of surface cracks much lower than out-of-phase cycling. The fracture path, however, appears mainly intergranular. These conclusions were supported by SEM fractographic observations.

TEM observations were made on the specimens fatigued to fracture. Foils were taken parallel to the loading axis and observed with a JEOL 100CX operated at 120 KeV. Figures 10 and 11 show typical dislocation substructures obtained under in-phase and out-of-phase conditions. In all cases, coarsening of the γ' phase has taken place, being more pronounced under in-phase conditions. In some grains of the specimens cycled under in-phase conditions, directional coarsening (rafting) was observed (Figure 12). Little or no rafting was observed under out-of-phase cycling. A tight dislocation network encapsulating the γ' (rafted and unrafted) can be observed in Figures 10 and 12 (in-phase cycling), whereas a looser dislocation network is observed in Figure 11 (out-of-phase cycling), as can be seen from the dislocation spacing. These observations indicate that the dislocation density is higher under in-phase than under out-of-phase cycling. The octahedral active systems were found to be (111)[110], (111)[101] and possibly (111)[011] in both cases. Three Burgers

vectors were identified using the invisibility criterion and assuming that the dislocations were screw in character. These Burgers vectors are a/2[110], a/2[101], and a/2[101] indicating that at least three slip systems were operative. Comparison with specimens failed under isothermal cycling [21] shows that the dislocation density ranked in increasing order; isothermal (T_{min} and T_{max}) out-of-phase, and in-phase cycling.

Discussion

The above results show that the two major microstructural features are: (1) changes in γ' precipitate morphology (Figures 10-12), and (2) introduction of a dislocation network about the γ' precipitates. It is well known [24-25] that coarsening of the γ' precipitates influences the mechanical behavior of nickel-base alloys. The task at hand is to separate the relative contribution of each structural feature to the cyclic behavior. In what follows, we will show that the increase in the cyclic flow stress during in-phase cycling is due to dislocation networks surrounding the γ', and the lower flow stress under out-of-phase cycling and pronounced softening behavior (Figure 6b) is a consequence of not only the dislocation networks strengthening, but also of the directional strain field around the γ' precipitates.

Cyclic Hardening/Softening Behavior

It is generally accepted that coherent particles can be sheared by dislocations and consequently, the work done in forcing the first dislocations through the particles will be important in determining the flow stress. The resistance to shear is governed by several factors:

1. The interaction of the cutting dislocation with the stress field of the precipitates.

2. If the lattice parameters of matrix and precipitate differ, then during shearing of the particles, misfit dislocations must be created at the precipitate-matrix interface. The magnitude of the Burgers vector of the interface dislocation will be the difference between the Burgers vector of the slip dislocation in the matrix and in the precipitate, i.e., $(b_m - b_p)$.

3. If the matrix and precipitate possess different atomic volumes, a hydrostatic interaction would be expected between a moving dislocation and the precipitate.

In the case of superalloys with high volume fraction of γ' (>50%), γ'-shearing is the primary strengthening mechanism. With the mean free edge-to-edge distance in the matrix between the precipitates being smaller than the average precipitate size itself, dislocation shearing of the particle is favored over dislocation looping around the particles.

As previously mentioned, coarsening and rafting of γ' develop in this alloy. This feature can be attributed to the large lattice misfit (misfit ~ -0.25% [26]), which generates sufficient interfacial strain to produce misfit dislocations at elevated temperature. Significant deformation can occur only by dislocation penetration of the γ' phase and it is postulated that the misfit dislocation nets at the interface retards this process. Therefore, more hardening should be expected when rafting takes place because the dislocation networks surrounding the γ' are more intense (see Figures 10 & 12). On the other hand, it has been shown by Shah and Duhl [27] that the flow stress decreases as γ' size increases provided the cubic shape of the γ' is conserved. These two superimposed phenomena, with opposite effects with regard to the flow stress, determine the apparent flow stress. Figure 6 shows that the

maximum stress (σ_{max}) of in-phase cycling (T_{max}) display continuous hardening with little appearance of stabilization. On the other hand, the σ_{min} curve of out-of-phase (T_{max}) displays continuous softening. This behavior has been previously observed on B-1900+Hf cycled in TMF [28] where continuous hardening of σ_{max} and softening of σ_{min} occurred until final fracture without evidence of saturation. This raises the question of the validity of the strain increment technique for measuring the CSS curves of low stacking-fault energy materials where continuous hardening (or softening) is observed until fracture [28-30] at low applied strain. This behavior is usually rationalized in terms of planar configuration of dislocations [29, 31]. At high strain, where cross-slip takes place, saturation of the CSS curves is observed. Although B-1900+Hf is also a low stacking fault energy material, the planar configuration of dislocation alone cannot explain the observed cyclic hardening/softening behavior (Figure 6).

At high temperature (T > 600°C) the flow stress depends on the APB energy and thermally activated cross slip of the glide dislocations [27, 32]. The directionality of the internal stress field around the γ' is small because thermal activation is important. Therefore, the flow stress will depend on the factors controlling the internal stress. The density of misfit dislocations around the γ' particles, which depends on the γ' size and shape (raft), affect the flow stress because it controls the internal stress on the glide dislocations. On the other hand, when coarsening takes place, the particle spacing increases, which leads to weakening because of the increased probability of avoiding shearing by Orowan-type mechanisms [34]. Under in-phase cycling, coarsening of the γ' takes place along with rafting, leading to high density of misfit dislocations without significant increase in interparticle spacing (Figure 12). The net result is an increase in the flow

stress because the internal stress increases faster than the relaxation time required by the glide dislocation to overcome the barrier created by the misfit dislocations. During out-of-phase cycling, isotropic coarsening takes place leading to a smaller increase of misfit dislocations and a more significant increase of γ' particle spacing. The net result is a decrease in flow stress.

At low temperature the directionality of the resultant stress field around the γ' particles will also contribute to the internal stress acting on the glide dislocations [26, 27, 33]. With coarsening, the hydrostatic tensile stress field around the γ' increases and that is one of the reasons why misfit dislocations are required. It is well known that the resistance to the movement of glide dislocation, i.e., the functional force, increases with increasing hydrostatic stress [35]. Therefore, the superposition of an external hydrostatic stress field will increase or decrease the flow stress depending on the magnitude and sign of the applied stress. If an external tensile stress field is applied, the frictional stresses increase and so does the flow stress. This corresponds to the out-of-phase cycling case where the applied stresses are tensile at low temperature (see Figure 6b). When the applied stress field in compressive, the flow stress decreases or remains unchanged, depending on the magnitude of the net stress field [33]. During in-phase cycling, the stresses are compressive at T_{min} and cancelled with the hydrostatic tensile stress field around the γ'. The net result is that the frictional forces on the glide dislocation are lower and the flow stress does not change much as cycling proceeds and coarsening takes place (at T_{max}), as can be seen in Figure 6a.

To fully understand the flow behavior with change in sign of the applied stress, we must also consider the resolved constriction stress of partial dislocations [27, 32]. The direction of the glide force per unit length, $F_{g/L}$, will reverse upon reversing the applied stress, σ [27]. While this has no physical

meaning in a macroscopic sense, since it only alters the direction of glide for a particular dislocation, reversing the direction of the glide forces acting on the partial dislocation,it leads to a distinctly different physical situation. The resulting force tends to constrict the partials under an applied tensile stress and extend them under a compressive stress [27]. Since constriction of the partials is required by the cross-slip process, the flow stress appears stronger in tension than in compression where the extended partials retard cross-slip activity. The previous argument implies that the flow behavior of B-1900+Hf is governed by octahedral slip activity. If such is the case, the flow stress can be written as

$$\sigma \alpha \ (1/R + 1/\lambda), \qquad (1)$$

where R is the particle size and λ the mean free distance between the two constricted nodes where the cross-slip event occurs [27]. At high temperature, λ is always smaller than R and the flow stress is governed by the dislocation network and internal stress which fixed λ [27, 36]. At low temperature, the flow stress depends on which of these two parameters (R, λ) is the smallest. If a tensile stress is applied, the partials tend to be constricted and the mean free distance between cross-slip event decreases. If a compressive stress is applied, the partials are pulled further apart (λ increases), and the flow stress is controlled by R, the particle size.

Cyclic Stress-Strain Behavior

The cyclic stress-strain curves (Figures 7,8 and 9) show that the flow stress, as a function of the strain amplitude ($\Delta\varepsilon_t/2$), is higher for in-phase than out-of-phase or isothermal cycling at the maximum temperature (T_{max}). This is consistent with the fact that dislocation density increases in the order of isothermal, out-of-phase and in-phase cycling (see Figures 10-12). At low

temperature (T_{min}), because cross-slip is a function of the magnitude and sign of applied stress, the flow stress is higher under out-of-phase cycling than under in-phase or isothermal cycling (see Figure 9).

The issue that needs to be addressed now is the cracking mode. Fracture is transgranular and proceeds interdentritically in out-of-phase cycling and intergranularly under in-phase cycling conditions. As expected, fracture is controlled by the favored mode of rupture in the tensile part of the cycle. Under in-phase cycling, tension occurs at high temperature where the cohesive strength of the grain boundary is low, which obviously promotes intergranular cracking. During out-of-phase cycling, the specimen is under tensile loading at low temperature and the weakest transgranular features (carbide film, secondary dendrites, inclusion stringers, etc.) control the rupture mode. The fact that the fracture mode depends on the maximum tensile stress, rather than on a critical plastic strain range, suggests that the failure criteria for B-1900+Hf is stress-based rather than strain-dependent. In other words, the testing condition (temperature and strain relationship) leading to the maximum tensile stress, will determine the number of cycles to initiation and the propagation rates.

As mentioned earlier, the major critical turbine components operate under strain-controlled conditions and, more specifically, under displacement-control. The stresses are not known a priori. Therefore, if the failure criteria in B-1900+Hf is stress-dependent, the relative crack growth rates for a given crack length can be determined from the CSS curves. At low strain amplitude (<0.25%) the stress range for TMF cycling is higher than for isothermal fatigue. Consequently, faster crack growth rates should be obtained for TMF cycling [37]. Under fully plastic conditions ($\Delta\varepsilon_t/2 > 0.25\%$), the isothermal stress range is higher than the stress

ranges obtained under TMF cycling and faster crack growth rates are expected under isothermal cycling (T_{max}).

Conclusion

The cyclic stress-strain behavior under TMF cycling differs from the isothermal behavior and shows more hardening, both on a high and low temperature basis. This indicates that it is difficult to predict the cyclic stress-strain behavior under realistic conditions (Figure 1) from isothermal data. The synergistic coupling between the cyclic strains and temperatures cannot be ignored.

It was shown that the cyclic flow stress at elevated temperature (T_{max}) is primarily controlled by the density of misfit dislocations, which depends on the amount of isotropic and directional coarsening. At low temperature (T_{min}) the flow stress is controlled by the directionality of the stress field around the γ', the magnitude of which depends on the sign of the applied stress. The cracking modes observed have indicated that TMF fracture is controlled by a critical tensile stress (σ_c) rather than a critical tensile strain. The implication of these results on the propagation rates was discussed.

Acknowledgement: This research work was sponsored by the National Aeronautics and Space Administration under Grant No. NAG3-280.

References

1. R.L. McKnight, J.H. Laflen, and G.T. Spaner, "Turbine Blade Tip Durability Analysis", NASA CR-165268, Feb. 1981, 112 pgs.

2. T. Udoguchi and T. Wada, "Thermal Effect on Low Cycle Fatigue Strength of Steels", in Thermal Stresses and Thermal Fatigue, ed. by D.J. Littler, Butterworth Press, London, 1971, pp. 109-123.

3. K.D. Sheffler, "Vacuum Thermal-Mechanical Fatigue Behavior of Two Iron-Base Alloys", ASTM STP 612, 1976, pp. 214-226.

4. S. Taira, "Relationship Between Thermal Fatigue and Low Cycle Fatigue at Elevated Temperature", ASTM STP 520, 1973, pp. 80-101.

5. N. Fujino and S. Taira, "Effects of Thermal Cycle on Low-Cycle Fatigue Life of Steels and Grain Boundary Sliding Characteristics", ICM 3, Vol. 2, 1979, pp. 49-58.

6. R. N. Stentz, J.T. Berling and J.B. Conway, "A Comparison of Combined Temperature and Mechanical Strain Cycling Data with Isothermal Fatigue Results", in Structural Mechanics in Reactor Technology (Proc. of Conf. on), Berlin, Vol. 6, 1971, pp. 391-411.

7. U.S. Lindholm and D.L. Davidson, "Low Cycle Fatigue with Combined Thermal and Strain Cycling", ASTM STP 520, 1973, pp. 473-481.

8. K. Kuwabara and A. Nitta, "Thermal-Mechanical Low Cycle Fatigue Under Creep-Fatigue Interaction in Type 304 Stainless Steel", ICM 3, Vol. 2, 1979, pp. 69-78.

9. K. Kuwabara, A. Nitta, and T. Kitamura, "Thermal-Mechanical Fatigue Life Prediction in High Temperature Component Materials for Power Plants", in Advances in Life Prediction Methods (Proc. of Conf. on), ASME-MPC, Albany, NY, 1983, pp. 131-141.

10. V.T. Troschenko and L.A. Zaslotskaya, "Fatigue Strength of Superalloys Subjected to Combined Mechanical and Thermal Loading", ICM 3, Vol. 2, pp. 3-12.

11. C.E. Jaske, "Thermal-Mechanical Low Cycle Fatigue of AISI 1020 Steel", ASTM STP 612, 1976, pp. 170-198.

12. A.A. Sheinker, "Exploratory Thermal-Mechanical Fatigue Results for Rene 80 in Ultrahigh Vacuum", NASA CR-159444, 1978.

13. S. Bhongbhobhat, "The Effect of Simultaneously Alternating Temperature and Hold Time in the Low Cycle Behavior of Steels", in Low Cycle Fatigue Strength and Elasto-Plastic Behavior of Materials, ed. by K.T. Rie and E. Harbach, DVM Pub., 1979, pp. 73-82.

14. H.J. Westwood and W.K. Lee, "Creep Fatigue Crack Initiation in 1/2 Cr-Mo-V Steel", in Creep and Fracture of Engineering Materials and Structure, ed. by B. Wilshire and W. Owen, Pineridge Press, Swansea, UK, 1982, pp. 517-530.

15. K.H. Kloos, J. Granacher, H. Barth, and P. Rieth, "Simulation of the Service Conditions of Heat Resistant Steels by Creep-Rupture Tests Under Variable Stress or Temperature and by Strain Controlled Service-Type Fatigue Tests", 5th Int. Conf. Fracture, Vol. 5, Pergamon Press, 1982, pp. 2355-2369.

16. W.R. Adams and P. Stanley, "A Programmable Machine for Simulated Thermal Fatigue Testing", J. Phys. E. Sci. Inst., Vol. 7, 1974, pp. 669-673.

17. R.A.T. Dawson, W.J. Elder, G.J. Hill, and A.T. Price, "High Strain Fatigue of Austenitic Steels", in Thermal and High Strain Fatigue, ed. by the Metals and Metallurgy Trust, London, 1967, pp. 239-269.

18. K. Kuwabara and A. Nitta, "Effect of High Temperature Tensile Strain Holding in Thermal Fatigue Fracture", in Creep-Fatigue Interactions, ed. by R.M. Curran, ASME-MPC, 1976, pp. 161-177.

19. A. Nitta, K. Kuwabara,and T. Kitamura, "The Characteristic of Thermal-Mechanical Fatigue Strength in Superalloys for Gas Turbines", Proc. of Int. Conf. on Gas Turbine, Tokyo, Japan, 1983, 8 pgs.

20. M.O. Speidel and A. Pineau, "Fatigue of High Temperature Alloys for Gas Turbines", in High Temperature Alloys for Gas Turbines, ed. by Coutsouradis, Felix, Tischmeister, Habraken, Lindblom and Speidel, Applied Sci. Pub., London, 1978, pp. 469-512.

21. V. Moreno, "Creep-Fatigue Life Prediction for Engine Hot Section Materials", NASA CR-168228, 1983, 85 pgs.

22. N. Marchand and R.M. Pelloux, "A Computerized Testing System for Thermal-Mechanical Fatigue Crack Growth", submitted to ASTM J. Test. and Eval. (JTEV).

23. N. Marchand and R.M. Pelloux, "Thermal-Mechanical Fatigue Crack Growth in Inconel X-750", in Time-Dependent Fracture, ed. by K. Krausz and A.S. Krausz, Martinus Nijhoff Pub. 1985, pp. 167-178.s

24. J.K. Tien and R.P. Gamble, "Effects of Stress Coarsening on Coherent Particle Strengthening", Met. Trans., Vol. 3, 1972, pp. 2157-2162.

25. D.D. Pearson, F.D. Lemkey, and B.H. Kear, "Stress Coarsening of γ' and its Influence on Creep Properties of a Single Crystal Superalloy", in Proc. of the 4th Intl. Symp. on Superalloys, ed. by J.K. Tien, ASM, Metals Park, 1980, pp. 513-520.

26. L.S. Lin and J.M. Walsh, "Lattice Misfit by Convergent-Beam Electron Diffraction--Part I: Geometry Measurement", in Proc. of 42nd Annual Meeting of the EMSA, 1984, pp. 520-523.

27. D.M. Shah and D.N. Duhl, "The Effect of Orientation, Temperature and Gamma Prime Size on the Yield Strength of a Single Crystal Nickel-Base Superalloy", in Superalloys 1984, ed. by M. Gell et al., AIME, Warrendale, PA, 1984, pp. 107-116.

28. J. Hill and R.M. Masci, Private Communication, Pratt & Whitney Aircraft, 1985.

29. J.O. Nilson, "The Influence of Nitrogen of High Temperature Low Cycle Fatigue Behavior of Austenitic Stainless Steels", Fat. Eng. Mater. Struct., Vol. 7, No. 1, 1984, pp. 55-64.

30. K. Hatanaka and T. Yamada, "Effect of Grain Size on Low Cycle Fatigue in Low Carbon Steel", Bull. of JSME, Vol. 24, No. 196, 1981, pp. 1692-1699.

31. T. Magnin, J. Driver, J. Lepinoux, and L.P. Kubin, "Aspects Microstructturaux de la Déformation Cyclique dans les Métaux et Alliages C. C. et C.F.C. I. Consolidation Cyclique", Rev. Phy. Appl., Vol. 19, 1984, pp. 467-482.

32. G.R. Leverant, B.H. Kears and J.M. Oblack, "Creep of Precipitation-

Hardened Nickel-Base Alloy Single Crystals at High Temperatures", Met. Trans., Vol. 4, 1973, pp. 355-362.

33. T. Miyazaki, K. Nakamura and H. Mori, "Experimental and Theoretical Investigations on Morphological Changes of γ'-Precipitates in Ni-Al Single Crystals During Uniaxial Stress-Annealing", J. Mater. Sci., Vol. 14, 1979, pp. 1827-1837.

34. R.R. Jensen and J.K. Tien, "Temperature and Strain Rate Dependence of Stress-Strain Behavior in a Nickel-Base Superalloy", Met. Trans., Vol. 16A, 1985, pp. 1049-1068.

35. R.W.K. Honeycombe, The Plastic Deformation of Metals, 2nd Ed., Edward Arnold Pub., 1984.

36. M. Gell and D.N. Duhl, "The Development of Single Crystal Superalloy Turbine Blades", Proc. of the N.J. Grant Symposium on Processing and Properties of Advanced High-Temperature Alloys, June 17-18, 1985, ASM Pub., In press.

37. N. Marchand and R.M. Pelloux, "Thermal-Mechanical Fatigue Crack Growth in B-1900+Hf", to be published in the Proc. of the Conf. on High Temperature alloys for Gas Turbines, Liege, Belgium, Oct. 6-9, 1986.

List of Captions

Figure 1. Stress-strain temperature cycle experienced by turbine components.

Figure 2. Micro-structure of B-1900+Hf fully heat treated: (a) Grain size (2.1X), (b) dendritic structure and two zones of γ' (100X), (c) γ' size (3350X).

Figure 3. Schematic diagram showing waveforms of temperature, strain and stress in thermal and isothermal fatigue tests.

Figure 4. Stress, mechanical strain, thermal strain, and total strain as a function of time (one cycle): (a) in-phase, (b) out-of-phase.

Figure 5. Typical hysteresis loop obtained under TMF conditions: (a) in-phase, (b) out-of-phase.

Figure 6. Typical cyclic hardening/softening curves obtained under in-phase and out-of-phase cycling.

Figure 7. Summary of the cyclic hardening behaviors for in-phase and out-of-phase cycling.

Figure 8. Cyclic stress-strain curves obtained under TMF and isothermal cycling.

Figure 9. Comparison of TMF and isothermal cycling.

Figure 10. Typical dislocation substructures obtained under in-phase cycling.

Figure 11. Typical dislocation substructures obtained under out-of-phase cycling.

Figure 12. Directional coarsening of the γ'-phase during in-phase cycling.

Table 1

a) Chemical Composition (at %)

;	Cr	Co	Mo	Al	Ti	Ta	B	Zr	Fe	W	Nb	Bi	Pb	Hf	Ni
.09	7.72	9.91	5.97	6.07	0.99	4.21	0.016	0.04	0.17	0.04	0.08	0.1	0.1	1.19	Remai

b) Heat Treatment

Temperature (°C)	Time (hr)	Quench
1080	4	air cool
900	10	air cool

Table 2

Tensile Properties

Temperature (°C)	$\dot{\varepsilon}$ (min^{-1})	$Ex10^3$ (MPa)	0.2% Yield (MPa)	UTS (MPa)	Elong (%)	RA (%)
RT	0.005	187.5	714	-	4.9	5.9
260	0.005	169.6	702	888	8.3	10.7
538	0.005	149.6	727	-	-	-
649	0.005	143.4	701	-	7.7	7.2
760	0.005	146.8	709	950	7.9	8.4
871	0.005	138.9	633	785	5.7	6.1
982	0.005	123.4	345	480	7.1	6.9

Table 3

Summary of Thermal-Mechanical Testing (In-Phase)

$\Delta\varepsilon_t$ (%)	N	ΔS_i (MPa)	ΔS_f (MPa)	$\Delta\varepsilon_{p_f}$ (%)
0.2000	347	328	356	0.000
0.2515	337	426	436	0.000
0.3030	556	527	524	0.000
0.3580	388	611	620	0.000
0.3830	490	657	664	0.005
0.4075	303	706	708	0.0120
0.4330	340	745	748	0.0150
0.4525	280	777	782	0.0275
0.4825	160	831	842	0.0475
0.5650	54	862	880	0.0700

Table 4

Summary of the Thermal-Mechanical Testing
(Out-of-Phase)

$\Delta\varepsilon_t$ (%)	N	ΔS_i (MPa)	ΔS_f (MPa)	$\Delta\varepsilon_{p_f}$ (%)
0.1765	475	304	310	0.0000
0.1925	426	450	369	0.0000
0.2155	312	416	408	0.0000
0.2500	360	460	455	0.0000
0.2760	260	492	485	0.0030
0.2880	274	565	558	0.0080
0.3280	274	605	585	0.0120
0.3655	316	650	640	0.0075
0.4040	374	711	684	0.0145
0.4375	326	754	745	0.0145
0.4675	222	794	787	0.0325
0.5375	142	885	876	0.0485
0.6000	60	981	958	0.0880

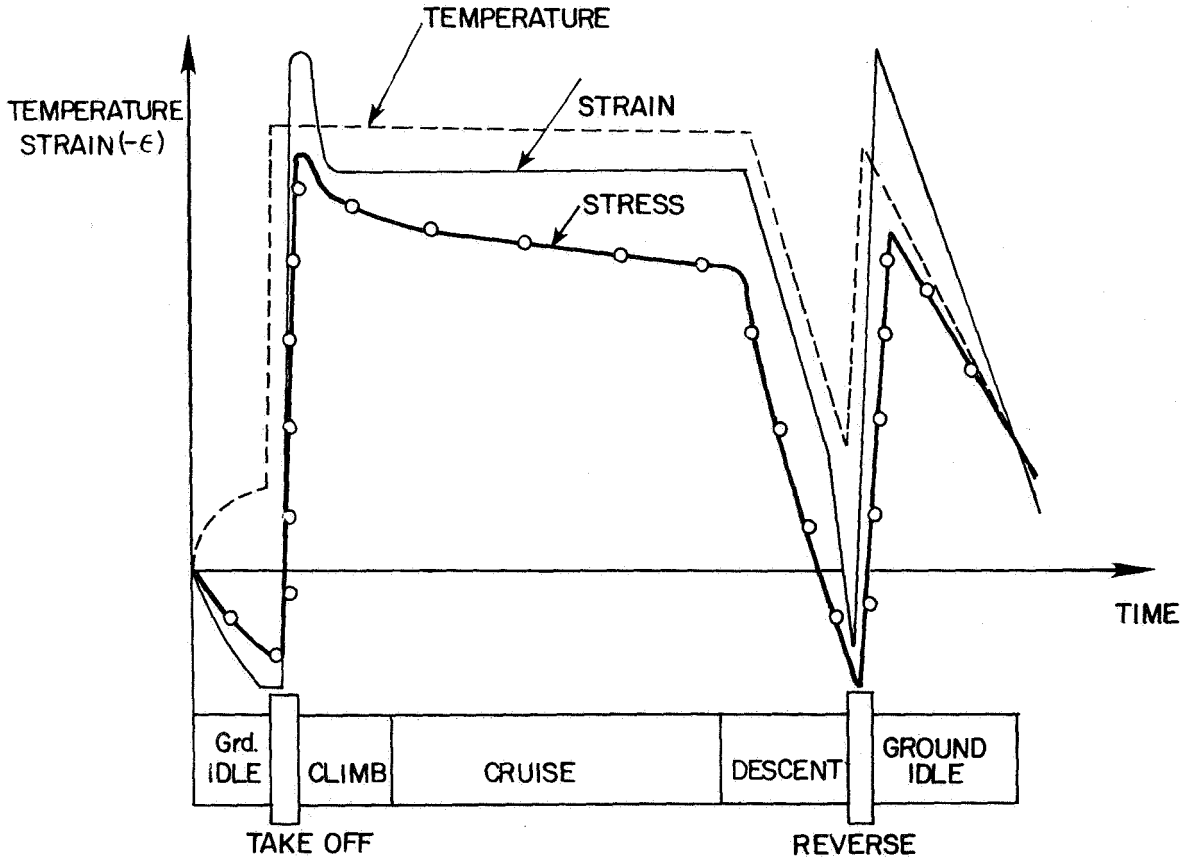

Figure 1. Stress-strain temperature cycle experienced by turbine components.

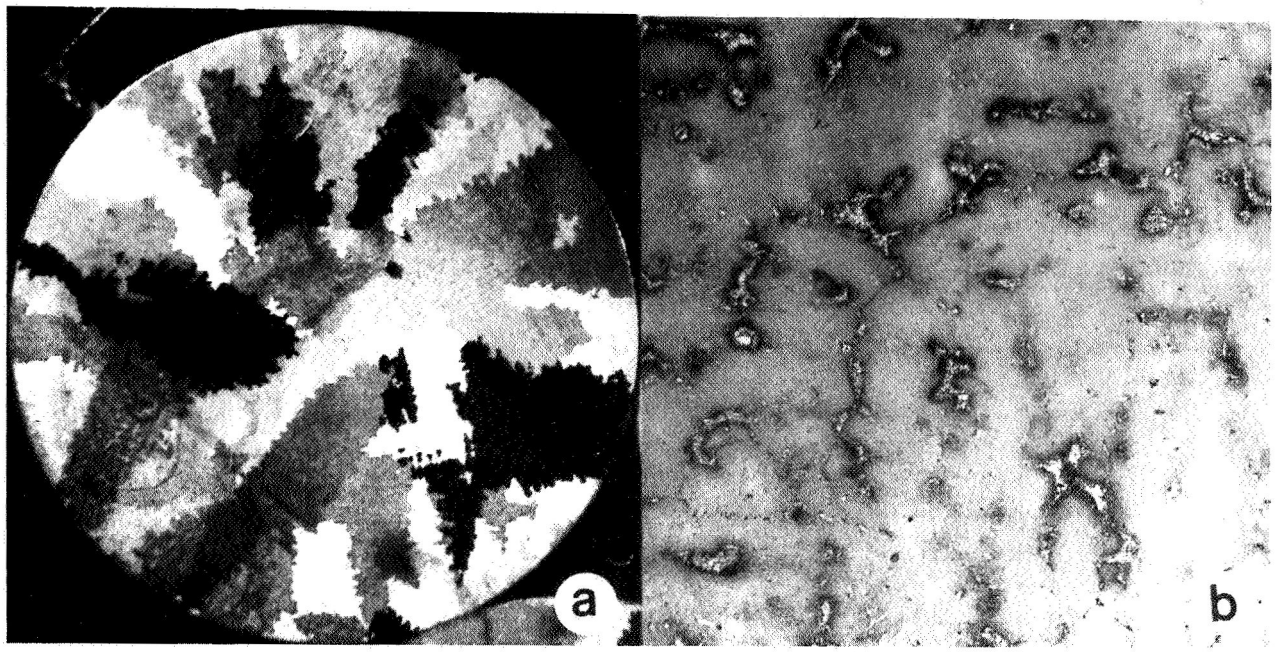

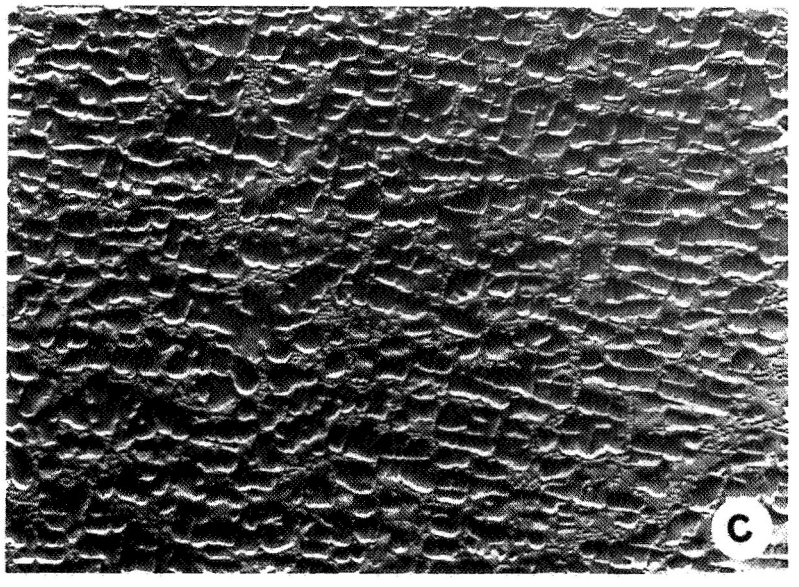

Figure 2. Micro-structure of B-1900+Hf fully heat treated: (a) Grain size (2.1X), (b) dendritic structure and two zones of γ' (100X), (c) γ' size (3350X).

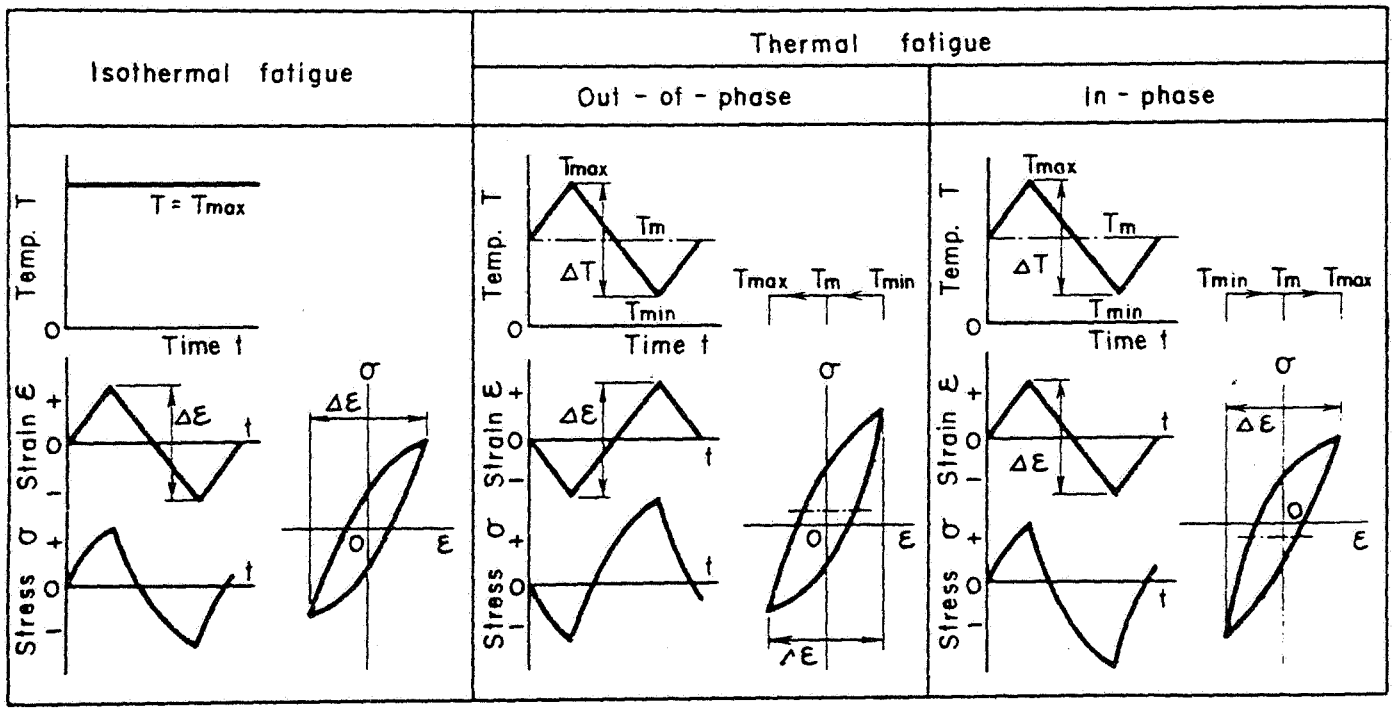

Figure 3. Schematic diagram showing waveforms of temperature, strain and stress in thermal and isothermal fatigue tests.

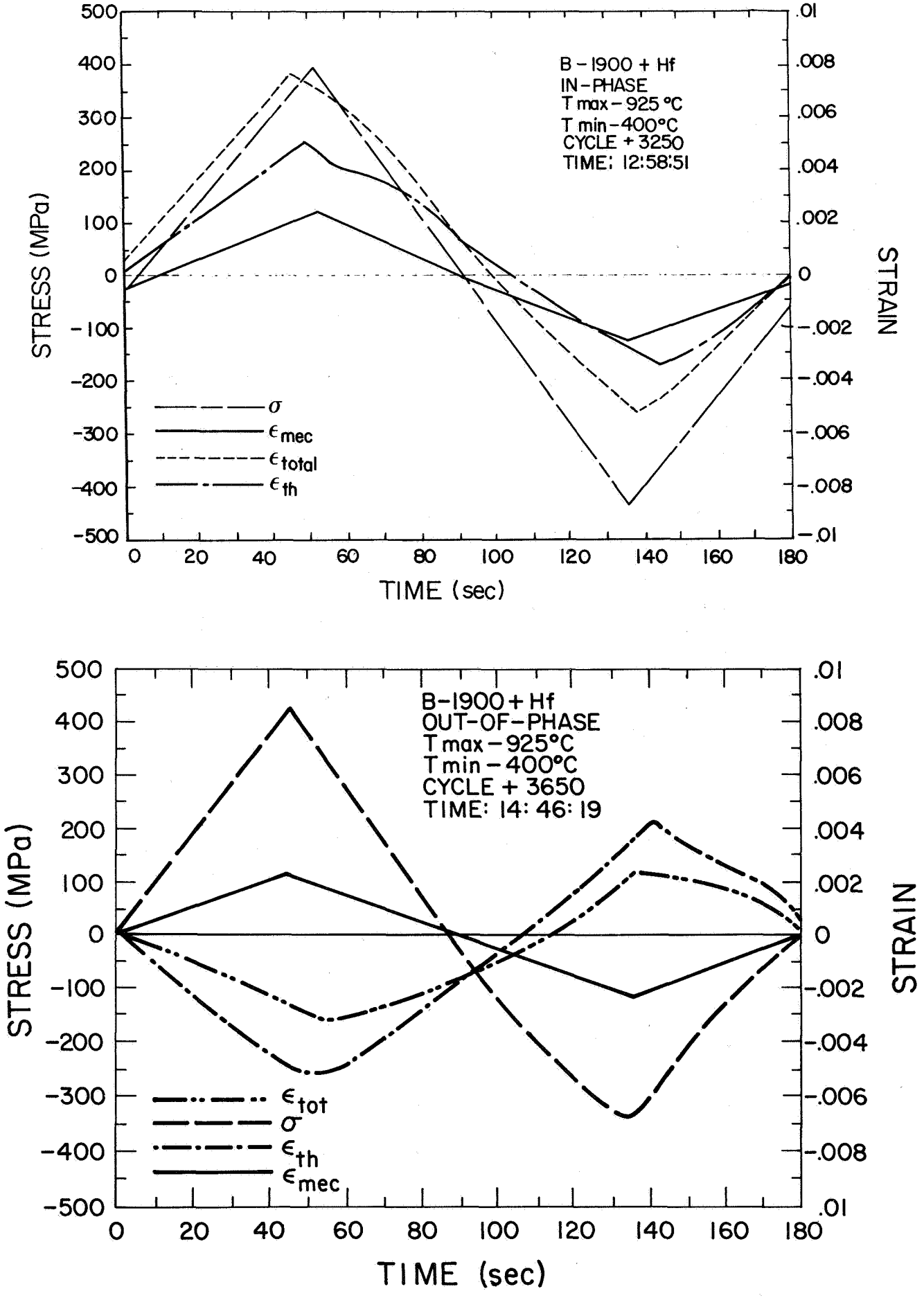

Figure 4. Stress, mechanical strain, thermal strain, and total strain as a function of time (one cycle): (a) in-phase, (b) out-of-phase.

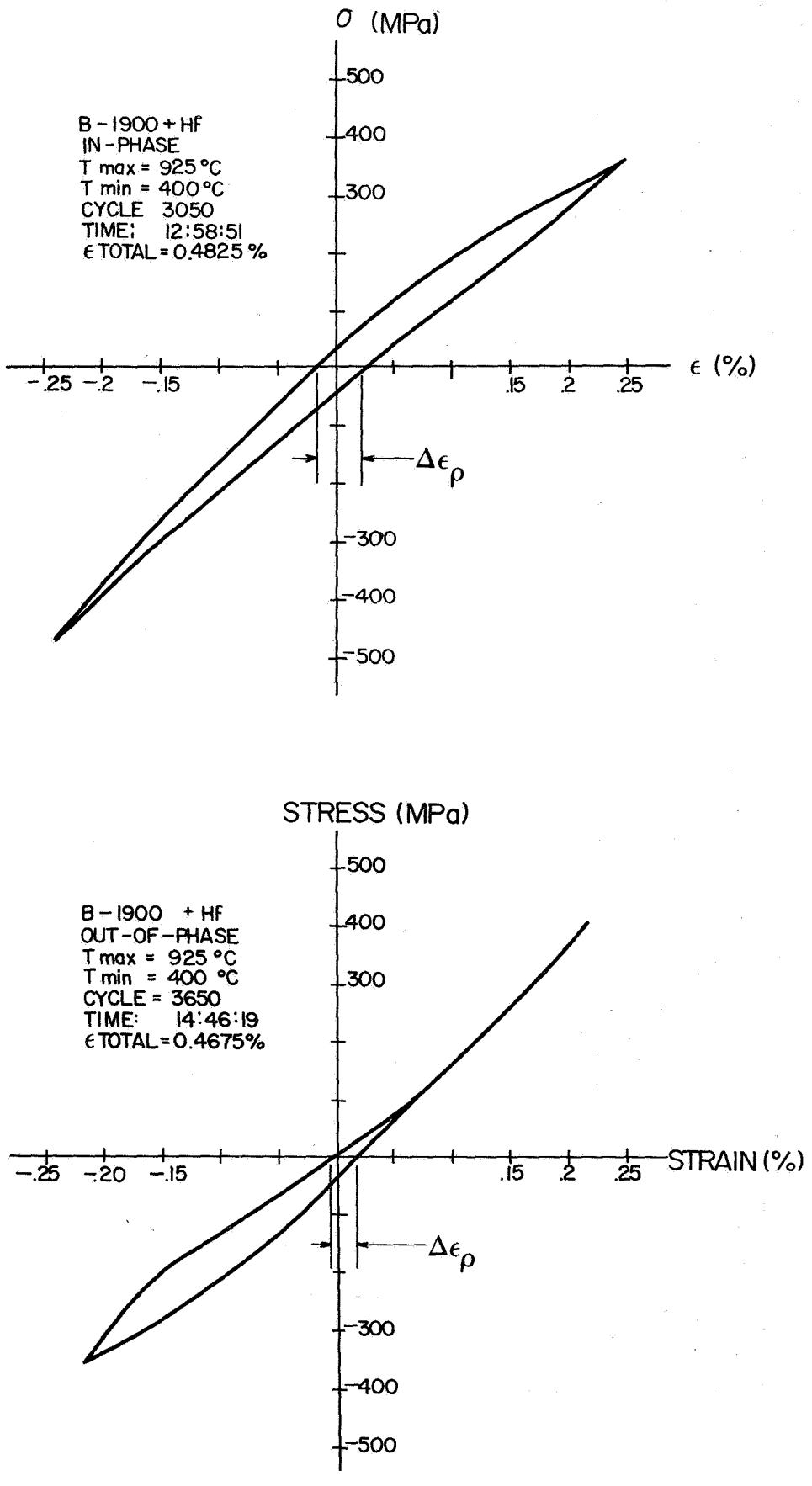

Figure 5. Typical hysteresis loop obtained under TMF conditions: (a) in-phase, (b) out-of-phase.

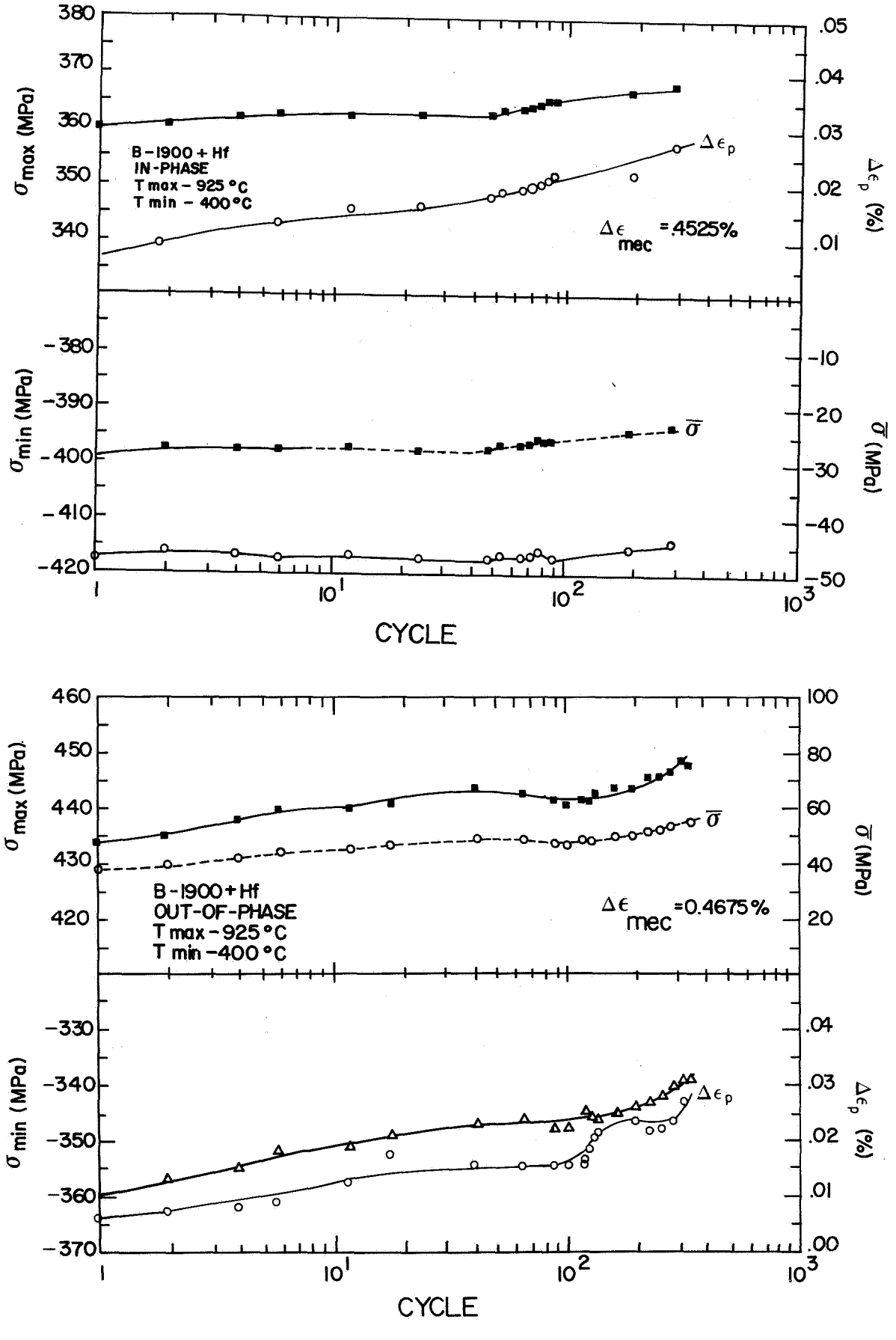

Figure 6. Typical cyclic hardening/softening curves obtained under in-phase and out-of-phase cycling.

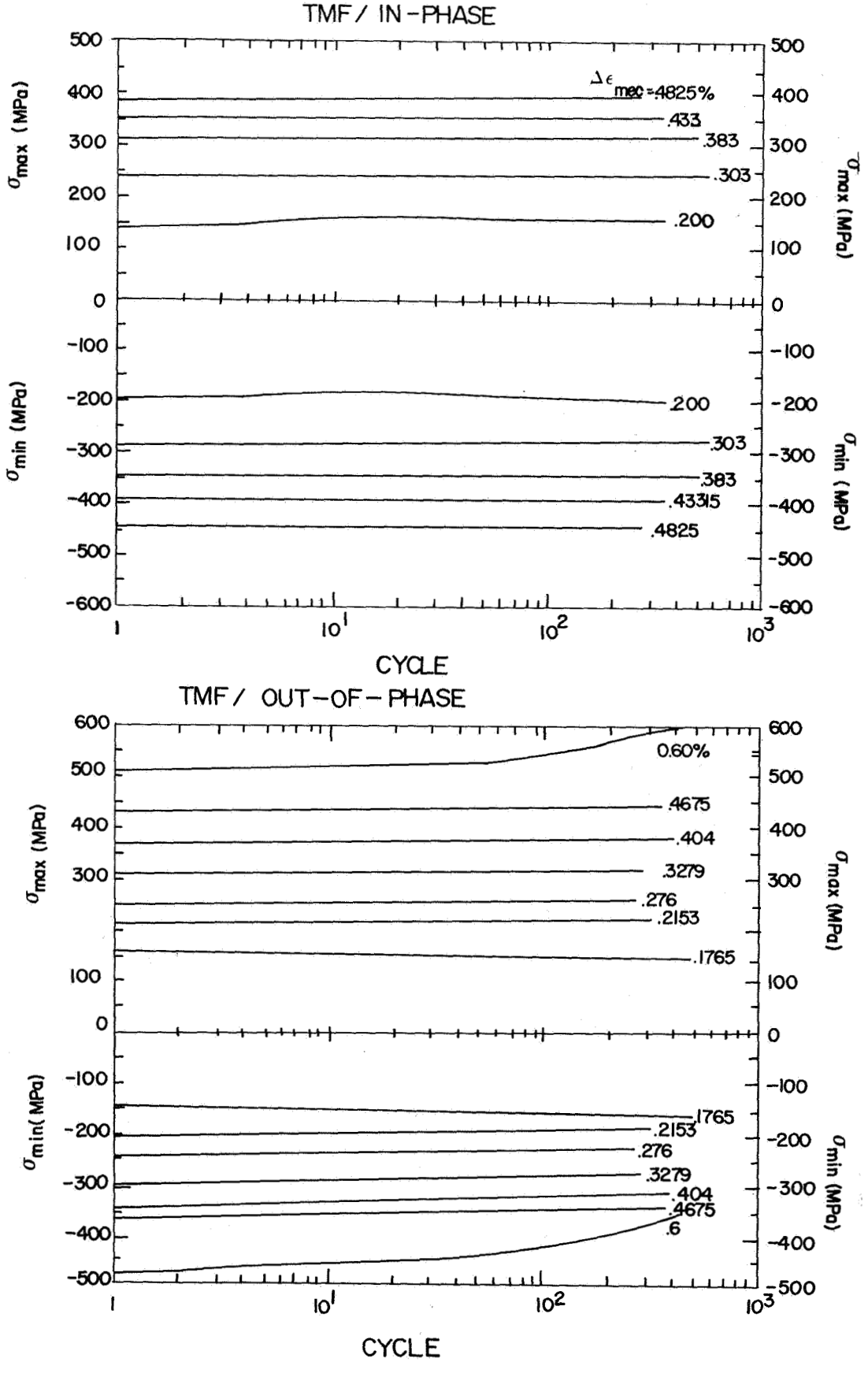

Figure 7. Summary of the cyclic hardening behaviors for in-phase and out-of-phase cycling.

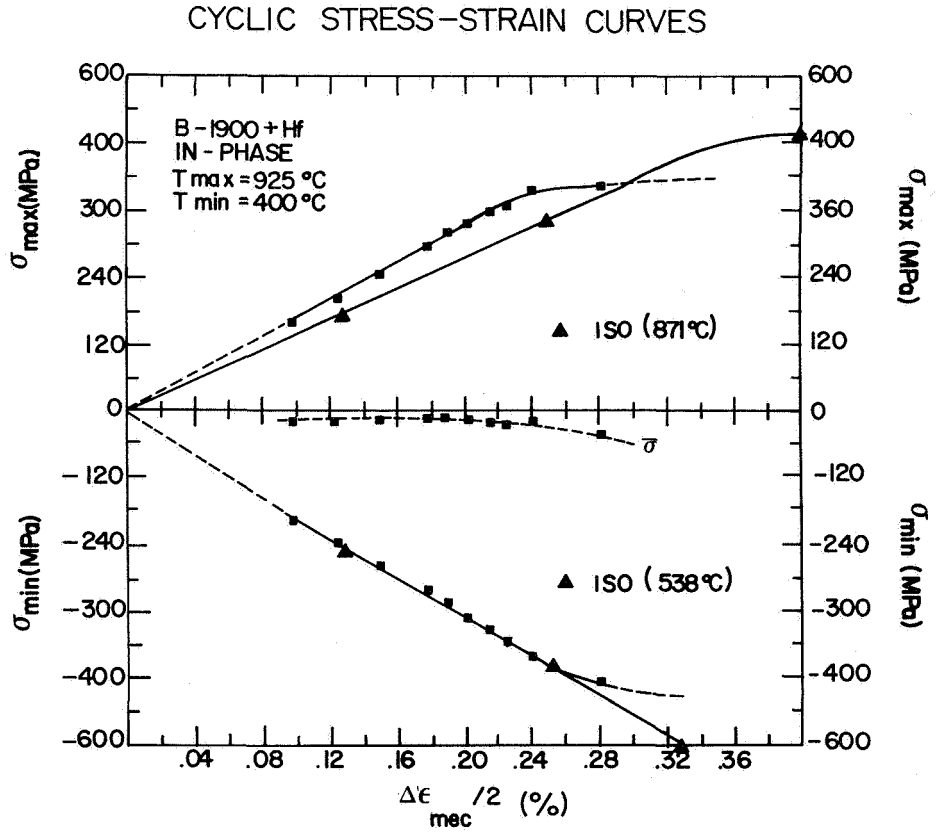

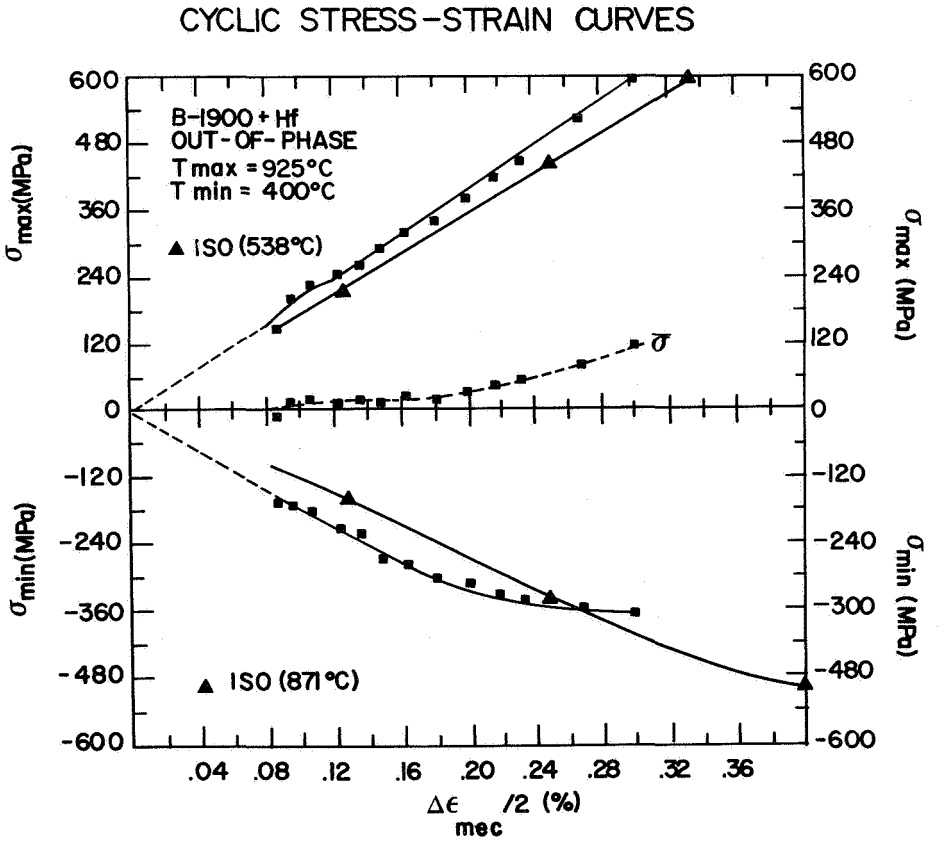

Figure 8. Cyclic stress-strain curves obtained under TMF and isothermal cycling.

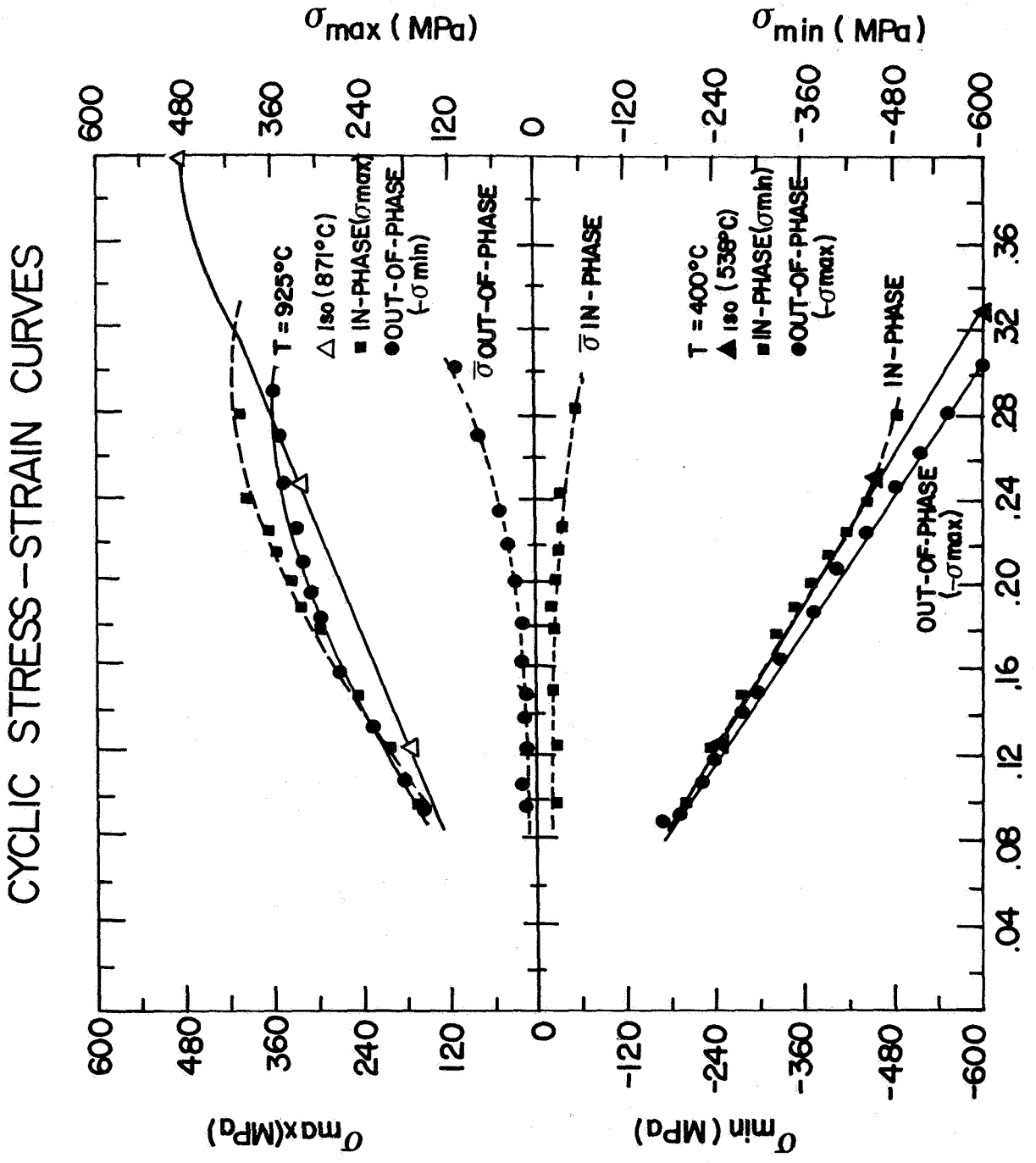

Figure 9. Comparison of TMF and isothermal cycling.

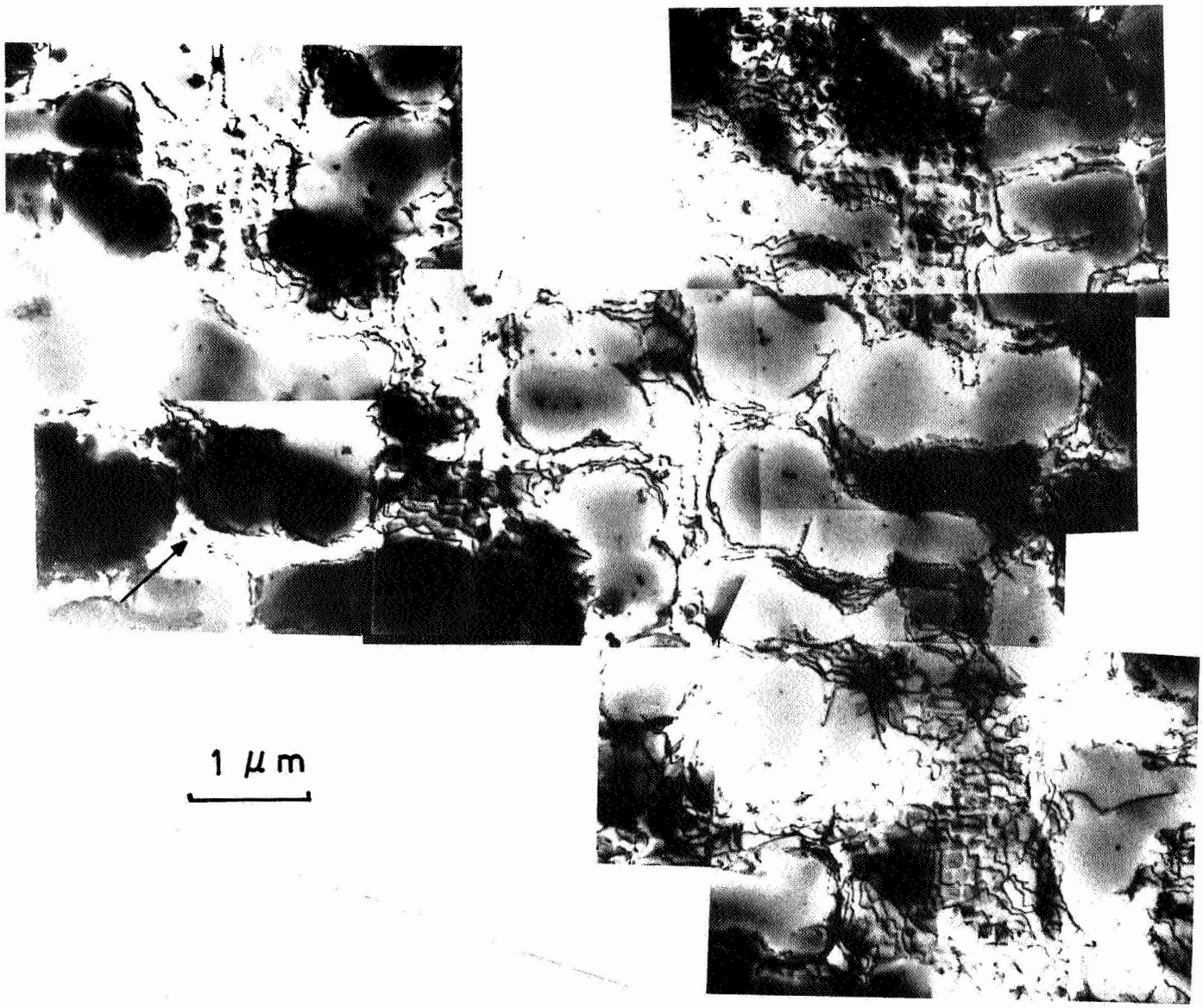

Figure 10. Typical dislocation substructures obtained under in-phase cycling.

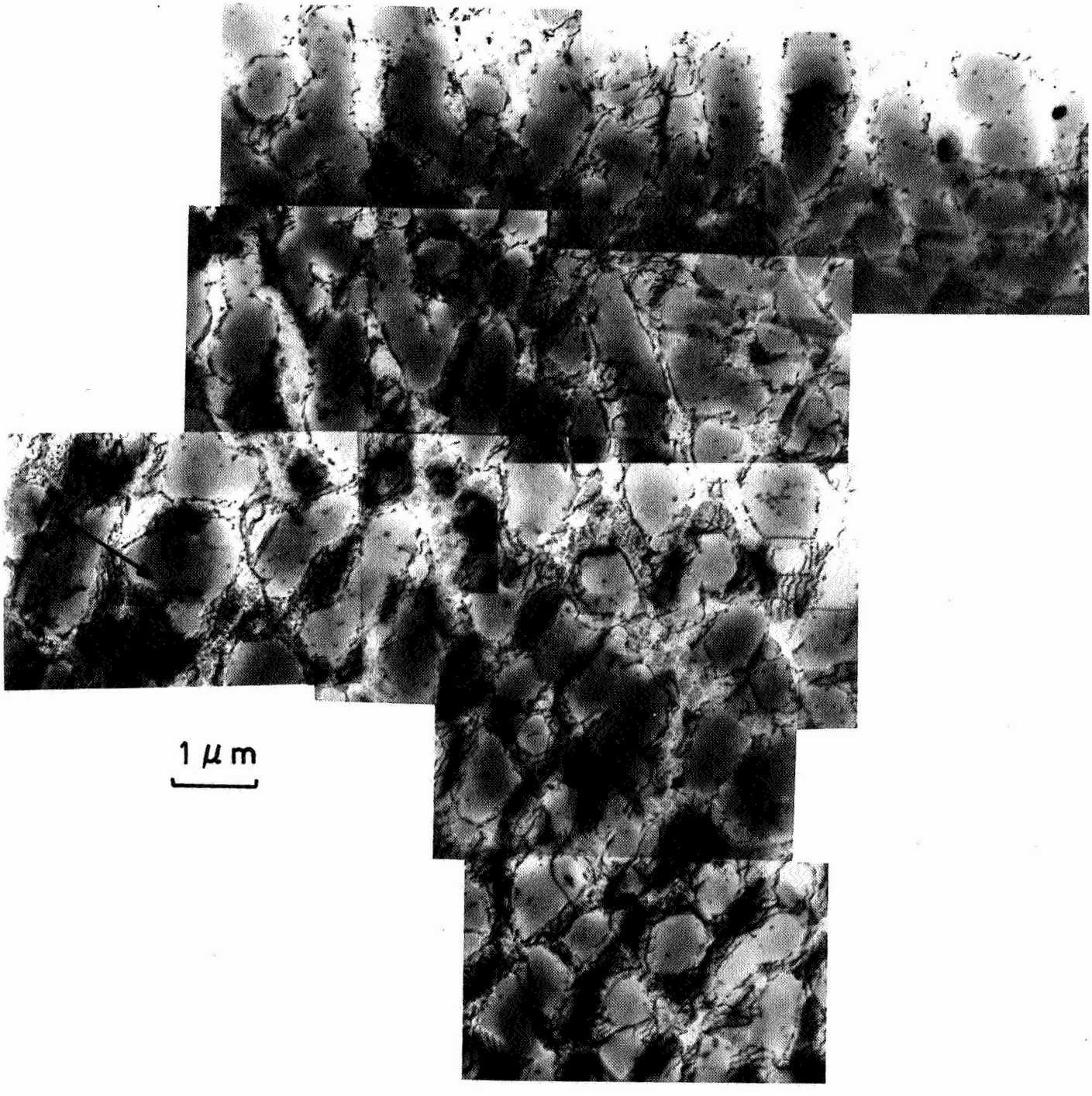

Figure 11. Typical dislocation substructures obtained under out-of-phase cycling.

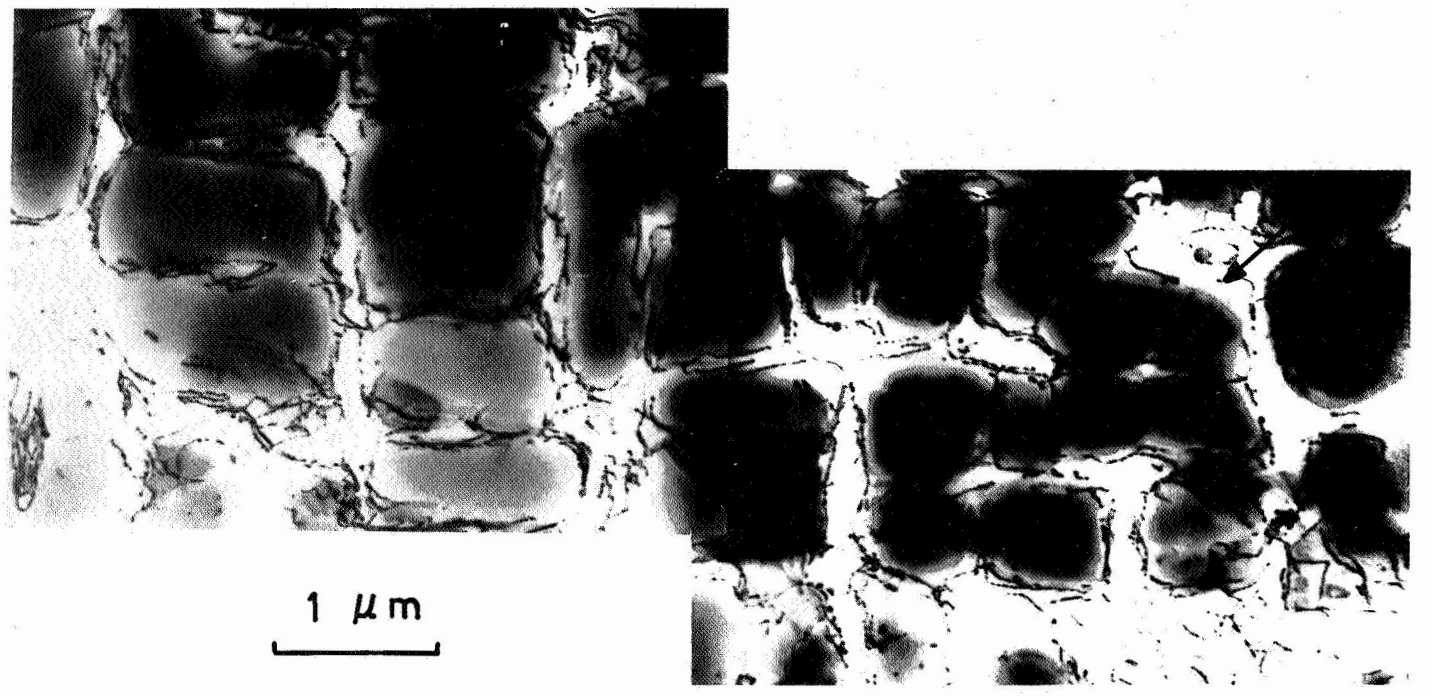

Figure 12. Directional coarsening of the γ′-phase during in-phase cycling.

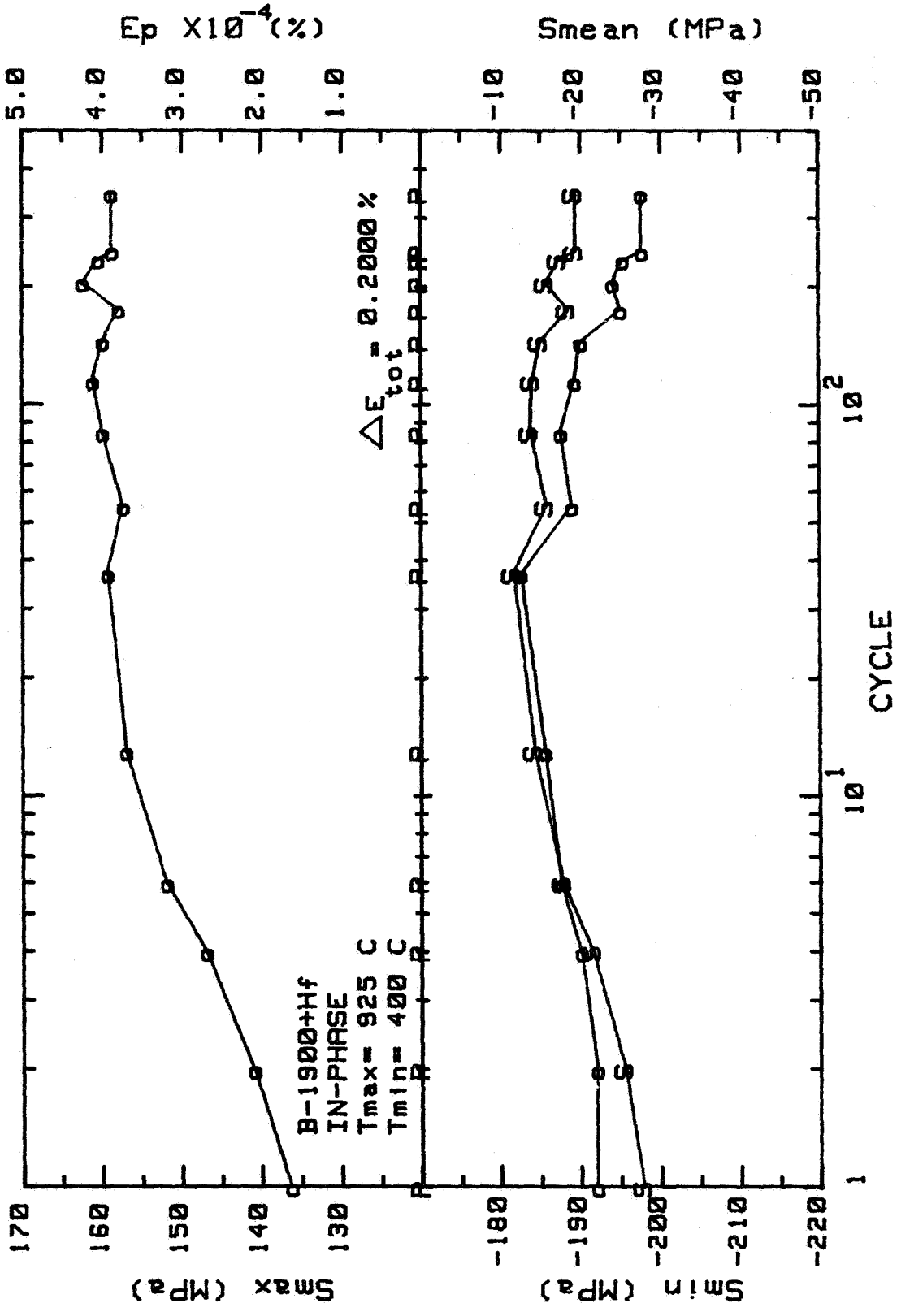
Ep X10^{-4}(%)
Smean (MPa)
5.0
4.0
3.0
2.0
1.0
-10
-20
-30
-40
-50
ΔE_{tot} = 0.2000 %
B-1900+Hf
IN-PHASE
Tmax= 925 C
Tmin= 400 C
170
160
150
140
130
Smax (MPa)
-180
-190
-200
-210
-220
Smin (MPa)
1
10^1
10^2
CYCLE

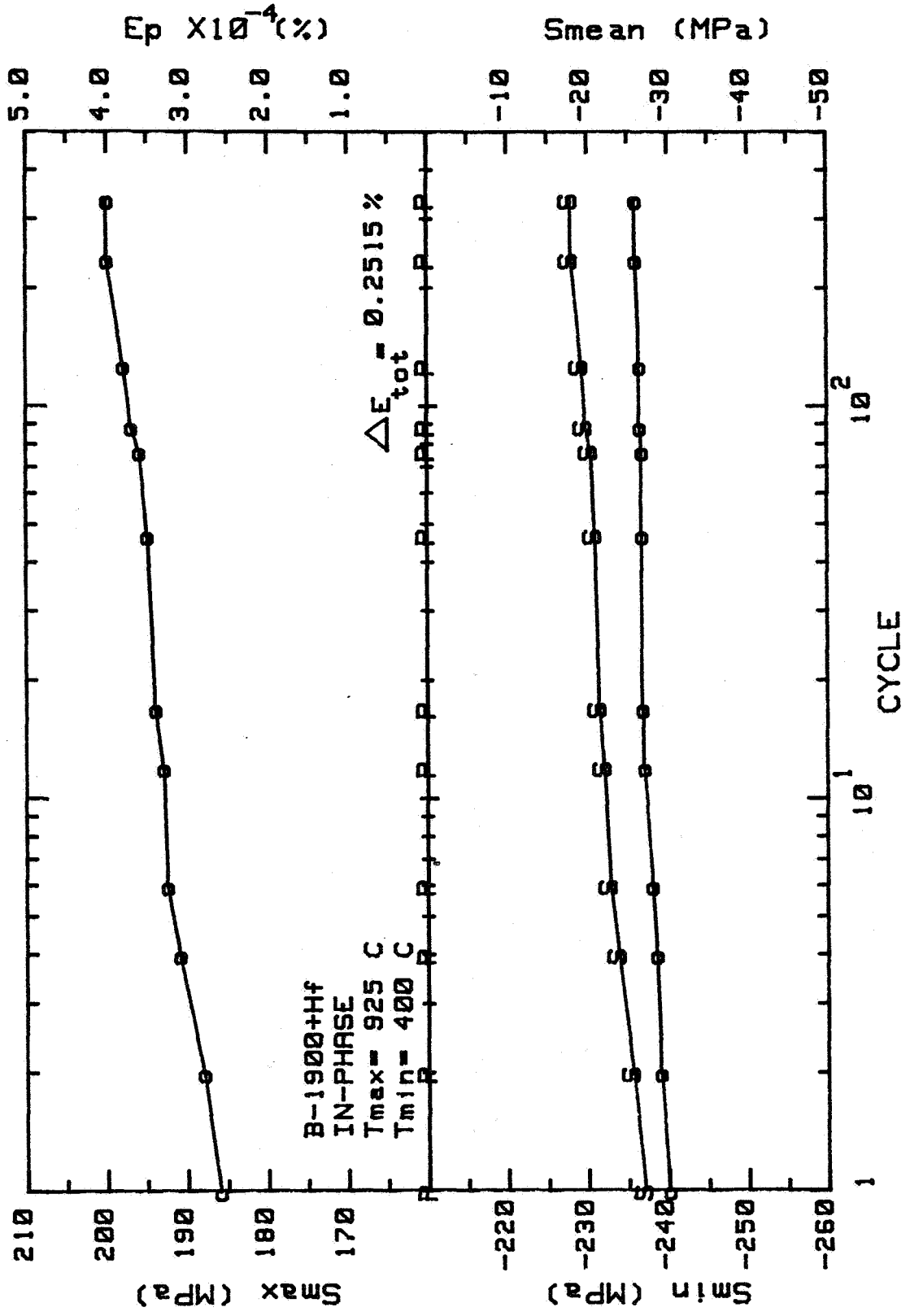
Ep X10⁻⁴(%)
Smean (MPa)
5.0
4.0
3.0
2.0
1.0
-10
-20
-30
-40
-50
ΔE_{tot} = 0.2515 %
B-1900+Hf
IN-PHASE
Tmax= 925 C
Tmin= 400 C
210
200
190
180
170
-220
-230
-240
-250
-260
Smax (MPa)
Smin (MPa)
1
10¹
10²
CYCLE

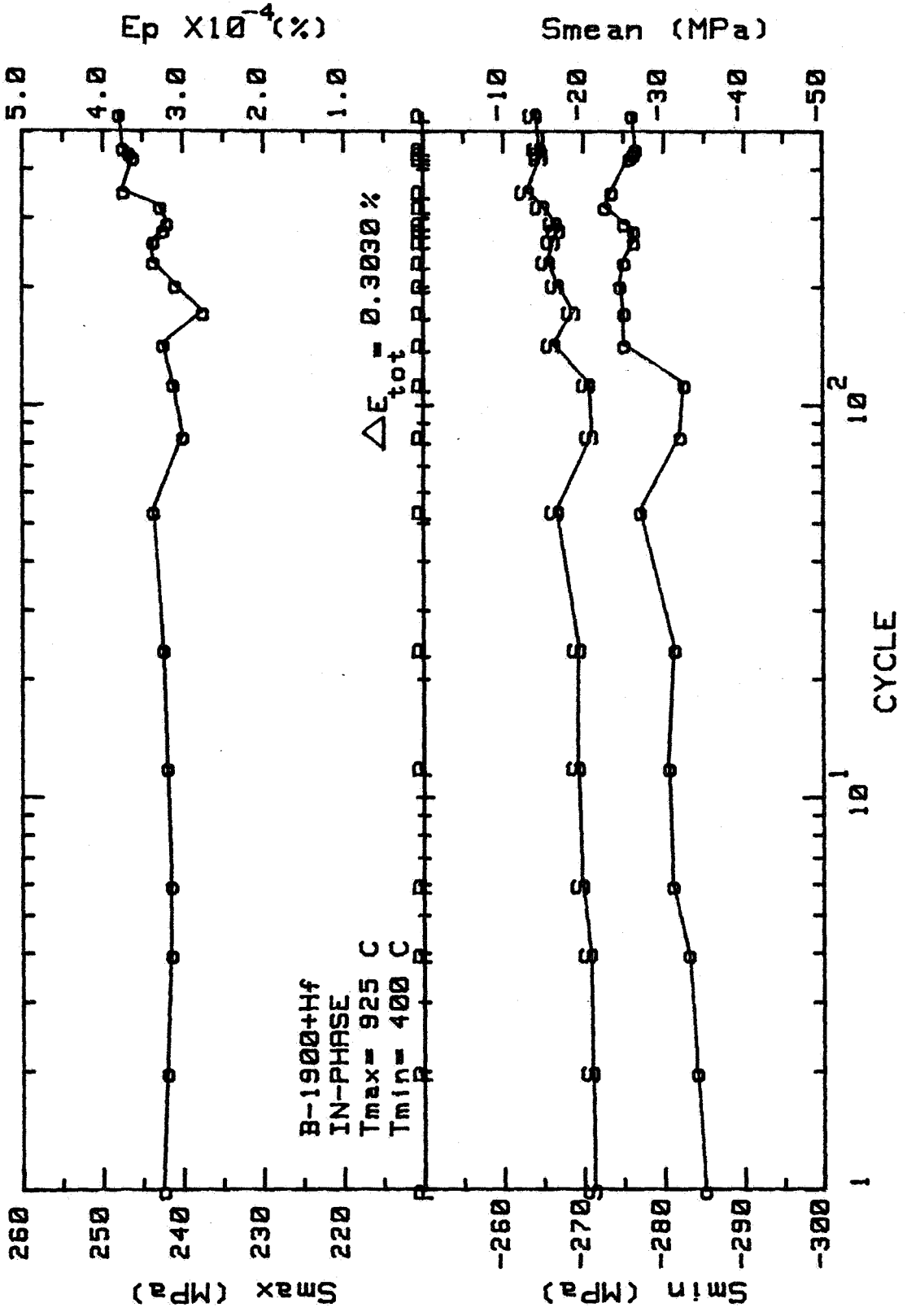
Ep X10^{-4}(%)
Smean (MPa)
5.0
4.0
3.0
2.0
1.0
-10
-20
-30
-40
-50
ΔE_{tot} = 0.3030 %
B-1900+Hf
IN-PHASE
Tmax= 925 C
Tmin= 400 C
260
250
240
230
220
-260
-270
-280
-290
-300
Smax (MPa)
Smin (MPa)
1
10^1
10^2
CYCLE

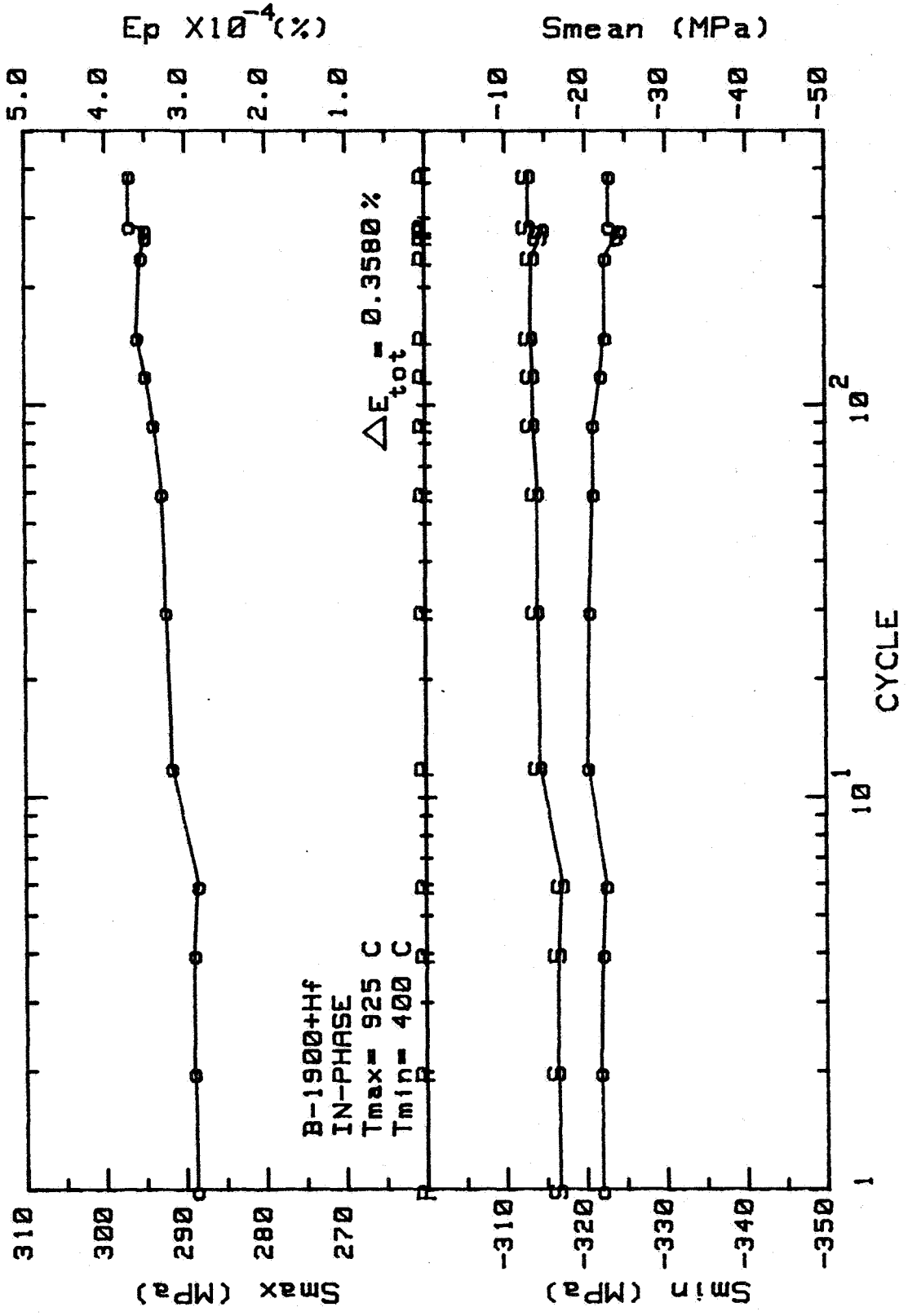
Ep X10^{-4}(%)
Smean (MPa)
5.0
4.0
3.0
2.0
1.0
-10
-20
-30
-40
-50
ΔE_{tot} = 0.3580 %
B-1900+Hf
IN-PHASE
Tmax= 925 C
Tmin= 400 C
310
300
290
280
270
-310
-320
-330
-340
-350
Smax (MPa)
Smin (MPa)
1
10^1
10^2
CYCLE

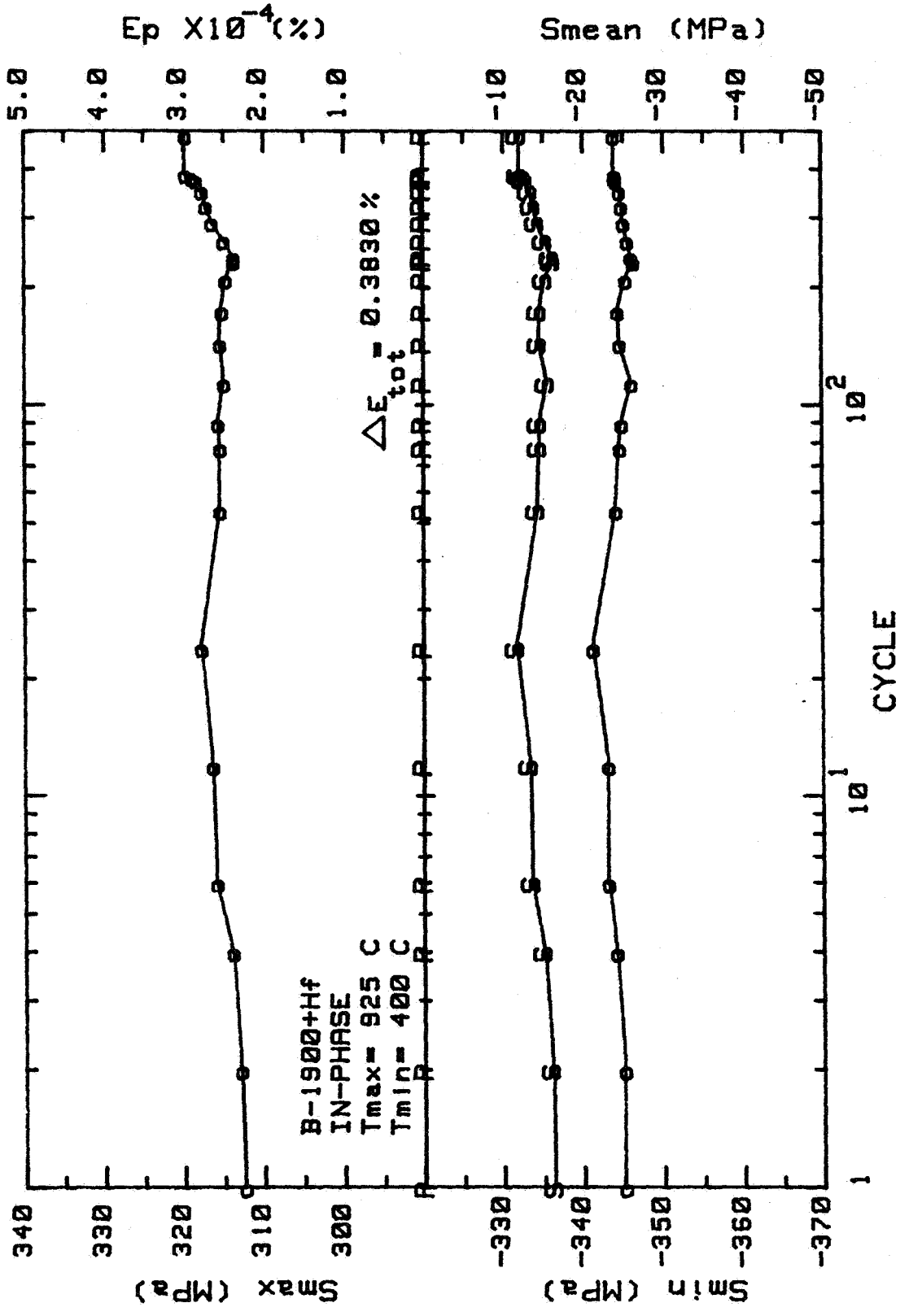
Ep X10^{-4}(%)
Smean (MPa)
5.0
4.0
3.0
2.0
1.0
-10
-20
-30
-40
-50
$\Delta\varepsilon_{tot}$ = 0.3830 %
B-1900+Hf
IN-PHASE
Tmax= 925 C
Tmin= 400 C
340
330
320
310
300
-330
-340
-350
-360
-370
Smax (MPa)
Smin (MPa)
1
10^1
10^2
CYCLE

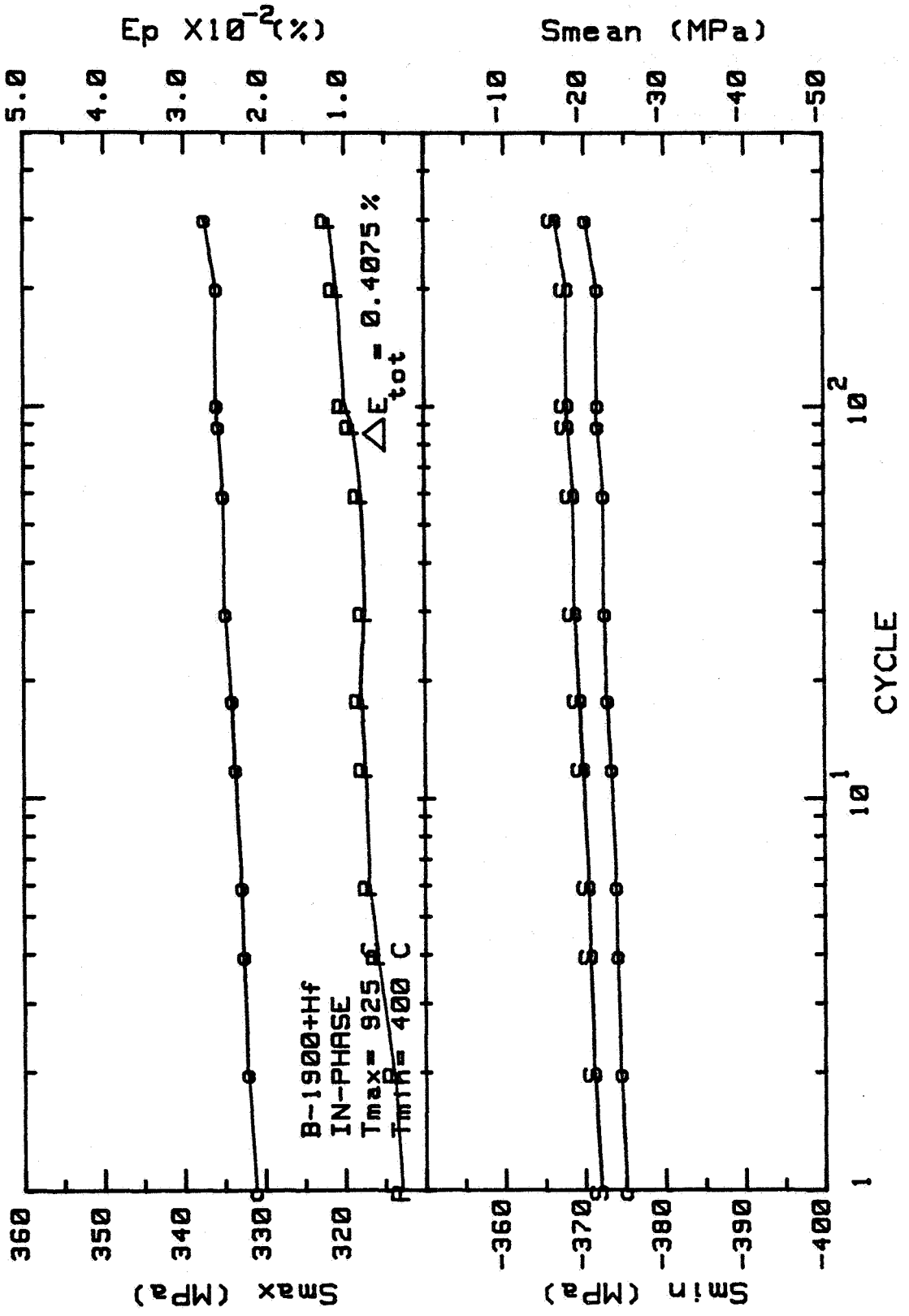
Ep X10^{-2}(%)
Smean (MPa)
5.0
4.0
3.0
2.0
1.0
-10
-20
-30
-40
-50
ΔE_{tot} = 0.4075 %
B-1900+Hf
IN-PHASE
Tmax= 925 C
Tmin= 400 C
360
350
340
330
320
-360
-370
-380
-390
-400
Smax (MPa)
Smin (MPa)
1
10^1
10^2
CYCLE

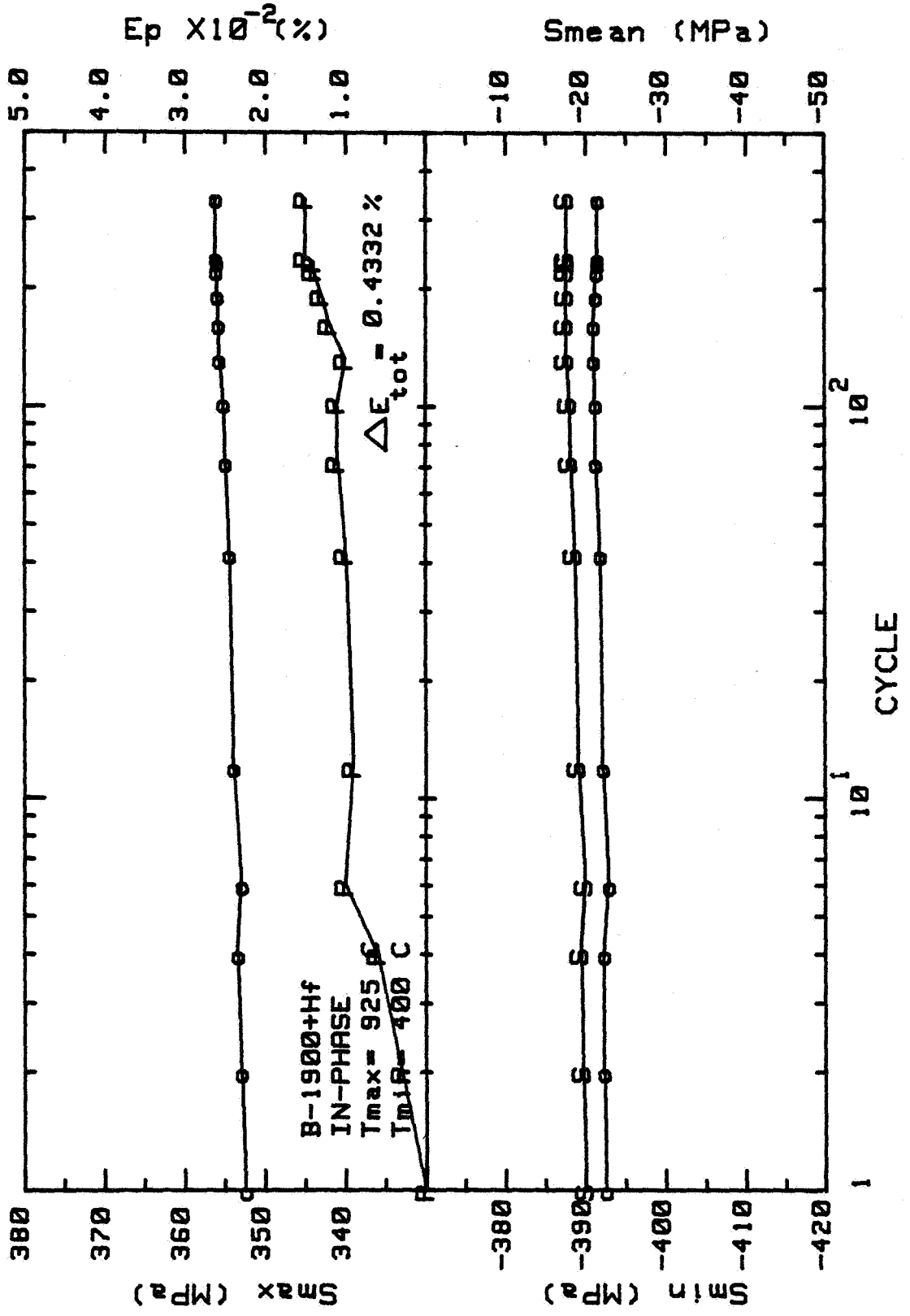
Ep X10^{-2}(%)
Smean (MPa)
5.0
4.0
3.0
2.0
1.0
-10
-20
-30
-40
-50
ΔE_{tot} = 0.4332 %
B-1900+Hf
IN-PHASE
Tmax= 925 C
TmiN= 400 C
380
370
360
350
340
-380
-390
-400
-410
-420
Smax (MPa)
Smin (MPa)
1
10^1
10^2
CYCLE

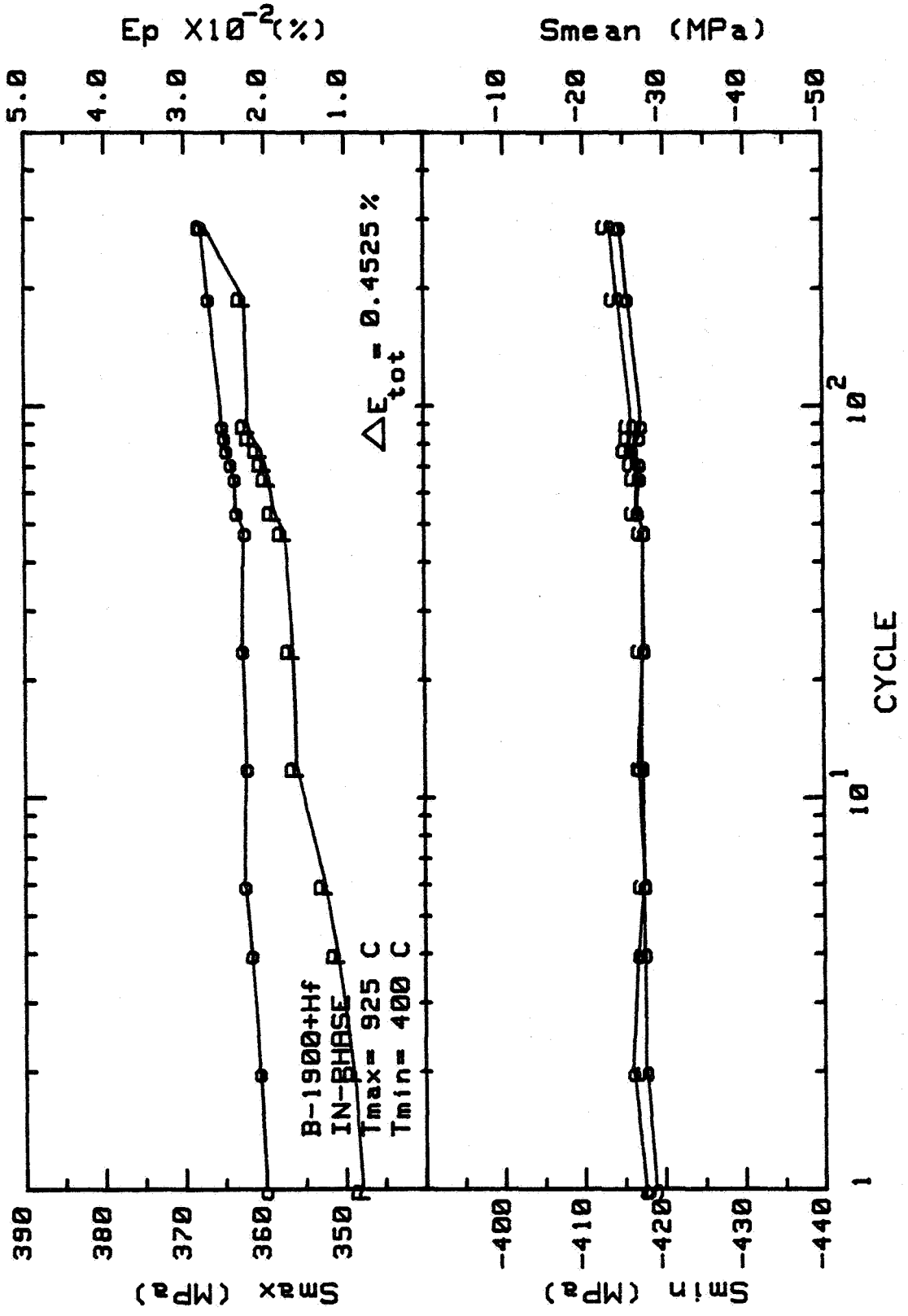
Ep X10^{-2}(%)
Smean (MPa)
5.0
4.0
3.0
2.0
1.0
-10
-20
-30
-40
-50
ΔE_{tot} = 0.4525 %
B-1900+Hf
IN-BHBSE
Tmax= 925 C
Tmin= 400 C
390
380
370
360
350
-400
-410
-420
-430
-440
Smax (MPa)
Smin (MPa)
1
10^1
10^2
CYCLE

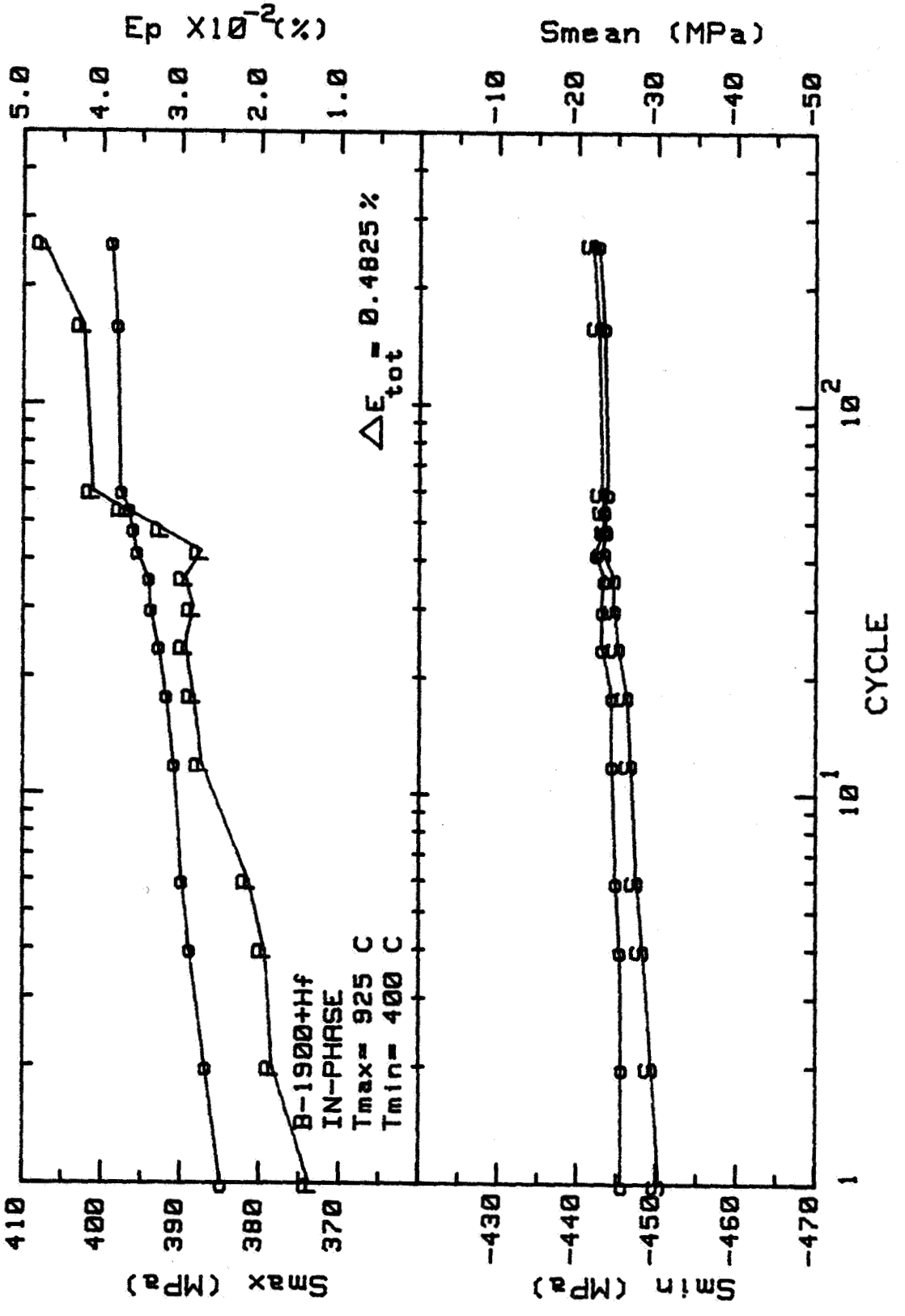
Ep X10^{-2}(%)
Smean (MPa)
5.0
4.0
3.0
2.0
1.0
-10
-20
-30
-40
-50
ΔE_{tot} = 0.4825 %
B-1900+Hf
IN-PHASE
Tmax= 925 C
Tmin= 400 C
Smax (MPa)
Smin (MPa)
410
400
390
380
370
-430
-440
-450
-460
-470
1
10^1
10^2
CYCLE

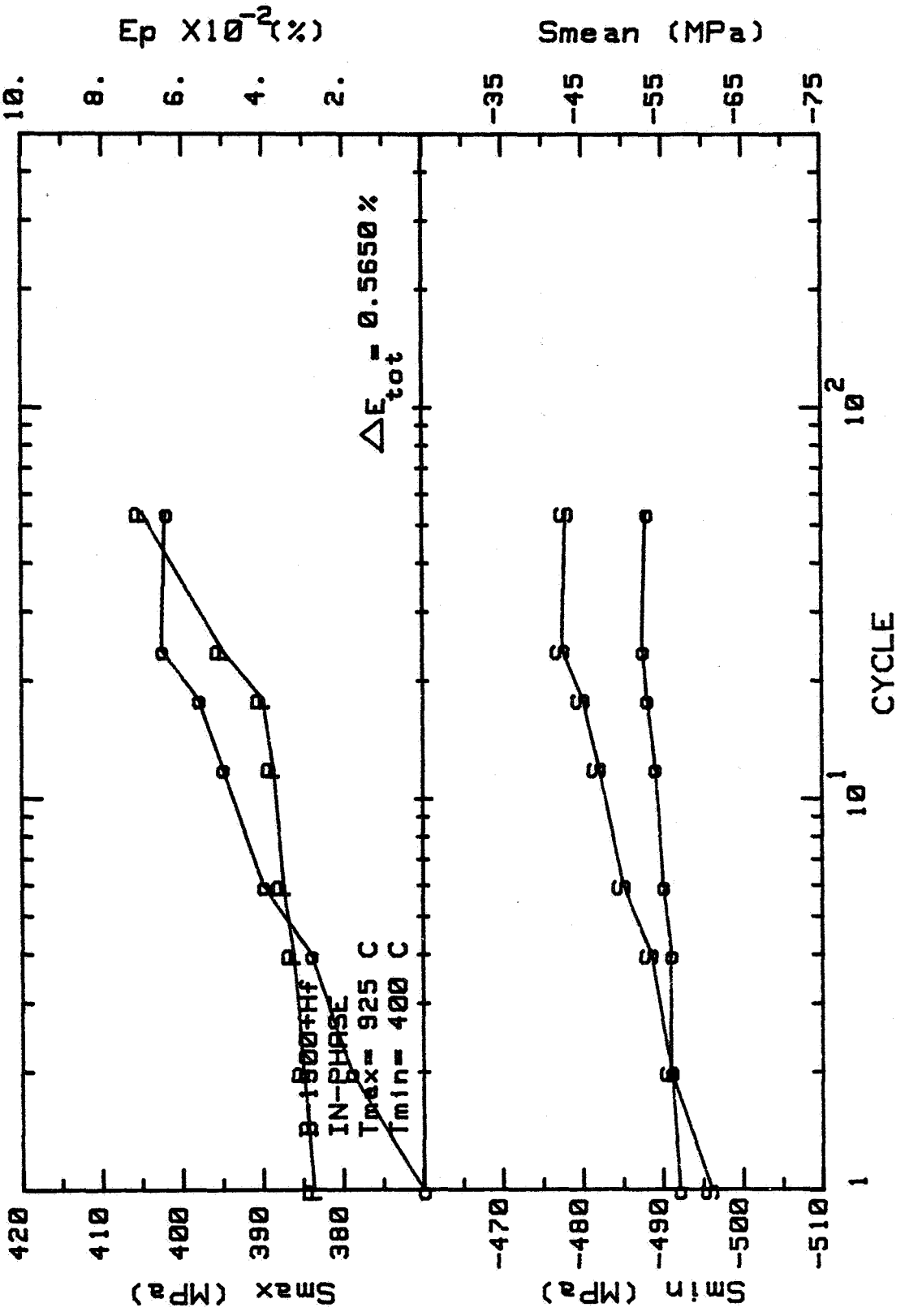
Ep X10^{-2}(%)
Smean (MPa)
10.
8.
6.
4.
2.
-35
-45
-55
-65
-75
ΔE_{tot} = 0.5650 %
IN-PHASE
Tmax= 925 C
Tmin= 400 C
420
410
400
390
380
-470
-480
-490
-500
-510
Smax (MPa)
Smin (MPa)
1
10^1
10^2
CYCLE

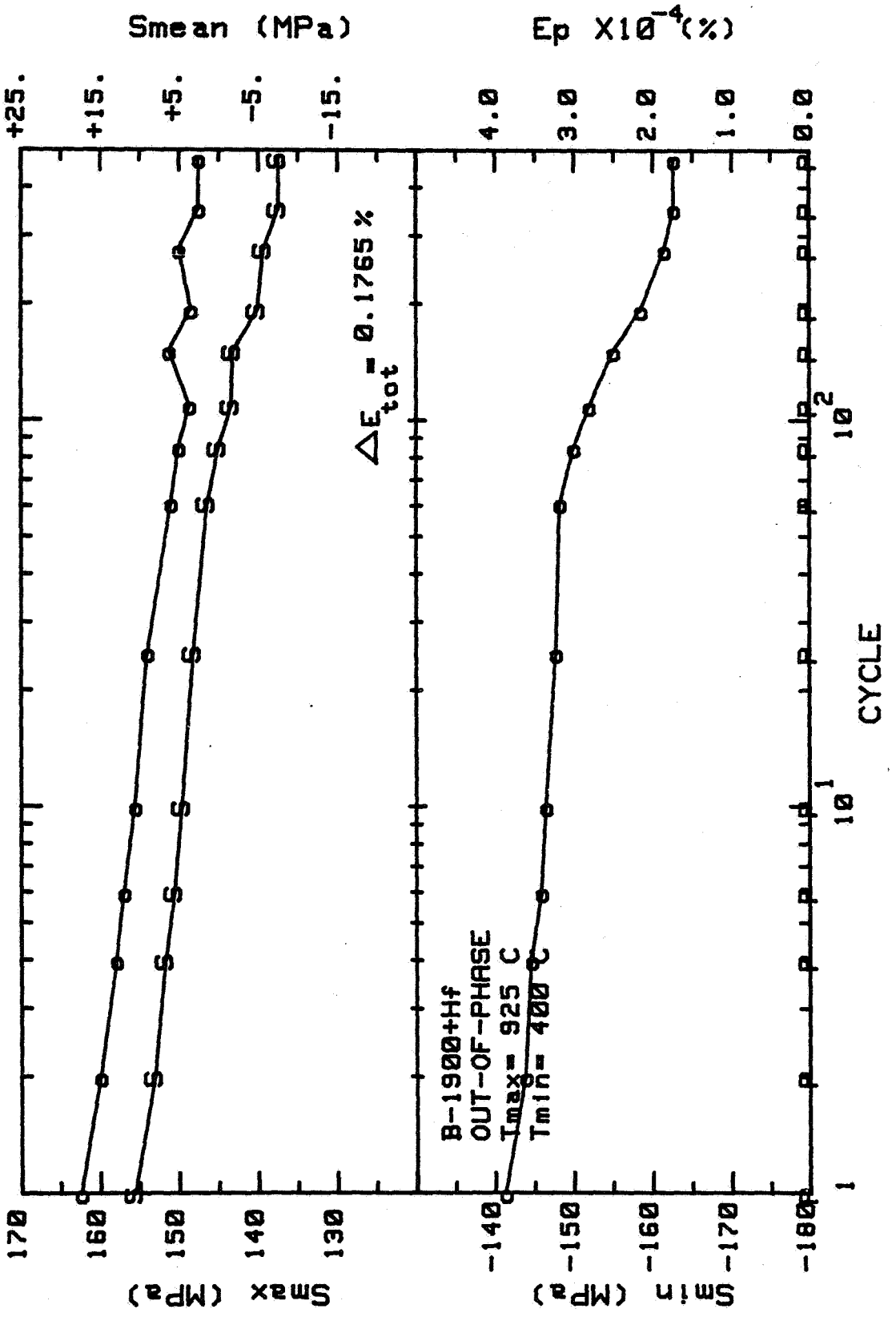
Smean (MPa)
Ep X10^{-4}(%)
+25.
+15.
+5.
-5.
-15.
4.0
3.0
2.0
1.0
0.0
ΔE_{tot} = 0.1765 %
B-1900+Hf
OUT-OF-PHASE
Tmax= 925 C
Tmin= 400 C
170
160
150
140
130
-140
-150
-160
-170
-180
Smax (MPa)
Smin (MPa)
1
10^1
10^2
CYCLE

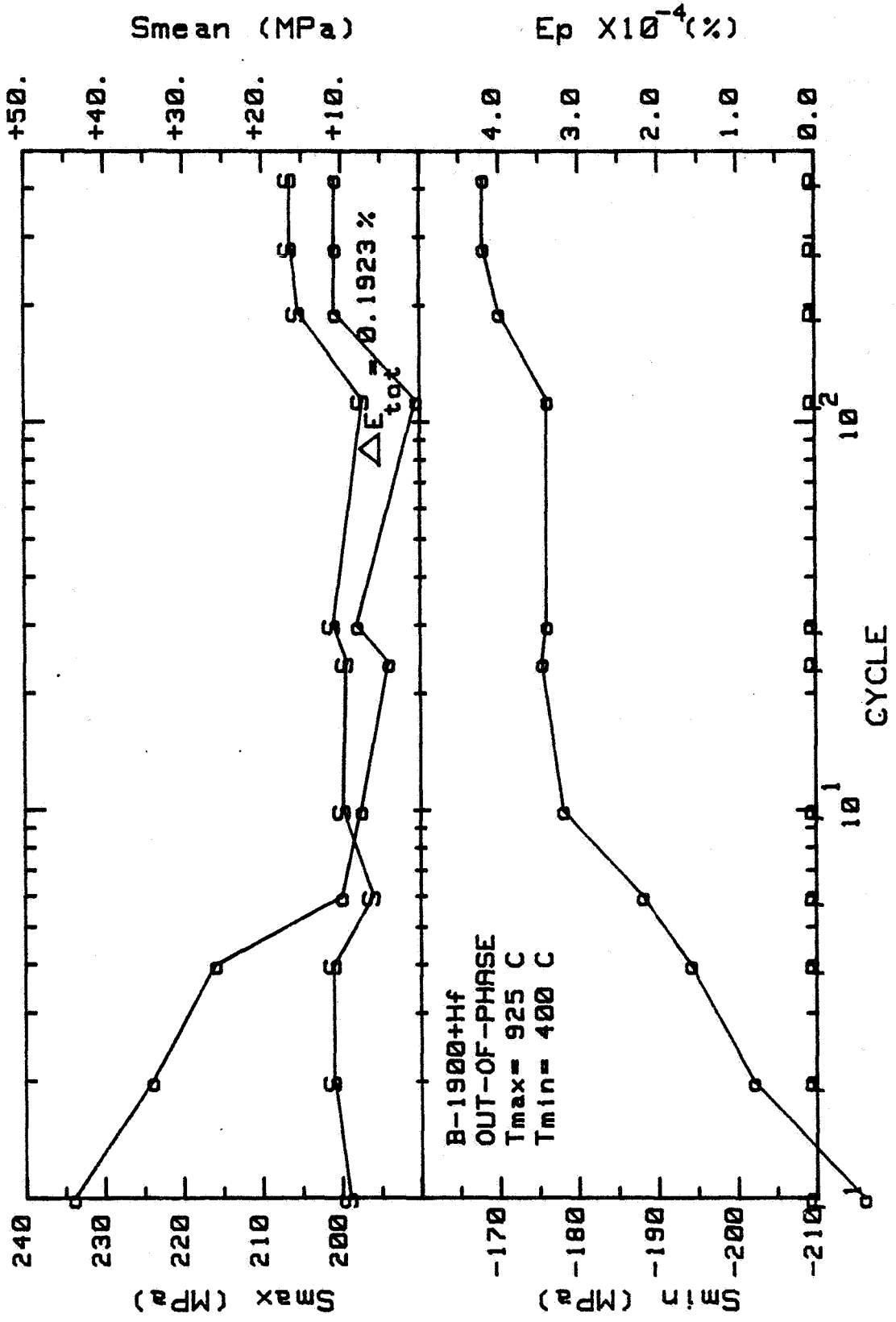
Smean (MPa)
Ep X10^{-4}(%)
+50.
+40.
+30.
+20.
+10.
4.0
3.0
2.0
1.0
0.0
ΔE_{tot} = 0.1923 %
B-1900+Hf
OUT-OF-PHASE
Tmax= 925 C
Tmin= 400 C
CYCLE
10^1
10^2
Smax (MPa)
240
230
220
210
200
Smin (MPa)
-170
-180
-190
-200
-210

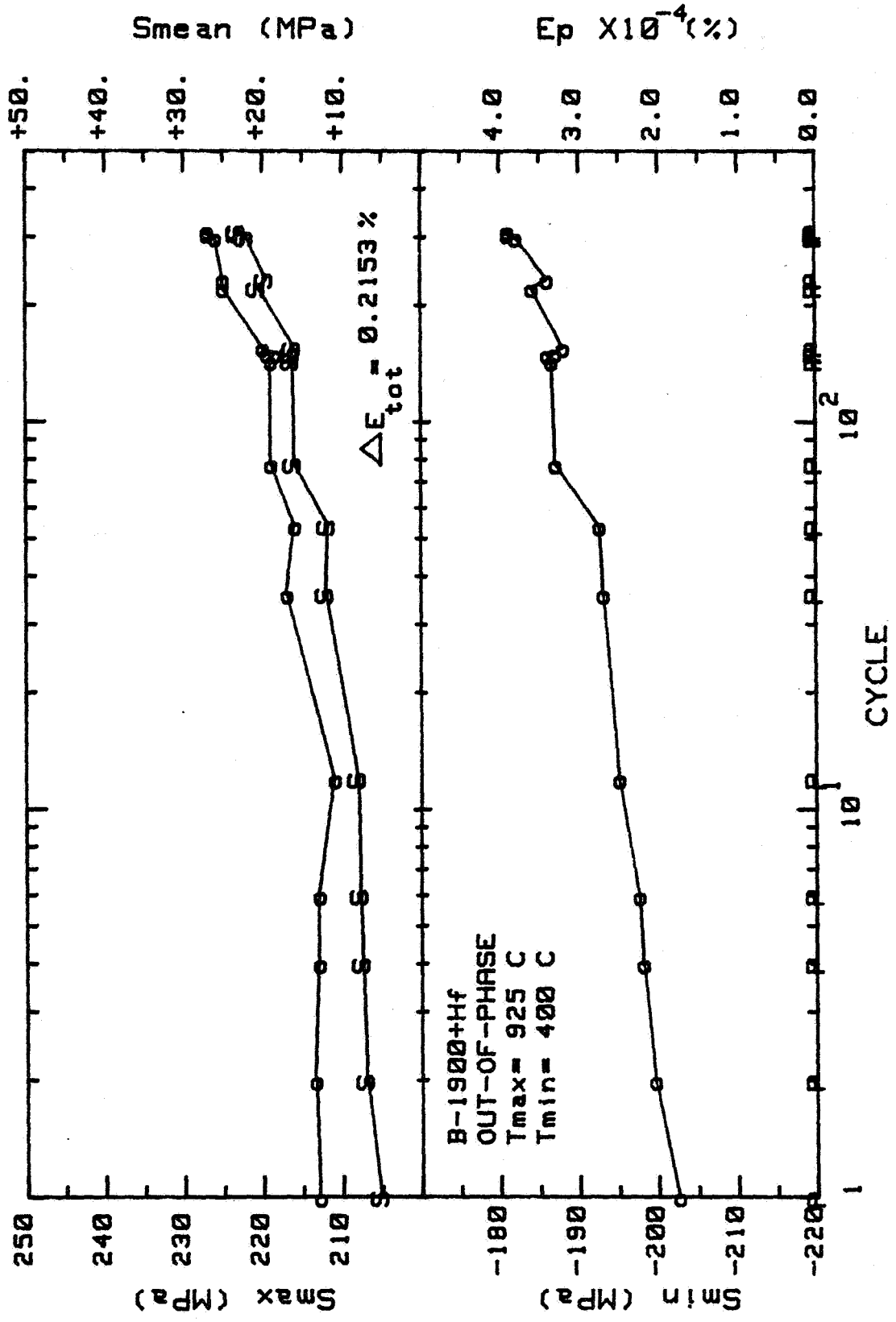
Smean (MPa)
Ep X10^{-4}(%)
+50.
+40.
+30.
+20.
+10.
4.0
3.0
2.0
1.0
0.0
ΔE_{tot} = 0.2153 %
B-1900+Hf
OUT-OF-PHASE
Tmax= 925 C
Tmin= 400 C
CYCLE
1
10^1
10^2
250
240
230
220
210
-180
-190
-200
-210
-220
Smax (MPa)
Smin (MPa)

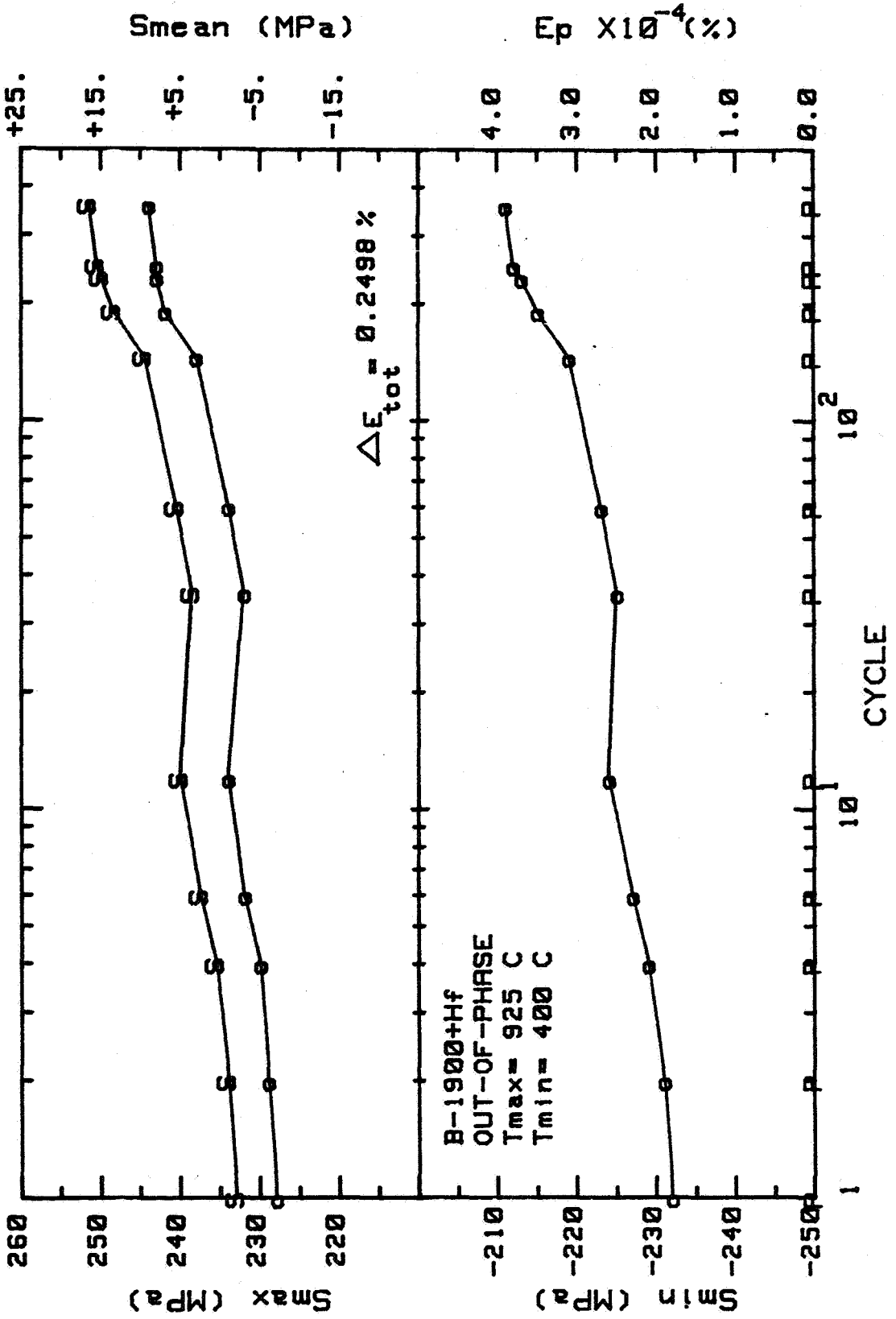
Smean (MPa)
Ep X10^{-4}(%)
+25.
+15.
+5.
-5.
-15.
4.0
3.0
2.0
1.0
0.0
$\Delta\varepsilon_{tot}$ = 0.2498 %
B-1900+Hf
OUT-OF-PHASE
Tmax= 925 C
Tmin= 400 C
Smax (MPa)
Smin (MPa)
260
250
240
230
220
-210
-220
-230
-240
-250
1
10
10^2
CYCLE

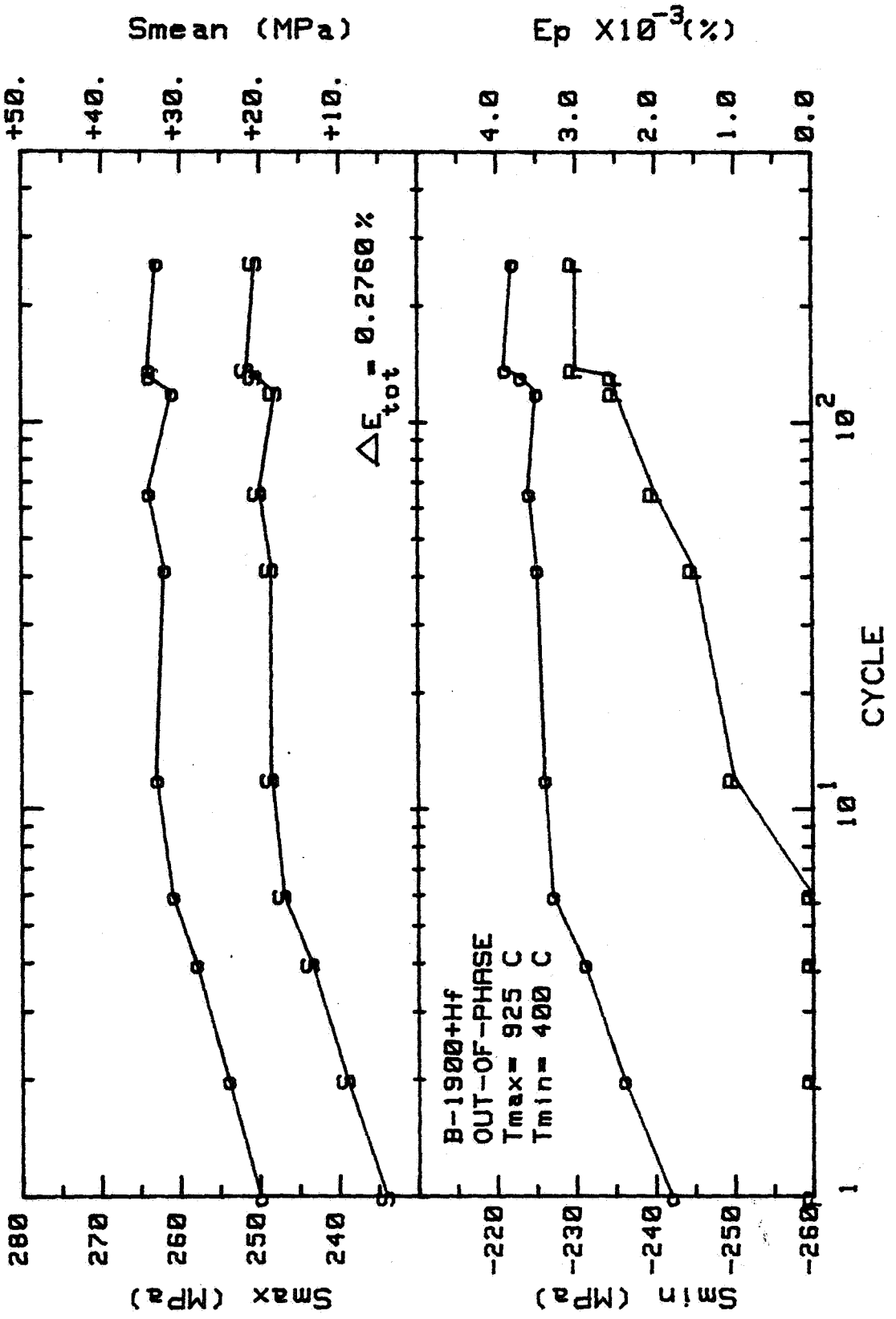
Smean (MPa)
Ep X10^{-3}(%)
+50.
+40.
+30.
+20.
+10.
4.0
3.0
2.0
1.0
0.0
ΔE_{tot} = 0.2760 %
B-1900+Hf
OUT-OF-PHASE
Tmax= 925 C
Tmin= 400 C
Smax (MPa)
Smin (MPa)
280
270
260
250
240
-220
-230
-240
-250
-260
1
10^1
10^2
CYCLE

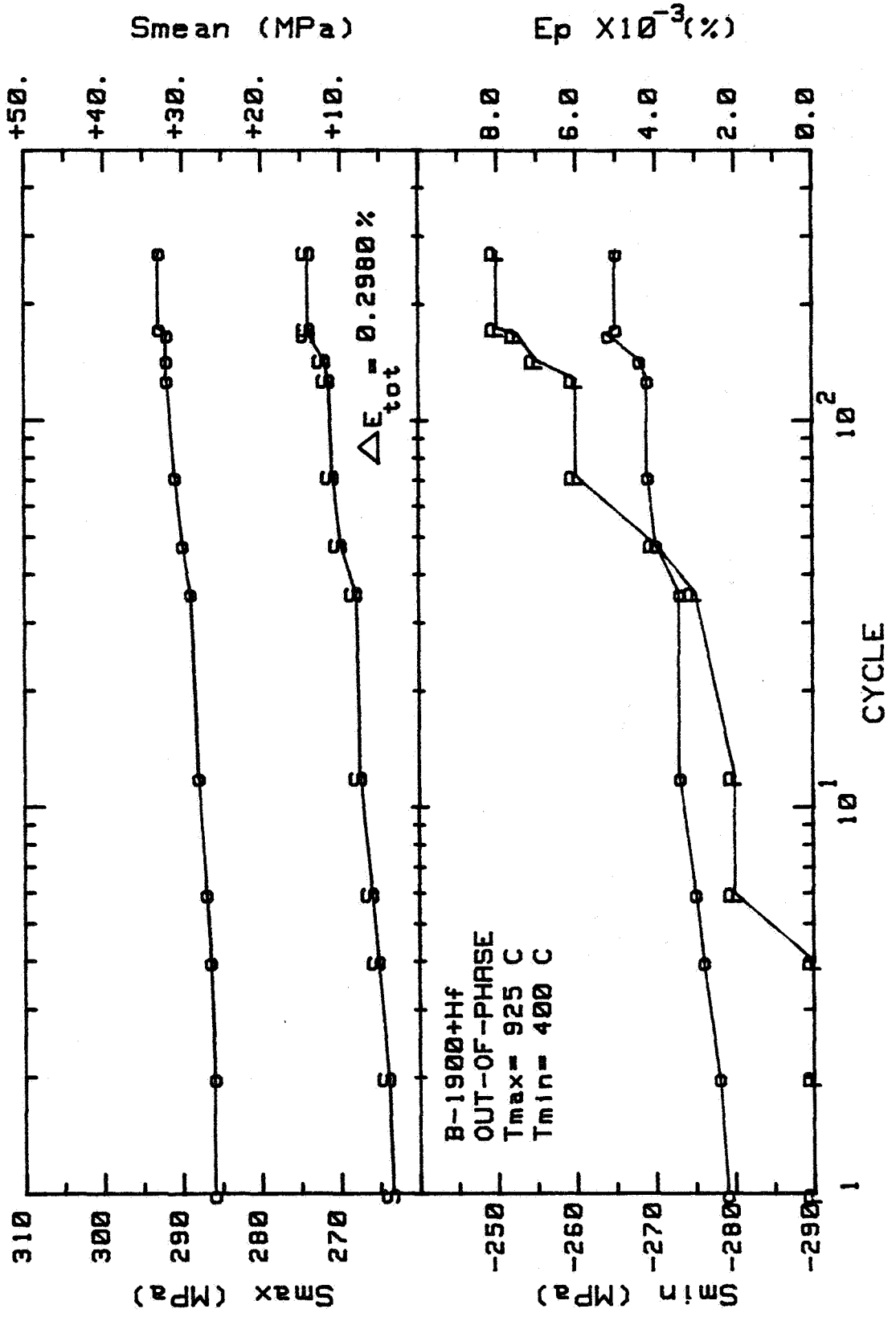
Smean (MPa)
Ep X10^{-3}(%)
+50.
+40.
+30.
+20.
+10.
8.0
6.0
4.0
2.0
0.0
ΔE_{tot} = 0.2980 %
B-1900+Hf
OUT-OF-PHASE
Tmax= 925 C
Tmin= 400 C
Smax (MPa)
Smin (MPa)
310
300
290
280
270
-250
-260
-270
-280
-290
1
10^1
10^2
CYCLE

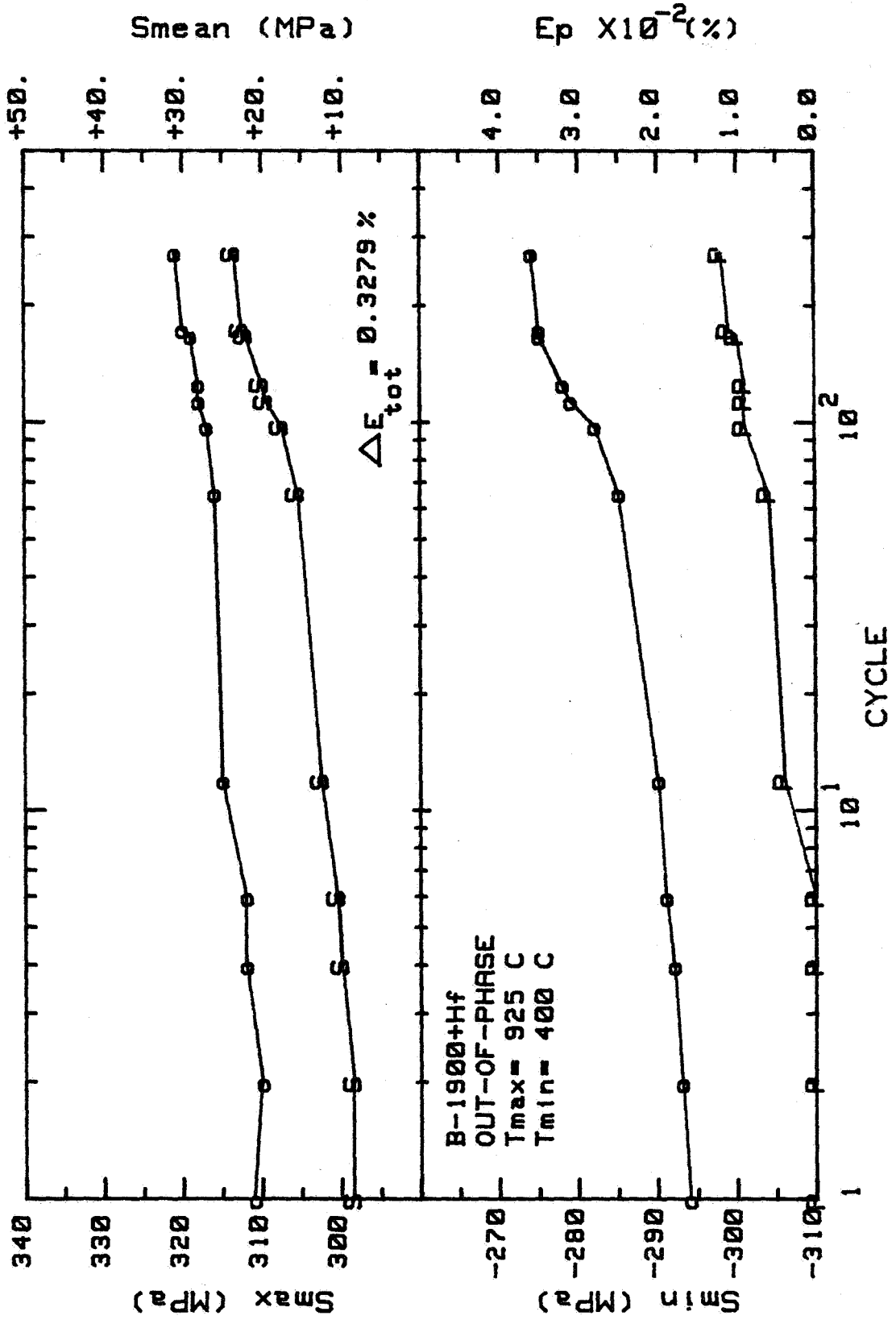
Smean (MPa)
Ep X10^{-2}(%)
+50.
+40.
+30.
+20.
+10.
4.0
3.0
2.0
1.0
0.0
ΔE_{tot} = 0.3279 %
B-1900+Hf
OUT-OF-PHASE
Tmax= 925 C
Tmin= 400 C
Smax (MPa)
Smin (MPa)
340
330
320
310
300
-270
-280
-290
-300
-310
1
10^1
10^2
CYCLE

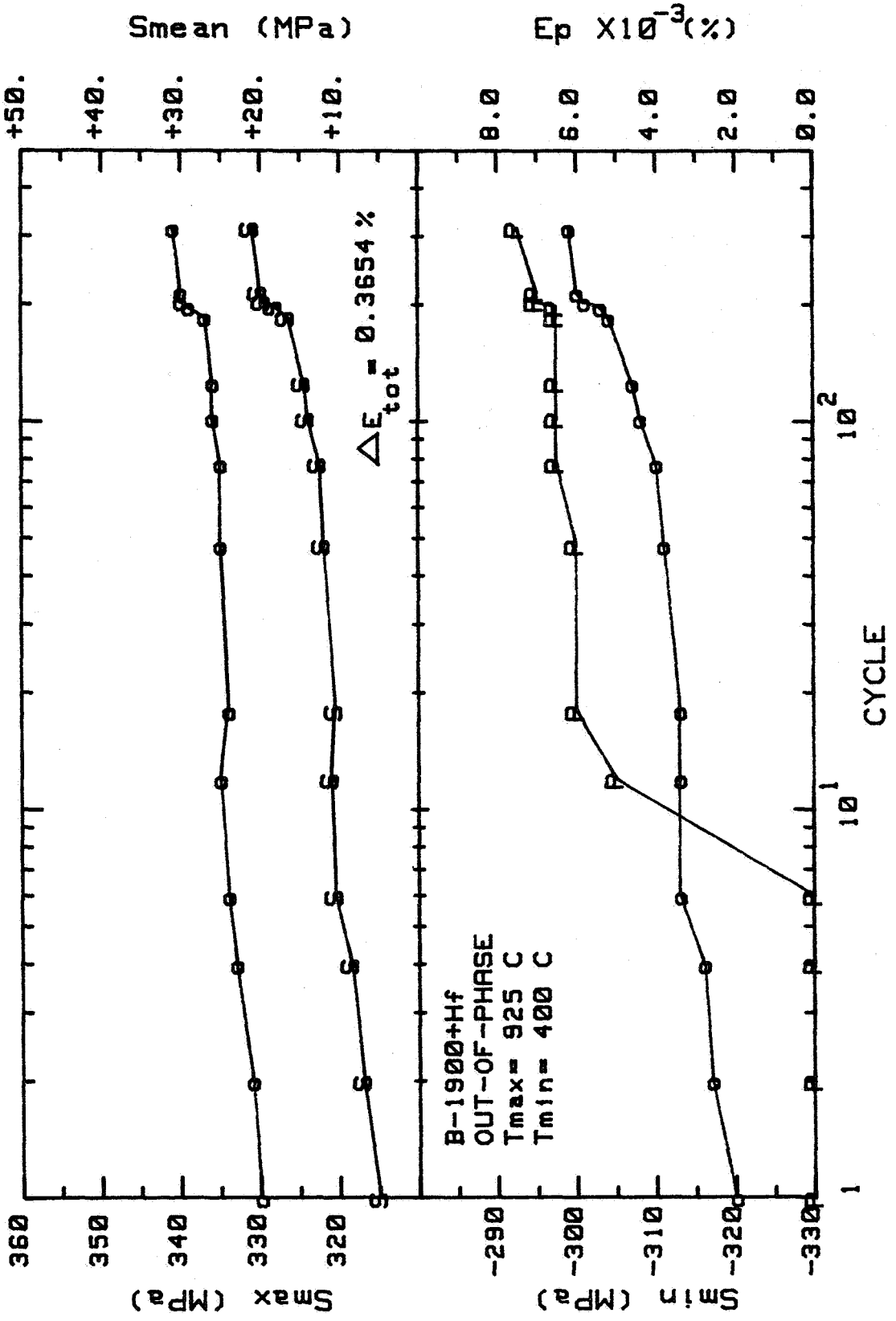
Smean (MPa)
Ep X10^{-3}(%)
+50.
+40.
+30.
+20.
+10.
8.0
6.0
4.0
2.0
0.0
ΔE_{tot} = 0.3654 %
B-1900+Hf
OUT-OF-PHASE
Tmax= 925 C
Tmin= 400 C
360
350
340
330
320
-290
-300
-310
-320
-330
Smax (MPa)
Smin (MPa)
1
10^1
10^2
CYCLE

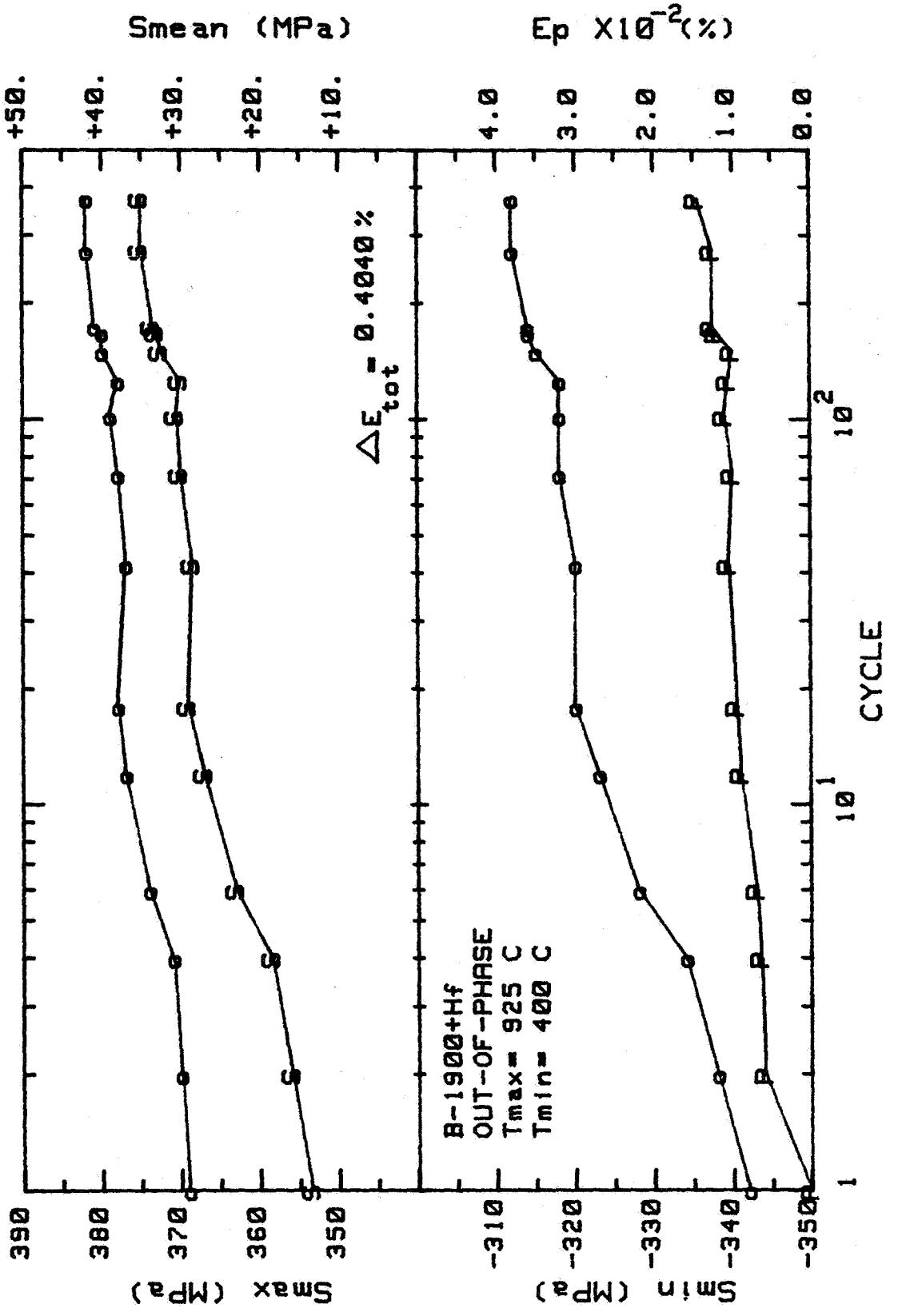
Smean (MPa)
Ep X10^{-2}(%)
+50.
+40.
+30.
+20.
+10.
4.0
3.0
2.0
1.0
0.0
ΔE_{tot} = 0.4040 %
B-1900+Hf
OUT-OF-PHASE
Tmax= 925 C
Tmin= 400 C
390
380
370
360
350
-310
-320
-330
-340
-350
Smax (MPa)
Smin (MPa)
1
10^1
10^2
CYCLE

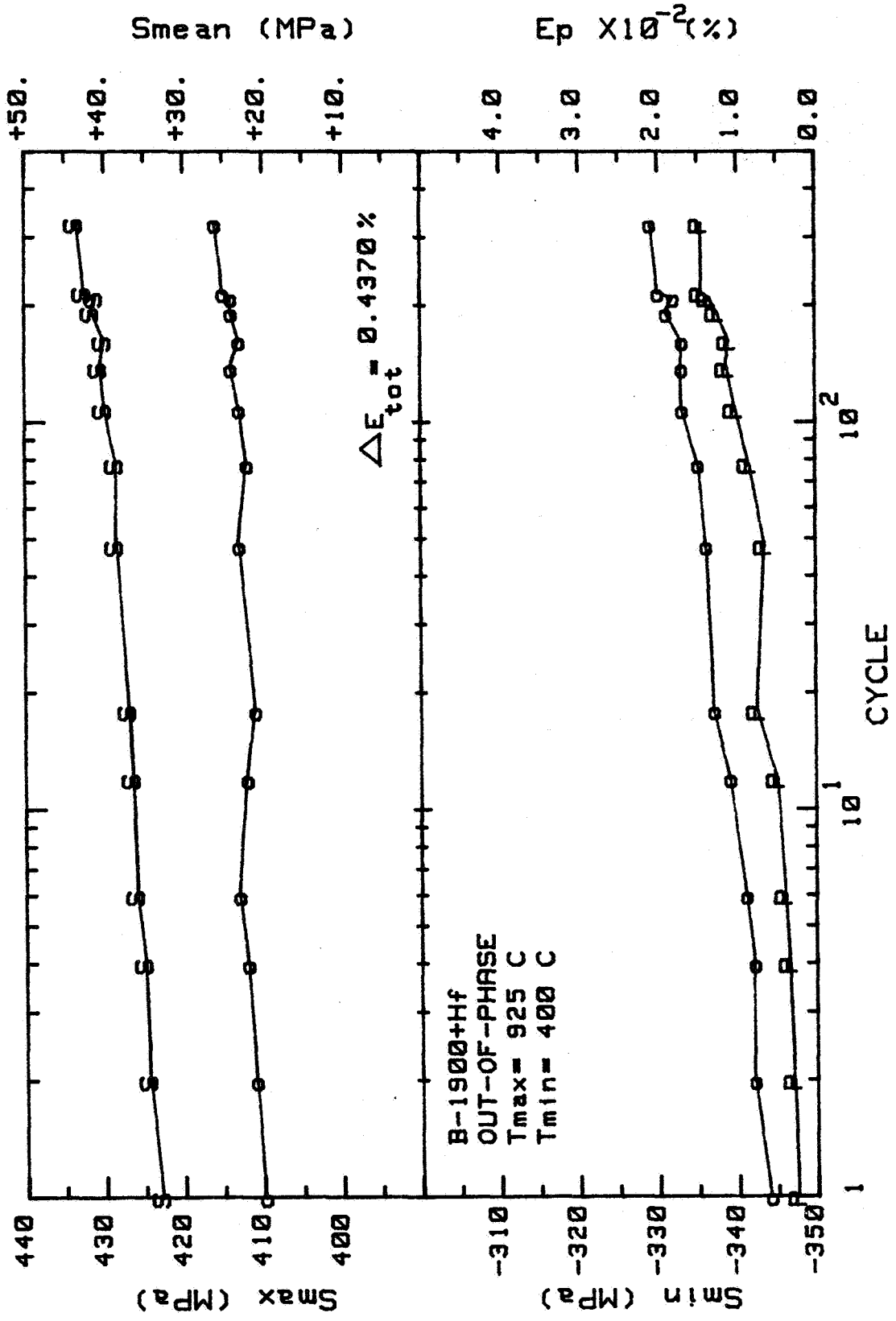
Smean (MPa)
Ep X10^{-2}(%)
+50.
+40.
+30.
+20.
+10.
4.0
3.0
2.0
1.0
0.0
ΔE_{tot} = 0.4370 %
B-1900+Hf
OUT-OF-PHASE
Tmax= 925 C
Tmin= 400 C
Smax (MPa)
Smin (MPa)
440
430
420
410
400
-310
-320
-330
-340
-350
1
10^1
10^2
CYCLE

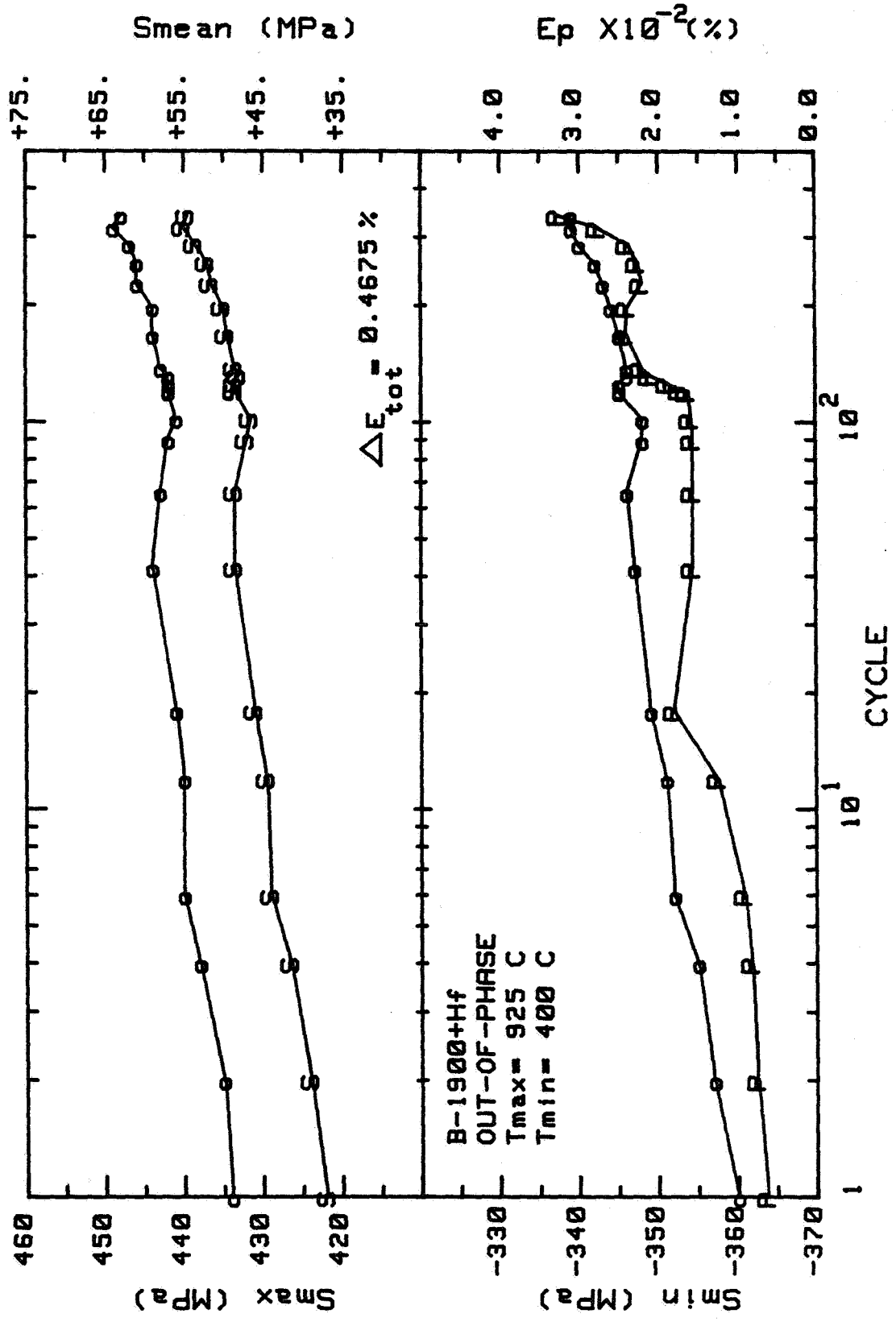
Smean (MPa)
Ep X10^{-2}(%)
+75.
+65.
+55.
+45.
+35.
4.0
3.0
2.0
1.0
0.0
ΔE_{tot} = 0.4675 %
B-1900+Hf
OUT-OF-PHASE
Tmax= 925 C
Tmin= 400 C
460
450
440
430
420
-330
-340
-350
-360
-370
Smax (MPa)
Smin (MPa)
1
10^1
10^2
CYCLE

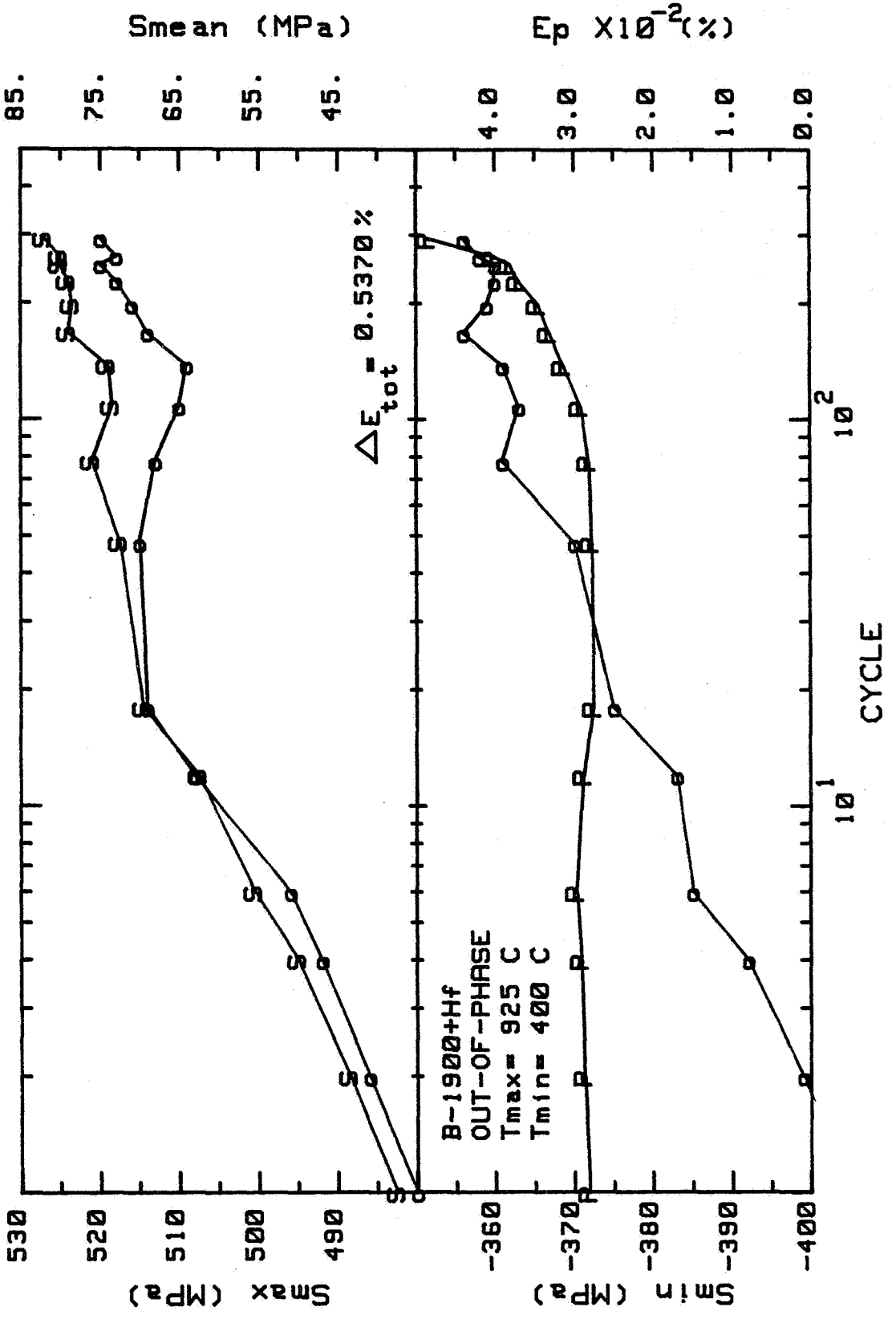
Smean (MPa)
Ep X10^{-2}(%)
85.
75.
65.
55.
45.
4.0
3.0
2.0
1.0
0.0
ΔE_{tot} = 0.5370 %
B-1900+Hf
OUT-OF-PHASE
Tmax= 925 C
Tmin= 400 C
530
520
510
500
490
-360
-370
-380
-390
-400
Smax (MPa)
Smin (MPa)
10^1
10^2
CYCLE

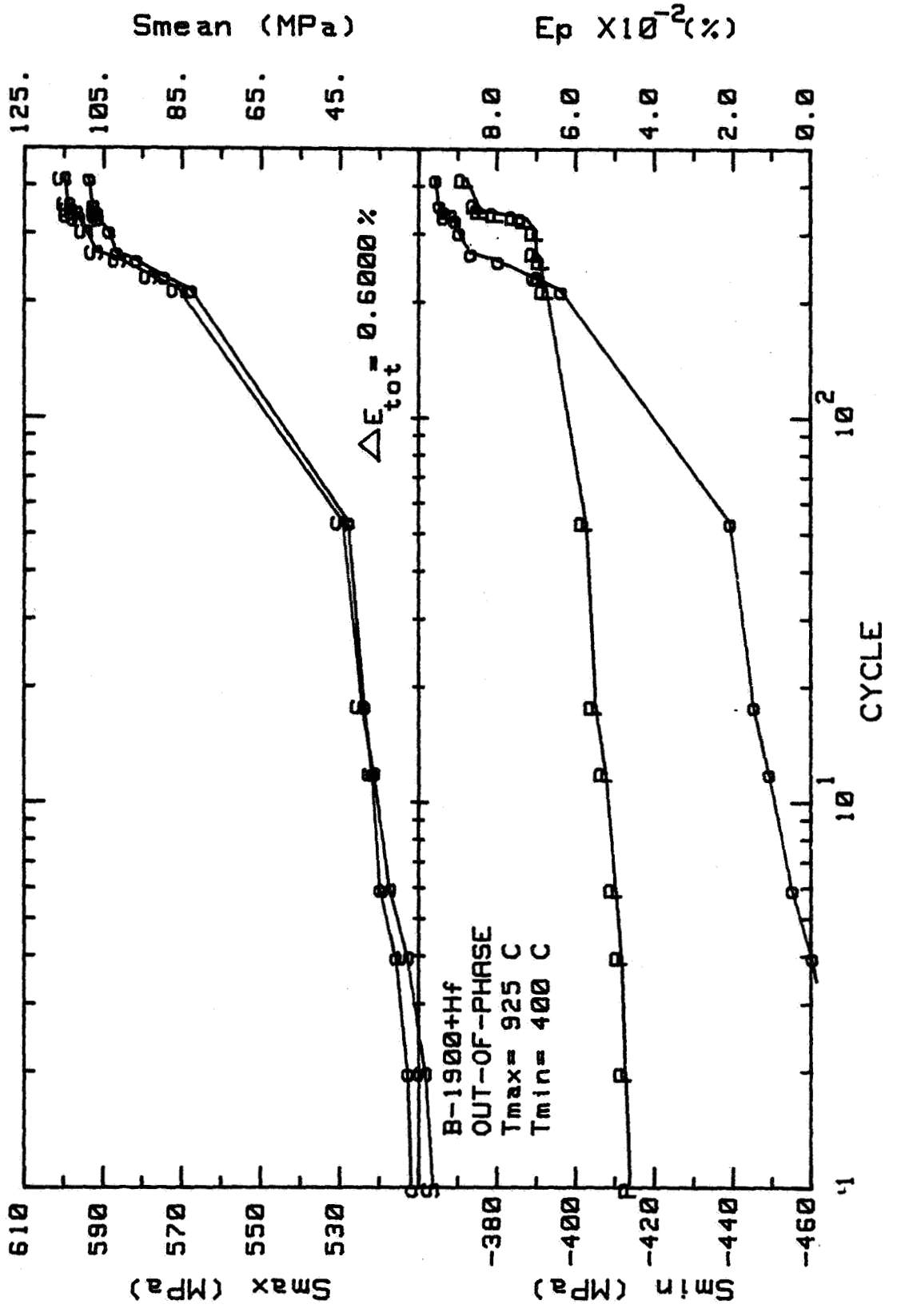
Smean (MPa)
Ep X10^{-2}(%)
125.
105.
85.
65.
45.
8.0
6.0
4.0
2.0
0.0
ΔE_{tot} = 0.6000 %
B-1900+Hf
OUT-OF-PHASE
Tmax= 925 C
Tmin= 400 C
610
590
570
550
530
-380
-400
-420
-440
-460
Smax (MPa)
Smin (MPa)
10^1
10^2
CYCLE

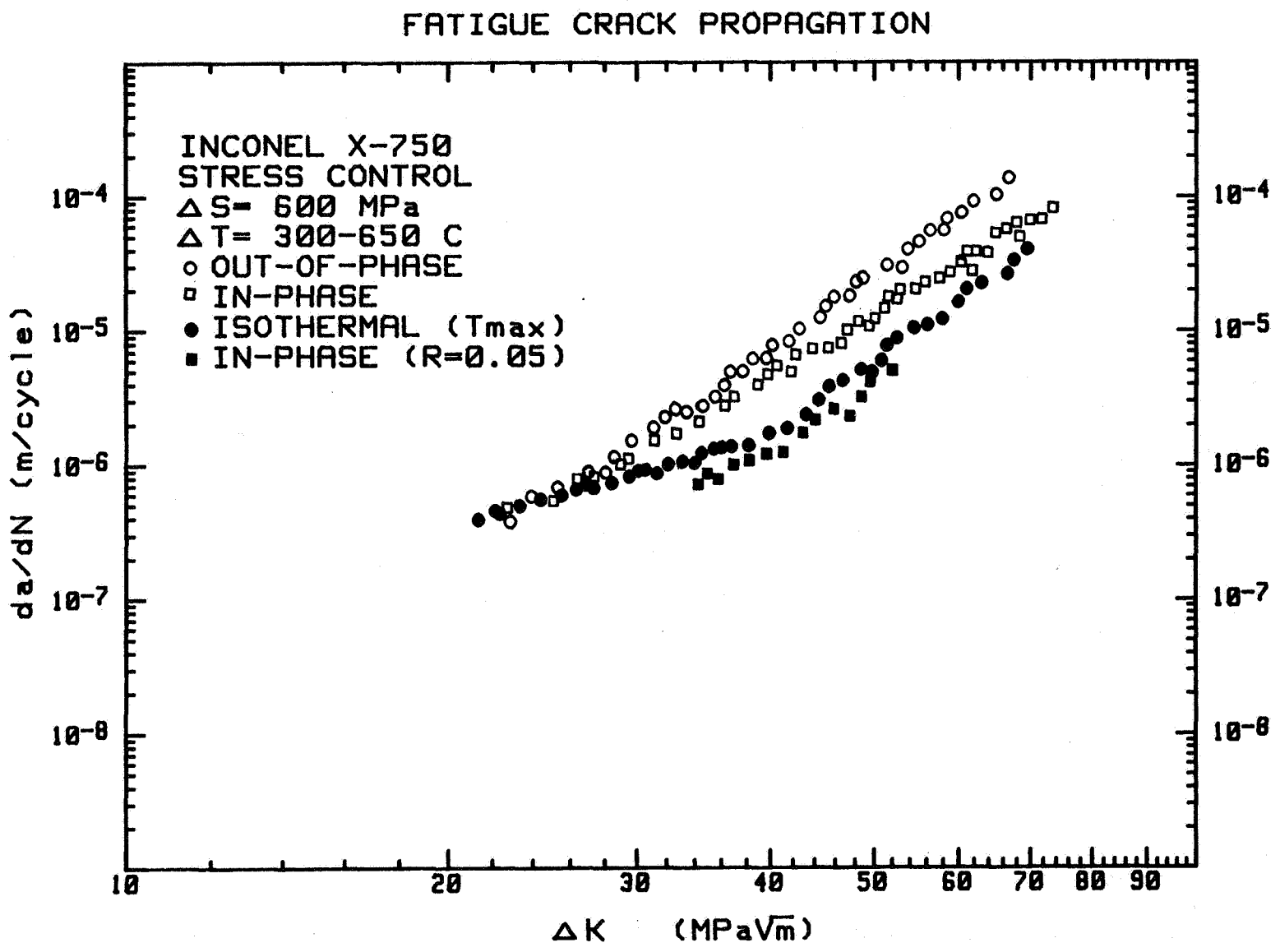
FATIGUE CRACK PROPAGATION
INCONEL X-750
STRESS CONTROL
△S= 600 MPa
△T= 300-650 C
○ OUT-OF-PHASE
□ IN-PHASE
● ISOTHERMAL (Tmax)
■ IN-PHASE (R=0.05)
da/dN (m/cycle)
10⁻⁴
10⁻⁵
10⁻⁶
10⁻⁷
10⁻⁸
10
20
30
40
50
60
70
80
90
△K (MPa√m)

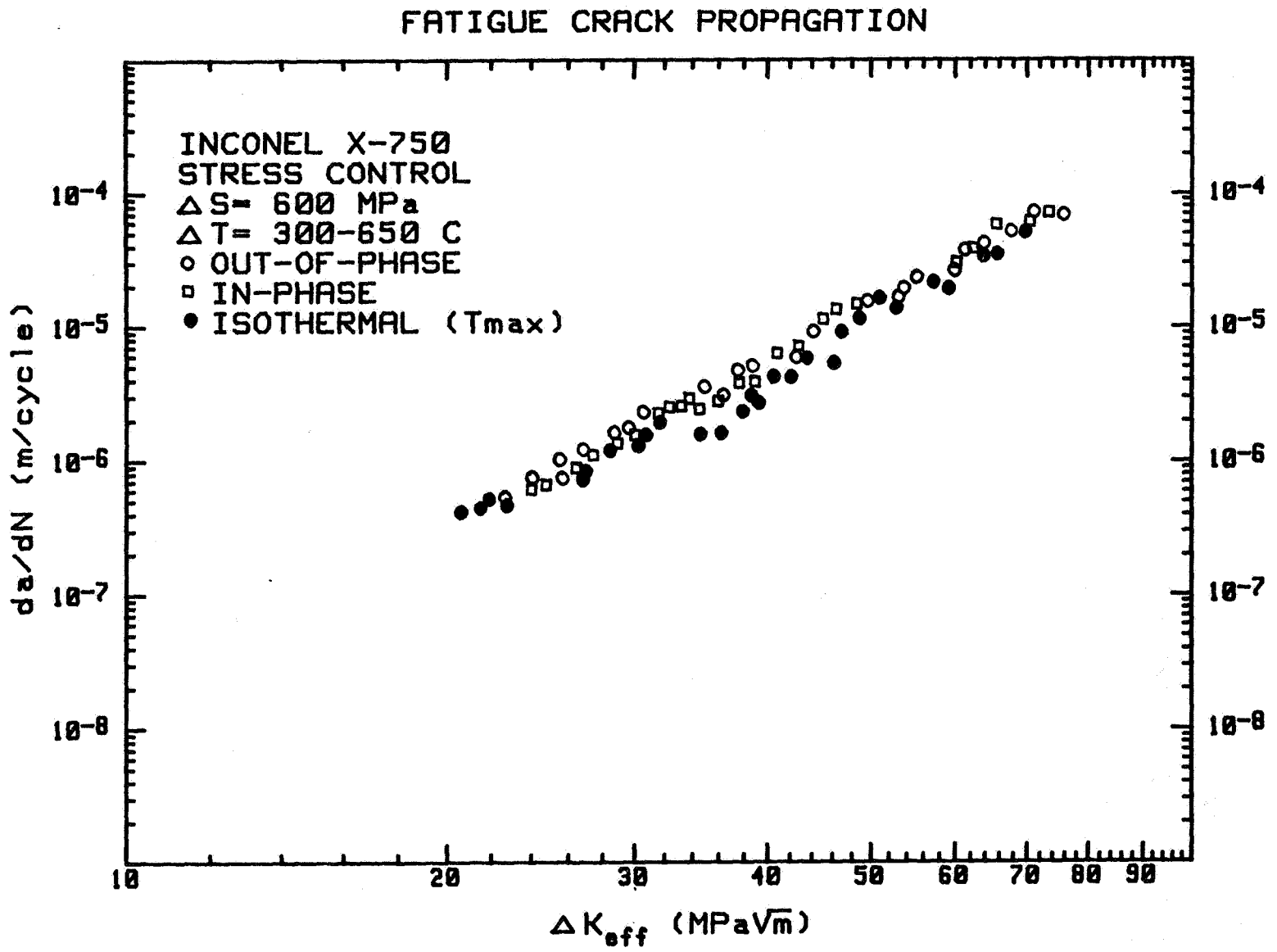
FATIGUE CRACK PROPAGATION
INCONEL X-750
STRESS CONTROL
△S= 600 MPa
△T= 300-650 C
○ OUT-OF-PHASE
□ IN-PHASE
● ISOTHERMAL (Tmax)
da/dN (m/cycle)
10-4
10-5
10-6
10-7
10-8
10
20
30
40
50
60
70
80
90
△K_eff (MPa√m)

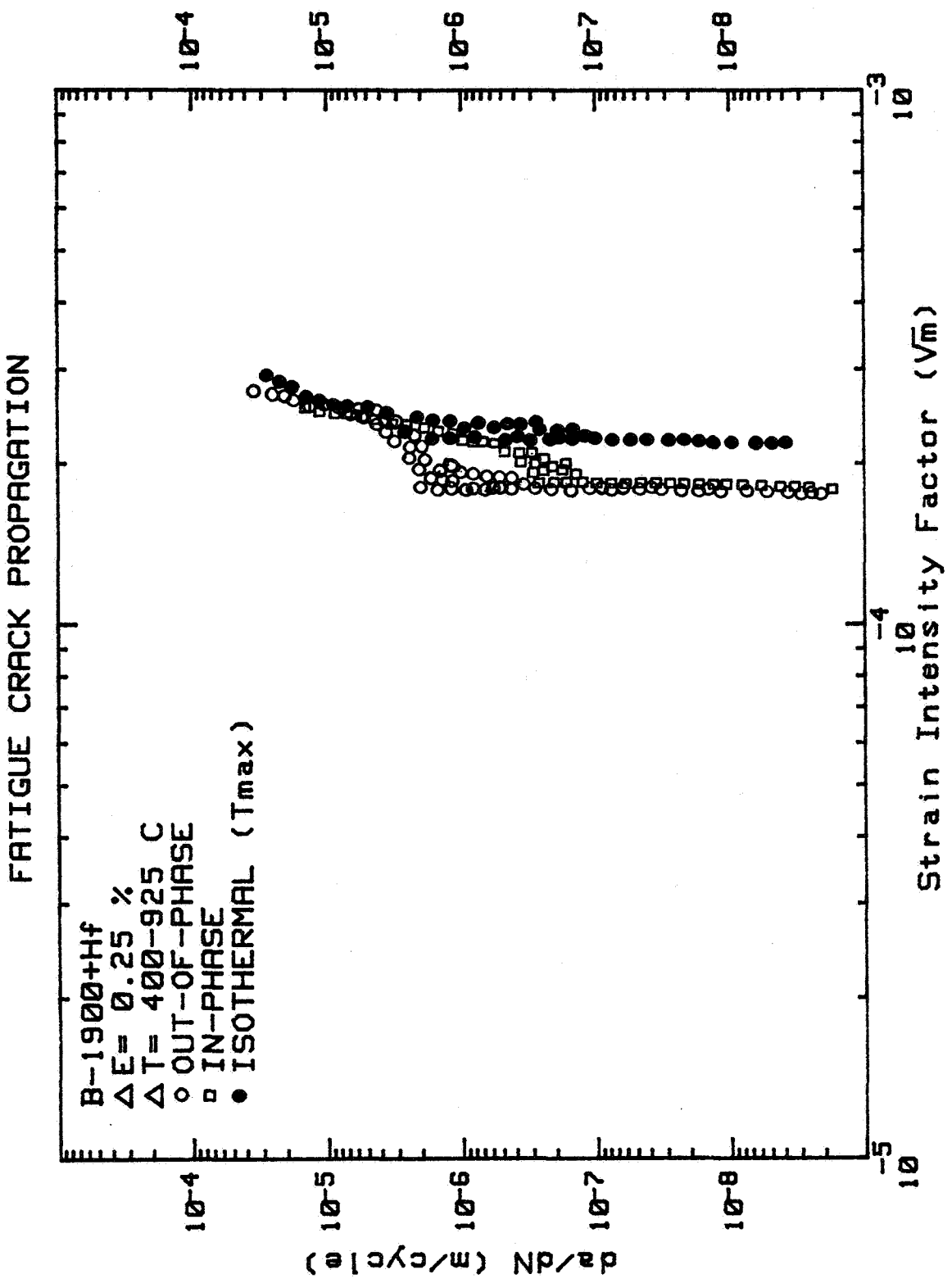
FATIGUE CRACK PROPAGATION
B-1900+Hf
ΔE= 0.25 %
ΔT= 400-925 C
o OUT-OF-PHASE
□ IN-PHASE
● ISOTHERMAL (Tmax)
da/dN (m/cycle)
Strain Intensity Factor (√m)
10-4
10-5
10-6
10-7
10-8
10-3
10-4
10-5

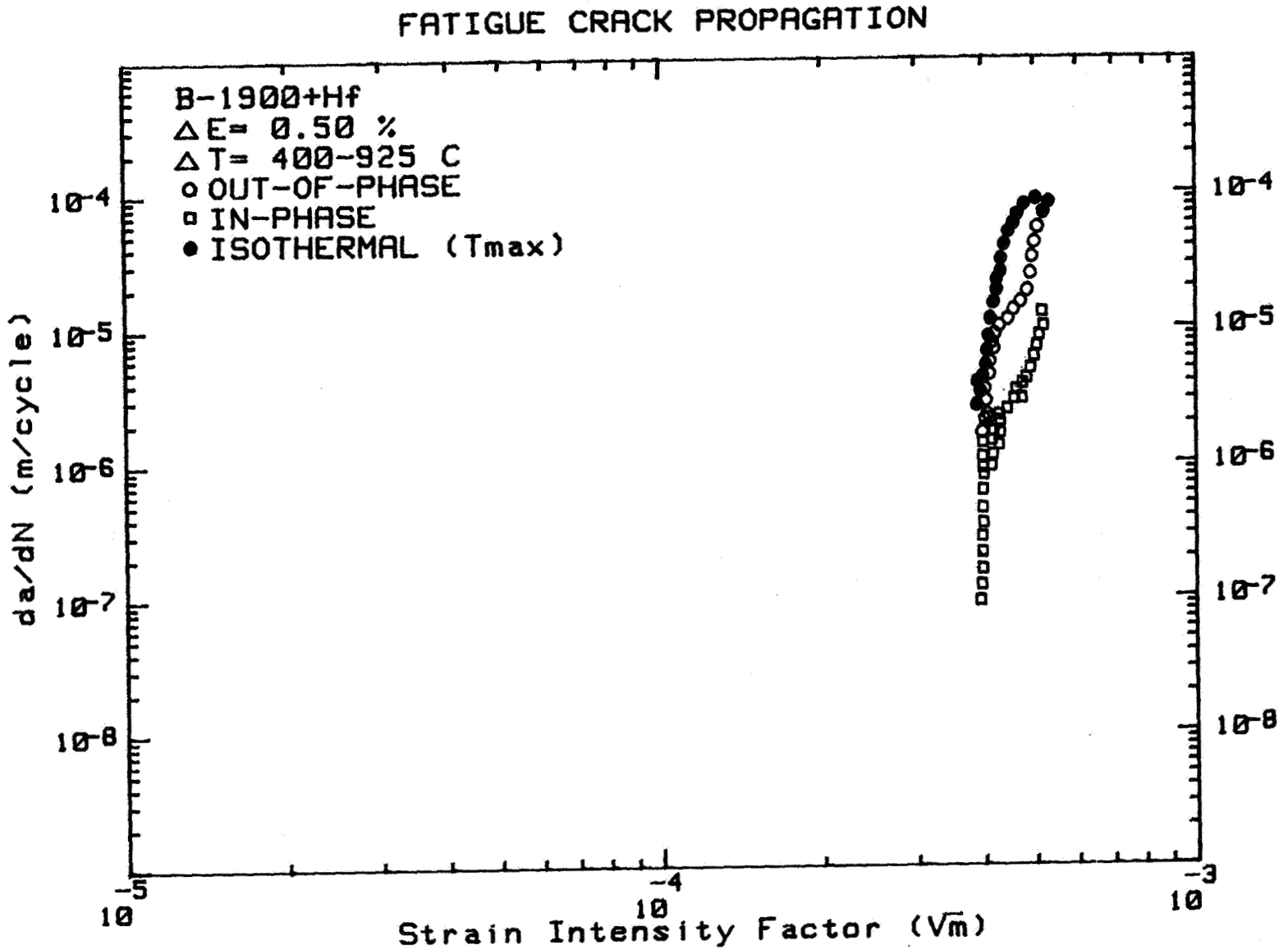
FATIGUE CRACK PROPAGATION
B-1900+Hf
ΔE= 0.50 %
ΔT= 400-925 C
o OUT-OF-PHASE
▫ IN-PHASE
● ISOTHERMAL (Tmax)
da/dN (m/cycle)
10-4
10-5
10-6
10-7
10-8
10-5
10-4
10-3
Strain Intensity Factor (√m)

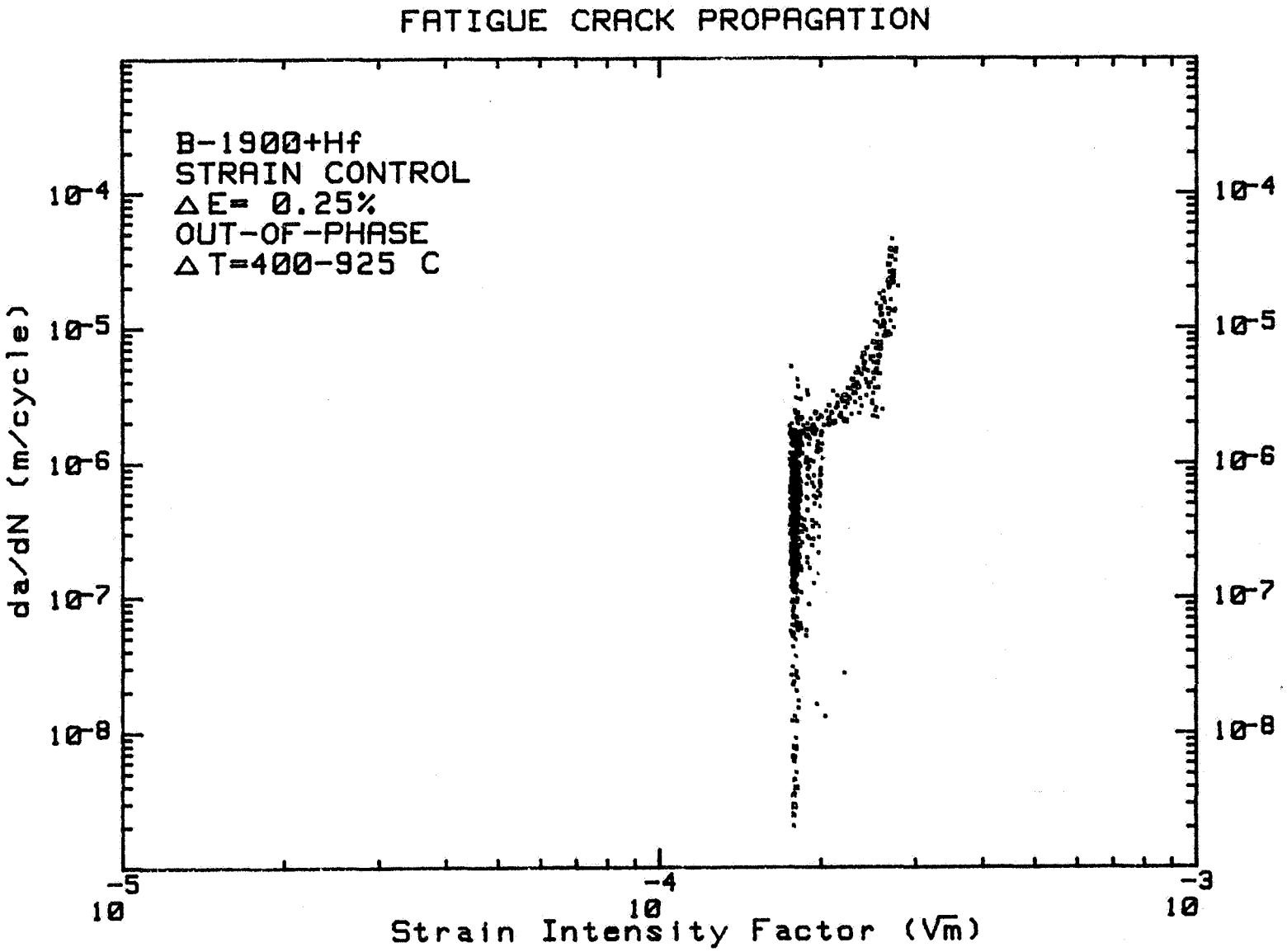
FATIGUE CRACK PROPAGATION
B-1900+Hf
STRAIN CONTROL
ΔE= 0.25%
OUT-OF-PHASE
ΔT=400-925 C
da/dN (m/cycle)
10-4
10-5
10-6
10-7
10-8
10-5
10-4
10-3
Strain Intensity Factor (√m)

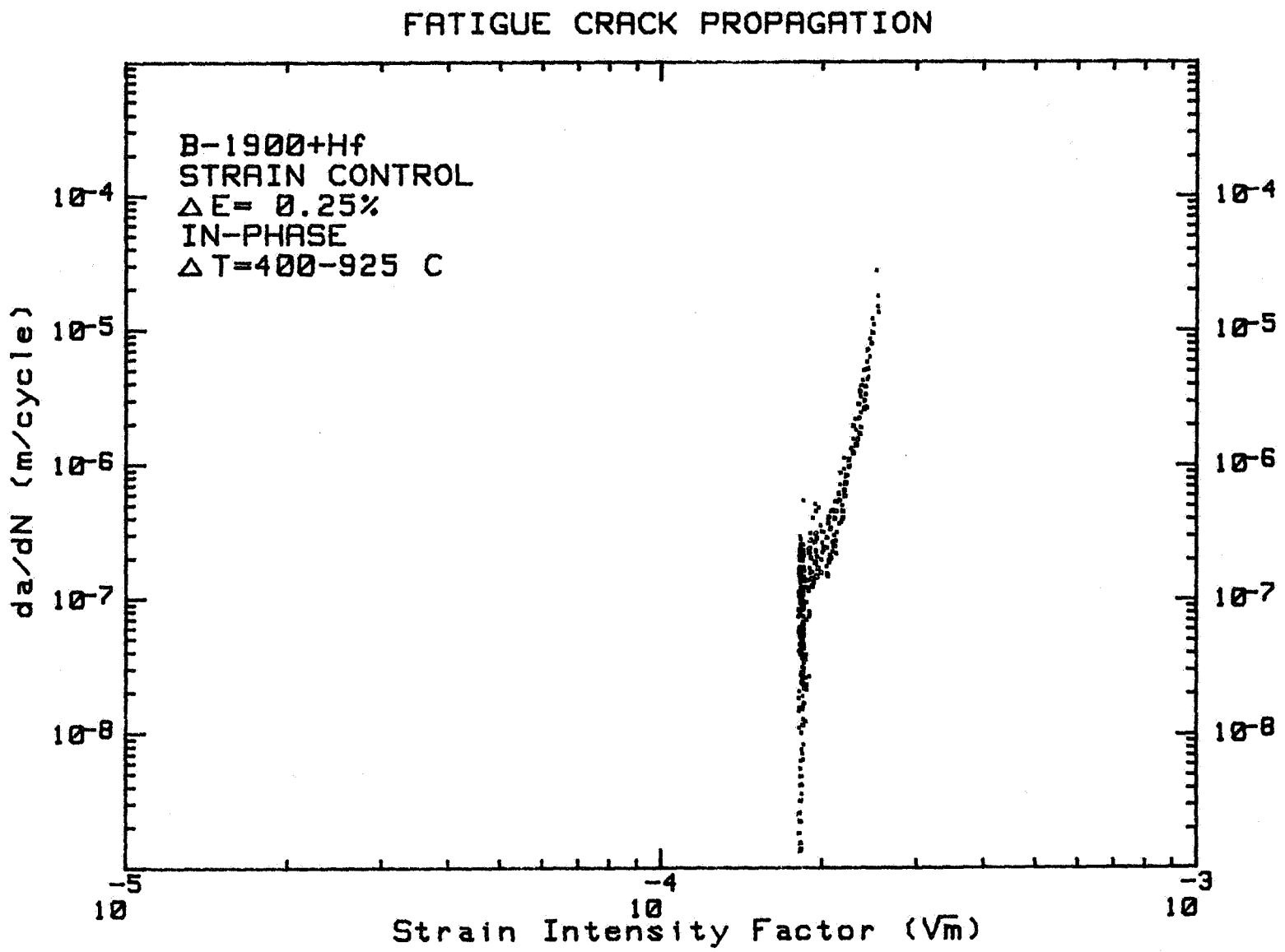
FATIGUE CRACK PROPAGATION
B-1900+Hf
STRAIN CONTROL
ΔE= 0.25%
IN-PHASE
ΔT=400-925 C
da/dN (m/cycle)
10-4
10-5
10-6
10-7
10-8
10-5
10-4
10-3
Strain Intensity Factor (√m)

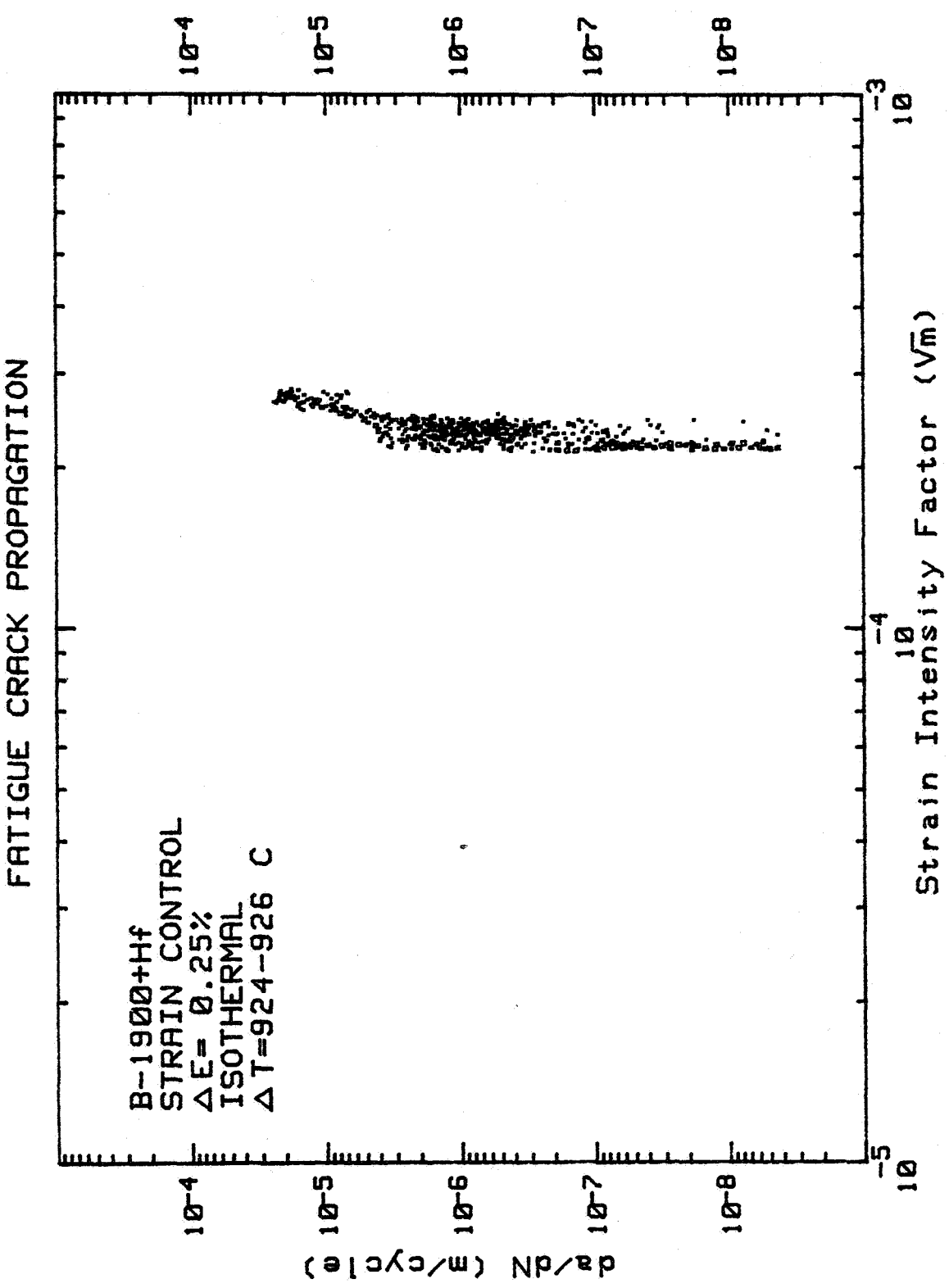
FATIGUE CRACK PROPAGATION
B-1900+Hf
STRAIN CONTROL
ΔE= 0.25%
ISOTHERMAL
ΔT=924-926 C
da/dN (m/cycle)
Strain Intensity Factor (√m)
10-4
10-5
10-6
10-7
10-8
10-3
10-4
10-5

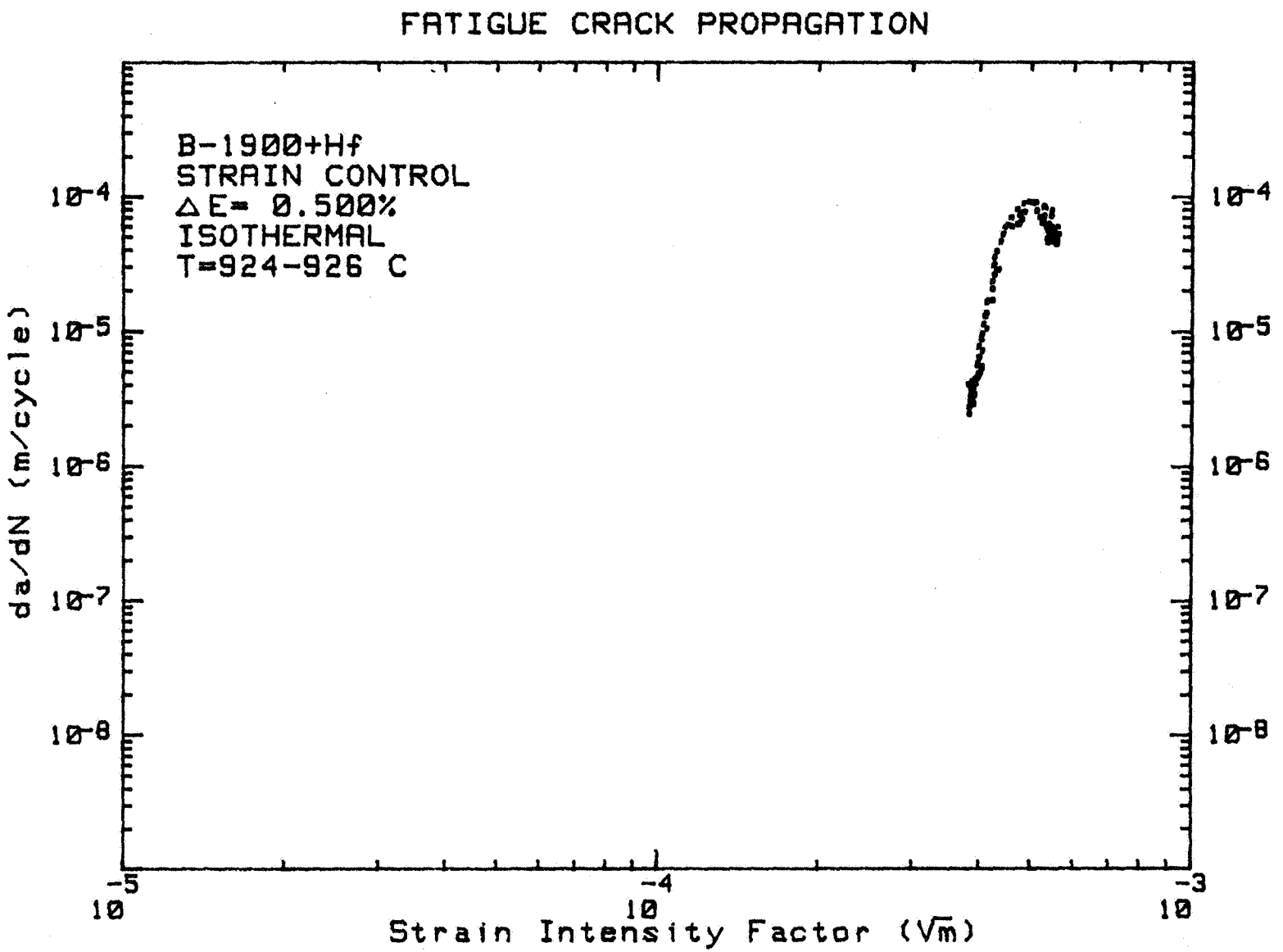
FATIGUE CRACK PROPAGATION
B-1900+Hf
STRAIN CONTROL
ΔE= 0.500%
ISOTHERMAL
T=924-926 C
da/dN (m/cycle)
10-4
10-5
10-6
10-7
10-8
10-5
10-4
10-3
Strain Intensity Factor (√m)

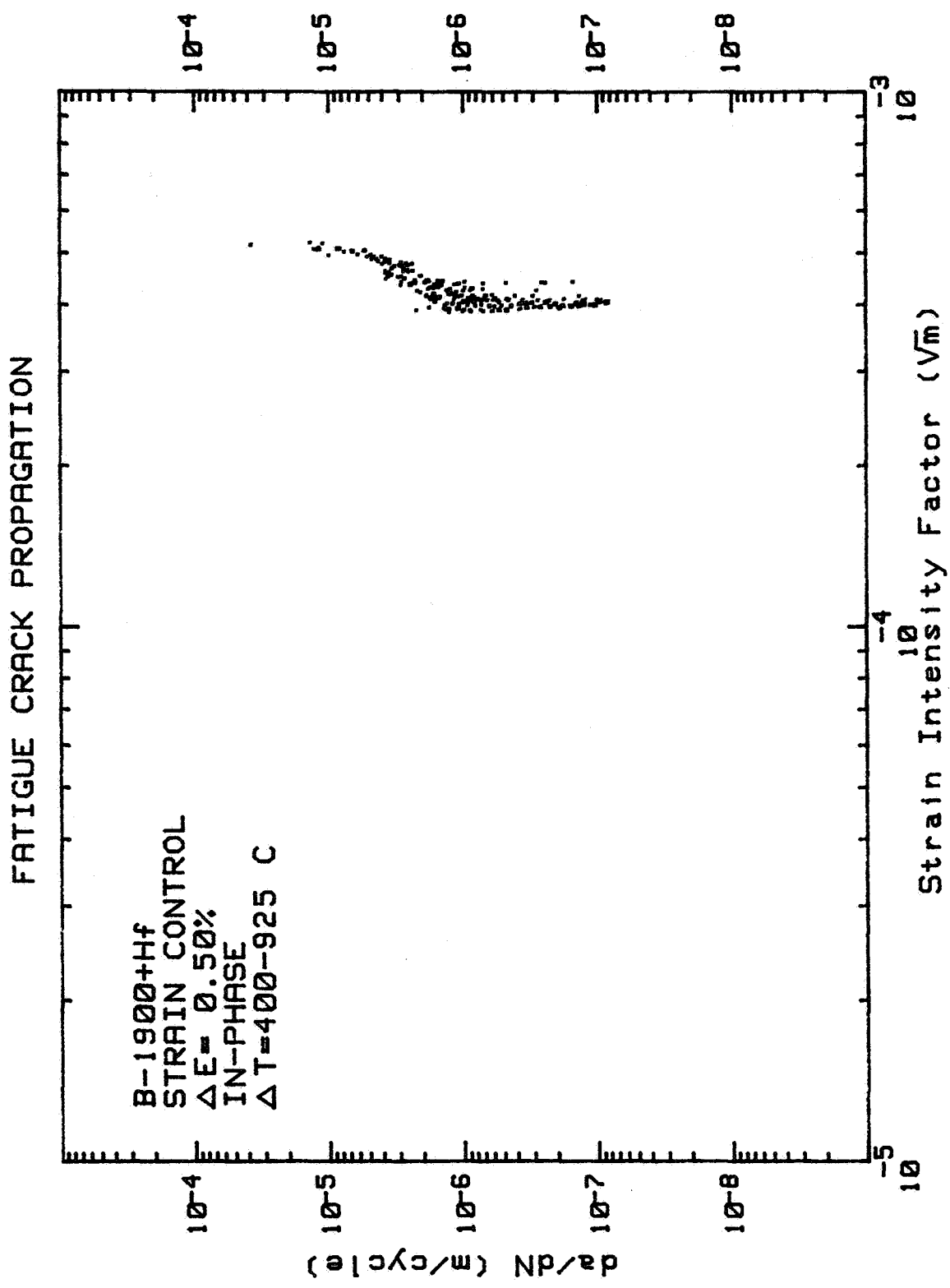
FATIGUE CRACK PROPAGATION
B-1900+Hf
STRAIN CONTROL
ΔE= 0.50%
IN-PHASE
ΔT=400-925 C
da/dN (m/cycle)
Strain Intensity Factor (√m)
10-4
10-5
10-6
10-7
10-8
10-3
10-4
10-5

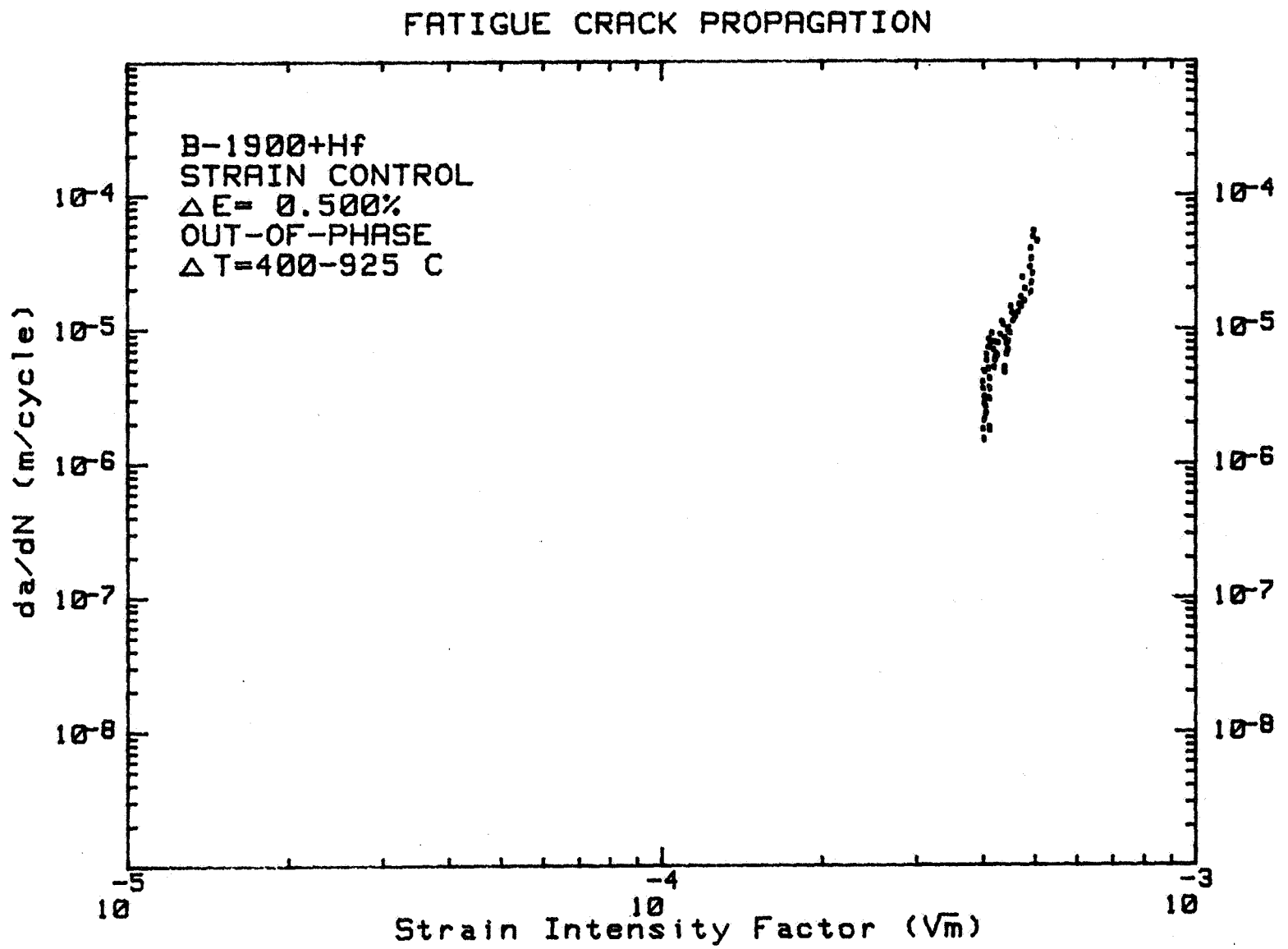
FATIGUE CRACK PROPAGATION
B-1900+Hf
STRAIN CONTROL
ΔE= 0.500%
OUT-OF-PHASE
ΔT=400-925 C
da/dN (m/cycle)
10-4
10-5
10-6
10-7
10-8
10-5
10-4
10-3
Strain Intensity Factor (√m)

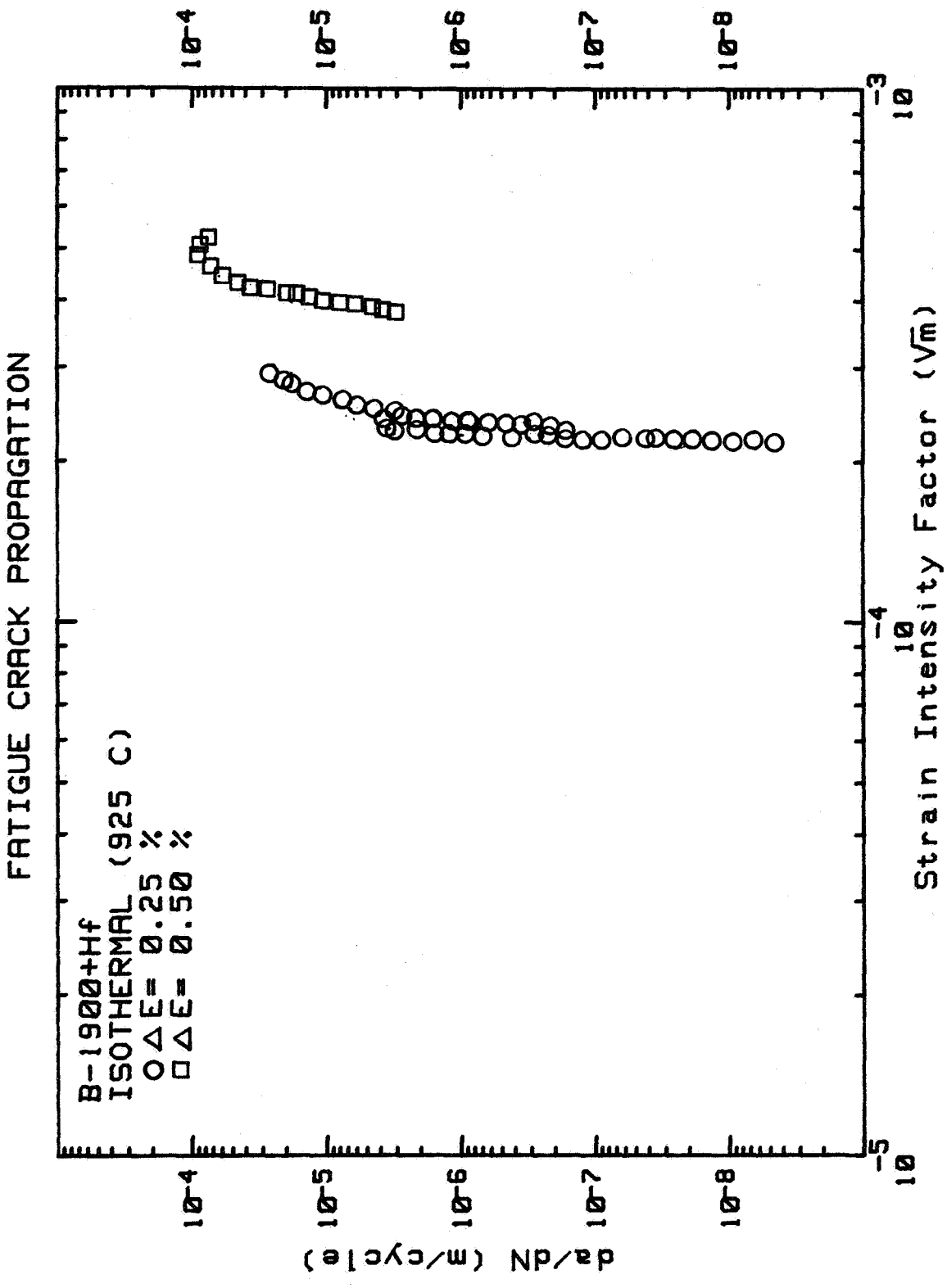
FATIGUE CRACK PROPAGATION
B-1900+Hf
ISOTHERMAL (925 C)
O△E= 0.25 %
□△E= 0.50 %
da/dN (m/cycle)
Strain Intensity Factor (√m)
10-4
10-5
10-6
10-7
10-8
10-3
10-4
10-5

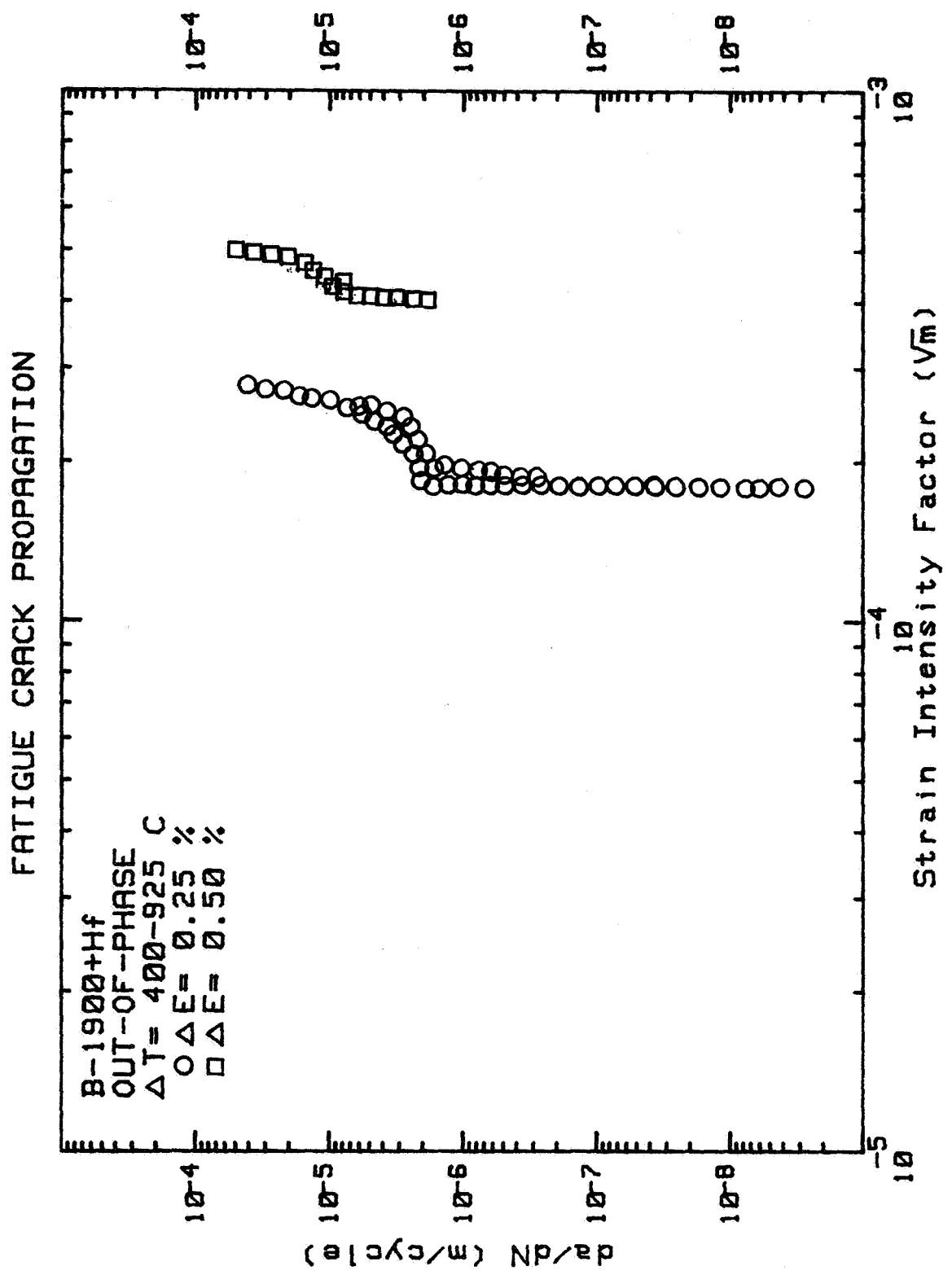
FATIGUE CRACK PROPAGATION
B-1900+Hf
OUT-OF-PHASE
ΔT= 400-925 C
○ Δε= 0.25 %
□ Δε= 0.50 %
da/dN (m/cycle)
Strain Intensity Factor (√m)
10-4
10-5
10-6
10-7
10-8
10-3
10-4
10-5

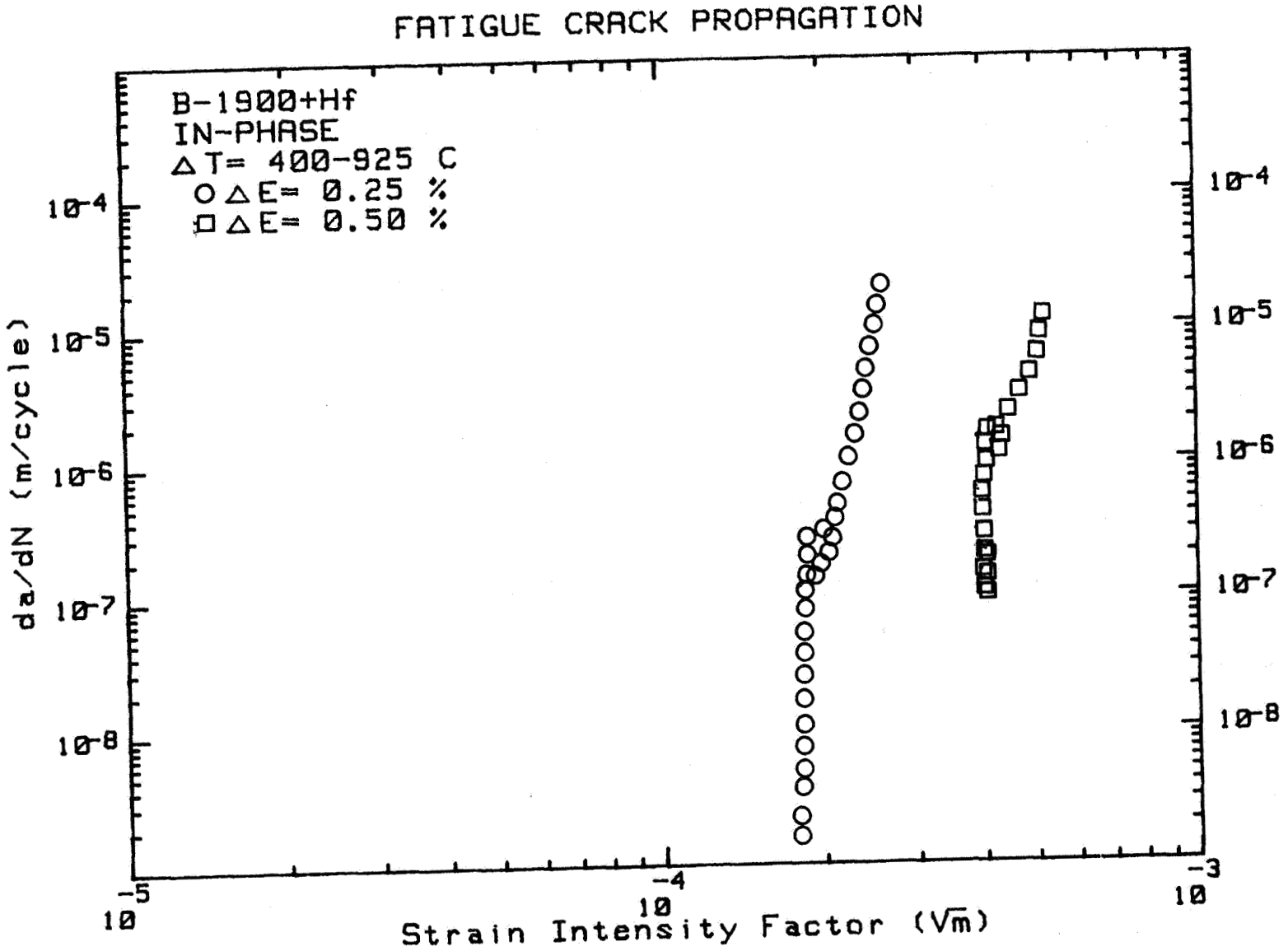
FATIGUE CRACK PROPAGATION
B-1900+Hf
IN-PHASE
ΔT= 400-925 C
O ΔE= 0.25 %
□ ΔE= 0.50 %
da/dN (m/cycle)
10-4
10-5
10-6
10-7
10-8
10-5
10-4
10-3
Strain Intensity Factor (√m)

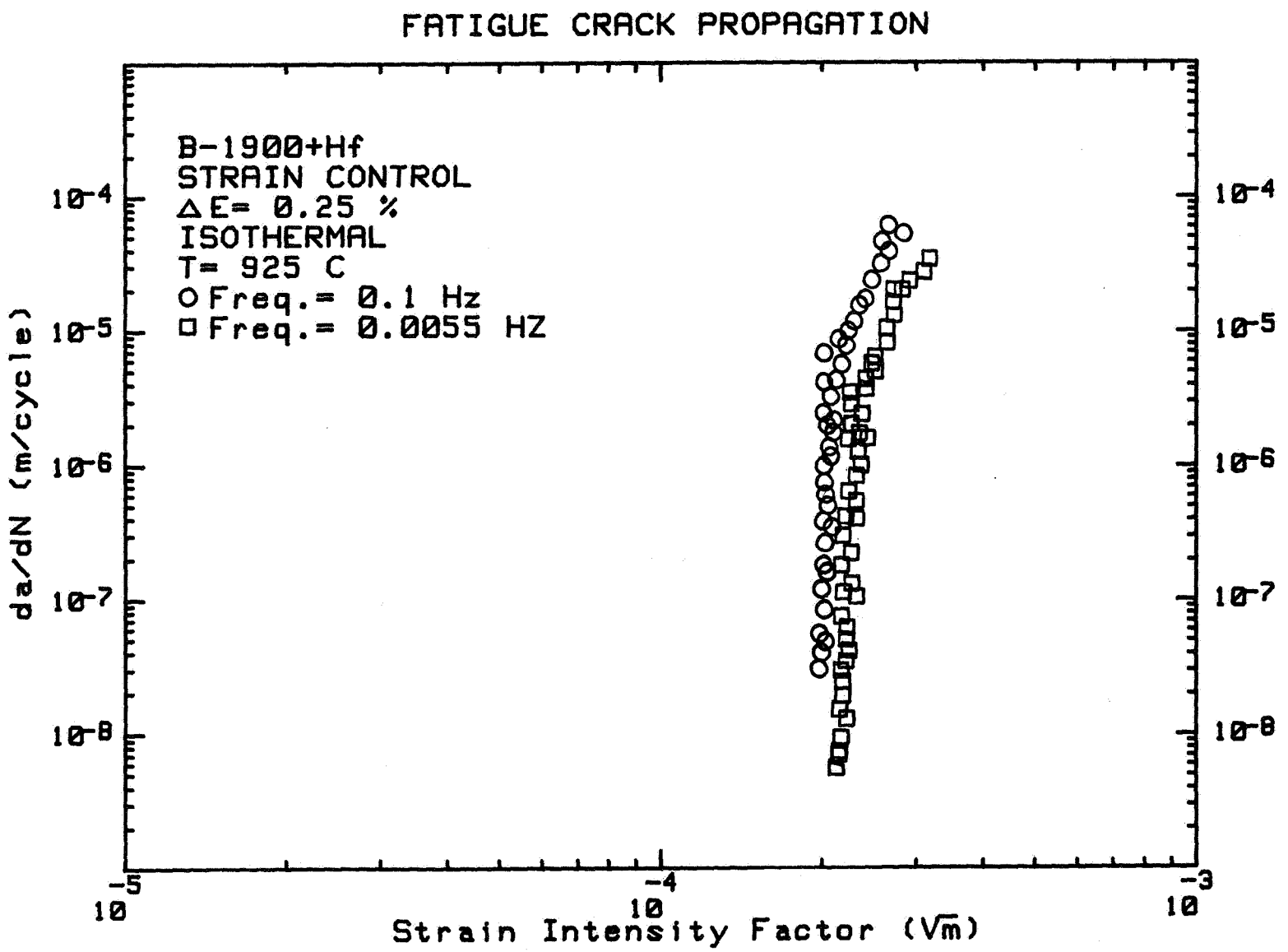
FATIGUE CRACK PROPAGATION
B-1900+Hf
STRAIN CONTROL
ΔE= 0.25 %
ISOTHERMAL
T= 925 C
○ Freq.= 0.1 Hz
□ Freq.= 0.0055 HZ
da/dN (m/cycle)
10-4
10-5
10-6
10-7
10-8
10-5
10-4
10-3
Strain Intensity Factor (√m)

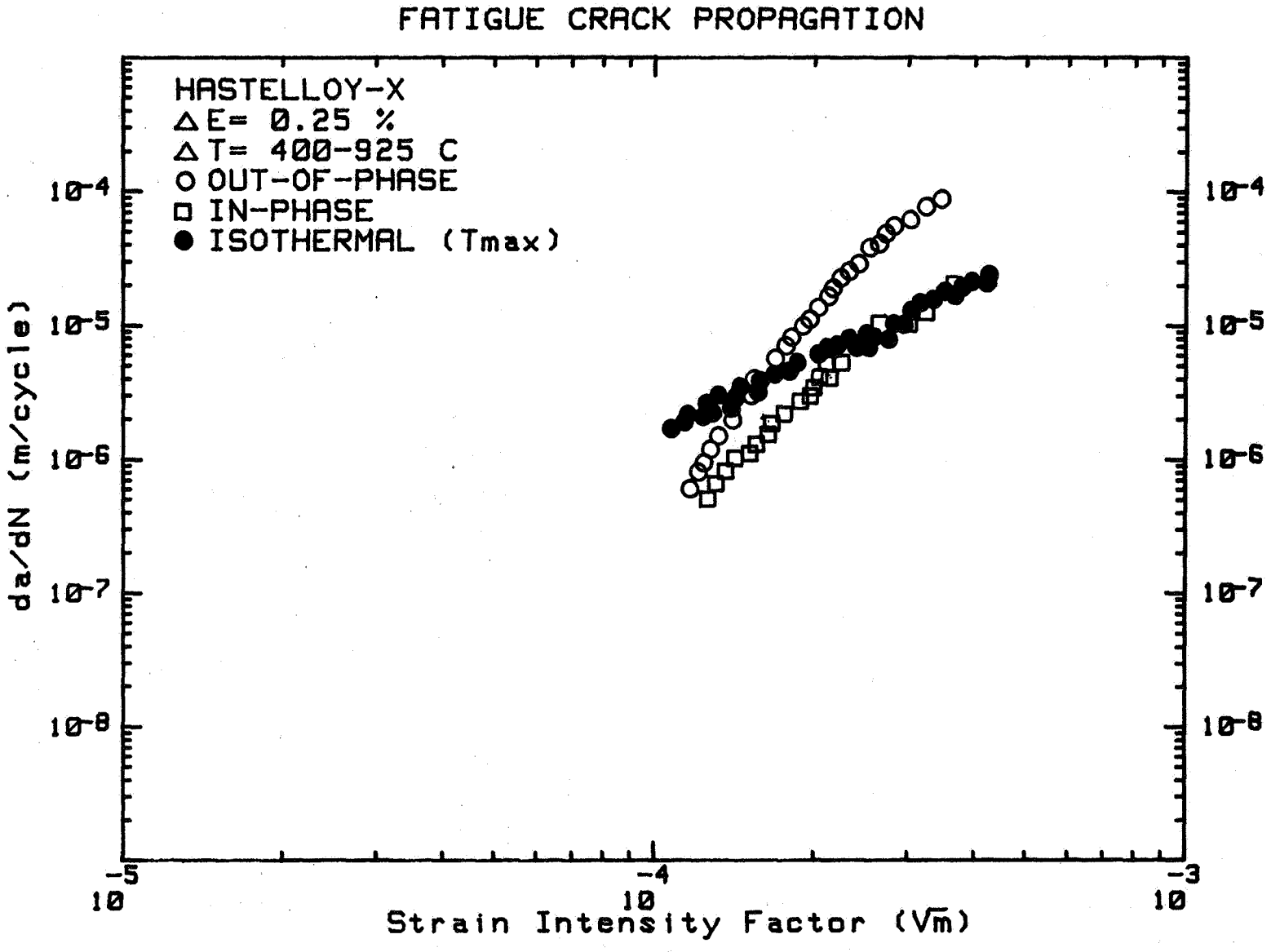
FATIGUE CRACK PROPAGATION
HASTELLOY-X
△ E= 0.25 %
△ T= 400-925 C
○ OUT-OF-PHASE
□ IN-PHASE
● ISOTHERMAL (Tmax)
da/dN (m/cycle)
10-4
10-5
10-6
10-7
10-8
10-5
10-4
10-3
Strain Intensity Factor (√m)

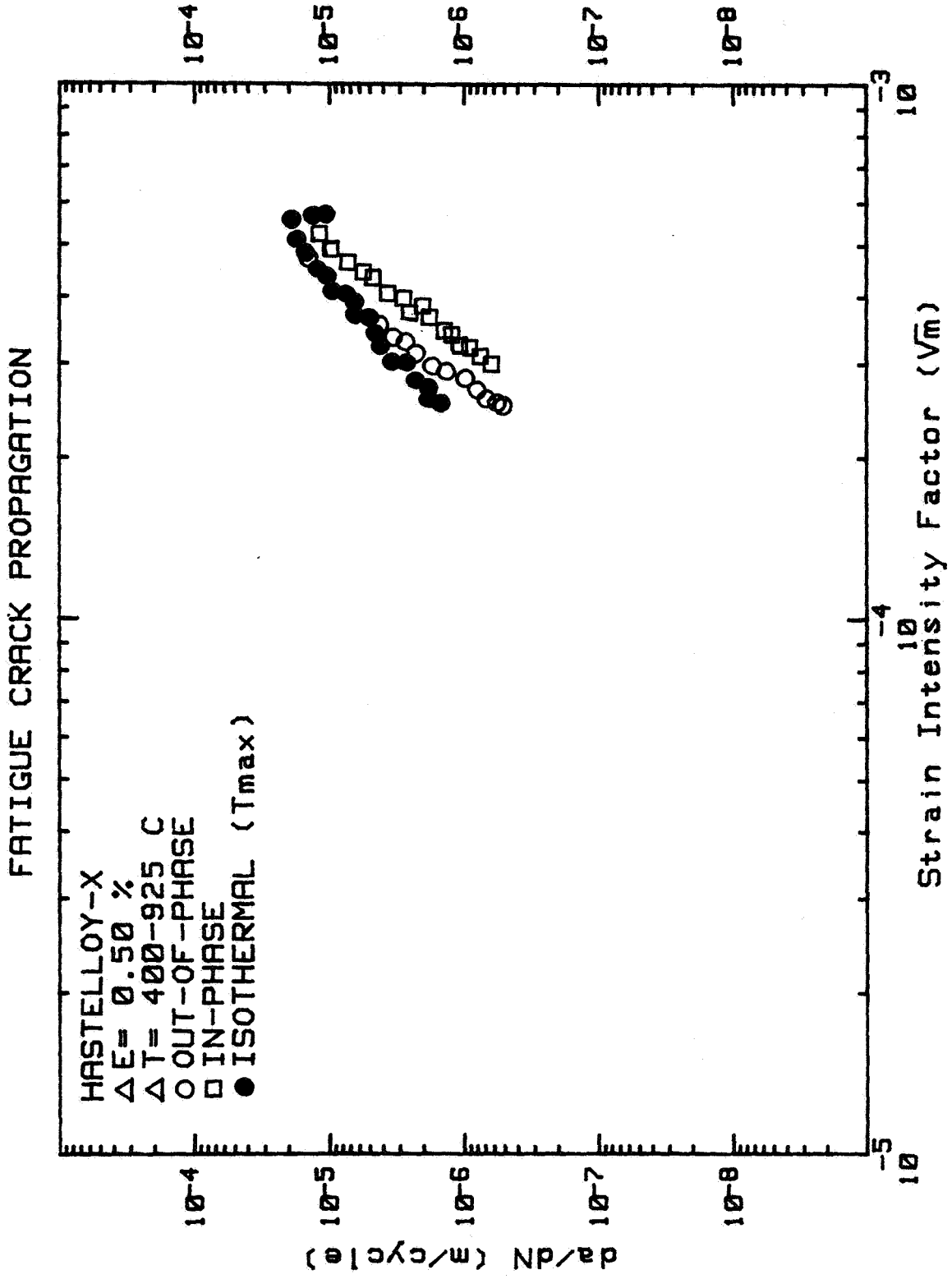
FATIGUE CRACK PROPAGATION
HASTELLOY-X
ΔE= 0.50 %
ΔT= 400-925 C
○ OUT-OF-PHASE
□ IN-PHASE
● ISOTHERMAL (Tmax)
da/dN (m/cycle)
Strain Intensity Factor (√m)
10-4
10-5
10-6
10-7
10-8
10-3
10-4
10-5

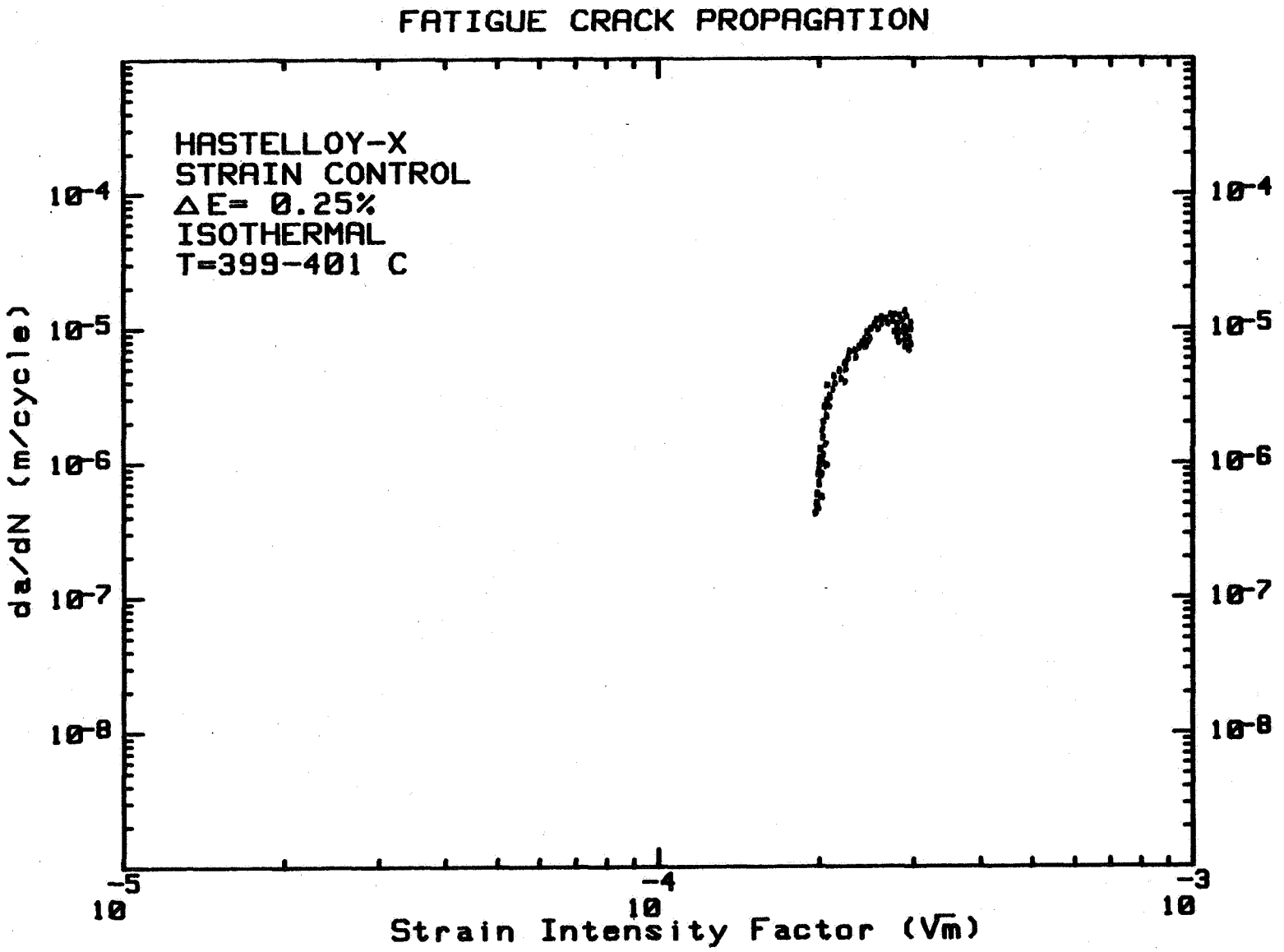
FATIGUE CRACK PROPAGATION
HASTELLOY-X
STRAIN CONTROL
ΔE= 0.25%
ISOTHERMAL
T=399-401 C
da/dN (m/cycle)
10-4
10-5
10-6
10-7
10-8
10-5
10-4
10-3
Strain Intensity Factor (√m)

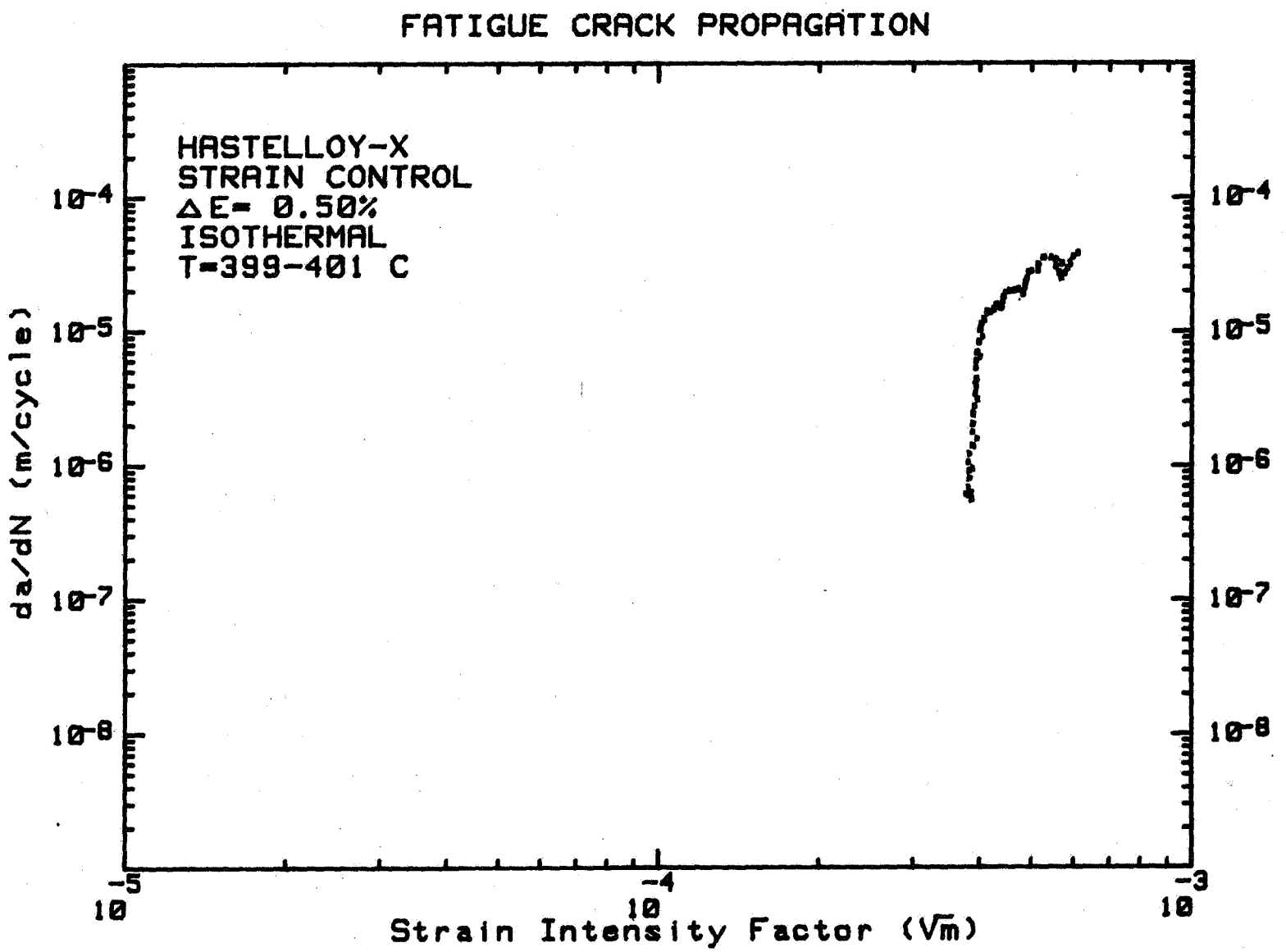
FATIGUE CRACK PROPAGATION
HASTELLOY-X
STRAIN CONTROL
ΔE= 0.50%
ISOTHERMAL
T=399-401 C
da/dN (m/cycle)
10-4
10-5
10-6
10-7
10-8
10-5
10-4
10-3
Strain Intensity Factor (√m)

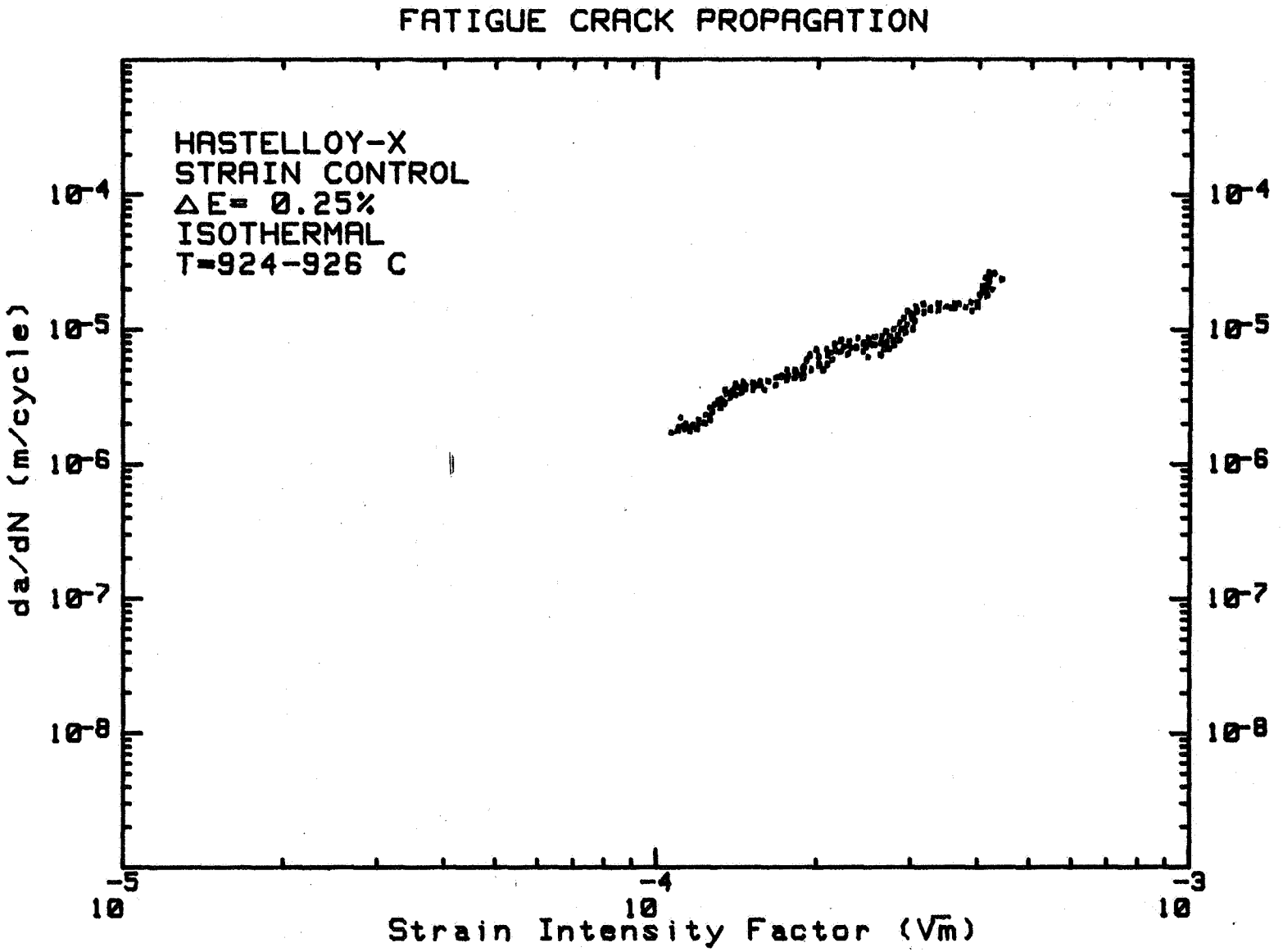
FATIGUE CRACK PROPAGATION
HASTELLOY-X
STRAIN CONTROL
ΔE= 0.25%
ISOTHERMAL
T=924-926 C
da/dN (m/cycle)
10-4
10-5
10-6
10-7
10-8
10-5
10-4
10-3
Strain Intensity Factor (√m)

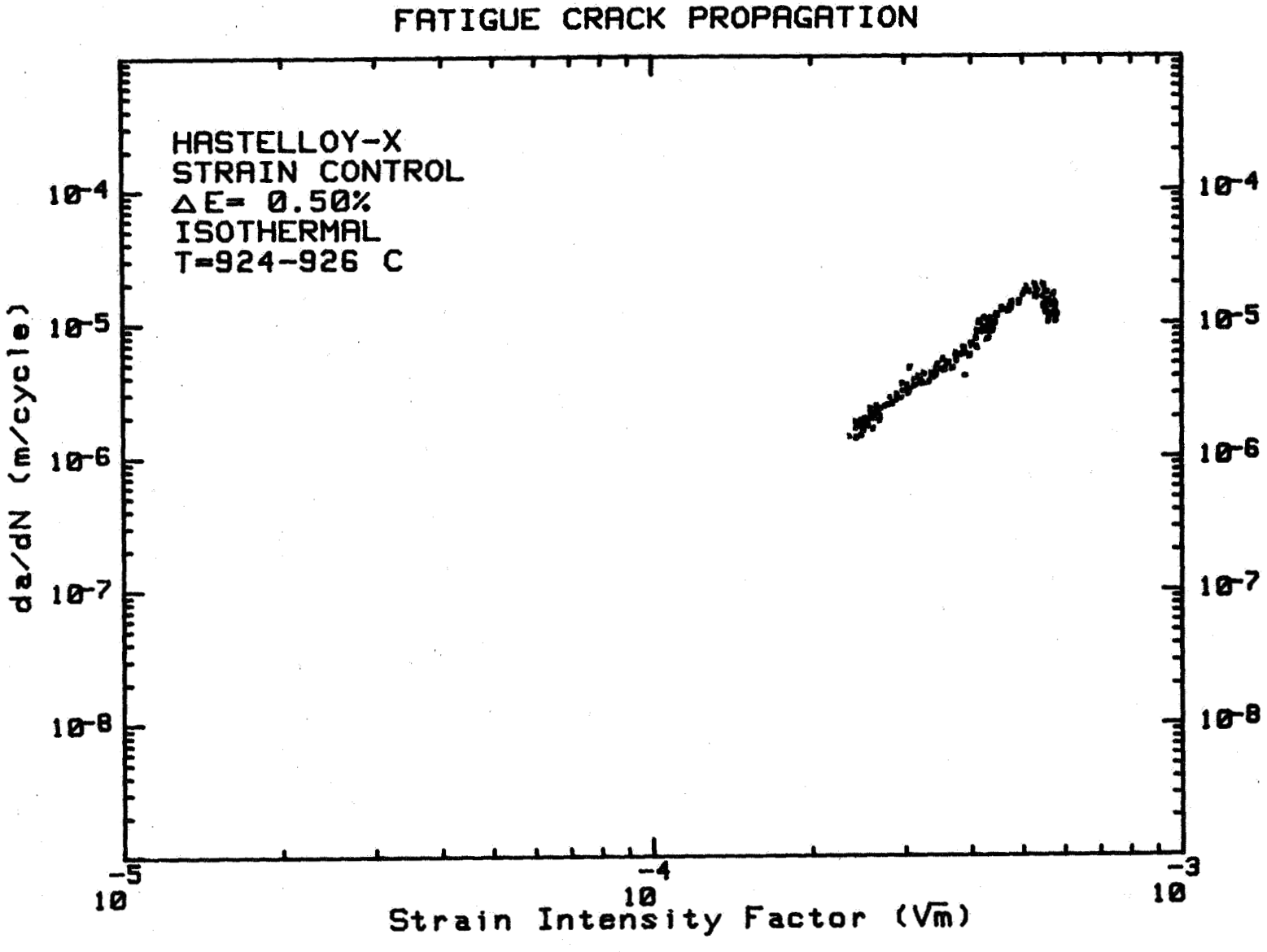
FATIGUE CRACK PROPAGATION
HASTELLOY-X
STRAIN CONTROL
ΔE= 0.50%
ISOTHERMAL
T=924-926 C
da/dN (m/cycle)
10-4
10-5
10-6
10-7
10-8
10-5
10-4
10-3
Strain Intensity Factor (√m)

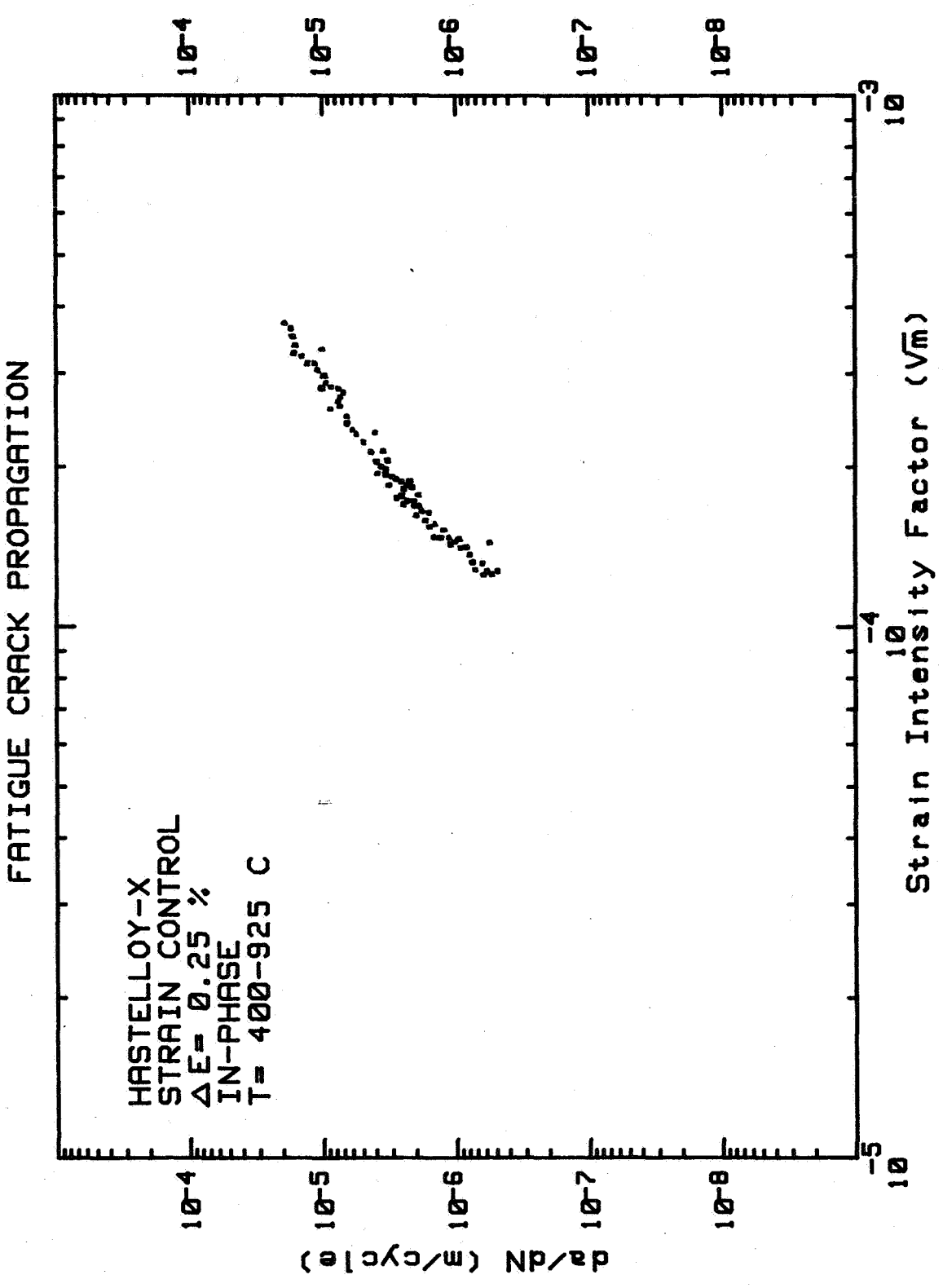
FATIGUE CRACK PROPAGATION
HASTELLOY-X
STRAIN CONTROL
ΔE= 0.25 %
IN-PHASE
T= 400-925 C
da/dN (m/cycle)
Strain Intensity Factor (√m)
10-4
10-5
10-6
10-7
10-8
10-3
10-4
10-5

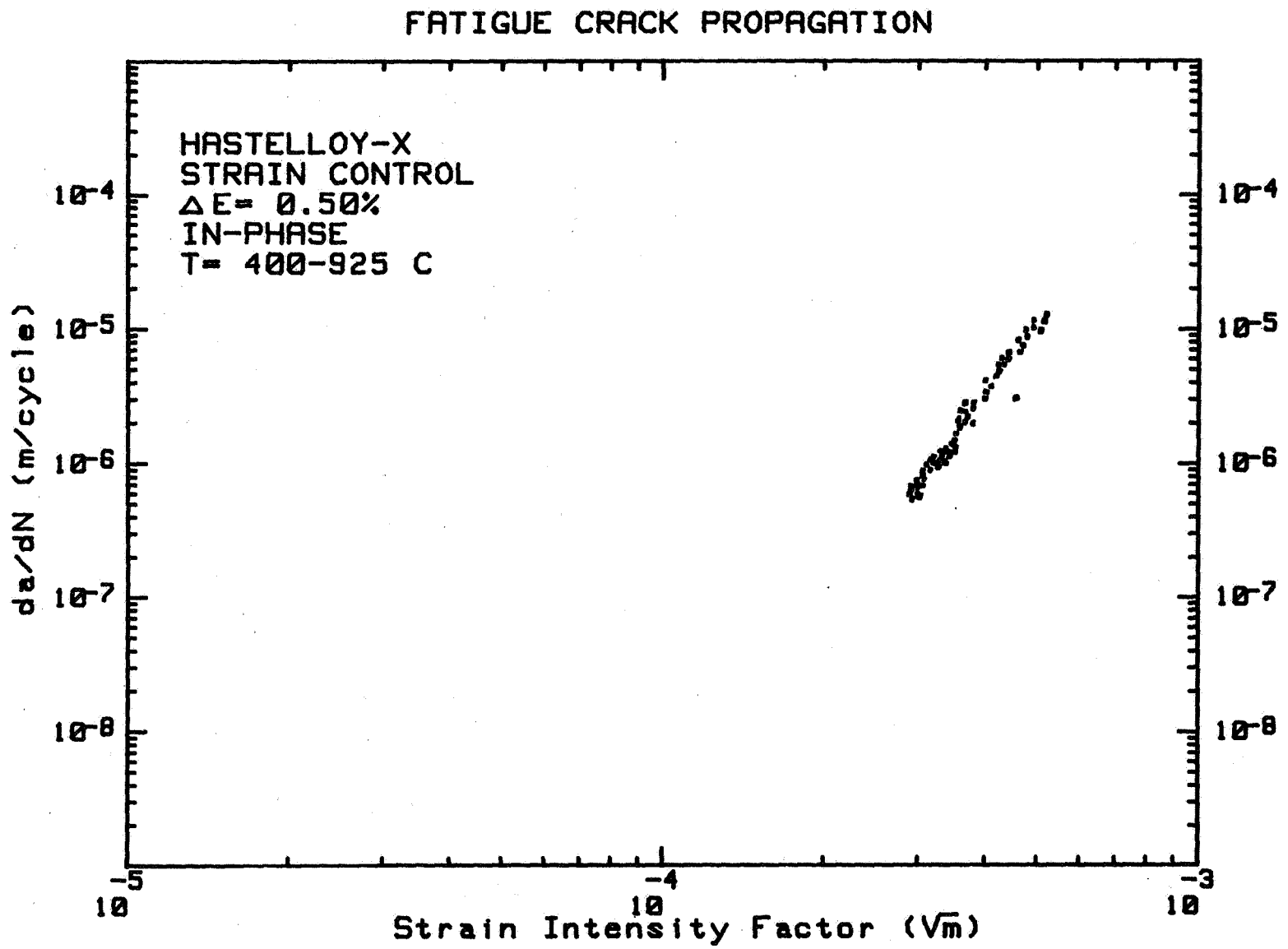
FATIGUE CRACK PROPAGATION
HASTELLOY-X
STRAIN CONTROL
ΔE= 0.50%
IN-PHASE
T= 400-925 C
da/dN (m/cycle)
10-4
10-5
10-6
10-7
10-8
10-5
10-4
10-3
Strain Intensity Factor (√m)

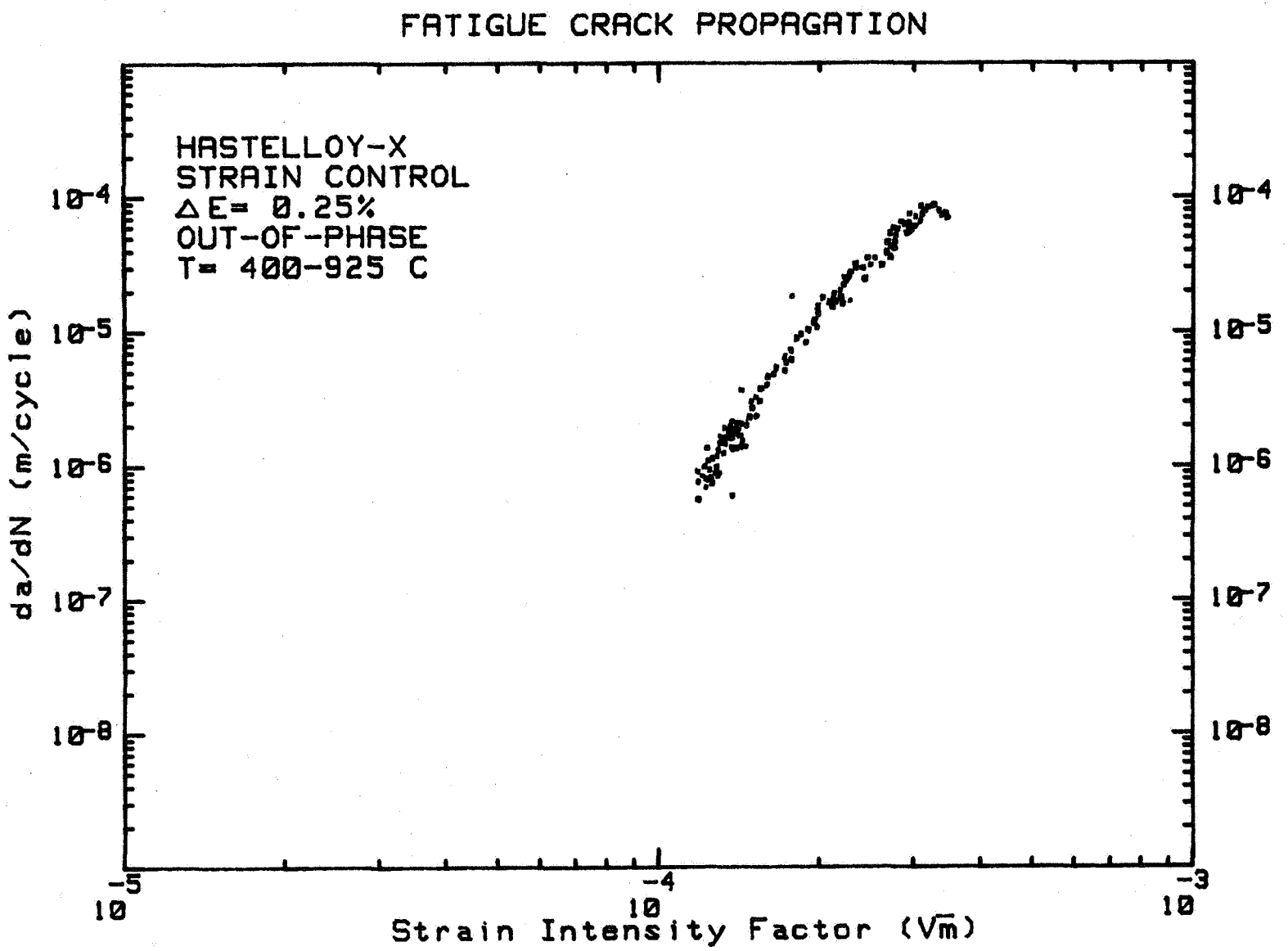
FATIGUE CRACK PROPAGATION
HASTELLOY-X
STRAIN CONTROL
ΔE= 0.25%
OUT-OF-PHASE
T= 400-925 C
da/dN (m/cycle)
10-4
10-5
10-6
10-7
10-8
10-5
10-4
10-3
Strain Intensity Factor (√m)

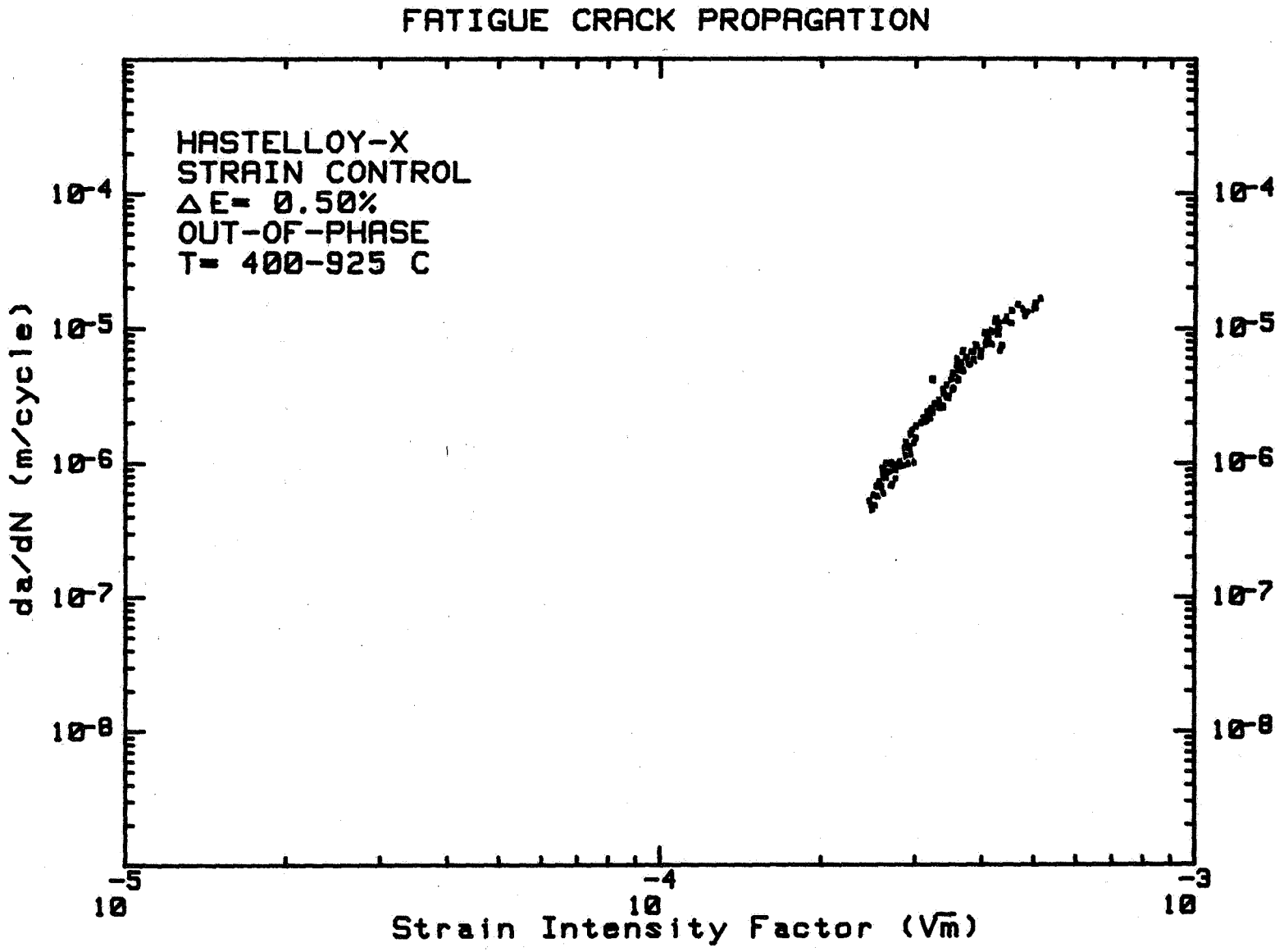
FATIGUE CRACK PROPAGATION
HASTELLOY-X
STRAIN CONTROL
ΔE= 0.50%
OUT-OF-PHASE
T= 400-925 C
da/dN (m/cycle)
10-4
10-5
10-6
10-7
10-8
10-5
10-4
10-3
Strain Intensity Factor (√m)

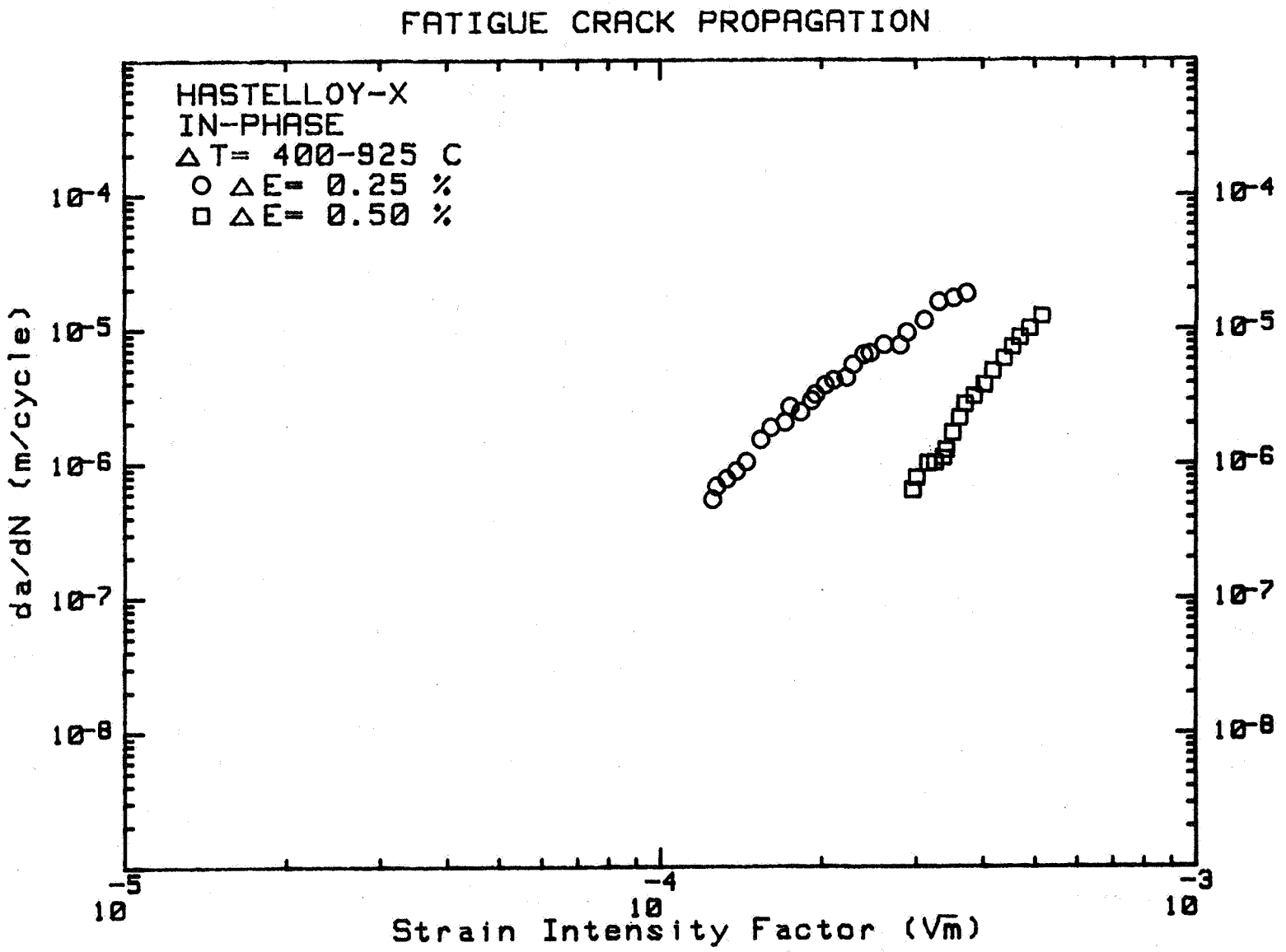
FATIGUE CRACK PROPAGATION
HASTELLOY-X
IN-PHASE
△T= 400-925 C
○ △E= 0.25 %
□ △E= 0.50 %
da/dN (m/cycle)
10-4
10-5
10-6
10-7
10-8
10-5
10-4
10-3
Strain Intensity Factor (√m)

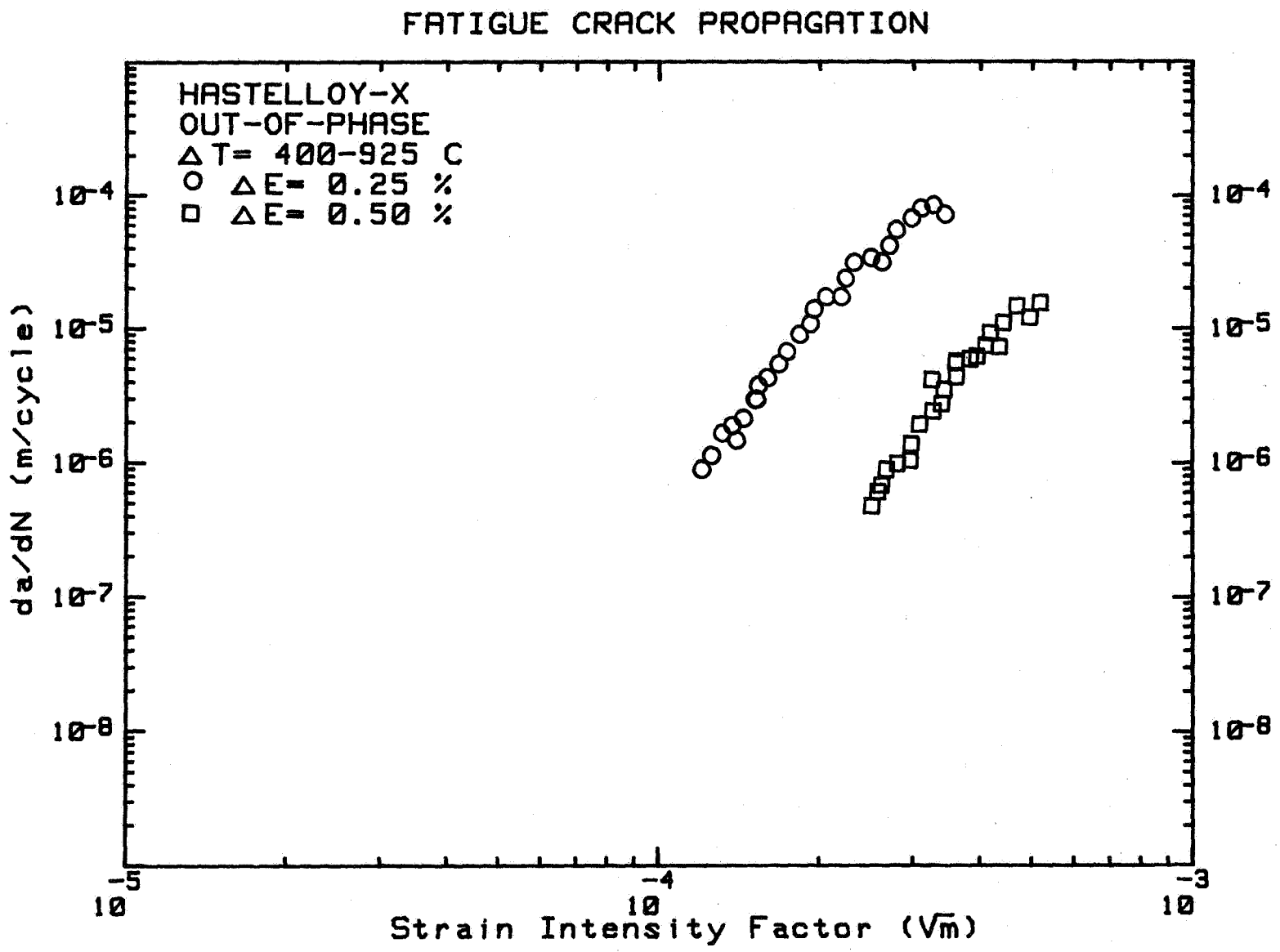
FATIGUE CRACK PROPAGATION
HASTELLOY-X
OUT-OF-PHASE
ΔT= 400-925 C
○ ΔE= 0.25 %
□ ΔE= 0.50 %
da/dN (m/cycle)
10-4
10-5
10-6
10-7
10-8
10-5
10-4
10-3
Strain Intensity Factor (√m)

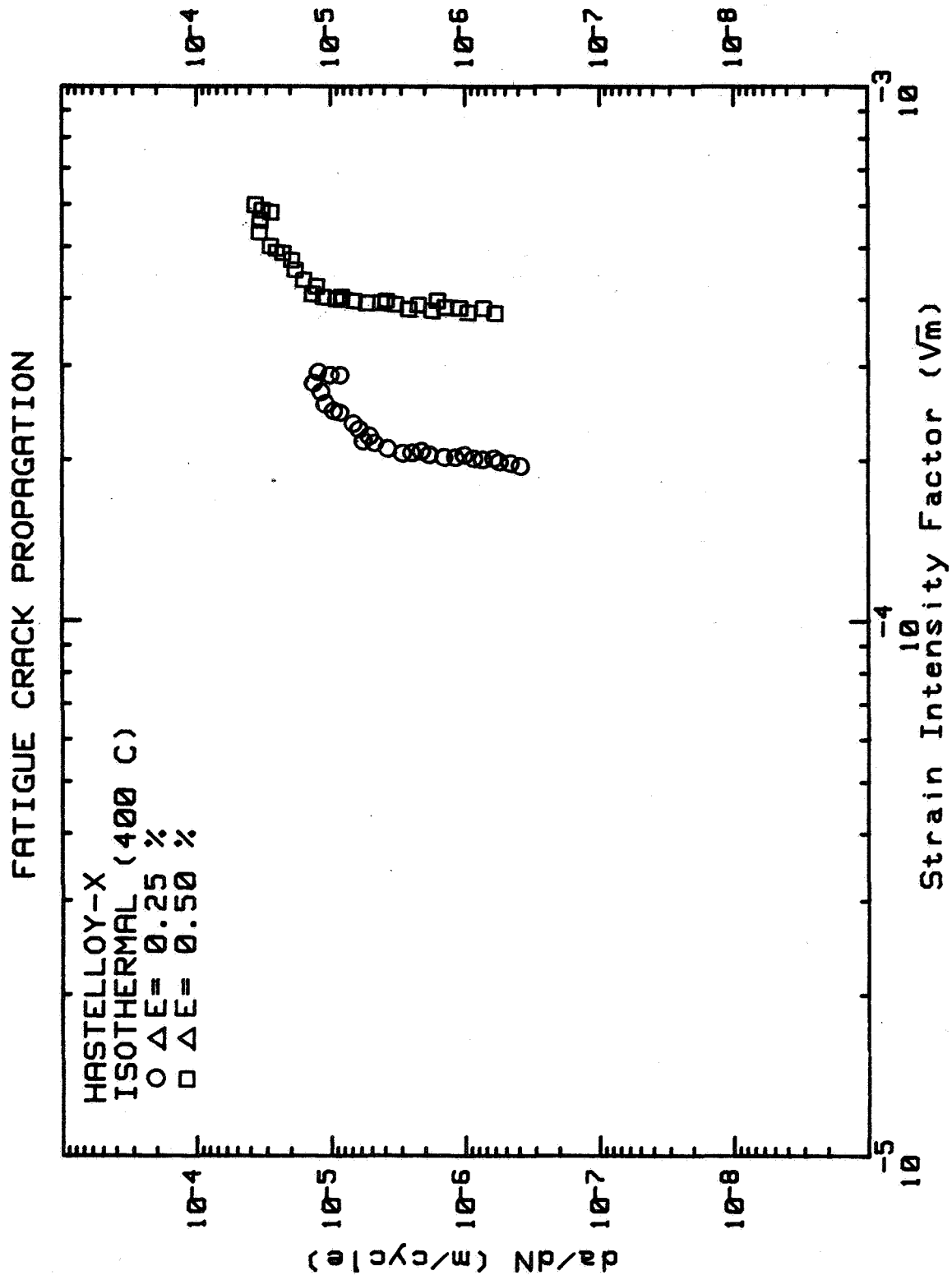
FATIGUE CRACK PROPAGATION
HASTELLOY-X
ISOTHERMAL (400 C)
○ ΔE= 0.25 %
□ ΔE= 0.50 %
da/dN (m/cycle)
Strain Intensity Factor (√m)
10-4
10-5
10-6
10-7
10-8
10-3
10-4
10-5

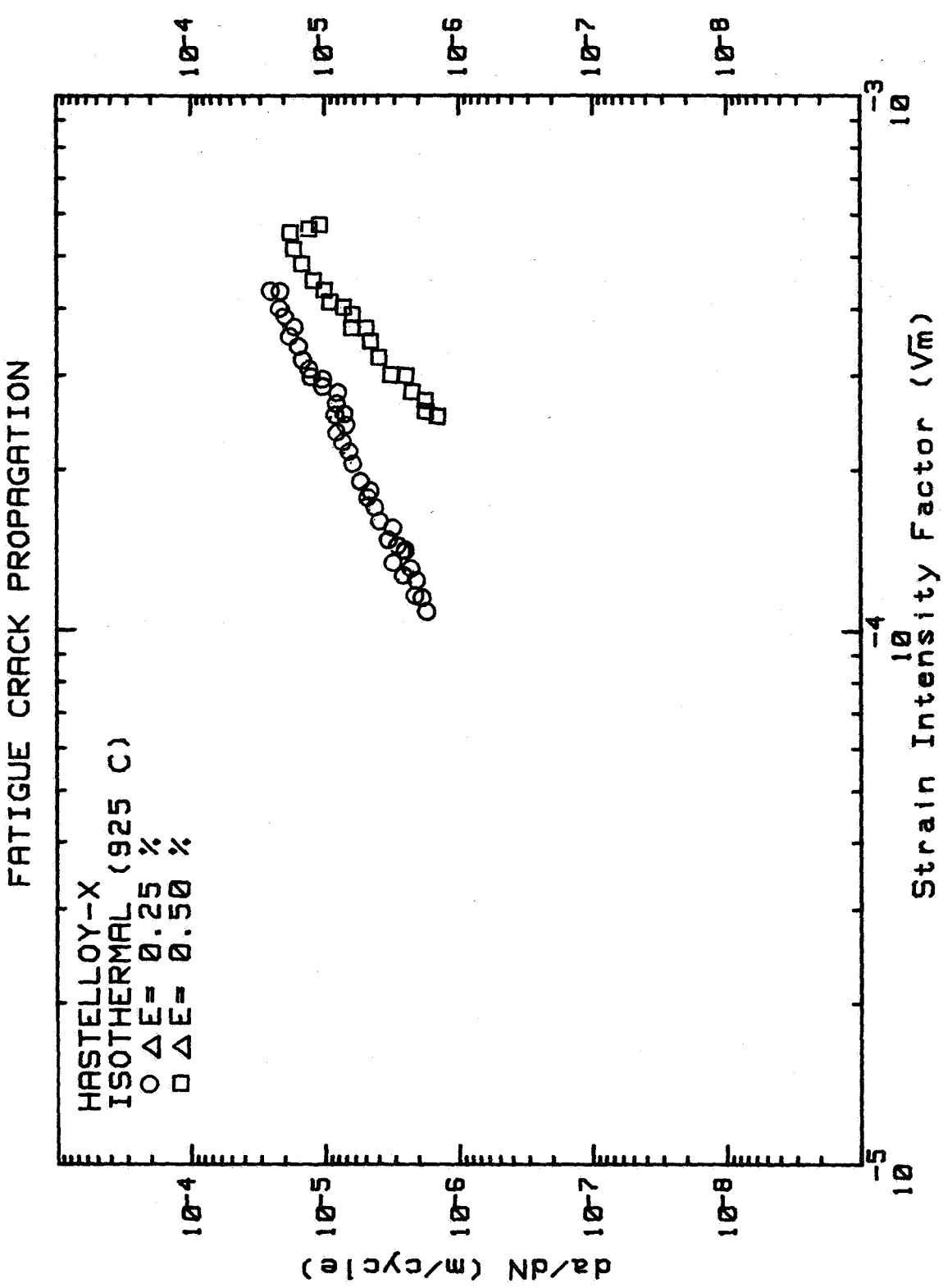
FATIGUE CRACK PROPAGATION
HASTELLOY-X
ISOTHERMAL (925 C)
○ ΔE= 0.25 %
□ ΔE= 0.50 %
da/dN (m/cycle)
Strain Intensity Factor (√m)
10-4
10-5
10-6
10-7
10-8
10-3
10-4
10-5

1. Report No.	2. Government Accession No.	3. Recipient's Catalog No.
NASA CR-175048 USAAVSCOM-TR-86-C-4		

4. Title and Subtitle	5. Report Date
Thermal-Mechanical Fatigue Behavior of Nickel-Base Superalloys	March 1986
	6. Performing Organization Code

7. Author(s)	8. Performing Organization Report No.
R.M. Pelloux and N. Marchand	None
	10. Work Unit No.

9. Performing Organization Name and Address	11. Contract or Grant No.
Massachusetts Institute of Technology Department of Materials Science and Engineering Cambridge, Massachusetts 02139	NAG 3-280
	13. Type of Report and Period Covered
12. Sponsoring Agency Name and Address	Contractor Report
U.S. Army Aviation Research and Technology Activity - AVSCOM, Propulsion Directorate, Lewis Research Center Cleveland, Ohio 44135 and NASA Lewis Research Center Cleveland, Ohio 44135	14. Sponsoring Agency Code 505-63-11

15. Supplementary Notes

Final report. Project Manager, Robert C. Bill, Propulsion Directorate, U.S. Army Aviation Research and Technology Activity - AVSCOM, Cleveland, Ohio 44135.

16. Abstract

This report presents the main achievements of a 36-month research program the main objective of which was to gain more insight into the problem of crack growth under thermal mechanical fatigue (TMF) conditions. This program was conducted at M.I.T. for the period of September 1982 to September 1985 for the NASA Lewis Research Center under Contract NAG 3-280. The program was arranged into five technical tasks. Under Task I, the literature of TMF data was reviewed. The goal was to identify the crack propagation conditions in aircraft engines (hot section) and to assess the validity of conventional fracture mechanics parameters to address TMF crack growth. The second task defined the test facilities, test specimen and the testing conditions needed to establish the effectiveness of data correlation parameters identified in Task I. Three materials (Inconel X-750, Hastelloy-X, and B-1900+Hf) were chosen for the program. Task II was accomplished in collaboration with Pratt & Whitney Aircraft engineers. Under Task III, a computerized testing system to measure the TMF behavior (LCF and CG behaviors) of various alloy systems was built. The software used to run isothermal and TMF tests was also developed. Built around a conventional servohydraulic machine, the system is capable of push-pull tests under stress or strain and temperature controlled conditions in the temperature range of 25°C to 1050°C. A crack propagation test program was defined and conducted under Task IV. The test variables included strain range, strain rate (frequency) and temperature. Task V correlated and generalized the Task IV data for isothermal and variable temperature conditions so that several crack propagation parameters could be compared and evaluated. The structural damage (mode of cracking and dislocation substructure) under TMF cycling was identified and contrasted with the isothermal damage to achieve a sound fundamental mechanistic understanding of TMF.

17. Key Words (Suggested by Author(s))	18. Distribution Statement
Fatigue; Crack growth; Thermo-mechanical fatigue; Superalloys; Mechanisms	Unclassified - unlimited STAR Category 26

19. Security Classif. (of this report)	20. Security Classif. (of this page)	21. No. of pages	22. Price*
Unclassified	Unclassified	183	A09

*For sale by the National Technical Information Service, Springfield, Virginia 22161